Multiscale Molecular Simulations of Heat and Mass Transfer at Multiphase Flow Interfaces

by

Kai Gu

A dissertation submitted to the Graduate Faculty in Mechanical Engineering in partial
fulfillment of the requirements for the degree of Doctor of Philosophy,
The City University of New York

2010

This manuscript has been read and accepted for the
Graduate Faculty in Mechanical Engineering in satisfaction of the
dissertation requirement for the degree of Doctor of Philosophy.

	Dr. Charles B. Watkins
Date	Chair of Examining Committee
	Dr. Mumtaz K. Kassir
Date	Executive Officer

Dr. Joel Koplik
Dr. Jeffrey Morris
Dr. Taehun Lee
Dr. Yiannis Andreopoulos
Dr. Charles B. Watkins
Supervision Committee

THE CITY UNIVERSITY OF NEW YORK

Abstract

Multiscale Molecular Simulations of Heat and Mass Transfer at Multiphase Flow Interfaces

by

Kai Gu

Advisor: Professor Charles B. Watkins

Co-advisor: Professor Joel Koplik

Molecular simulation is employed to investigate heat and mass transfer at multiscale, multiphase flow interfaces for solid-gas, liquid-vapor and solid-liquid-vapor interfacial systems in argon. The multiscale systems considered involve a gas/vapor Knudsen layer with a length scale on the order of several mean free paths over an interface with nanoscale molecular interactions between the gas and the condensed phase. To improve simulation efficiency for such systems, a multiscale hybrid method for coupling the direct simulation Monte Carlo (DSMC) method to the nonequilibrium molecular dynamics (NEMD) method is introduced. It incorporates a new, modified generalized soft sphere (MGSS), DSMC molecular collision model to improve the poor computational efficiency of the traditional generalized soft sphere GSS model and to achieve DSMC compatibility with the Lennard-Jones molecular interactions of the NEMD method. Both equilibrium and nonequilibrium gas-solid systems are simulated to validate the method. For liquid-vapor interfaces, physically consistent procedures are developed to define the boundaries of the interphase region between the liquid and vapor phases, which can be applied to equilibrium or nonequilibrium systems. Simulations of liquid-vapor equilibrium systems are performed to demonstrate the improved precision of this new method over alternative methods. The new hybrid molecular simulation method and interphase boundary definitions are employed to study the condensation of saturated argon vapor flowing tangentially across a stationary cooled substrate, at nanoscale resolution. Unsteady and quasi-steady interfacial properties and heat and mass transfer parameters are analyzed. Results within the Knudsen layer are compared with kinetic theory analytical and molecular simulation results.

Acknowledgements

I would like to thank my advisor, Dr. Charles B. Watkins, for his enthusiastic advisement and the great opportunity of this challenging research experience. I am also grateful to my co-advisor, Dr. Joel Koplik, for his invaluable suggestions and precious guidance. Their intelligence and patience have given me inspiration and encouragement throughout this work. I must thank those who have provided me all possible support, both technically and financially that enabled this work to keep progressing: Drs. Jeffrey Morris, Yiannis Andreopoulos and Taehun Lee.

I would like to thank my parents for their support during my entire 20-year student career. Finally, I am very grateful to my fiancée, Desiree for her companionship and encouragement during these years.

Table of Contents

List of Tables

List of Figures

List of Symbols and Abbreviations

a	cut-off relative speed in MGSS model
b	parameter in MGSS model
b_2	second virial coefficient.
BTE	Boltzmann transport equation
$\mathbf{c}$	individual molecular velocities vector
$\mathbf{c}^{'}$	thermal velocities
$c_{i,\alpha}^{'}$	thermal velocities of molecule i at α
$\mathbf{c}_j^{'''}$	difference between molecule velocity and its IP velocity
c_m	most molecular thermal velocity
$\mathbf{c}_0$	mean molecular velocities vector; stream velocity
c_r	relative velocity of two collision particle
$\mathbf{c}_\mathbf{r}^*$	post collision relative velocity
c_x, c_y, c_z	molecular velocities in *x, y, z* directions
CBA	Consistent Boltzmann Algorithm
C_g	criteria number of neighboring particles in gas phase
C_l	criteria number of neighboring particles in liquid phase
d	molecular diameter, liquid-vapor thickness
DSMC	Direct Simulation Monte Carlo
$\dot{E}$	energy conservation flux
E_{int}	internal energy
E_t	translational energy

E_{pot}	potential energy
EOS	equation of state
$f(.)$	velocity distribution function
f_0	Maxwellian distribution function
f^{out}	outgoing distribution function at liquid boundary
f^*	post collision distribution function
$F(.)$	normalized velocity distribution function
F_e	normalized evaporation distribution function
F_N	number of real molecules represented by the simulated one
$\mathbf{F}$	force vector
$\mathbf{F}_i$	force exerted on molecule i
$\mathbf{F}_{ij}$	interaction force between molecule i and molecule j
$g(.)$	density radial distribution function
GHS	generalized hard sphere
GSS	generalized soft sphere
ΔH	latent heat of vaporization per unit mass
h	specific enthalpy
h'	“slice” thickness in y direction
L_K	thermal resistance length
MGSS	modified generalized soft sphere
IP	information preservation technique
I-J	Lennard-Jones potential

$\left\langle J_{evap}^{sp} \right\rangle$	ensemble average of spontaneous evaporation number flux
$\left\langle J_{out} \right\rangle$	ensemble average of coming out number flux above the interphase
$\left\langle J_{cnds} \right\rangle$	ensemble average of condensation number flux
$\left\langle J_{coll} \right\rangle$	ensemble average of colliding-on-liquid number flux
k_B	Boltzmann constant
k	slope of the curve
K	thermal conductivity
Kn	Knudsen number
l_j	parameters in MGSS model
L	length scale
LTE	local thermal equilibrium
m	molecular mass
m_r	reduced mass of two colliding molecules
MD	molecular dynamics
MGHS	modified general hard sphere
MSD	mean square displacement
NTC	no timer counter
n_∞	upstream number density
n	number density
N	molecule number in the cell or volume
$< N >$	average molecule number

N'	molecule number in the thin slice volume
N_c,	number of candidate collision pairs from each cell
N_μ	total number of real molecules in one cell
NEMD	nonequilibrium molecular dynamics
NS	Navier-Stokes equation
ODE	ordinary differential equation
p	pressure
q_α	heat flux
Q	physical quantity
r_{list}	radial of Verlet neighbor list
$\mathbf{r}_i$	molecule *i* position
r_{ij}	distance of molecule *i* and *j*
$r_{\max}$	distance maximizing *g(r)*
R	gas constant
R'	region of a thin slice of sphere
RDF	radial distribution function
$R^2(\tau)$	mean square displacement
R_f	random number (0-1) uniform distribute
R_K	thermal resistance
S_∞	velocity ration in condensation direction
$S_{x\infty}$	velocity ration in tangential direction
SRK	Soave-Redlich-Kwong EOS

ΔT_w	temperature slip at the solid surface
T_∞	upstream temperature
T_L	liquid surface temperature (Kinetic theory)
T_l	liquid surface temperature (molecular simulation)
T_I	liquid-vapor interphase temperature
U_∞	upstream tangential velocity in x direction
$U(y)$	macro velocity at x direction as a function of y
VHS	variable hard sphere
VSS	variable soft sphere
V_∞	upstream velocity in y direction
$V(y)$	macro velocity at y direction as a function of y
V_{cell}	cell volume
V_J	volume of bin J
V^{LJ}	Lennard-Jones potential energy
V'	volume of thin slice of a sphere
W	start and end time point of window period
x	*x* direction
y	*y* direction
y_v	vapor boundary location
y_l	liquid boundary location
y'	moving interface normal coordinate
Y	CBA factor

z	z direction

Greek

α	parameter
β	parameter
β_j	parameter in MGSS model
β_c	inverted temperature criteria number
δ	mean molecular spacing
δ_2	correcting value in Predictor-corrector algorithm
ε	the characteristic energy
ε_{sg}	interaction parameter between solid and gas molecules
γ	surface tension
$\Gamma(.)$	gamma function
$\Gamma(.,.)$	upper incomplete gamma function
$\gamma(.,.)$	lower incomplete gamma function
χ	the deflection angle, mass flux ratio
κ	thermal conductivity
λ	mean free path
λ_e	reference mean free path
μ	viscosity
Ω	collision angle parameter
$\Omega^{(1,1)*}$	integral relations in [62]

$\Omega^{(2,2)*}$	integral relations in [62]
ρ	mass density
σ	molecular collision or interaction parameter
σ_c	condensation coefficient
σ_D	viscosity cross section
σ_μ	momentum cross section
σ_e	condensation coefficient
σ_T	molecular collision cross section
σ_w	virtual density of reflected vapor molecules
θ	collision referent plane angle
τ	time
$\Delta\tau$	time steps
τ_{ij}	stress tensor
$\Pi_{\alpha\beta}$	stress tensor
Φ	potential energy
Π'	viscous stress tensor
ν	mean collision frequency
η	reduced mass density
ζ	reduced molecular velocity

Subscripts

1	solution for unity evaporation/condensation coefficient moment

c	critical condition; cut-off
cell	sampling cell
coll	vapor molecules colliding on liquid surface
cnds	condensation
e	evaporation
evap	evaporation
film	liquid film
v	vapor boundary
l	liquid
i	molecular i
I	interphase
max	max value
out	coming out molecules
ref	reference
sg	solid-liquid interaction
S	substrate
cell	sampling cell
v	vapor
w	wall, liquid/vapor next to the solid surface
x	coordinate paralleling to interface
y	coordinate normal to interface
α	direction

β	direction
∞	upstream condition
$\perp$	normal to the surface
$\parallel$	parallel with the surface

Superscripts

bar	time average
LJ	Lennard-Jones potential energy
p	predictor steps
c	corrector steps
sp	spontaneous
$*$	normalized
$+$	direction upward to vapor phase
$-$	direction downward to liquid phase
$\langle\ \rangle$	ensemble average
$\{\ \}$	average over a group of molecules

Chapter 1

Introduction

Molecular simulation of interfacial heat and mass transport in multiscale, multiphase flow systems is the focus of the present research. These systems have length scales spanning the disparate scales of molecular diameters and molecular collisions. (For argon at standard conditions, the effective hard sphere molecular diameter is 0.4 nm, while the mean free path is 63 nm.) The present system of ultimate interest is the unsteady, nonequilibrium deposition of a nanoscale liquid film onto a solid substrate from a microscale bulk saturated vapor flow over it. Interfacial transport phenomena involving condensation or evaporation have not been examined at this resolution in the presence of bulk flow but are of immense scientific interest and practical relevance for heat and mass transfer involving phase change in microscale heat exchangers, chemical or physical vapor deposition in micro fabrication and thin-film coating processes, dew and frost formation with wind, and post-nucleation cloud and fog microphysics.

In the first part of the research described herein, an atomistic hybrid multiscale method for molecular simulation of multiphase interfacial flow systems was developed by coupling direct simulation Monte Carlo (DSMC) to nonequilibrium molecular dynamics (NEMD). The development of the method is a preliminary step that facilitates the simulation of the solid-liquid-vapor condensation system. The method is initially tested on solid-gas systems.

As a further preliminary step for investigation of transport in unsteady, nonequilibrium condensation, a robust procedure was developed to resolve the diffuse interface that exists between liquid and vapor at the nanoscale level. The method, which is more precise and adaptable to nonequilibrium systems than previous approaches, is validated by extensive molecular simulation of an equilibrium solid-liquid-vapor interfacial system.

With these preliminary developments in place, the molecular simulation of nonequilibrium condensation or evaporation from a nanoscale liquid film onto a molecular solid substrate and the study of interfacial properties in the system are made possible. Finally, the research culminates in the investigation of multiscale molecular heat and mass transport phenomena in the solid-liquid-vapor interfacial system of condensing flow onto a substrate with bulk flow.

1.1 Objectives and Motivation

The context of the present research is systems where nanoscale effects dominate in a small but significant portion of a microscale physical region, as opposed to only at the boundaries. Investigation of solid-liquid-vapor heat and mass transport phenomena from this perspective is in its infancy and has been hampered by lack of an appropriate simulation tool. Development of such a tool was called for almost a decade ago in the molecular dynamics heat transfer review paper by Maruyama [1], but no satisfactory tool emerged until the present development of an atomistic hybrid multiscale method for flow over a multiphase interface, which was initially applied to a solid-gas interface [2]. The primary goals of the present research were two-fold:

1. To develop the necessary molecular simulation tools for multiphase interfacial flow systems; and

2. To demonstrate the power of these tools by applying them to investigate, for the first time, molecular, heat and mass transport phenomena at a solid-liquid-vapor interface with bulk flow over the interface.

The fundamental approach can be extended to the study of systems with many different configurations. Although herein the solid substrates considered will be solid molecular crystalline structures with uniform surfaces, the approach can be extended to cases with nanoscale surface features. The formation of any intermediate condensate states in systems involving initially bare surfaces can be studied and the bulk flow gases can be the vapor of the condensed state, noncondensable gas, or mixtures of both species. The approach can clarify the thermophysics surrounding unusual phenomena, such as, inverted temperature profiles in the vapor [3] that occur under certain conditions. The simulation tools also can probe the effects of system parameters on heat and mass transfer at the interface to establish a qualitative knowledge base for the design of engineered systems. The imposed gas bulk parameters can include density, velocity, temperature, and vapor concentration and saturation. It will be possible to examine the influence of solid surface interaction characteristics such as wettability, solid molecular mass, lattice temperatures, and surface roughness. In addition, the role of interfacial characteristics such as fluid shear and surface tension can be explored.

As an example of the perspective of the present research, consider how it applies to condensation and evaporation phenomena with flow. At nanoscale, liquid-vapor phase interfaces are distinguished by transitions in molecular density across a finite length, so-called “interphase,” interfacial region, which away from the triple point, is a few molecular diameters thick. See Fig. 1, reproduced from Carey [4]. The density profiles and thickness of this region can be obtained under equilibrium conditions with molecular capillary theory but the region is subject to a high degree of fluctuations within its core [4]. In this mesoscale perspective, the bulk vapor region of interest extends several mean free paths or more above the interface and is in shear and slip motion generally parallel to the interface. The bulk flow is induced by an external driving flow.

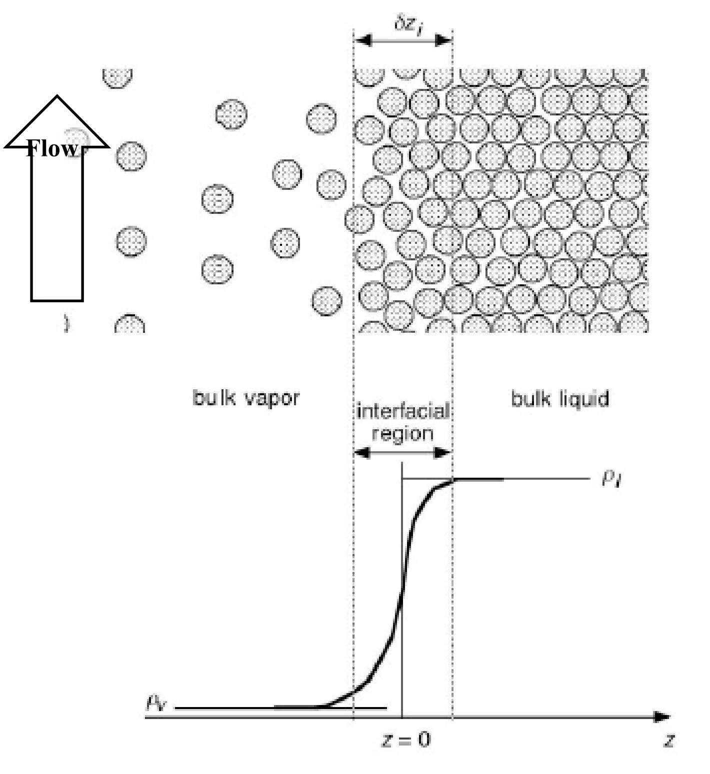

Fig. (1. 1) liquid-vapor interface with flow [4]

To capture the nanoscale physics of phase transition, the proposed simulations will resolve vapor/liquid interfaces by tracking individual molecules even though the ultimate engineering interest is on averaging the nanoscale detail of individual molecules and their thermal motions. The effect of nanoscale dynamics in the liquid-vapor interface has an important effect on vapor/liquid phase change processes in microscale and nanoscale thermophysics and transport [4].

1.2 Micro/Nano/Mesoscale Interfacial Simulation

1.2.1 Direct Simulation Monte Carlo Method for Microscale Systems

Gas or vapor flow phenomena at length scales on the order of a mean free path are no longer governed by continuum fluid dynamics but are in the transition regime between continuum and free molecular flow. This regime is distinguished by a Knudsen number (Kn $=\lambda/d$), the ratio of mean free path to a characteristic flow dimension, greater than 0.1. Gas flow within a few mean free paths of a surface and flow about an object with dimensions of the order of a few mean free paths are examples of such flows. In the case of transition flow near a surface, a kinetic boundary layer, known as the Knudsen layer, exists.

Kinetic theory modeling, based on the Boltzmann equation, can be applied to analyze the molecular motions that comprise the flow within the Knudsen layer. Knudsen layer analyses for vapor flow over its dense phase in single component condensing or evaporating flow systems was reviewed by Ytrehus [5]. However, kinetic theory cannot resolve the detailed nanoscale thermophysics of the interphase region. Kinetic theory approaches rely on modeled interfacial boundary condition approximations using the concepts of evaporation and condensation coefficients, and cannot readily model complex flow geometries and complex transient dynamics.

Molecular kinetic simulation can overcome some of the restrictions of kinetic theory analyses for transition flows. Direct simulation Monte Carlo or DSMC [6,7] is a relatively efficient and adaptable method for molecular simulation of dilute gas flows in the transition regime; it is equivalent to solution of the Boltzmann equation. It employs simulation particles to represent the motions and collisions of molecules using simplified molecular interaction mechanics. The particle statistics, when "sampled" by ensemble averaging the results of a sufficient number of independent simulation trials are a representation of the molecular statistics. The particle statistics are then used to compute macroscopic thermodynamic properties and fluid dynamic velocities.

In DSMC simulation, as in kinetic theory solutions, modeled interface boundary conditions are required. They are necessarily restricted to simplified mechanical models based on average surface collision dynamics or to statistically averaged particle flux distributions based on simplified molecular interactions at an interface [8]. This latter fact is actually an advantage in devising simple gas/gas outer boundary treatments in molecular simulations. However, nanoscale multiphase interfacial physics cannot be resolved. Carey [8] cites a number of examples where DSMC has been applied to microscale problems involving vapor/liquid phase transition under these restrictions. Moreover, DSMC simulation is limited to dilute gases and, like other kinetic theory methods, cannot resolve the interphase region. It is also inefficient at resolving low mean flow velocities because of statistical error.

Traditional DSMC can be modified to improve its ability to handle denser gas and lower speed flow but, in some cases, these modifications impose other limitations. The statistical error in low-speed simulations is due to the difficulty in extracting a weak velocity signal from both physical (thermal fluctuations) and non-physical (Monte Carlo stochastic variance) noise. It can generally be reduced to an acceptable level by sufficiently large sampling and applying more advanced DSMC algorithms [9]. The level of sampling required for low speeds is traditionally regarded in the DSMC community as excessive but in the present context, where nonequilibrium molecular dynamics simulation is also sampled, it becomes less so since it is comparable to the level of sampling required for molecular dynamics. More details about the DSMC method are given in Appendix A.

1.2.2 Nonequilibrium Molecular Dynamics Method for Nanoscale Systems

Classical molecular dynamics simulation (MD) and its history are described in a number of texts and reference works [10-12]. It is a simulation method that tracks the motions of individual atoms, molecules, molecular clusters, or ions. It is based on applying Newtonian mechanics to these motions with interparticle attractive and repulsive forces determined by specified potential energy functions. The MD method is appealing for interfacial physics because it can treat both dilute and concentrated molecular systems and thereby study the interaction of individual gas molecules with the liquid or solid molecules comprising a multiphase interface. Both phase coexistence and phase transitions at a wall [13-15], as well as interfacial coalescence and rupture of free liquid droplets [16,17] have been modeled in this way. Related applications of MD to interfacial dynamics include the spreading of liquid nanodroplets and films on solid surfaces [18-20], atomic vibrations in realistic lattice solids

[21], and flow over nanoscale chemical and topographical features [22-24].

Application of MD to nanoscale heat transfer phenomena has been reviewed in a number of articles [1,25,26]. Among those recent studies that have investigated vapor/liquid/solid interfacial systems are the equilibrium thin film simulations of Wemhoff and Carey [27,28], the vaporization and recondensation studies of Yi et al. [29], the near triple-phase contact line simulation of Ji and Yan [30], and the heterogeneous nucleation simulations of Kimura and Maruyama.[31] and Rozas and Kraska [32].

When the MD method is applied to fluids that are not in equilibrium because they are subjected to imposed mechanical or thermal driving, it is often referred to as nonequilibrium molecular dynamics or NEMD. The substantial disadvantage of MD and NEMD simulations is that they are so highly computationally intensive that its use is restricted to microscopically small systems. For a liquid, for example, even current large-scale simulations at the million-atom level treat systems only tens of nanometers in size. In pure dilute gas simulations much larger sizes are possible, but practical *multiphase* microscale systems of engineering interest are not directly accessible to NEMD. In the proposed research, NEMD cannot be applied simultaneously to the interfacial region and a much larger bulk gas flow region, which motivates the coupling methods discussed in the section that follows. Nevertheless, NEMD is a valuable tool for investigating interfacial physics and, by focusing on the nanoscale interfacial region, has often been used to develop effective parameter approximations for microscale phenomena [e.g., 8,26,33] and to derive boundary conditions for macroscale phenomena [e.g., 34-36].

A large number of investigators have employed MD and NEMD simulation in the study of evaporation and/or condensation coefficients for vapor/liquid systems under equilibrium and nonequilibrium conditions. The evaporation coefficient can be defined as the ratio of the mass flux of spontaneously evaporating molecules from the interface to the total mass flux going out from it. The condensation coefficient can be defined as the ratio of the condensed mass flux of molecules to the flux colliding at the interface. Determination of the nonequilibrium condensation coefficient, in particular, is not straightforward and has been a topic of controversy [35, 37-40]. Simulation results have generally not agreed with experimental data. However condensation coefficients for water derived from recent shock tube measurements by Kobayashi et al. [41] seem to have validated the condensation coefficient formulation and NEMD simulation results of Ishiyama et al. [37-39]. One motivation behind the interest in condensation and evaporation coefficients is that they can be used to construct a kinetic boundary condition at a vapor/liquid interface for application of kinetic methods to the vapor region. Since the interest is in an integrated simulation of the interface and the vapor region, the primary interest in these coefficients is any utility they may have in characterizing the systems to be simulated. In some cases, they also provide a convenient way of comparing the results with the experimental or simulation results of other investigators.

The key features of the interaction potential functions employed in NEMD modeling are an attractive well to form a condensed phase and a short-distance repulsion to prevent collapse. The Lennard-Jones (LJ) potential V_{LJ}

$$V_{LJ}(r) = 4\varepsilon\left[\left(\frac{\sigma}{r}\right)^{12} - \left(\frac{\sigma}{r}\right)^{6}\right] \qquad V_{WW} = \sum_{i,j=1}^{3} \frac{1}{4\pi\varepsilon_0}\frac{q_i q_j e^2}{r_{ij}} + 4\varepsilon_O\left[\left(\frac{\sigma_O}{r_{OO}}\right)^{12} - \left(\frac{\sigma_O}{r_{OO}}\right)^{6}\right] \tag{1.1}$$

is the simplest, semi-realistic example in common use, and has attractive r^{-6} and repulsive r^{-12} terms incorporating these two features, respectively. The LJ interaction is quantitatively accurate for only neutral spherically symmetric atoms such as the inert gases, but it does incorporate the key elements of any interaction and can be used to simulate generic material properties. This means that any macroscopic physical process will occur in an LJ simulation, but the numerical values of the material parameters and transport coefficients need not agree with those of any particular material. A multi-component material, such as a mixture of gases, can be modeled at this level by introducing a species-dependent coefficient for the attractive term. Most real materials involving non-inert atoms or molecules have asymmetric charge distributions requiring Coulomb, dipole, etc. interactions as well. A water molecule, for example, is quite asymmetric and explicit charges must be included in the interaction to capture its properties. The most widely used interaction potentials, SPC/E and TIP3P [42] have the form given in V_{WW} involving Coulomb interactions between the oxygen and hydrogen atoms with adjusted values of the charges q_i plus an LJ interaction centered on the oxygen to treat the remaining polarization effects. In water and in other covalently bonded materials the bond lengths are fixed by length constraints or additional interactions, and in larger molecules further such interactions are needed to treat the orientation-dependence of adjacent bonds.

The numerical values of the parameters in these interaction potentials are determined by quantum mechanical calculations, where possible, or by fitting simulation results to experimental data, otherwise. Complete, if approximate, force fields for certain classes of material have been developed in this way. Ionic solids require additional collective interactions to properly account for their distributed electrons [21], and a number of additional interaction parameters must be determined.

The effective range of the interaction provides an important qualitative distinction between Coulomb and LJ interactions. The Coulomb interaction is long-ranged and couples all charges in the system, and since the computation time is proportional to the number of interacting atomic pairs, it is $O(N^2)$ if there are N charged atoms present. In contrast, the LJ potential falls rapidly with distance and little is lost if it is cut off at a separation r well beyond the minimum of the potential well. In this case, each atom interacts only with those within the cutoff radius, and the computation time is much smaller, O(N), and simulations with much larger values of N are feasible.

Some details of NEMD are presented in Appendix B. NEMD, like DSMC, requires sampling to recover macroscopically useful quantitative results. As discussed above, it is also subject to the requirement for a large number of samples for low-speed flows.

1.2.3 DSMC-NEMD Hybrid Method for Mesoscale Systems

For engineering simulation of microscale or mesoscale gas flows interacting with a complex interface, a multiscale method with the ability to efficiently simulate the molecular gas dynamics of bulk microscale flow over an interface while resolving the computationally demanding nanoscale molecular interactions in a domain surrounding the interface would be invaluable. The ability of DSMC and NEMD, respectively, to handle these types of problems [9,12] suggests that a hybrid, combing the two, could be an effective approach to development of a multiscale method. The method developed in the present research [2] is such a hybrid.

The hybrid method employs the NEMD method to resolve nanoscale transport phenomena in the interphase region along with coupled DSMC simulation of gas flow in the remainder of the physical flow region. A hybrid simulation method with this type of flow region partitioning scheme was developed by Nedea et al. [33,43]. They coupled NEMD solution domains to Monte Carlo (MC) solution domains through the use of a buffer zone. The primary emphasis of their work is on dense hard-sphere gas systems in contrast to the emphasis on dilute real gas systems, at or below atmospheric pressure. A hybrid DSMC-NEMD gas-solid simulation method for one-way DSMC to near-surface NEMD matching, which involves repositioning of incident DSMC molecules, was developed by Yamamoto et al. [44].

The hybrid coupling method of Nedea et al. matches the macroscopic properties in overlapping buffer layers, and is not focused on ensuring mass, momentum, and heat flux continuity across the method interface. The buffer layers and the other modeling artifices they employed prevent their method from completely capturing the physics of systems with large gradients through the inter-method boundary or systems with unsteady flow. Moreover, they have not yet reported any results using their method for phase transitions with flow.

The present DSMC-NEMD hybrid method is completely particle based. There is no buffer zone between the DSMC and NEMD solution domains. Particles are freely exchanged between the domains and molecular interactions are modeled realistically. The method incorporates a new, modified generalized soft sphere (MGSS) [2] molecular collision model for the DSMC simulation domain for better computational efficiency and low temperature performance than the traditional generalized soft sphere GSS [45] model. The GSS model was developed to improve DSMC compatibility with molecular interaction potentials, such those employed in the NEMD simulation domain. The MGSS collision model is compatible with the LJ collision model for non polar molecules and the Stockmayer potential [45] approximation to potential functions such as SPC/E for polar molecules.

1.3 Interfacial System Modeling

The argon interfacial system studied is condensation from a saturated vapor flowing over an initially bare FCC solid molecule substrate maintained below the solidification temperature of argon. The solid molecules are maintained at a fixed temperature through the use of a MD thermostat as shown in Fig. (1.2). During the simulations, the liquid layer is building up constantly through the vapor molecules keeping condensing on the liquid/solid side with velocity $V(y)$. Liquid layer will be ultra thin in the order of molecule diameters, while the vapor will be in the scale of several mean free paths. The vapor flow is controlled by the upper boundary with specified temperature T_∞, density n_∞, and an imposed velocity component parallel to the interface, U_∞ and periodic boundary conditions will be applied to the directions, x and z.

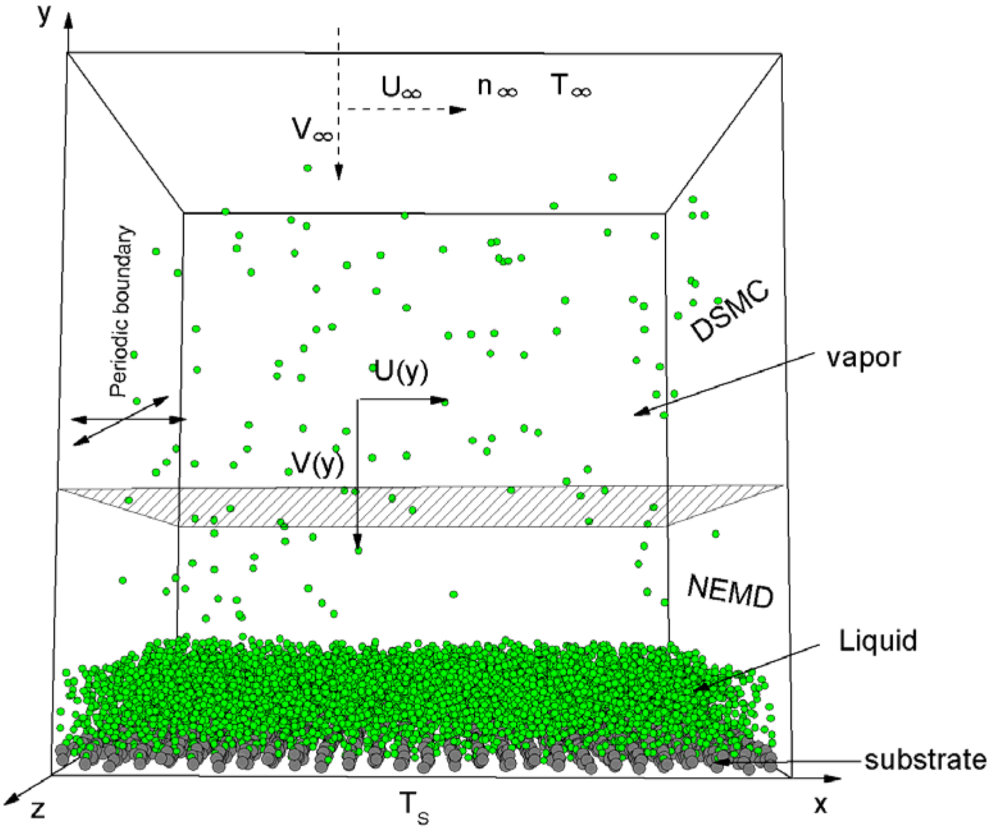

Fig. (1. 2) Physical system of ultra thin liquid films condensed on solid substrates (MD vertical region greatly exaggerated)

An implicit DSMC flux boundary condition [46] is imposed in the vertical direction at the entrance to the reservoir, while the bottom DSMC boundary condition is replaced by the hybrid coupling algorithm. It should be noted that, in addition to the computational efficiency achieved by using DSMC for most of the vapor phase simulation, it simplifies the upper boundary treatment over the various flux treatments of such boundaries implemented by researchers for vapor simulations using only NEMD [e.g. 27,28,37,40] in systems without imposed flow. Furthermore, issues associated with maintenance of DSMC reservoirs, such as the upper boundary, were systematically studied by Garcia and Wagner [47] and found to be substantially less complex than those associated with NEMD.

1.4 Organization of the Dissertation

This dissertation is divided into five chapters plus appendices, A through D.

- Chapter 1, the introduction, gives an overview of the research.
- Chapter 2 presents the hybrid DSMC-MD method and applies it to study gas-surface molecular interactions.
- Chapter 3 describes the physically consistent MD procedures developed to define the boundaries between the interphase and the liquid and vapor phases and applies them to study an equilibrium solid-liquid-vapor interfacial system, including freezing.
- Chapter 4 describes the hybrid simulation method of condensation of saturated argon vapor flowing tangentially across a stationary cooled substrate.
- Chapter 5 presents an overall summary, conclusions, and possible areas for future work.
- Appendix A and Appendix B present some details pertaining to DSMC and MD algorithms, respectively.
- Appendix C presents definite integral formulas, used in the research, that arise in kinetic theory from taking moments of the velocity distribution function.
- Appendix D presents the derivation of the modified moment solution for Knudsen layer structure used in Chapter 4.

Chapter 2

Atomistic hybrid DSMC-NEMD method for nonequilibrium multiscale simulations

2.1 Chapter Summary

A multiscale hybrid method for coupling the direct simulation Monte Carlo (DSMC) method to the nonequilibrium molecular dynamics (NEMD) method is introduced. The method addresses Knudsen layer type gas flows within a few mean free paths of an interface or about an object with dimensions of the order of a few mean free paths. It employs the NEMD method to resolve nanoscale phenomena closest to the interface along with coupled DSMC simulation of the remainder of the Knudsen layer. The hybrid DSMC-NEMD method is a particle based algorithm without a buffer zone. It incorporates a new, modified generalized soft sphere (MGSS) molecular collision model to improve the poor computational efficiency of the traditional generalized soft sphere GSS model and to achieve DSMC compatibility with Lennard-Jones NEMD molecular interactions. An equilibrium gas, a Fourier thermal flow, and an oscillatory Couette flow, are simulated to validate the method. The method shows good agreement with Maxwell-Boltzmann theory for the equilibrium system, Chapman-Enskog theory for Fourier flow, and pure DSMC simulations for oscillatory Couette flow. Speedup in CPU time of the hybrid simulator is benchmarked against a pure NEMD simulator baseline for different system sizes and simulator domain partitions. Finally, the hybrid method is applied to investigate interaction of argon gas with solid surface molecules in a parametric study of the influence of wetting effects and solid molecular mass on energy transfer and thermal accommodation coefficients. It is determined that wetting effect strength and solid molecular mass have a significant impact on the energy transfer between gas and solid phases and thermal accommodation coefficient.

2.2 Introduction

With continued improvements in computer speed and storage capabilities, atomistic simulation methods, such as direct simulation Monte Carlo method (DSMC) and molecular dynamics (MD), have become increasingly viable options for gas dynamics research at sub-macroscopic scales. The scales of interest are distinguished by a flow Knudsen number ($Kn = \lambda/d$), the ratio of mean free path to a characteristic flow dimension, greater than 0.1.

DSMC, in particular, has been widely applied to investigate dilute gas flow phenomena at length scales on the order of a mean free path that are no longer governed by continuum fluid dynamics but are in the transition regime between continuum and free molecular flow ($0.1 \leq Kn \leq 10$). Knudsen layer type gas flows within a few mean free paths of an interface or about an object with dimensions of the order of a few mean free paths are in the transition regime.

When applied to flow over an interface, the relatively efficient DSMC method has significant limitations in its ability to address the important nanoscale interactions of gas molecules with solid or liquid molecules comprising the interface. The present research is aimed at removing this limitation with the development of a hybrid, multiscale simulation method that uses the MD method to resolve nanoscale phenomena closest to the interface along with DSMC simulation of the remainder of the Knudsen layer. Thus, the method spans the disparate scales of molecular diameters and molecular collisions. (For argon at standard conditions, the mean free path is 63 nm, while the effective hard sphere molecular diameter is 0.4 nm.) The nanoscale domain resolved near the interface may be a small but not insignificant portion of the Knudsen layer. The convention is adopted of referring to the overlapping scales of these flow domains and their resident phenomena as mesoscale.

The DSMC method was originally developed by Bird [6] and subsequent developments have been catalogued by Oran et al. [48], and Prasanth and Kakkassery [49]. It has produced strikingly accurate results in a variety of dilute gas flow simulations by introducing the notion of stochastic representative particles in place of actual gas molecules. The simulation divides tracks the motions and collisions of these particles through a flow domain, which is divided into cells, by simplified molecular interaction mechanics. DSMC collisions take place with kinetic outcomes determined by modeled molecular scattering probabilities. Macroscopic flow properties are computed from sampled particle statistics over a number of independent simulation trials, represented by ensemble or time averages. A binary collision assumption limits DSMC simulation to dilute gases.

DSMC requires interface boundary conditions for the simulation particles. These are necessarily restricted to simplified mechanical models based on average surface collision dynamics or to statistically averaged particle flux distributions based on simplified molecular interactions at the interface. Since DSMC simulation is limited to dilute gases with simplified boundary interactions, it cannot resolve complex mesoscale interfacial phenomena involving interphase molecular interaction and exchange at an interface.

Classical molecular dynamics simulation or MD dates from its conception by Alder and Wainwright [50] in the late 1950's. Its history and algorithms are described in a number of texts and reference works [e.g. 11, 12]. It is essentially a simulation method that tracks the motions of modeled individual atoms, molecules, molecular clusters, or ions. MD is based on applying Newtonian mechanics to these motions with interparticle attractive and repulsive forces determined by specified potential energy functions. Most commonly, short range interactive forces are derived from a Leonard Jones (L-J) intermolecular potential function.

The MD method is appealing for interfacial physics because it can model interaction of individual gas molecules with the liquid or solid molecules comprising a multiphase interface and can also model interphase transitions. Furthermore, it is not restricted to dilute gases and can simulate the motions of denser gases and liquid near the interface. Technically, when the MD method is applied to fluids that are not in equilibrium because they are subjected to imposed mechanical or thermal drivers, it is known as nonequilibruim molecular dynamics (NEMD).

The substantial disadvantage of MD or NEMD simulation is that it is so highly computationally intensive that its application is restricted to nanoscale systems comprised of relatively small numbers of molecules within dimensions of hundreds of nanometers. It cannot be applied to analyze mesoscale flow systems of engineering interest since it is infeasible to simultaneously apply it to the interfacial region and the larger, bulk incident-gas region. Nevertheless, it is a valuable tool for investigating interfacial physics. As in the case of DSMC, macroscopic properties can be obtained by sampling.

A multiscale method with the ability to efficiently simulate the molecular gas dynamics of bulk microscale flow over an interface, while resolving the computationally demanding nanoscale molecular interactions in a domain surrounding the interface, would be invaluable. The ability of DSMC and NEMD to handle molecular collision-scale and molecular diameter-scale types of problems, respectively, suggests that a hybrid, combing the two, could be an effective approach to development of a robust multiscale method.

Hybrid simulation schemes are abundant for microscale/continuum gas flows using DSMC coupled with Navier-Stokes, Stokes, or Euler continuum CFD methods [51-55]. Likewise, many approaches have been developed for NEMD coupled with continuum Navier-Stokes CFD for nanoscale/microscale liquid flows [56-61]. However, there has been far less work on hybridized DSMC-NEMD methods and the methods that have been developed, so far, either have substantial limitations or are untested for their ability to model certain important systems.

A combined DSMC and NEMD study of laser ablation was reported by Zeifman and Garrison [62] in which information was transferred from a NEMD flow domain to a DSMC flow domain but there was no two-way active coupling between the two domains. A hybrid DSMC-NEMD gas/solid simulation method for one-way DSMC to near-surface NEMD matching, which involves repositioning of incident DSMC molecules, was developed by Yamamoto et al. [44].

A simulation method was developed by Nedea et al. [33, 43], coupling NEMD solution domains to Monte Carlo (MC) solution domains. The MC method used is an extension of DSMC [6] that avoids the restriction of traditional DSMC to dilute gases. The primary emphasis of their work is on dense hard-sphere gas systems but they also demonstrate good results for thermally driven flow in a dilute gas channel bounded by isothermal walls [33]. However, their hybrid method is coupled by matching the macroscopic properties in overlapping buffer layers, and not focused on ensuring mass, momentum, and heat flux continuity across the method interface. This and the modeling artifices they employed may make it difficult for their method to completely capture the physics of systems with large gradients in the method interface region or unsteady flows.

In this article a new DSMC-NEMD hybrid method is introduced, which is based on DSMC particle/NEMD molecule coupling with consistent particle flux dynamics across the interface between separate DSMC and NEMD solution domains. In developing this hybrid method, special attention was paid to the molecular collision model in the DSMC domain to insure compatibility near the interface with the Leonard Jones (L-J) intermolecular potential function used in the NEMD domain. A new collision model with improved efficiency and low-temperature capability that is suitable for maintaining compatibility was also developed and implemented.

The results of validating the particle flux continuity at the DSMC-NEMD interfaces in both equilibrium and nonequilibrium systems are presented by comparisons with Maxwellian and Chapman Enskog theory, respectively. To verify the method’s accuracy in unsteady systems, an oscillatory Couette flow simulation was compared with a pure DSMC solution. In addition, the hybrid method’s computational efficiency was compared with that of the pure NEMD method for different DSMC-NEMD simulator partition size ratios and system particle numbers.

Finally, the hybrid method was applied to investigate interaction of argon gas with solid surface molecules in a mesoscale parametric study of the influence of wetting effects and solid molecular mass on energy transfer and thermal accommodation coefficients. The results are compared with results from DSMC simulations using the thermal accommodation coefficients determined from the hybrid simulations.

2.3 DSMC molecular collision modeling

Various molecular collision cross section models have been developed for use in DSMC through consideration of the intermolecular force or potential. For DSMC applications, the goal generally is to reproduce the dependence of viscosity and self diffusion on temperature of actual gases. The traditional and most widely used collision model is the variable hard sphere (VHS) model [6]. Some newer molecular collision models, such as the variable soft sphere (VSS) [63] and the generalized hard sphere (GHS) [64], have been developed to replicate more closely the actual viscosity cross section behavior of gas molecules for certain interaction potentials. The modified general hard sphere (MGHS) [65] model was developed to improve on the computational efficiency of the GHS model, which in its original form was an excessive DSMC computational burden. The MGHS model also improved low temperature performance over the GHS model.

Fan [45] proposed a physically more accurate model, generalized soft sphere (GSS), by deriving a Leonard-Jones potential function-based collision cross-section, dependent on particle collision speed. The L-J (12-6) potential function,

$$V(r_{ij}) = 4\varepsilon[(\frac{\sigma}{r_{ij}})^{12} - \varepsilon_{sg}(\frac{\sigma}{r_{ij}})^{6}] \tag{2.1}$$

is commonly used to determine the intermolecular forces in molecular dynamics simulations and was adopted for the NEMD domain of the present hybrid simulations. It characterizes both the short range repulsive forces as well as the longer range weakly attractive forces. In Eq. (2.1), r_{ij} is the distance between molecule i and molecule j; ε and σ are the characteristic energy and interaction lengths, respectively. ε_{sg} is a parameter that is not present for interactions between gas molecules but is introduced for gas-surface molecule interactions and describes the wetting effect at the gas-solid interface. It would be assigned a value of 1.0 for complete wetting. A value of 0.75 would be partial wetting and values less than 0.5 are considered non-wetting.

Since the GSS model replicates most closely the intermolecular physics in the NEMD implementation of Eq. (2.1), it is more compatible with interfaces between NEMD and DSMC domains than the other collision models. Therefore, it would seem to be a good choice for the DSMC collision model in the present hybrid method. However, if implemented as developed by Fan [45], GSS, like GHS, is computationally inefficient because its parameters cannot be obtained explicitly. A new, modified GSS (MGSS) model is introduced here, patterned after the MGHS model developed from GHS. It will be shown that MGSS improves computational efficiency and low temperature accuracy over GSS.

In the no-time counter (NTC) DSMC procedure [6], the number of candidate collision pairs from each cell is determined as

$$N_c = \frac{N\overline{N}F_N(\sigma_T c_r)_{\max}\Delta t}{2V_{cell}} \tag{2.2}$$

where N is the number of molecules in the cell, $\overline{N}$ is the average number of molecules in the cell, F_N is the number of real molecules represented by the simulated one. $(\sigma_T c_r)_{\max}$ is the maximum value of the product of total cross section and relative velocities; i.e., the maximum pairwise collision probability; and V_{cell} is the collision sampling cell volume. Subcells are used to increase the likelihood of collision pairs taking place between near neighbors. Collisions are accepted if

$$R_f < \frac{\sigma_T c_r}{(\sigma_T c_r)_{\max}} \tag{2.3}$$

where R_f is a uniformly distributed random number. To implement the GSS model, the total cross section can be written as follows:

$$\frac{\sigma_T}{\sigma^2} = \sum_j \beta_j (\frac{E_t}{\varepsilon})^{l_j} \tag{2.4}$$

where $E_t = \frac{1}{2} m_r c_r^2$, m_r is the reduced mass of two colliding molecules, and β_j and l_j are constants that are determined from a numerical least–square fit of the coefficients of viscosity

$$\mu = \frac{5}{6}(\frac{\sqrt{\pi m k_B T}}{\pi \sigma^2 \Omega^{(2,2)^*}}) \tag{2.5}$$

and self-diffusion

$$D = \frac{3kT}{16p}(\frac{\sqrt{2\pi k_B T / m_r}}{\pi \sigma^2 \Omega^{(1,1)^*}}) \tag{2.6}$$

for a simple gas in which m is the particle mass, T is the temperature, p is pressure and k_B is the Boltzmann constant, and $\Omega^{(1,1)^*}$ and $\Omega^{(2,2)^*}$ represent integral relations [45, 66] for computing the two transport coefficients from the L-J potential. Fan's GSS model [45] uses a two term formula for the diffusion and viscosity integrals, $\Omega^{(1,1)^*}$ and $\Omega^{(2,2)^*}$, to fit the data tabulated by Hirschfelder, Curtiss, and Bird [66] from numerical evaluation of the integrals. Fan's fitting results are shown in Fig. (2.1) and Fig. (2.2).

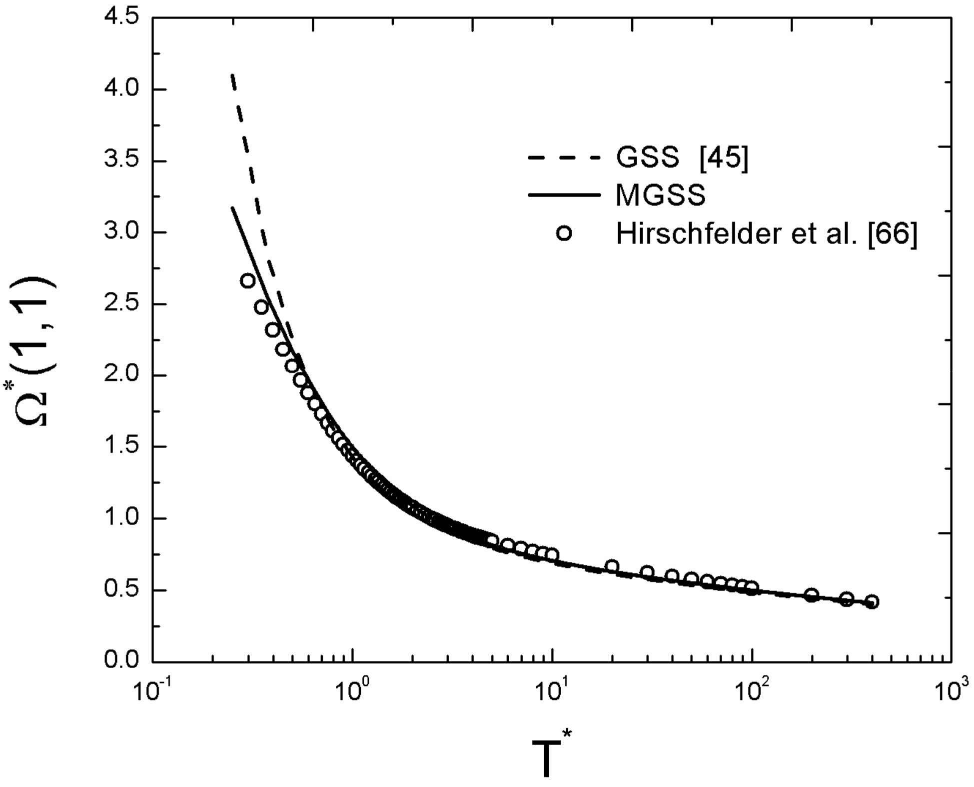

Fig. (2. 1) Comparison of viscosity integral versus normalized temperature. The temperature is normalized by ε / k_B *; for argon* $\varepsilon / k_B = 120^o K$.

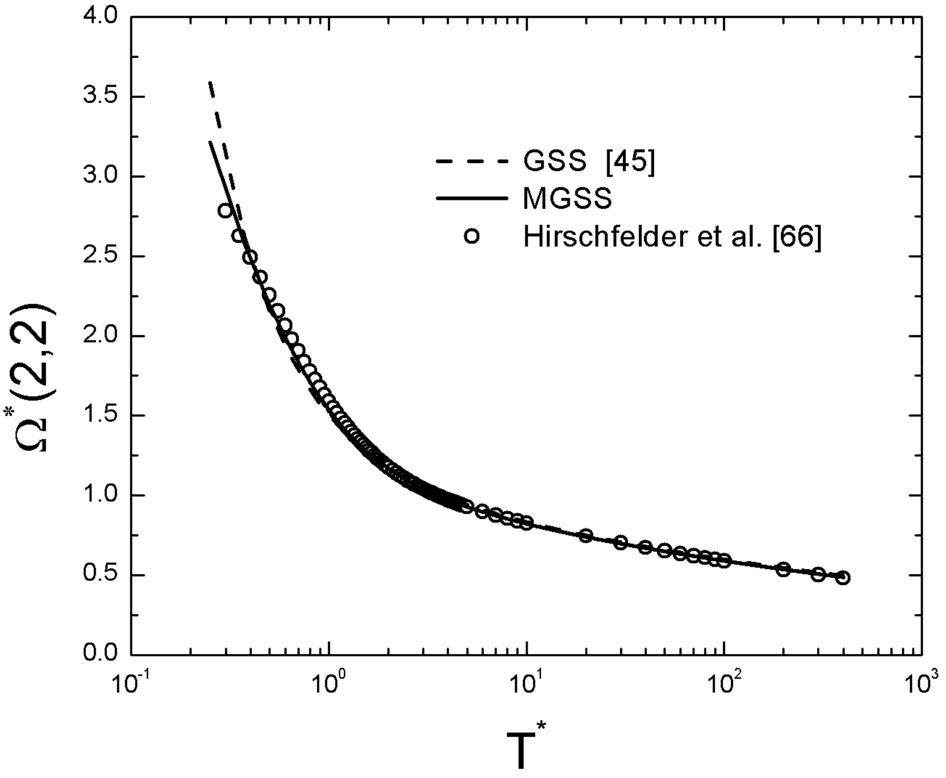

Fig. (2. 2) Comparison of diffusion integral versus normalized temperature. The temperature is normalized by ε / k_B *; for argon* $\varepsilon / k_B = 120^o K$..

The GSS model [45] has significant limitations on its implementation in a DSMC simulation. One issue is that its total cross section tends toward infinity when particles encounter low relative speed collisions. Based on Eqs. (2.2) and (2.3), this means that the number of collision candidates tested inevitably increases while the probability of a successful selection decreases during the DSMC collision algorithm. Hence, the computational expense increases due to both increased collision candidates and the testing necessary to determine collision pairs.

For the GSS model the mean pairwise collision probability can be written from Eq. (2.4) as

$$\overline{c_r\sigma_T} = \sigma^2 \iint \sum \beta_j \left(\frac{\frac{1}{2}m_r}{\varepsilon}\right)^{l_j} c_r^{2l_j+1} F_1 F_2 d\mathbf{c}_1 d\mathbf{c}_2 \tag{2.7}$$

in which F_1 and F_2 are the distribution functions of the collision pair, which has masses, m_1 and m_2. This probability, then, is a function of temperature with the resulting mean collision frequency, $\nu = n\overline{c_r\sigma_T}$, where n is the number density.

The dependence of pairwise collision probability on relative collision velocity is shown in the normalized plot of Fig. (2.3). The figure shows that the GSS collision probability rises in an unphysical manner with decreasing relative speed, eventually tending to infinity. In addition to lower computational efficiency, this results in unphysical, large collision frequencies for GSS due to the larger mean values determined from Eq. (2.7). These effects are particularly significant to simulation efficiency and accuracy at lower temperatures, where molecules are actually physically more inert.

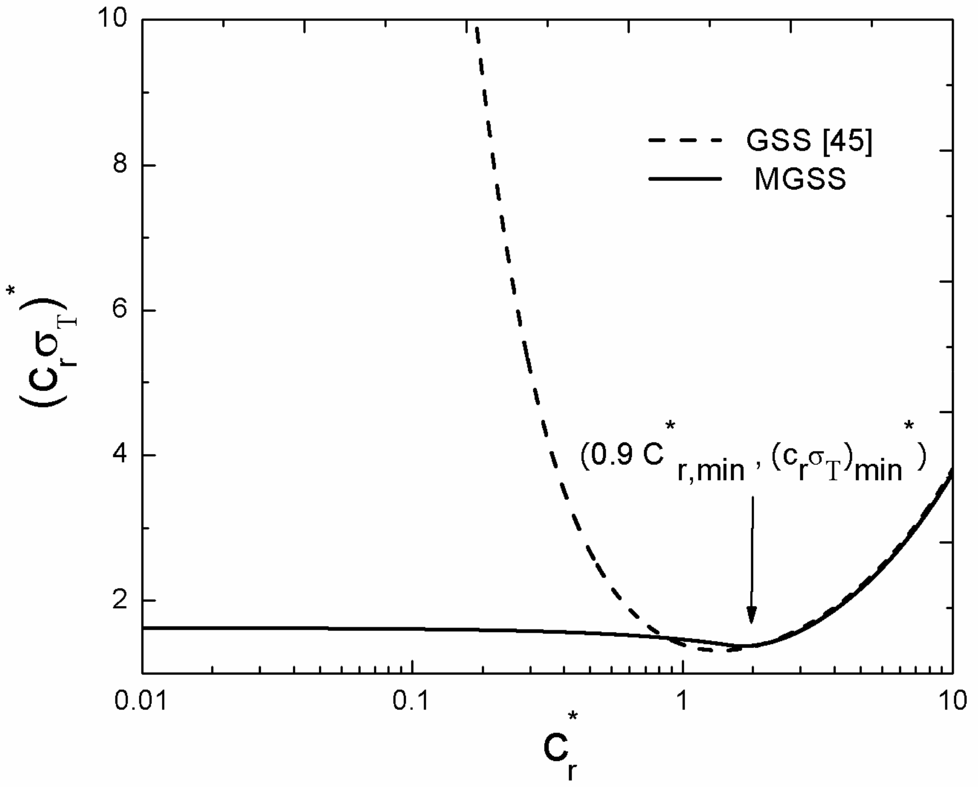

*Fig. (2. 3) Comparison of normalized collision probability, $(C_r\sigma_T)^*$, versus normalized relative speed, C_r *. Relative speed is normalized by the most probable velocity, $\sqrt{2k_B T_{ref}/m}$ and $C_r\sigma_T$ is normalized by $\overline{C_r\sigma_T}$, Eq. (2.11), at reference temperature, $T_{ref} = 273\ {}^0K$*

To eliminate the unphysical characteristics of GSS, instead of defining the cross-section uniformly as polynomials, the present MGSS model follows an approach similar to that used by Macrossan and Lilley [65] for development of the MGHS model. In particular, the GSS model was modified with a cut-off speed for the higher-order polynomial function such that it is linear below it. The result is

$$(c_r\sigma_T)_{MGSS} = \begin{cases} k(a)c_r + b(a) & c_r < a \\ \sigma^2 \sum \beta_j \left(\frac{\frac{1}{2}m_r}{\varepsilon}\right)^{l_j} c_r^{2l_j+1} & c_r > a \end{cases} \tag{2.8}$$

where to maintain first-derivative continuity, k is the slope of the $c_r\sigma_T$ curve (as shown in Fig. (2.3)) at the cut-off speed, a, and b is chosen to make the curve continuous at the cut-off speed, a. Therefore,

$$k(a) = \sigma^2 \sum \beta_j (2l_j + 1)\left(\frac{\frac{1}{2}m_r a^2}{\varepsilon}\right)^{l_j} \tag{2.9}$$

and

$$b(a) = \sigma^2 \sum \beta_j \left(\frac{\frac{1}{2}m_r}{\varepsilon}\right)^{l_j} a^{2l_j+1} - ak(a) \tag{2.10}$$

By reducing the order of total cross section at low relative speed, and limiting the polynomial at higher speed to order two, $\overline{c_r\sigma_T}_{MGSS}$ can be obtained in the form:

$$(\overline{c_r\sigma_T})_{MGSS} = AI_1(I_{21} + I_{22}) \tag{2.11}$$

where

$$A = \frac{2(m_1 m_2)^{3/2}}{\pi(k_B T)^3} \tag{2.12}$$

$$I_1 = \frac{\sqrt{\pi}(2k_B T)^{3/2}}{4(m_1 + m_2)^{3/2}} \tag{2.13}$$

$$I_{21} = -\frac{k(a)k_B T}{m_r}\{\exp[-(a\sqrt{\frac{m_r}{2k_B T}})^2] - 1\} + \frac{b(a)\sqrt{\pi 2k_B T}}{2\sqrt{m_r}} erf(a\sqrt{\frac{m_r}{2k_B T}}) \tag{2.14}$$

$$I_{22} = \sigma^2 \sum_j \frac{1}{2}\left(\frac{m_r}{2k_B T}\right)^{-\frac{2l_j+4}{2}} \beta_j \left(\frac{\frac{1}{2}m_r}{\varepsilon}\right)^{l_j} \Gamma(l_j + 2, a\sqrt{\frac{m_r}{2k_B T}}) \tag{2.15}$$

and $\Gamma(l_j + 2, a\sqrt{\frac{m_r}{2k_B T}})$ is the upper incomplete gamma function, defined as

$$\Gamma(a,x)=\int_x^{\infty} t^{a-1}\exp(-t)dt \tag{2.16}$$

Based on numerical experimentation, a set of parameters was selected that matches the Hirschefelder, Curtiss, and Bird [66] data quite well, $\beta_1 = 4.0$, $\beta_2 = 7.0$, $l_1 = -0.137$ and $l_2 = -1.55$ with $\alpha = 1.4$ for argon, and $a = 0.9c_{r,\min}$, in which $c_{r,\min}$ is the value at the minimum of the GSS $c_r\sigma_T$ curve, as illustrated in Fig. (2.3).

The improvement in low relative speed behavior of the MGSS model over the GSS model is obvious in Fig. (2.3). Fig. (2.4) shows that the MGSS model also improves the mean collision frequency behavior at low temperature over the GSS model. Hence, both the computational efficiency and low temperature behavior are significantly improved.

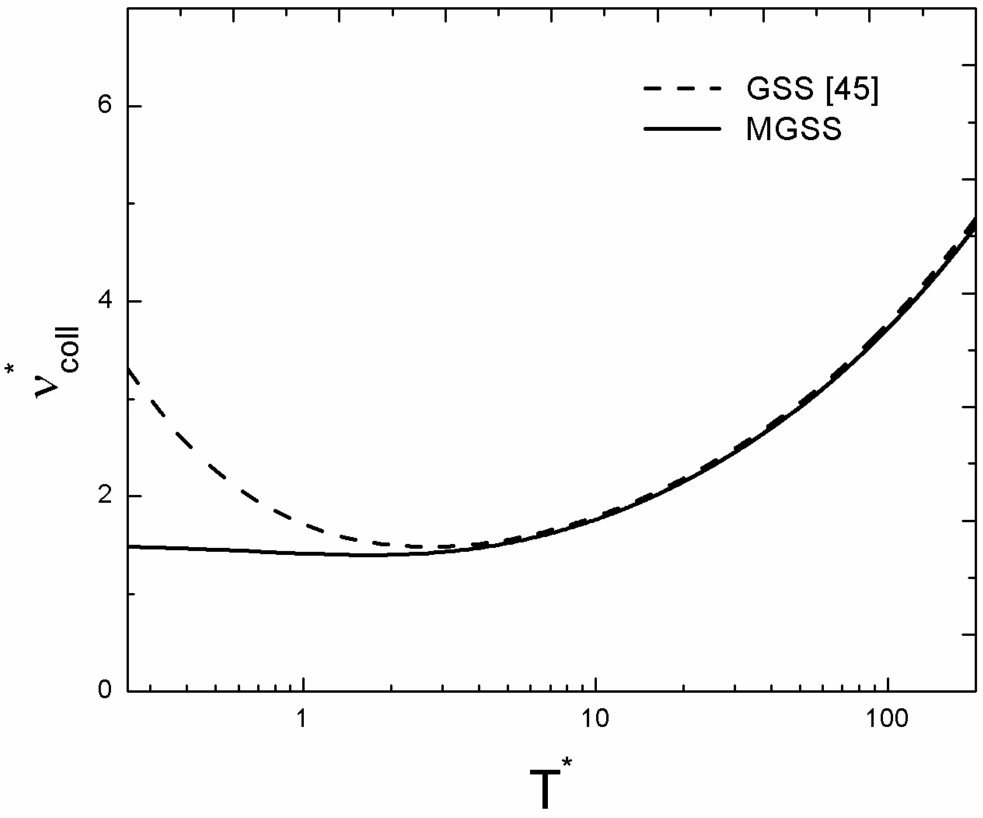

Fig. (2. 4) Normalized mean collision frequency versus normalized temperature. The temperature is normalized by ε / k_B*; for argon* $\varepsilon / k_B = 120^o K$ *; the collision frequency is normalized by the* $4\rho k_B T_{ref} / \pi\mu^{GSS}_{ref}$ *, where* k_B *is the Boltzmann constant;* T_{ref} *and* μ^{GSS}_{ref}*, Eq. (2.5), are taken at 273* ^0K.

Referring back to Figs (2.1) and (2.2), the comparisons of $\Omega^{(1,1)*}$ and $\Omega^{(2,2)*}$ for GSS and MGSS clearly demonstrate that the new MGSS model achieves substantial improvements in the viscosity and diffusion coefficients at low temperature, compared with the GSS model. However, in typical applications of DSMC, the primary advantage of MGSS over GSS is its computational efficiency. The pure DSMC and hybrid DSMC-NEMD simulations presented herein, unless otherwise noted, all employed MGSS collision modeling.

2.4 Description of DSMC/MD hybrid method

In most hybrid methods that divide the physical domain to two or more parts and assign each one to different method simulator, matching is achieved by establishing overlapping or “buffer” regions along the interfaces between the methods extending into their respective domains, wherein both methods are applied. The mean properties and momentum or heat fluxes from each domain are “copied” to the buffer, to generate the mean properties or flux continuities between the methods.

Wang and He [56] recently reviewed the various continuum/NEMD hybrid methods and proposed a new flux-based method for unsteady continuum/NEMD problems based on the introduction of an external force acting on the NEMD molecules. Likewise, Delgado-Buscalioni and Coveney [59] developed an unsteady flux-based hybrid method for continuum/NEMD coupling, introducing a fictitious force acting on the NEMD molecules to compensate for the momentum flux discontinuity across the continuum/NEMD interface. In principle, sampled DSMC domain results could be used as the basis for adapting a continuum/NEMD hybrid method for use as a DSMC-NEMD hybrid. However, issues such as the effect of force additions in creating non-physical density gradients and the need to maintain molecular energy and momentum conservation in individual molecular interactions discourage it. Furthermore, information is lost in the process of sampling and reconversion to a particle focus.

The basic hybrid steps that were employed were quite simple. First, a one-to-one correspondence of DSMC particles to molecules was established, as opposed to the usual DSMC implementation of representing actual molecules with a far fewer number of simulation particles. Hence, the present simulation in the DSMC domain is computationally expensive compared with the usual DSMC simulation but, as will be shown, the overall computational burden of the hybrid method is largely determined by the NEMD portion of the simulation.

The NEMD molecules in the present examples were initially deployed in a FCC arrangement. Then, the simulation was begun and they were allowed to migrate until an equilibrium state was reached. At that point, the barrier between the DSMC and NEMD domains was removed, allowing all particles to travel through each domain freely by the algorithm that was developed.

For computational efficiency, the DSMC time steps are larger than the NEMD time steps (one DSMC time step is equal to several NEMD steps). Therefore, the coupling procedure synchronizes the DSMC computation with the NEMD computation at the beginning of each DSMC time step. The DSMC and NEMD computations then proceed in parallel.

In the DSMC domain, the DSMC method dictates that particles move freely throughout the DSMC time step with their trajectories determined by their velocity vectors at the beginning of the time step. Particle collisions take place instantaneously at the end of the time step. The collision algorithm determines the particle velocity vectors for the next time step. The coupling procedure identifies those DSMC particles with velocity vectors that will carry them across the boundary into the NEMD domain during the DSMC time step. Then these particles are removed from the DSMC domain and copied into their corresponding locations in a fictitious free-flight particle region adjacent to the NEMD boundary. These free-flight particles enter the NEMD domain to become NEMD molecules during the NEMD time stepping process according to their DSMC determined trajectories.

The purpose of creating a fictitious free flight region adjacent to the NEMD domain is to facilitate assigning the DSMC and NEMD domains to separate processors with communication required only during the synchronization process. It is, in effect, a “ghost” DSMC particle region that facilitates particle exchange during synchronization. NEMD molecules inside the NEMD domain do not interact with the particles in the free flight region until they enter the NEMD domain. When these particles do enter the NEMD domain, they encounter an insertion procedure that avoids an overlap in positions with the NEMD molecules already inside.

Some NEMD particle insertion algorithms (e.g., [67]) have been developed to minimize the influence on system potential energy of particle insertion too close to another particle. But for the dilute gas, particle spacing is usually larger than the interaction cut-off distance, r_c. Hence, a complex insertion routine can be avoided by directly creating a new NEMD particle in the position, where the free-flight particle enters the NEMD region with its DSMC velocity. If the distance between the new NEMD particle created and the existing NEMD particles is exceptionally small or actually overlaps with an existing NEMD particle, this new particle is randomly shifted in the neutral direction (i.e., z direction) to fulfill the criteria for the smallest distance allowed. In this work, a minimum distance equal to σ was chosen, based on the observation that the peak of the radial distribution function (RDF) is around σ for a dilute gas.

NEMD molecules also escape from the NEMD region to become free-flight particles in the fictitious free-flight region. These out flux NEMD particles are removed in the NEMD simulator, but keep moving in the free-flight region with their NEMD velocity vectors as

NEMD time is advanced. When the NEMD time steps are synchronized with the DSMC step, new DSMC particles are created from these former NEMD particles and inserted into the DSMC domain with their positions in the DSMC domain corresponding to their free-flight region position at synchronization.

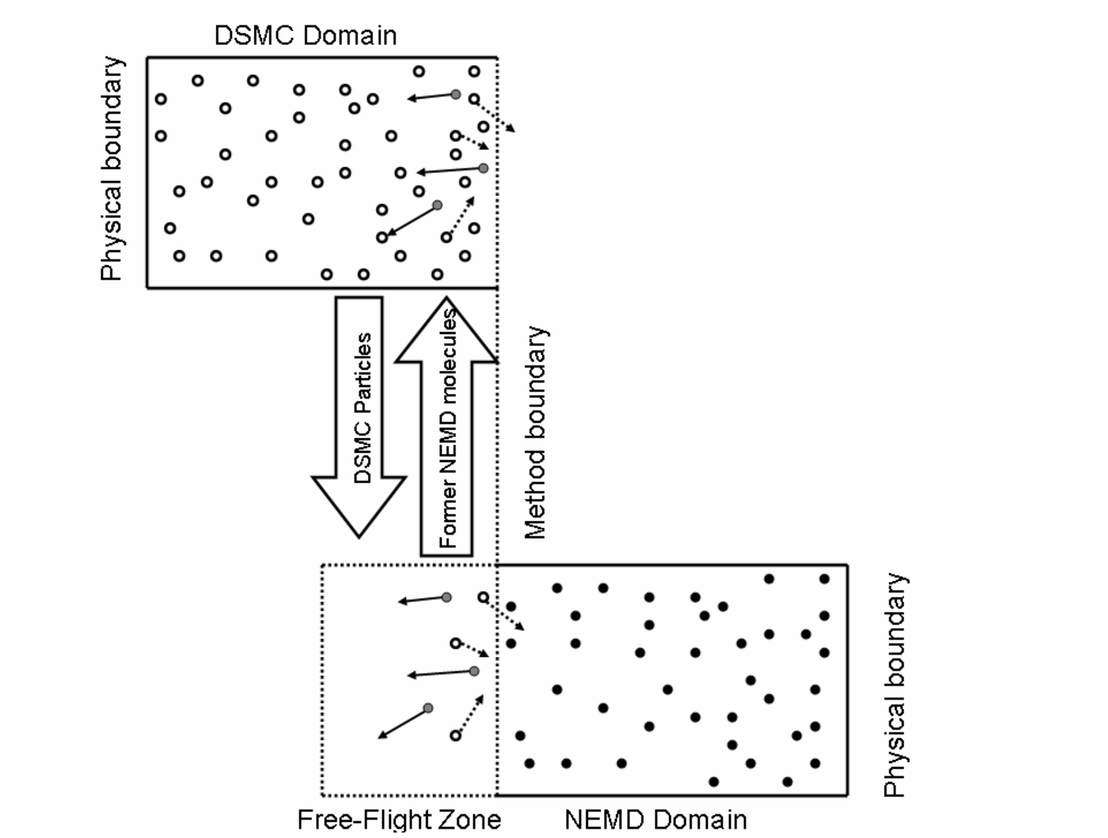

Fig. (2. 5) Conceptual diagram for inter-method particle exchange at synchronization. ○ *open circle dot: DSMC particles;* ● *black dot : NEMD molecules ;* ● *grey dot: former NEMD molecules ; dashed arrow: DSMC velocity vector; solid arrow: NEMD velocity vector.*

The details are illustrated in Fig. (2.5). The present hybrid method ensures particle conservation and does not lose molecular information (i.e. velocities and positions) in its coupling steps, hence, mean flow property and flux values match implicitly. It should be easily extendable to couple across an interface between three-dimensional flow domains because in the free flight zone, particles are moving in three dimensions. No directional vector information is lost in the zone so the three-dimensional momentum components, as well as energy, are conserved.

In general, the free flight zone is a fictitious dilute gas region of arbitrary shape overlaying a portion of the DSMC domain that is adjacent to the NEMD domain. In applications where this method is likely to be useful, the physical region occupied by dilute gas is at least mesoscopic in size, and a subregion away from boundaries delimited by smooth surfaces can always be identified. This includes geometrically three-dimensional flow regions, which can be handled unambiguously with the new method.

One parameter that must be set for the DSMC-NEMD hybrid is the time step. DSMC has a larger particle interaction time scale than NEMD. To avoid a low particle exchange frequency at the interface and possible momentum loss, the procedure set $\Delta\tau_{\mathrm{DSMC}} = 20\Delta\tau_{MD}$, which is equal to the NEMD Verlet list update interval [12].

Further reduction in the DSMC time step to approach the NEMD time step reduces the DSMC computational efficiency. It should be noted that the number of particles is not conserved in the NEMD domain. Since particles leave the dilute gas NEMD domain, the small time period $20\Delta\tau_{MD}$ between coupling steps, based on Verlet list principles, in effect, assures that during such a small time period, particle interactions are not influenced by adding and removing molecules.

DSMC time steps considerably larger than $20\Delta\tau_{MD}$ still produced good results in some preliminary simulations. Therefore, if needed, the DSMC time steps can be expanded in regions further from the method interface, where a larger time step will not affect the hybrid coupling. This is unnecessary for the systems studied in the present research because the physical scale is small for DSMC and most of the computational overhead is due to the NEMD simulator. Obviously, for multiscale problems with a much larger upper scale, the present method could be embedded within a continuum/DSMC hybrid.

The simulation method is explicitly designed for non-equilibrium processes and does not correspond to any of the standard statistical mechanical equilibrium ensembles. As a matter of normal statistical averaging, an "experimental" ensemble was used that was based on averaging over repetitions of the calculation with different random number seeds and therefore a different set of initial velocities and positions.

2.5 Validation of the method

The newly developed DSMC-NEMD method, which has no buffer zone, raises the question of whether the method interface is continuous in a particle sense and physically realistic. To validate the method and its boundary treatment, three benchmark problems were chosen, an equilibrium gas system between isothermal diffusive walls, a Fourier thermal system and an oscillatory Couette flow. In the NEMD simulator, molecular motions are driven by intermolecular forces derived from Eq. (2.1) with the force cutoff distance, $r_c = 2.5\sigma$.

The stress tensor and the heat flux vector components are calculated as

$$\Pi_{\alpha\beta,J} = \frac{1}{V_J}(m\sum_{i=1}^{N_J} c'_{i,\alpha} c'_{i,\beta} + \sum_{i<j} F_{ij,\alpha} r_{ij,\beta}) \tag{2.17}$$

$$q^{tot}_{\alpha,J} = \frac{1}{V_J}[\sum_{i=1}^{N_J} c'_{i,\alpha}(\frac{1}{2}mc'^2_i + E^{pot}_i) + \frac{1}{2}\sum_{i,j}^{N_J}(\mathbf{F}_{ij}.\mathbf{c}'_i)\ r_{ij,\alpha}] \tag{2.18}$$

in which N_J is the number of molecules in the sampling cell J with volume, V_J; α and β indicate the x, y, or z direction; $c_\alpha' = c_\alpha - \overline{c_\alpha}$ is the thermal velocity in the α direction; and $F_{ij,\alpha}$ is the interaction force between molecule i and molecule j in the α direction; $r_{ij,\beta}$ is the interaction vector in the β direction; and E_i^{pot} is the potential energy of particle i. The first terms in Eq.(2.17) and Eq.(2.18) represent the kinetic contributions, while the remaining terms, which are not included in the DSMC simulator, represent the interaction contributions and, for the heat flux, potential energy flux. In the present simulation, argon gas is chosen with the initially uniform density, $n_0 = 0.001\ \sigma^{-3}$, and temperature, $T_0 = 1.0\ \varepsilon / k_B$. To achieve accurate results, an average of 100 particles per cell were employed in the DSMC simulator. For steady solution, results were obtained by time averages over 2×10^6 NEMD steps, and unsteady solution samples contained ensemble averages of over 1.5×10^7 molecules in a computational cell.

2.5.1 Equilibrium gas system and Fourier thermal system

In the equilibrium gas system and Fourier thermal system simulations, two thermally accommodating diffusive walls sit at the top and bottom of a gas domain. The DSMC simulator is assigned to the lower-half y domain I, while the NEMD simulator is assigned to the upper-half y domain II. Periodic boundary conditions are applied in the x and z (lateral) directions and Kn, based on the wall spacing, is around 1.25 (see Fig. (2.6)). Without a temperature difference between the diffusive walls, the system reaches an equilibrium state.

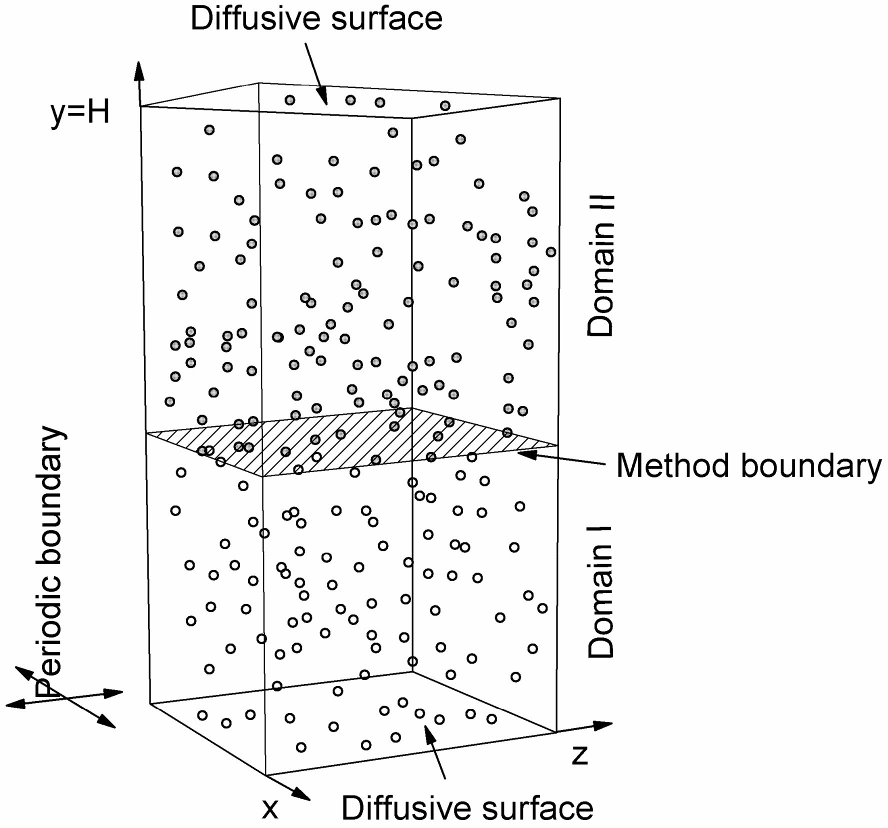

Fig. (2. 6) Region partition for hybrid DSMC-NEMD Fourier flow simulation.

For validation purposes, the distributions of the wall-perpendicular and lateral components of the outward velocity fluxes from the two domains were considered, which can be determined from the following Maxwell-Boltzmann equilibrium distributions

$$F_\alpha = \pm 2\zeta_\alpha \exp(-\zeta_\alpha^{\,2}) \qquad \alpha = y$$

$$(2.19)$$

$$F_\alpha = \frac{1}{\sqrt{\pi}} \exp(-\zeta_\alpha^{\,2}) \qquad \alpha = x, z$$

where $\zeta_\alpha = c_\alpha / \sqrt{2k_B T / m}$ is the normalized thermal velocity component in the α

direction, and the where the positive sign in the distribution function in the $\alpha = y$ direction refers to DSMC efflux and the negative sign refers to NEMD efflux.

Fig. (2.7) shows the results of the simulation velocity histogram data collected from sampling efflux particles in each domain near the simulator domain interface. These data are compared with the Maxwell-Boltzmann distributions of Eq. (2.19). The efflux particle distribution statistics are consistent with Maxwell-Boltzmann equilibrium theory and demonstrate excellent agreement in particle exchange flux statistics, comparing the efflux distributions for the NEMD domain with the efflux distributions for the DSMC domain.

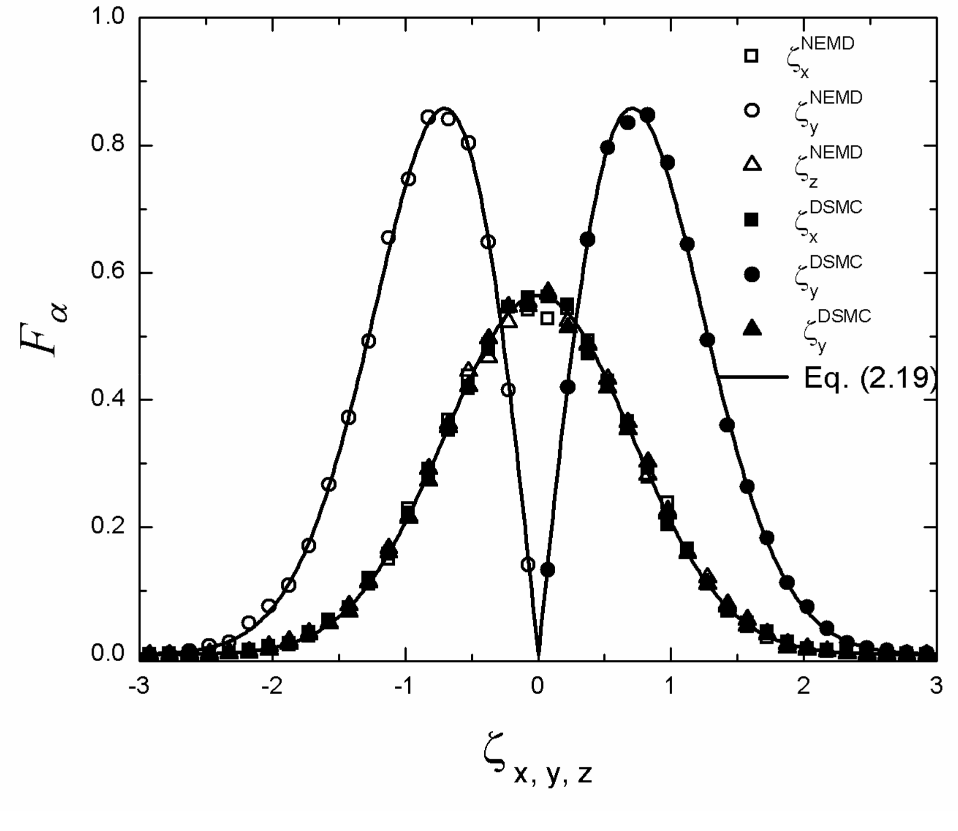

Fig. (2. 7) Comparison of hybrid DSMC-NEMD, equilibrium, domain efflux statistics near inter-method interface with corresponding Maxwell Boltzmann distributions (Eq. 2.19). Data point labels refer to the particle velocity data set from which the statistical histogram was constructed.

To examine the accuracy of the method for simulation of a nonequilibrium system, a Fourier flow system was also simulated. The physical configuration was the same as the equilibrium system except the upper wall temperature was set to The upper wall temperature was set to $2T_0$, with the lower wall temperature, $T_0 = 273^oK$.

Sampling-obtained temperature and density from the DSMC-NEMD hybrid simulation and from a pure DSMC simulation for this system are shown in Fig. (2.8). The figure demonstrates good agreement of hybrid results with pure DSMC results.

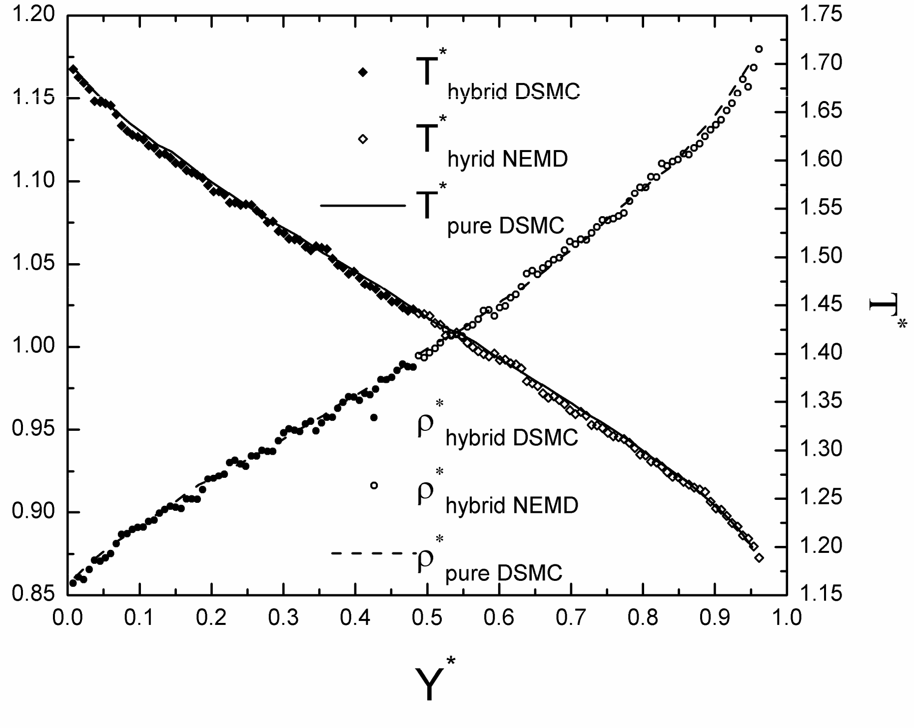

Fig. (2. 8) Comparison of normalized Fourier temperature and density profiles. Density is normalized by initial density, ρ_0,. Temperature is normalized by initial temperature, T_0. Wall distance coordinate is normalized by wall separation.

The sampled heat fluxes for the two cases are shown in Fig. (2.9). The DSMC heat flux is continuous with the NEMD kinetic heat flux, and lower than that of the total NEMD heat flux because of the absence of the interaction and potential energy contributions. The overall heat flux discrepancy from the pure DSMC solution of approximately one percent is acceptably small.

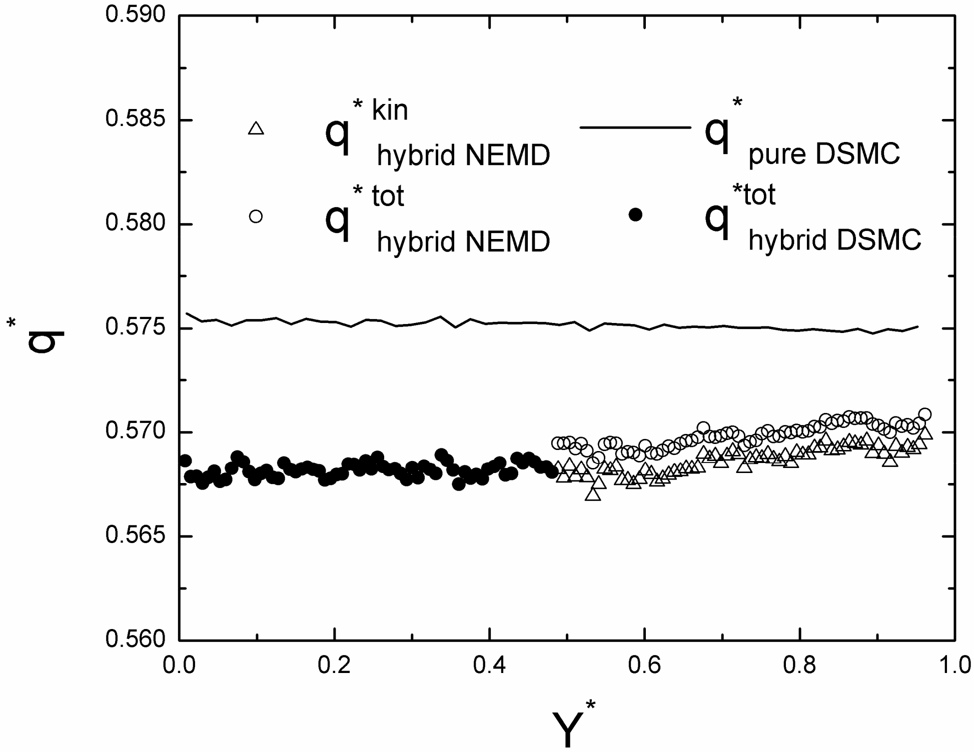

Fig. (2. 9) Comparison of normalized Fourier heat flux profiles. Heat flux is normalized by $m^{-1/2} n_0 (k_B T_0)^{3/2}$ *, where* n_0 *and* T_0 *are the initial number density and temperature, respectively. Wall distance coordinate is normalized by wall separation.*

For a moderately non-equilibrium system such as this one, the particle speed distribution can be expressed in the form of the first order Sonine polynomial expansion of the

Chapmann-Enskog distribution [68],

$$f^{CE}(\boldsymbol{\zeta}) = F^0(\boldsymbol{\zeta})\Gamma(\boldsymbol{\zeta}) \tag{2.20}$$

where

$$F^0(\boldsymbol{\zeta}) = \prod_{\alpha} \frac{1}{\sqrt{\pi}} \exp(-{\zeta_\alpha}^2), \tag{2.21}$$

and

$$\Gamma(\boldsymbol{\zeta}) = 1 + (\sum_{\alpha} {q^*}_{\alpha}\zeta_\alpha)(\frac{2}{5}\boldsymbol{\zeta}^2 + 1) - \sum_{\alpha\neq\beta} {\tau^*}_{\alpha\beta}\zeta_\alpha\zeta_\beta - {\tau^*}_{xx}({\zeta_x}^2 - {\zeta_z}^2) - {\tau^*}_{yy}({\zeta_y}^2 - {\zeta_z}^2)$$

$$(\alpha, \beta = x, y, z) \tag{2.22}$$

In Eq. (2.22) ${q^*}_{\alpha} = p^{-1}\sqrt{2m / k_B T} q_\alpha$ and ${\tau^*}_{\alpha\beta} = \tau_{\alpha\beta} / p$ are the normalized heat flux and viscous stress.

As in the validation of the hybrid method for the equilibrium case, the distribution functions for the wall-perpendicular velocity efflux components and the lateral velocity efflux components from the two domains were considered. These can be obtained as,

$$F_\alpha^{CE} = A_\alpha \int_{-\infty}^{+\infty} d\zeta_x \int_{-\infty}^{+\infty} d\zeta_z f^{CE}(\boldsymbol{\zeta})\zeta_\alpha \qquad (\alpha = y)$$

$$\tag{2.23}$$

$$F_\alpha^{CE} = A_\alpha \int_{-\infty}^{+\infty} d\zeta_\beta \int_{0/-\infty}^{+\infty/0} d\zeta_y f^{CE}(\boldsymbol{\zeta})\zeta_y \qquad (\alpha, \beta) = (x, z) \, \text{or} \, (z, x)$$

where ζ_y is evaluated from $-\infty$ to 0 for efflux from the NEMD domain toward the DSMC domain and from 0 to $+\infty$ for DSMC domain efflux toward the NEMD domain. Based on the fact that macroscopic gradients exist only in the y direction, A_α, the normalization parameter, is $A_\alpha = \pm 2\sqrt{\pi} / (1 - 0.5\tau_{yy}^*)$, where the positive sign refers to DSMC efflux and the negative sign refers to NEMD efflux.

In Figs. (2.10) and Fig. (2.11), histogram data obtained from the efflux particle velocities at locations near the DSMC-NEMD interface in each of the hybrid simulator domains are compared with the corresponding Chapman-Enskog distributions computed from Eq. (2.23). The heat flux and stress components determined from the simulations are used to rescale Eq. (2.23) so that the distributions can be applied more confidently to the Knudsen number of the present case, which is slightly greater than 1. Given that the heat flux and shear stress components were not also obtained from theory, the theoretical and simulated results are not completely independent. Nevertheless, the excellent matching of the simulation data with the Chapman-Enskog distribution across the spectrum of particle speeds in these comparisons clearly illustrates that the DSMC-NEMD hybrid method captures the nonequlibrium statistical kinetic behavior of particles. This agreement extends to the nonequilibrium particle flux transferring from one simulator to the other and it demonstrates that the artifice of a buffer zone is unnecessary.

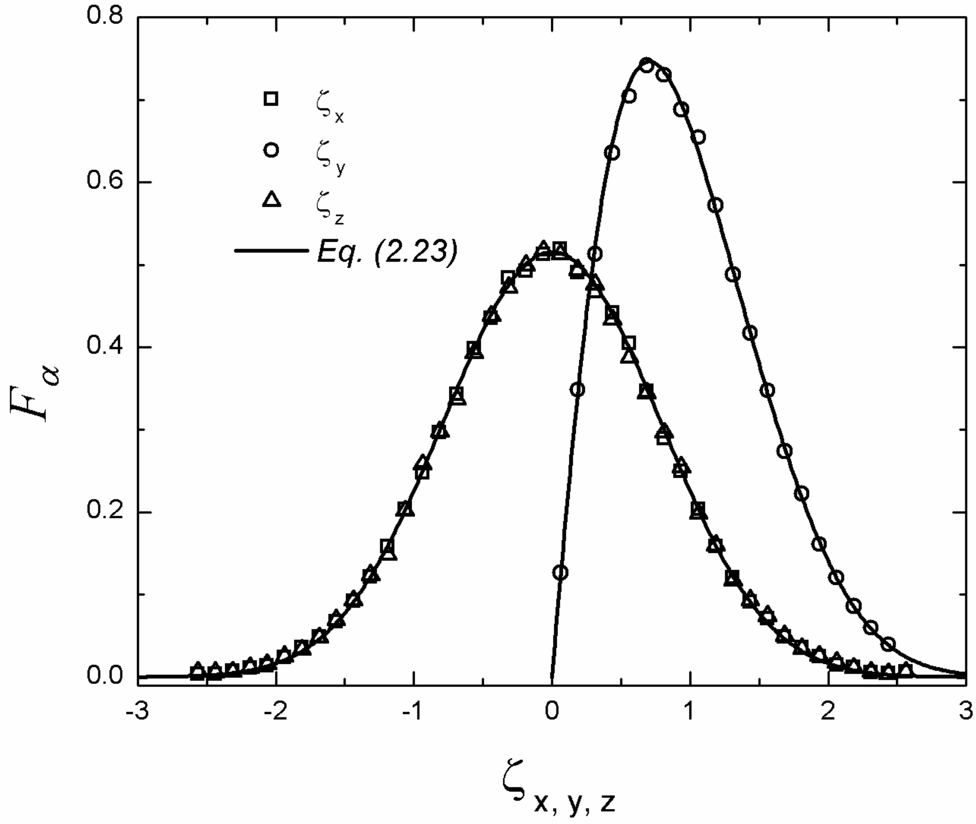

Fig. (2. 10) Comparison of Fourier flow hybrid DSMC-NEMD, nonequilibrium DSMC efflux statistics near inter-method interface with corresponding Chapman-Enskog distributions [i.e. Eq. (2.23)] . Data point labels refer to the particle velocity data set from which the statistical histogram was constructed.

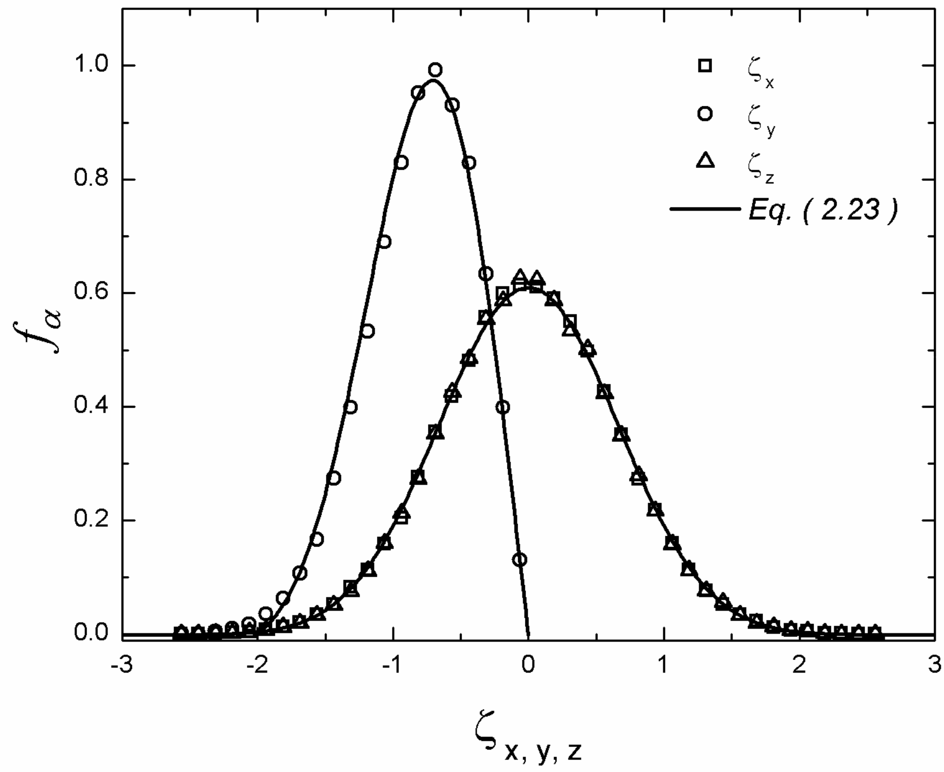

Fig. (2. 11) Comparison of Fourier flow hybrid DSMC-NEMD, nonequilibrium NEMD efflux statistics near inter-method interface with corresponding Chapman-Enskog distributions [i.e. Eq. (2.23)]. Data point labels refer to the particle velocity data set from which the statistical histogram was constructed.

2.5.2 Oscillatory Couette Flow

The Fourier thermal flow results show that the present DSMC-NEMD hybrid method produces good agreement with pure DSMC simulations for a steady nonequilibrium problem. To study the ability of the method to accurately simulate unsteady flow systems, an argon gas flow between two horizontal isothermal surfaces was considered, the bottom surface is stationary, while the top is oscillating in the x direction with velocity, $U_w = U_0 \sin(\omega t)$, where $U_0 = 0.63\sqrt{\varepsilon / m}$ is the magnitude of the velocity and ω is the oscillation frequency. Periodic boundary conditions are maintained in the other directions. The gas is initially at rest, with the same temperature, $T = 1.0\varepsilon / k_B$, as that at which the upper and lower wall will be maintained. The Stokes number, $\sqrt{mn_0\omega H^2 / \mu}$, which represents the balance between the unsteady and viscous effects, equals 1.0 and Kn=0.81 in this simulation.

We assigned an MD simulator to each of the upper and lower domains (i.e. domain I and domain III) of the gas flow with a DSMC domain in the middle (i.e. domain II), so that each simulator was responsible for a third of the region between the surfaces [see Fig. (2.12)].

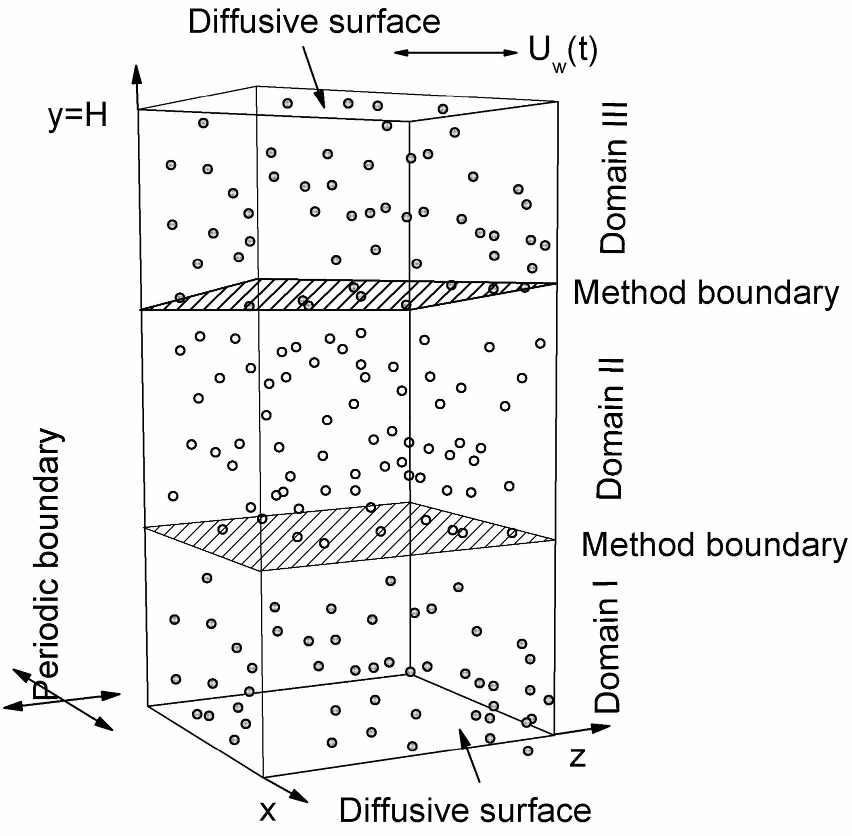

Fig. (2. 12) Region partition for hybrid DSMC-NEMD oscillatory flow simulation

Figs. (2.13) and. (2.14) show the resulting hybrid velocity and shear stress profiles at four different time points ($\tau = 0.25\tau_0$, $\tau = 0.5\tau_0$, $\tau = 0.75\tau_0$, $\tau = \tau_0$, where τ_0 is the period of the oscillation wall velocity) compared with a pure DSMC solution. The results in Figs. (2.13) and (2.14) demonstrate that the DSMC-NEMD hybrid method captures the time response of the system quite well, without any unphysical manipulations or artifices.

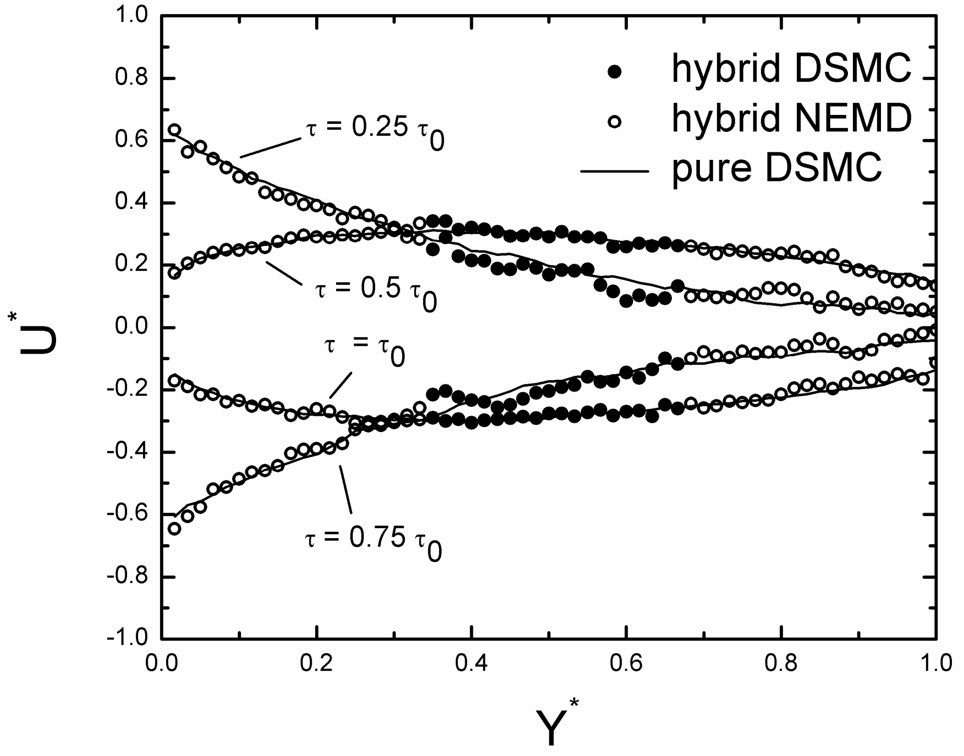

Fig. (2. 13) Comparison of oscillating Couette flow normalized velocity profiles. Velocity is normalized by the magnitude of oscillatory wall velocity, U_0. *Wall distance coordinate is normalized by wall separation.*

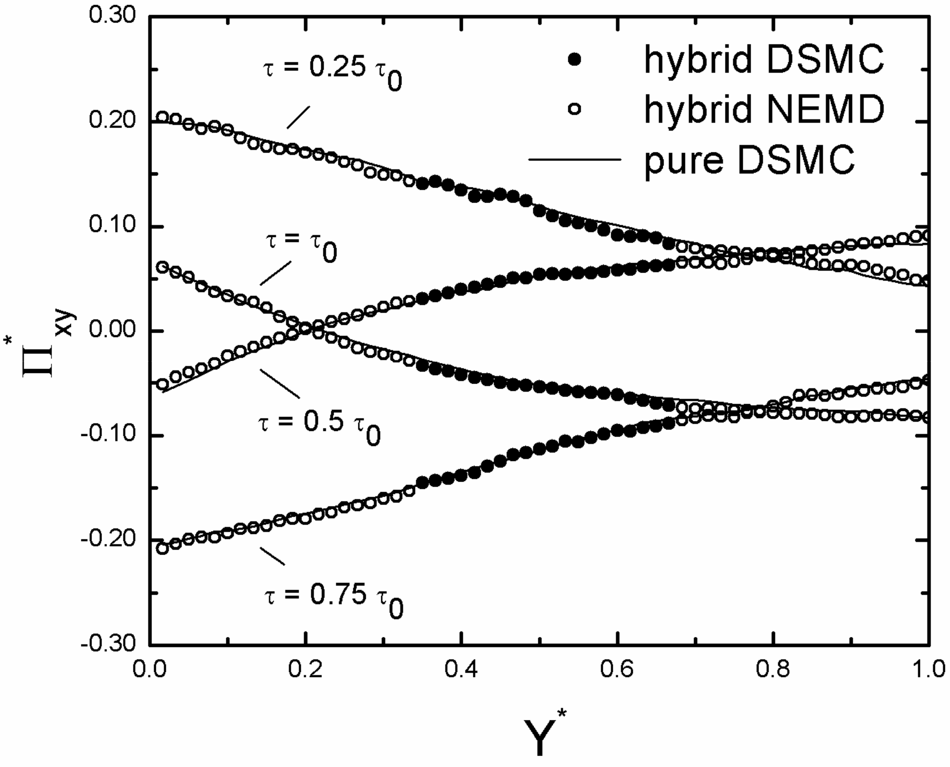

Fig. (2. 14) Comparison of oscillating Couette flow normalized shear stress profiles. Shear stress is normalized by p_0*, the initial pressure. Wall distance coordinate is normalized by wall separation.*

The pure DSMC simulation of Figs. (2.13) and (2.14) is, again, performed with the present DSMC formulation using MGSS. In testing the MGSS model, DSMC simulations of the Couette system and the thermal system in the preceding section were performed, both with Bird's VHS [6] collision model. The results, not shown here, were compared with pure NEMD simulations and demonstrated the improved accuracy of the MGSS model over VHS for shear stress in the Couette system and heat flux in the thermal system. This was expected, given the better fits for GSS and, hence, MGSS with the L-J potential and the better experimental agreement of GSS compared with VHS [45].

2.6 Assessment of computational performance

To assess the computational performance of the hybrid method, the hybrid CPU times in the simulation of the equilibrium gas system were compared for three different partitions of the region between the isothermal diffusive walls into NEMD and DSMC domains. Systems were simulated containing 8000, 16000, and 32000 gas molecules. For each size of the system, three different values for the NEMD/DSMC simulator partition ratio, r_{MD} were chosen: 25%, 50%, and 100%. To facilitate the comparison, the hybrid codes were executed by the serial processor.

The results of the simulator split and system size comparisons are shown in Fig. (2.15), where the x axis represents the DSMC partition fraction, $1-r_{MD}$. The CPU time, normalized by the pure NEMD CPU time for each system size, t^*_{CPU}, was determined for 2×10^5 hybrid NEMD steps, which are equivalent to 10^4 hybrid DSMC steps. It is apparent that the CPU time is reduced substantially by reducing the NEMD simulator partition and increasing the DSMC simulator partition.

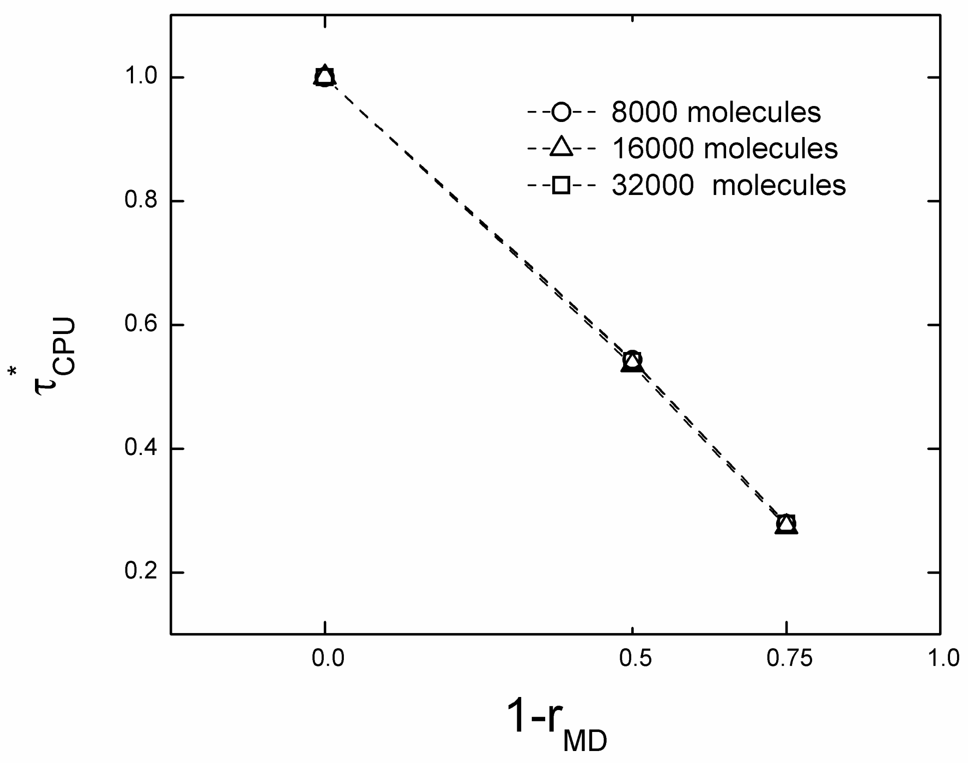

Fig. (2. 15) Normalized CPU time dependence on simulator partition fraction for different system sizes.

The present performance results compare favorably with the increase in computational efficiency due to hybridization reported by Nedea et al. [43]. In the present study, for 25% MD -75 % DSMC, the CPU time is reduced by 80% and for 50% MD-50% DSMC, the CPU time is reduced by 50%. For the dilute gas case of [43], at 10% MD -90% MC, the CPU time is reduced by 82 %, whereas for the partition studied in common with the present investigation, 50% MD -50% MC, the CPU time is reduced by less than 1%. However, an indisputable determination of which algorithm is more efficient is not possible from the results presented due to differences in the densities of the systems studied and the degrees of parallelization.

The CPU time scales with the system size for both simulators in the present testing. The DSMC simulator is at least ten times more efficient than the MD simulator for particle statistics within the coupling procedure. However, even though an order of magnitude increase in performance is achieved at the particle level, the DSMC simulator algorithm produces some non-physical noise due to its probabilistic nature, which may require more sampling than the NEMD statistics if accurate macroscopic properties in the DSMC domain are of interest. On the other hand, the "memory" scale of NEMD molecules is short and, as a consequence, DSMC noise will not penetrate very far into the NEMD domain so NEMD sampling to obtain macroscopic properties there should not be affected.

Although it was not attempted in the present investigation, a strategy to reduce the DSMC noise in the parallel implementation of the method, where DSMC is assigned to a separate processor, is to make use of the dead time in the DSMC processor after a DSMC time step, while the processor is waiting for the NEMD processor to catch up. Thus, better load balance would be achieved.

2.7 Application of method to investigate thermal accommodation at a surface

One of the advantages for using the NEMD method at a surface is its capability of studying the physics of interface phenomena. One use of this capability is the determination of the thermal accommodation coefficient often used as an approximate boundary condition for molecular interaction surface physics in kinetic theory-based computations such as DSMC.

A thermal accommodation coefficient for total energy of molecules at the gas- solid surface, a_E can be defined as [cf. 44]

$$a_E = \frac{\overline{E_i} - \overline{E_r}}{\overline{E_i} - \overline{E_w}} \tag{2.24}$$

where $\overline{E}$ is the total energy and subscripts i and r refer to the incident and reflected molecules, respectively. The subscript w indicates the molecules that would be outgoing in equilibrium with the wall under diffuse reflection. The accommodation coefficient of normal component, a_E^n, and tangential component, a_E^t, can be obtained from the energy in the normal and tangential directions to the solid surface, respectively.

Positing the Maxwell-type reflection condition that reflected particles are classified into two categories, equilibrium or specular reflection, K. Yamamoto et al. [44] address the accommodation coefficient of for energy in the following form, which allows the accommodation coefficient to be computed from NEMD simulation at the surface

$$f^r = a_E f^w + (1 - a_E) f^{i-} \tag{2.25}$$

where f^w is the Maxwell-Boltzmann distribution described in Eq. (2.19) and f^{i-} is the distribution function of the incident molecules' specular reflections, which is determined from the statistics of simulated molecules, as is f^r

In the present gas-solid interaction simulation, mesoscale wall phenomena in a micro-channel with two solid wall boundaries were considered. The walls were each formed by FCC layer structures and separated by 10λ in the y direction. Periodic boundary conditions were applied in the x and z directions. The solid NEMD molecules employed in the hybrid simulations were tethered together and anchored within a FCC lattice by a fictitious spring force. Unlike the thermal diffusive wall simulations, the explicit solid wall temperatures for these hybrid simulations were controlled by a velocity rescaling method applied to the wall molecules.

The thermal accommodation coefficients were obtained from the hybrid simulations by calculating the incident (f^i) and reflected molecular distributions (f^r) at a distance r_c away from the mean solid surface. Applying Eq. (2.25), the thermal accommodation coefficient, assuming the Maxwell-like reflection condition, was readily obtained. In these simulations, the NEMD simulators were assigned to the regions comprising the solid walls and the gas just above them, while a DSMC simulator was devoted to the remaining computational space in the middle. Each NEMD simulator domain occupied 8.33 percent of the computational space and the DSMC domain was devoted to the remaining 83.33 percent. The temperature of the upper solid wall was twice the lower wall temperature, T_0. A steady state was reached after 10^7 NEMD steps. To reduce statistical fluctuations to an acceptable level, the macroscopic properties were obtained by averaging over 4×10^6 NEMD steps after steady state is reached, with around 10^8 MD samples per cell and 1.6×10^7 DSMC samples per cell. NEMD cells are defined merely for sampling purposes and were selected as the minimum size to yield good spatial resolution while encompassing an adequate number of particles to yield a meaningful sample.

Accommodation coefficients from several simulations with different L-J gas-solid interaction parameters, ε_{sg}, and ratios of solid particle mass, m_s, to gas particle mass m_g are compared in Table 2.1.

Table 2. 1Accommodation coefficient with different wall and temperature

	T_0=1.0 $\frac{\varepsilon}{k_B}$		T_0=2.0 $\frac{\varepsilon}{k_B}$	
	a_n	a_t	a_n	a_t
$m_s = 100m_g, \varepsilon_{sg} = 1.0$	0.15	0.15	0.085	0.14
$m_s = 25m_g, \varepsilon_{sg} = 1.0$	0.40	0.41	0.30	0.30
$m_s = 25m_g, \varepsilon_{sg} = 0.5$	0.19	0.19	0.17	0.19

Figs. (2.16-2.24) show the temperature, density, and heat flux results, respectively, from the hybrid simulations for the parameter sets of Table 2.1. They are compared with the results of pure DSMC simulations that used the accommodation coefficients obtained from the hybrid simulations and shown in Table 2.1. Three cases, large m_s with complete wetting ($m_s = 100m_g$, $\varepsilon_{sg} = 1.0$), small m_s with complete wetting ($m_s = 25m_g$, $\varepsilon_{sg} = 1.0$), and small m_s with non-wetting ($m_s = 25m_g$, $\varepsilon_{sg} = 0.5$) are compared. From the hybrid results, the density achieves a higher value near the wall for $\varepsilon_{sg} = 1.0$ than for $\varepsilon_{sg} = 0.5$. Because of weaker interaction taking place, the case of $m_s = 25m_g, \varepsilon_{sg} = 0.5$ has a larger temperature slip than the case of $m_s = 25m_g$, $\varepsilon_{sg} = 1.0$. On the other hand, the completely wetting wall of $m_s = 100m_g$ has a larger temperature slip than the completely wetting wall of $m_s = 25m_g$.

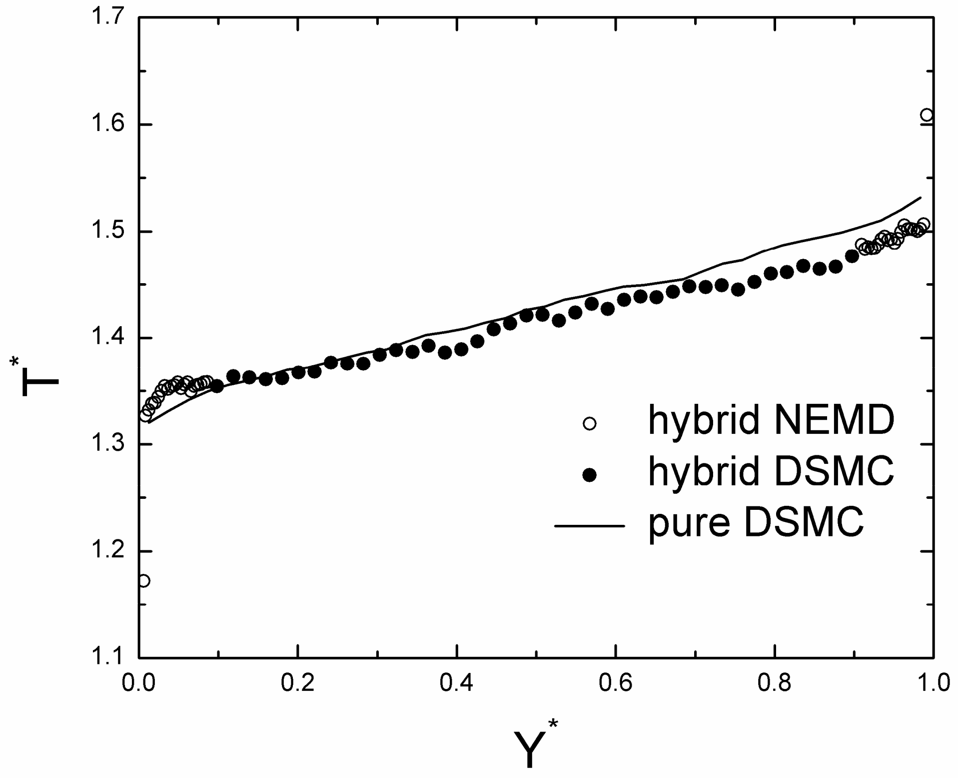

Fig. (2. 16) Normalized temperature profiles for solid molecule wall case:

$m_s = 100 m_g$, $\varepsilon_{sg} = 1.0$. *Temperature is normalized by initial temperature,* T_0. *Wall distance*

coordinate is normalized by mean wall separation.

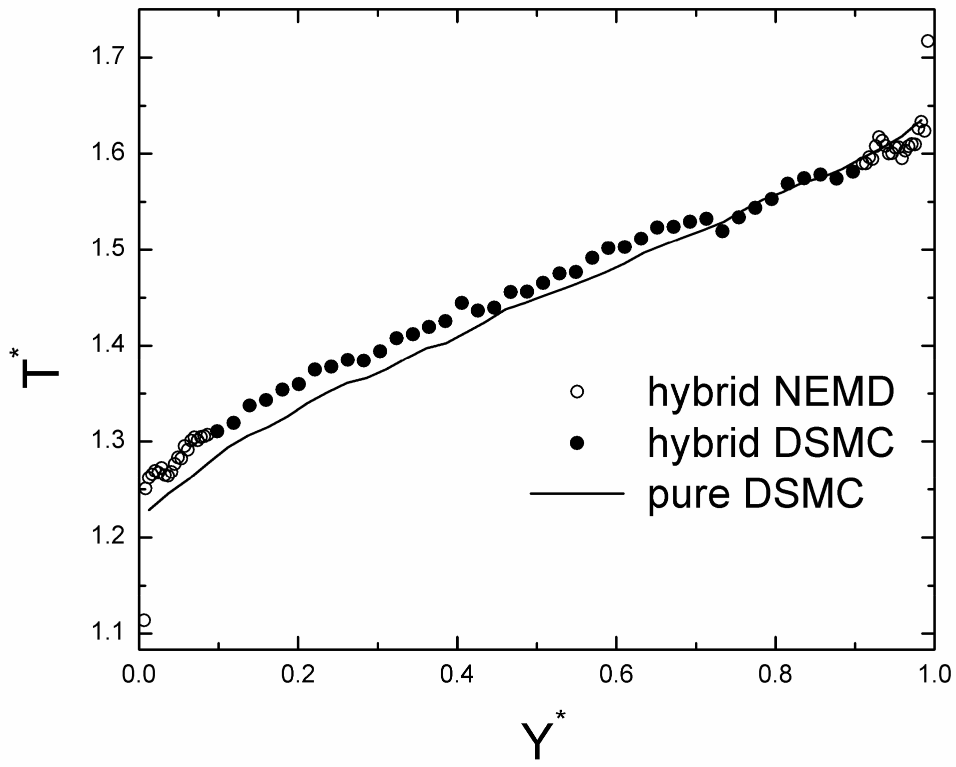

Fig. (2. 17) Normalized temperature profiles for solid molecule wall case: $m_s = 25m_g$, $\varepsilon_{sg} = 1.0$. *Temperature is normalized by initial temperature,* T_0. *Wall distance coordinate is normalized by mean wall separation.*

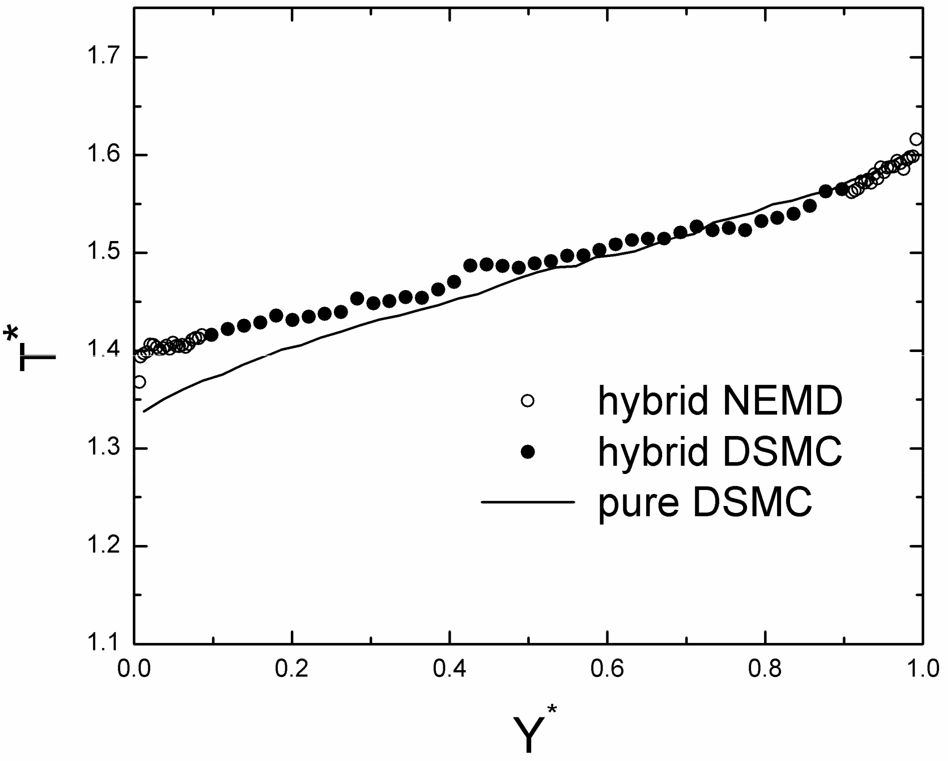

Fig. (2. 18) Normalized temperature profiles for solid molecule wall case: $m_s = 25m_g$, $\varepsilon_{sg} = 0.5$. *Temperature is normalized by initial temperature,* T_0. *Wall distance coordinate is normalized by mean wall separation.*

DSMC, with an accommodation coefficient determined from applying the Maxwell condition to the hybrid simulation, was able to reproduce the temperature profile away from the wall, including the apparent "slip" temperature with only a slight discrepancy as shown in Figs. (2.16) to (2.18). However, as shown in Figs. (2.22) to (2.24), it could not describe the temperature and density variations and wetting effect closer to the wall; neither could it describe the energy flux across the solid–gas interface with the result that its computed overall heat flux is erroneous.

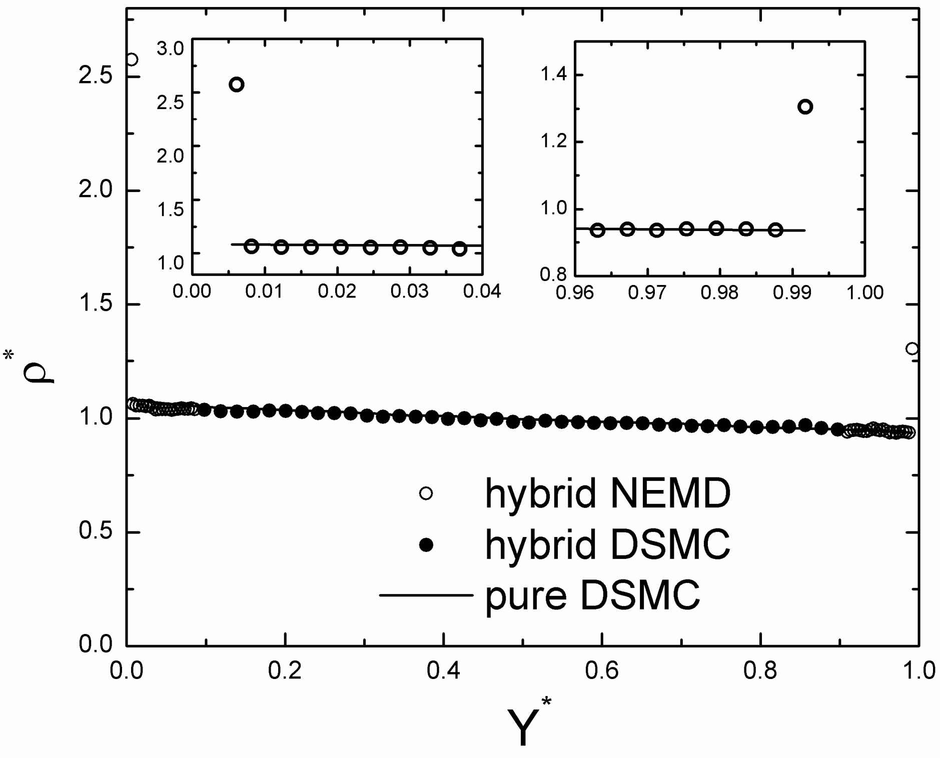

Fig. (2. 19) Normalized density profiles for solid molecule wall case: $m_s = 100m_g$, $\varepsilon_{sg} = 1.0$. *The left inset shows the density detail profiles near the cool wall. The right inset shows the density detail profiles near the hot wall. Density is normalized by initial density,* ρ_0. *Wall distance coordinate is normalized by mean wall separation.*

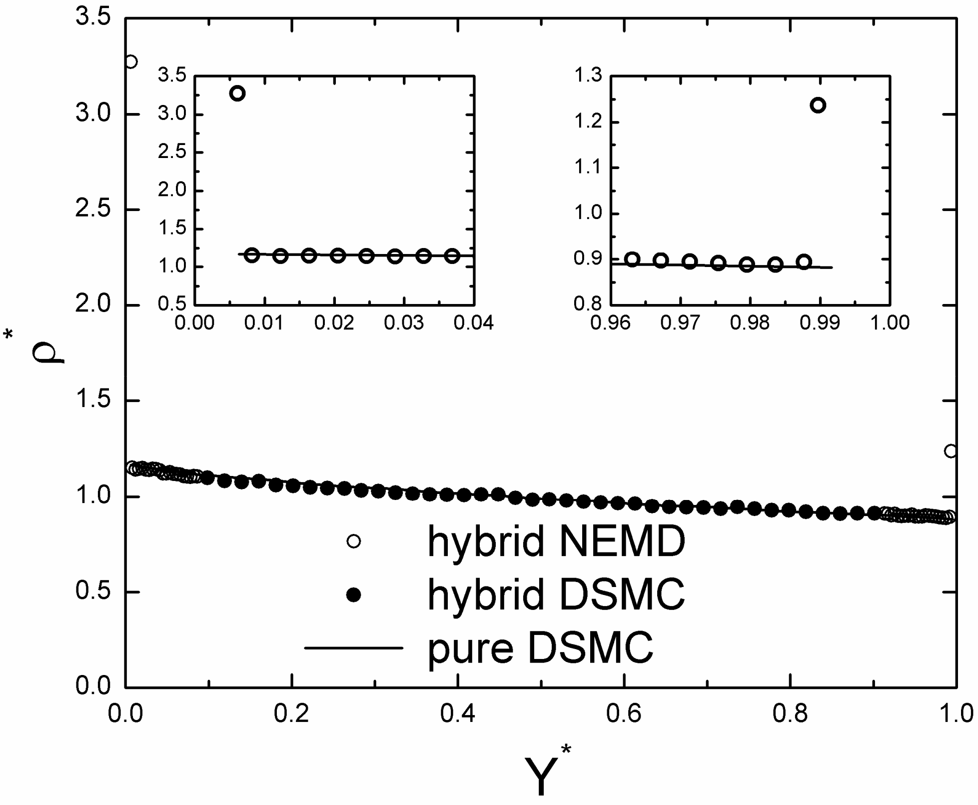

Fig. (2. 20) Normalized density profiles for solid molecule wall case: $m_s = 25m_g$, $\varepsilon_{sg} = 1.0$. *The left inset shows the density detail profiles near the cool wall. The right inset shows the density detail profiles near the hot wall. Density is normalized by initial density,* ρ_0. *Wall distance coordinate is normalized by mean wall separation.*

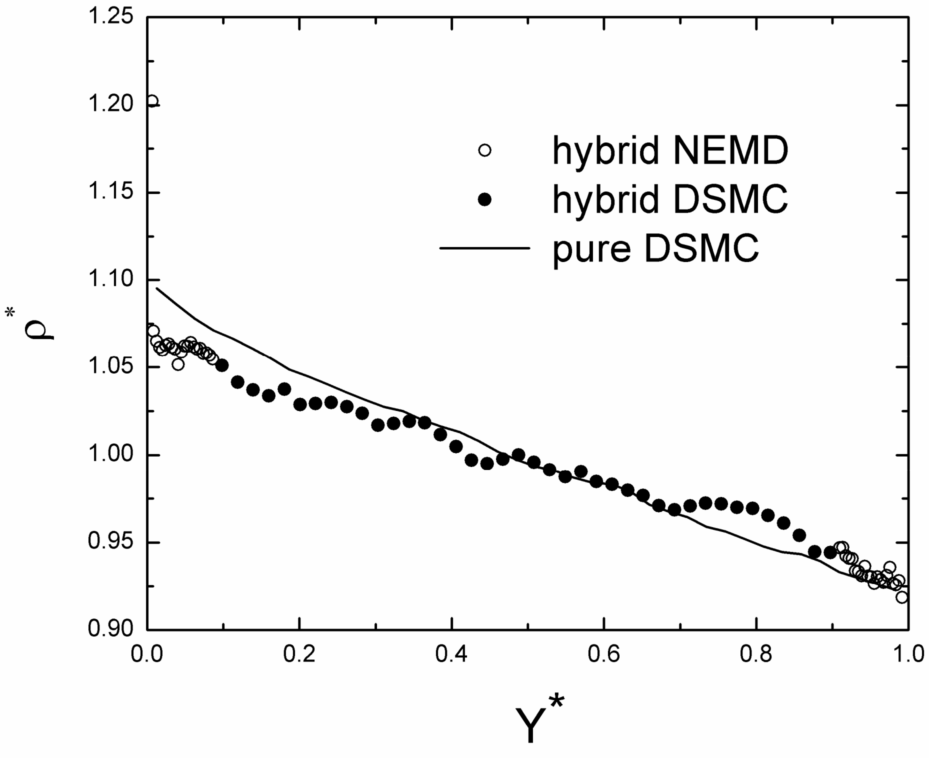

Fig. (2. 21) Normalized density profiles for solid molecule wall case: $m_s = 25m_g$, $\varepsilon_{sg} = 0.5$. *Density is normalized by initial density,* ρ_0. *Wall distance coordinate is normalized by mean wall separation.*

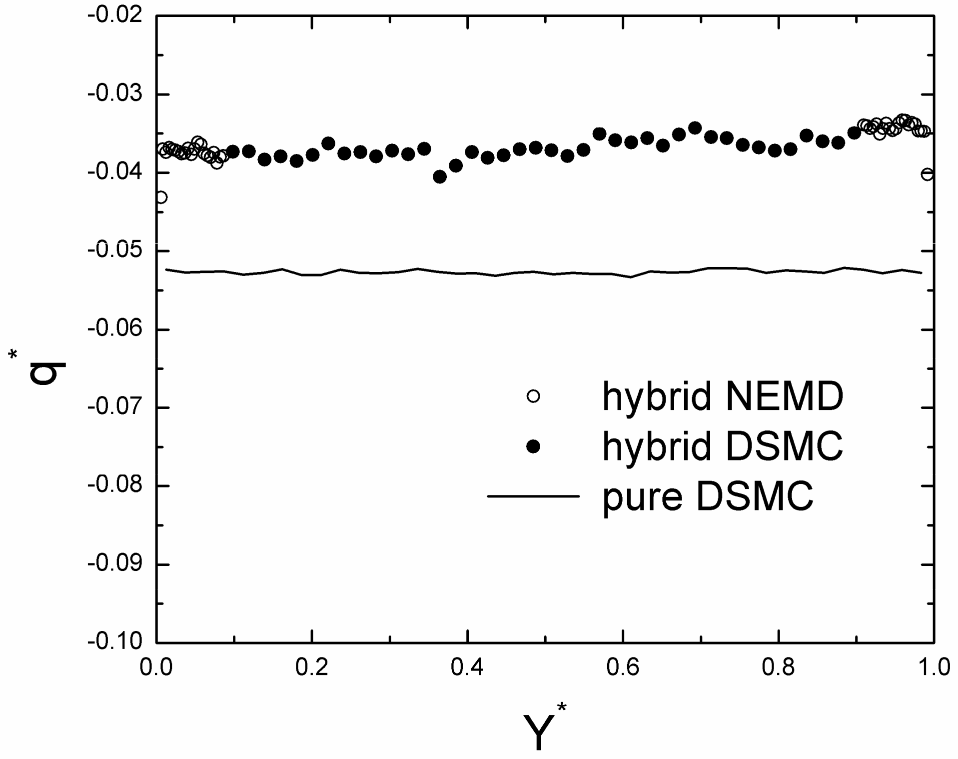

Fig. (2. 22) Normalized heat flux profiles for solid molecule wall case: $m_s = 100m_g$, $\varepsilon_{sg} = 1.0$. *Heat flux is normalized by* $m^{-1/2}n_0(k_BT_0)^{3/2}$, *where* n_0 *and* T_0 *are the initial number density and temperature, respectively. Wall distance coordinate is normalized by mean wall separation.*

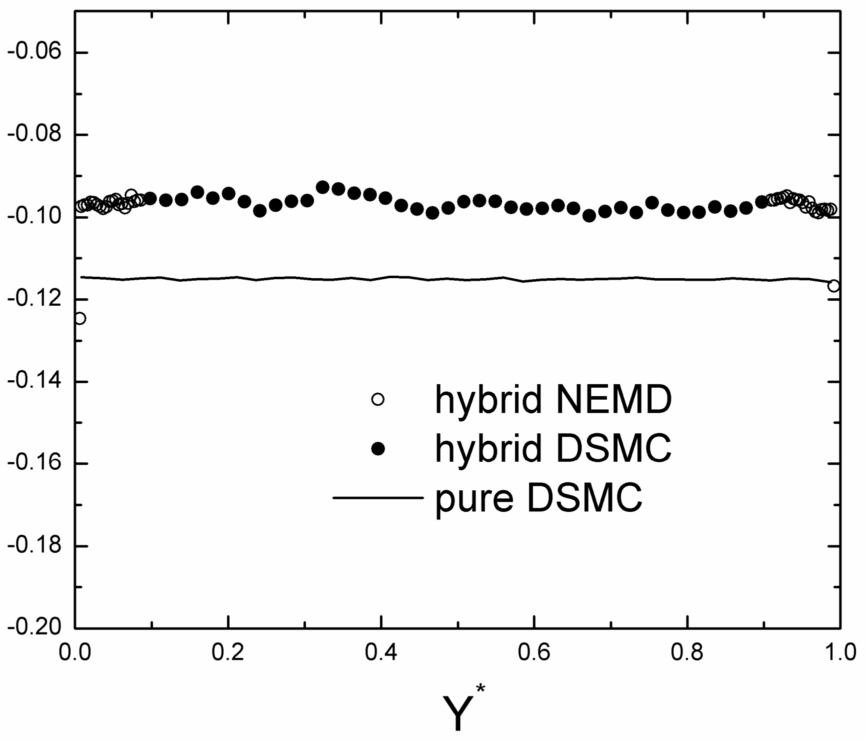

Fig. (2. 23) *Normalized heat flux profiles for solid molecule wall case:* $m_s = 25m_g$, $\varepsilon_{sg} = 1.0$. *Heat flux is normalized by* $m^{-1/2} n_0 (k_B T_0)^{3/2}$, *where* n_0 *and* T_0 *are the initial number density and temperature, respectively. Wall distance coordinate is normalized by mean wall separation.*

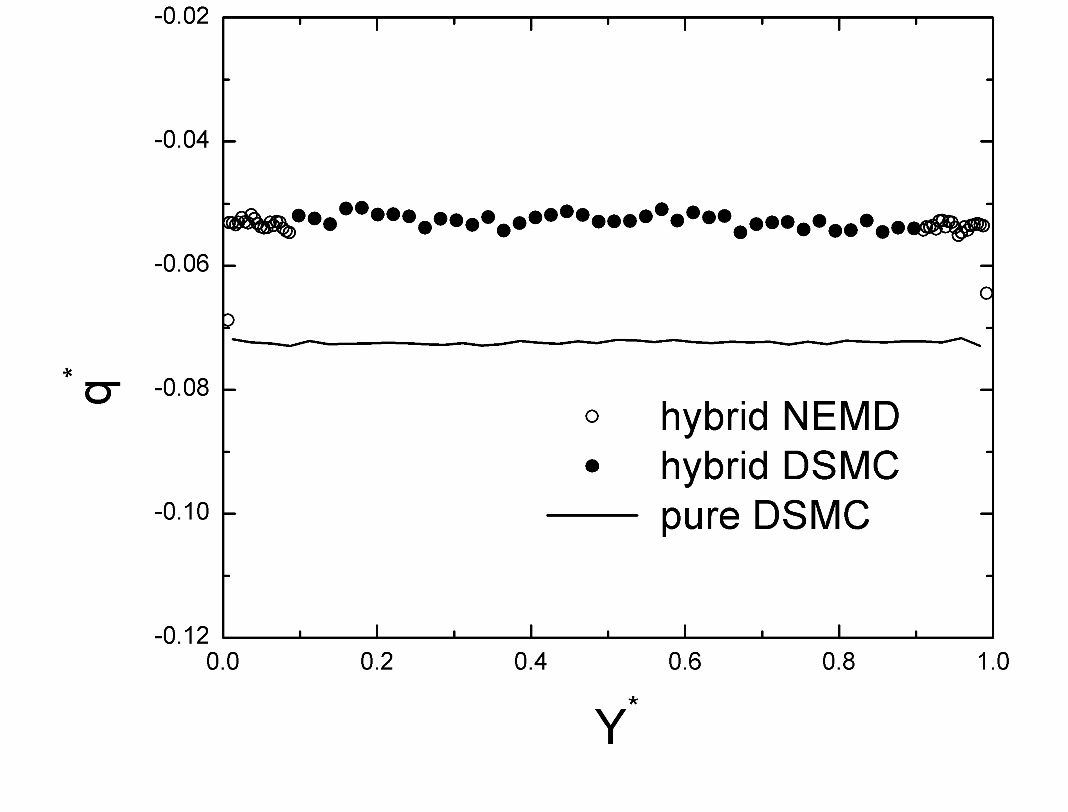

Fig. (2. 24) Normalized heat flux profiles for solid molecule wall case: $m_s = 25m_g$, $\varepsilon_{sg} = 0.5$. *Heat flux is normalized by* $m^{-1/2} n_0 (k_B T_0)^{3/2}$*, where* n_0 *and* T_0 *are the initial number density and temperature, respectively. Wall distance coordinate is normalized by mean wall separation.*

In Figs. (2.25) and (2.26), the normal and tangential thermal accommodation coefficients of the upper wall are shown in relation to m_s and ε_{sg}, separately for the cases of Table 2.1 with some additional parameter sets added. The accommodation coefficients increase with an increase in the wetting effect. Molecules tend to spend more time near the solid molecules with a large ε_{sg} than a small ε_{sg}. Hence, more energy is transferred from solid phase to gas phase, reducing the temperature slip and thermal residence. Similarly, with small m_s, the relative surface energy accommodation of the wall also increases. Considering a single interaction between one gas molecule and one solid molecule, a smaller m_s achieves more energy transfer from the solid to the gas in the interaction. The small m_s wall molecules have larger vibrational amplitudes and frequencies than the large m_s wall molecules. Thus, the much smaller incident gas molecules have more frequent and stronger energy exchanging interactions with the small wall molecules. These effects on molecular energy exchange account for all the variation of the accommodation coefficients with m_s and ε_{sg} shown in Figs. (2.25) and (2.26).

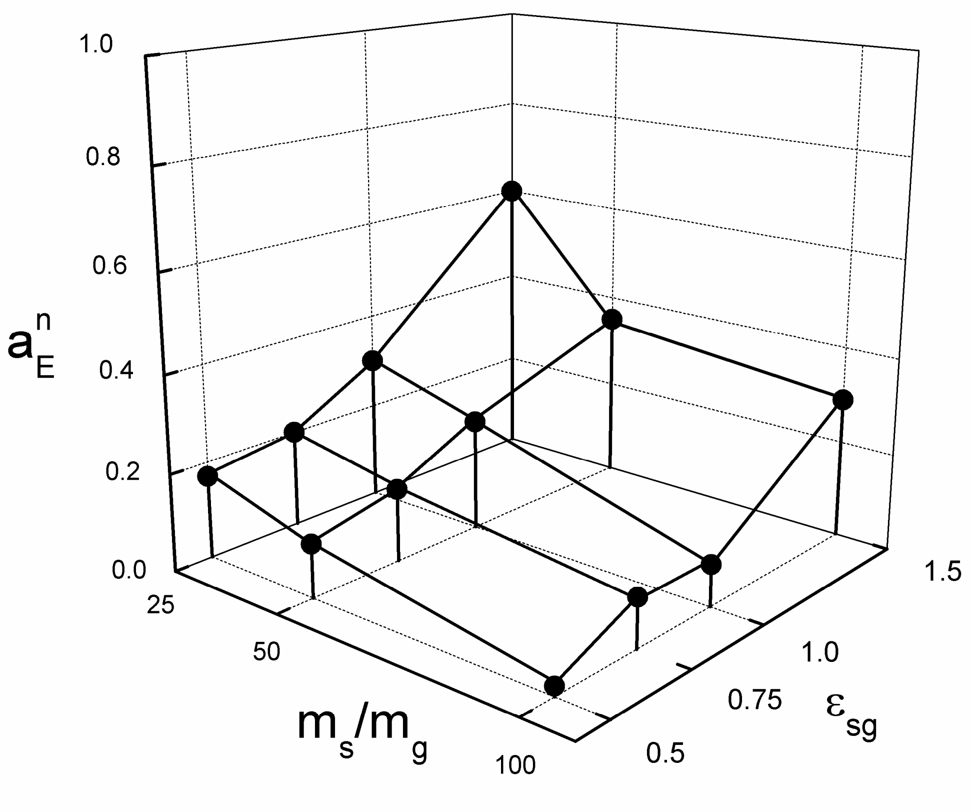

Fig. (2. 25) Normal accommodation coefficient variation for simulated solid molecule wall cases.

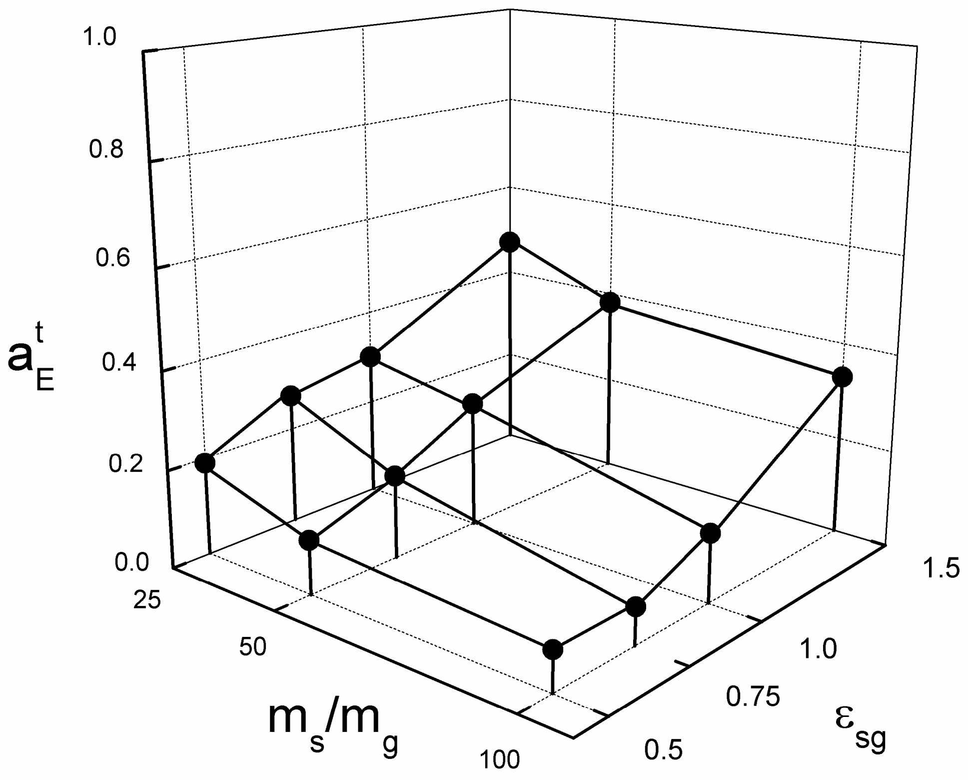

Fig. (2. 26) Tangential accommodation coefficient variation for simulated solid molecule wall cases.

Chapter 3

Molecular Dynamics Simulation of the Equilibrium Liquid-Vapor Interphase with Solidification

3.1 Chapter Summary

The equilibrium structure of the finite, interphase interfacial region that exists between a liquid film and a bulk vapor is resolved by molecular dynamics simulation. Argon systems are considered for a temperature range that extends below the melting point. Physically consistent procedures are developed to define the boundaries between the interphase and the liquid and vapor phases. The procedures involve counting of neighboring molecules and comparing the results with boundary criteria that permit the boundaries to be precisely established. Two-dimensional radial distribution functions at the liquid and vapor boundaries and within the interphase region demonstrate the physical consistency of the boundary criteria and the state of transition within the region. The method developed for interphase boundary definitions can be extended to nonequilibrium systems. Spatial profiles of macroscopic properties across the interphase region are presented. A number of interfacial thermodynamic properties and profile curve-fit parameters are tabulated, including evaporation/condensation coefficients determined from molecular flux statistics. The evaporation/condensation coefficients away from the melting point compare more favorably with transition state theory than those of previous simulations. Near the melting point, transition theory approximations are less valid and the present results differ from the theory. The effects of film substrate wetting on evaporation/condensation coefficients are also presented.

3.2 Introduction

At nanometer scales, the concept of a Gibbs dividing surface is invalid and liquid-vapor phase interfaces are distinguished by transitions in molecular density across an “interphase,” interfacial region. Away from the triple point, this region is at least a few molecular diameters thick. The structure of the region is of great theoretical and practical importance. Precise resolution of the instantaneous spatial distribution of macrosopic properties within the interphase and accurate determination of the interphase boundary with the liquid region and with the vapor region are essential to many phase interface simulation studies.

Molecular dynamics (MD) simulation can be used to study molecular transit across the liquid-vapor interphase. However, for this purpose, the two interphase boundary surfaces need to be defined correctly from a molecular perspective. One of the boundaries is a vapor surface, i.e., the boundary between vapor and interphase regions. Vapor molecules coming from the vapor bulk will cross this surface into the interphase region, where they interact with molecules coming from the liquid. The other boundary is a liquid surface, separating the liquid from the interphase. Evaporating liquid molecules coming from the liquid bulk will cross this surface into the interphase region and interact with molecules coming from the vapor. The two surfaces are illustrated in Fig. (3.1).

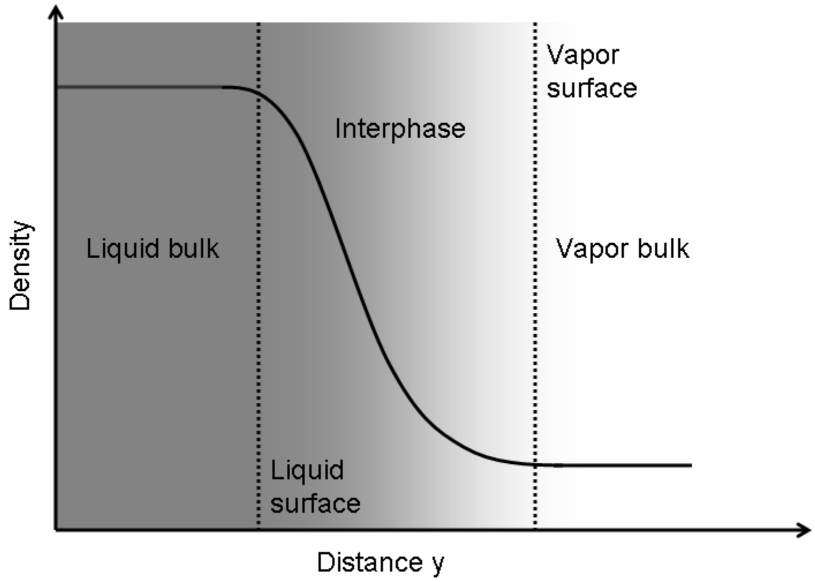

Fig. (3. 1) Illustration of interphase structure.

There is a considerable body of research literature devoted to molecular dynamics (MD) simulation of liquid-vapor interfaces. Much of the emphasis has been on the determination of density and pressure profiles across the interface and on the investigation of surface tension and capillary phenomena. Among the most noteworthy research contributing to the current state of knowledge is the work of Holcomb et al. [69-70] who assessed the importance of various simulation conditions and parameters to obtaining accurate results in Lennard-Jones liquid-vapor systems. Nijmeijer et al. [71] explored issues related to the effect of cut-off radius on the accuracy of surface tension results. Chapela et. al. [72], Holcomb et al. [69,70], and later Blokhius et al. [73] examined the role of tail corrections employed with a moderate cut-off radius for improvement in surface tension results. This topic was further investigated by

Mecke et al. [74] with consideration of long-range corrections. Wang et al. [75] reviewed the literature on liquid-vapor interphase simulation and studied energy phenomena at the interface. More recently P. J. in’t Veld et al. [76] reviewed the literature on long-range corrections and emphasized their importance, in addition to tail corrections, near the critical point. Wemhoff and Carey [27] summarized the simulation work on solid-liquid-vapor systems, where the liquid is a thin film residing on a molecular solid substrate, which is the system simulated in the present research.

MD simulation of evaporation and condensation phenomena to determine the nonequilibrium condensation or evaporation coefficient at the interface between liquid and vapor requires unambiguous resolution and tracking of the moving phase-boundary surfaces. A number of investigators have employed MD simulation to study evaporation and/or condensation coefficients for various liquid-vapor systems under equilibrium and/or nonequilibrium conditions (e.g., [35, 38,39,75]).

Condensation and evaporation coefficients derived from simulation are of interest because they characterize the interfacial mass transfer occurring during phase change and are related to interfacial heat transfer. Furthermore, for nonequilibrium systems, condensation and evaporation coefficients can be used to construct a kinetic boundary condition at an assumed Gibbs interface for application of kinetic theory-based analytical or simulation methods to the vapor region. In addition, the coefficients provide a direct way to compare the results of liquid-vapor simulations to theory or experiments.

The evaporation coefficient can be defined as the ratio of the mass flux of spontaneously evaporated molecules entering the vapor from the interphase to the total mass flux entering it.

The term “spontaneously evaporated” was used by Ishiyama et al. [37-39] to refer to the flux of molecules entering the vapor that originate in the liquid. (For convenience, the flux terminology and conventions of Ishiyama et al. were adopted in the present work.) This is equivalent to the flux evaporated from the liquid into a vacuum, where there are no collisions above the liquid surface. Ishiyama et al. simulated evaporation into a vacuum with MD to obtain the spontaneous evaporation flux at a given liquid temperature for equilibrium liquid-vapor evaporation coefficient studies. This was necessary because they could not, with confidence, discriminate between spontaneously evaporated and reflected molecules in the interphase in their liquid-vapor MD simulations.

The condensation coefficient can be defined as the ratio of the mass flux of condensed molecules entering the liquid phase that originate in the vapor to the total incident flux from the vapor. (The incident flux from the vapor includes molecules that are reflected back into the vapor from the interphase. [35]) Determination of the nonequilibrium condensation coefficient from MD has been a topic of controversy because of ambiguities in collection and use of molecular mass flux statistics. [35,37-40]

At equilibrium, the evaporation and condensation coefficients are effectively equal and their determination from MD simulations is less challenging. However, results for these coefficients from various molecular dynamics studies [39, 75, 77, 78] differ somewhat with each other and with the transition state theory of Nagayama and Tsuruta [77]. One issue is the consistency of the molecular flux collection statistics with respect to the physical definition of the liquid-vapor interface. It is critical to have a precise location for the liquid and vapor interphase boundaries when following molecules during a MD simulation for purposes of determining if they are to be considered condensed, reflected, or spontaneously evaporated. If the vapor interphase boundary can be precisely defined, the need to simulate liquid evaporation into a vacuum to obtain the spontaneously evaporated flux is eliminated.

From the foregoing, it is clear that a precise and consistent method for identifying the interphase liquid and vapor boundaries is important for the precision and consistency of interfacial molecular data collection and interfacial property definitions under a wide range of equilibrium and nonequilibrium conditions. Furthermore, criteria for identification of the boundaries and the resulting interphase thickness should not be conceptually arbitrary and should be molecular physics-based to take advantage of MD simulation capabilities.

The heart of the present research is a molecular physics-based MD procedure for the precise and consistent determination of liquid-vapor interphase boundaries and collection of molecular mass flux samples at these boundaries. Computations of condensation and evaporation coefficients and fluid properties within the interphase then proceed in the usual manner from the MD statistics. The interphase boundary treatment is based on physically meaningful definitions and can be readily extended to nonequilibrium systems. In the present work, it is applied to the study of an equilibrium system comprised of an argon condensed phase film on a solid substrate in equilibrium with an argon vapor bulk over the film. The system is investigated within a range of temperatures that extends below the melting point of argon. Argon was selected as a specific example of a Lennard-Jones potential simulation model applied to a monatomic species.

3.3 Interphase Boundary and Mass Flux Method

Definitions of both interphase boundaries are necessary to collect molecular mass flux statistics for computation of interfacial mass transfer in MD simulations. The sample-average vapor colliding mass flux, $\langle J_{coll} \rangle$, and the outgoing mass flux, $\langle J_{out} \rangle$, are computed from the number of molecules crossing the vapor surface that originate in the vapor region or in the interphase region, respectively. The sample-average condensation mass flux, $\langle J_{cnds} \rangle$, is computed from the number of molecules that originate in the vapor and cross the liquid surface and the sample-average mass flux of spontaneously evaporating molecules, $\langle J_{evap}^{sp} \rangle$, is computed from the number of molecules that originate in the liquid and cross the vapor boundary. Therefore, consistent with their verbal definitions given earlier, the condensation and evaporation coefficients are, respectively

$$\sigma_c = \frac{\langle J_{cnds} \rangle}{\langle J_{coll} \rangle} \qquad \text{and} \qquad \sigma_e = \frac{\langle J_{evap}^{sp} \rangle}{\langle J_{out} \rangle} \tag{3.1}$$

Meland et al. [35] used the Soave-Redlich-Kwong (SRK) equation of state in their MD simulation to distinguish between the vapor bulk and interphase region for simulation of net evaporation and condensation. The SRK equation, relating pressure (*p*), temperature (*T*), and density (ρ) is

$$p_{SRK} = \frac{RT}{v\ -b} - \frac{a}{v(v-b)} \tag{3.2}$$

in which *v* is the molar volume and *R* is the gas constant; the constants, *a* and *b*, can be estimated by fitting molecular dynamics data from simulation of a Lennard-Jones gas. To determine the vapor boundary surface, the RSK equation of state was compared with molecular dynamics results from different locations across the interface region. As the liquid is approached from the vapor side, the position where $\left|p - p_{SRK}\right|$ becomes greater than the maximum of $\left|p - p_{SRK}\right|_{v}$, i.e., the maximum statistical fluctuations in the vapor bulk, was designated as the vapor surface.

For determining the liquid surface interphase boundary, Meland et al. applied a purely geometrical method. In this method the liquid surface location was defined as the position where a tangent line at the center of interphase region on the density profile crossed the liquid density extended profile.

These ways of defining the vapor and liquid boundary surfaces are impractical for an unsteady nonequilibrium state where a liquid layer keeps growing or decreasing due to condensation or evaporation. Without having enough quasi-steady samples, the MD results contain considerable statistical noise; thus, it is difficult to compare the local state obtained from MD to the SRK equation of state. The same difficulty is encountered in trying to locate the liquid surface based on the geometry of the density profile.

The present work focuses on a new procedure to address these problems. By employing an improved method for vapor-liquid interphase boundary definition, the evaporation/condensation coefficients and interphase properties can be evaluated more robustly. The procedure eliminates reliance on the macroscopic (mean) quantities, which would have to be collected from successive MD iterations to define the boundaries as in [71]. Instead, a molecular interaction approach is applied to define them, bypassing the problems inherent in the macroscopic approach.

Molecular interaction or spacing information at a microscopic level can be utilized directly from MD simulation for boundary definitions without significantly increasing the computational cost. This is because the MD algorithm directly identifies the interacting pairs of molecules whose separation is less than the interaction cutoff distance, r_c.

For a planar liquid-vapor surface, locating the vapor or liquid surface can be realized by counting the interacting molecular partners per molecule in a specially constructed volume, V', about each molecule in the simulation. The volume, V', is a thin region sliced from the center of a sphere about the molecule with radius, r_c, by planes parallel to the interface and equidistant from the molecule at the center of the sphere. This geometry is shown in Fig. (3.2). Because the volume is sliced from the cut-off distance sphere, every molecule in the slice is an interaction partner for the molecule at the center. As illustrated in Fig. (3.2), there are more interacting partners, $N'(t)$, in the "slice" about a liquid molecule than those in a corresponding region about a vapor bulk molecule (or gas molecule since the method can be extended to include a mixture of vapor and noncondensable species). As a part of a sphere, the volume's magnitude is described by a three-dimensional integral in spherical coordinates (r,θ,ϕ) about the molecule as

$$V' = \iiint_{R'} r^2 \sin\theta dr d\theta d\phi \tag{3.3.a}$$

where

$$R' = \{(r,\theta,\phi) \mid 0 \le r \le r_c, \chi \le \theta \le \pi\text{-}\chi, 0 \le \phi \le 2\pi\} \cup \{(r,\theta,\phi) \mid 0 \le r \le r_c \frac{\cos\chi}{\cos\theta}, 0 \le \theta \le \chi, 0 \le \phi \le 2\pi\}$$
$$\cup \{(r,\theta,\phi) \mid 0 \le r \le r_c \frac{\cos\chi}{\cos\theta}, \pi\text{-}\chi \le \theta \le \pi, 0 \le \phi \le 2\pi\} \tag{3.3.b}$$

in which

$$\chi = \arccos(\frac{h'}{2r_c}) \tag{3.3.c}$$

In Eq. (3.3), $R^{'}$ represents the thin slice region domain and $h^{'}$ is the y thickness of the slice.

The primary reason for choosing spherical coordinates and the thin slice in the y direction is that the MD simulation is three-dimensional and interaction molecules are identified within a sphere, while the boundary location must be identified as a y coordinate. Any other chosen volume with a constant thickness in the y direction would either contain molecules that are not interaction partners or fewer interaction partners so in this sense the slice geometry is optimal. The y thickness of the slice, $h^{'}$, was optimized to be 0.2σ; it was carefully chosen to achieve the purpose of locating the liquid or vapor planar boundary to a resolution of the slice thickness or less, while containing a sufficient number of partners to be physically representative of the microscopic partner distribution.

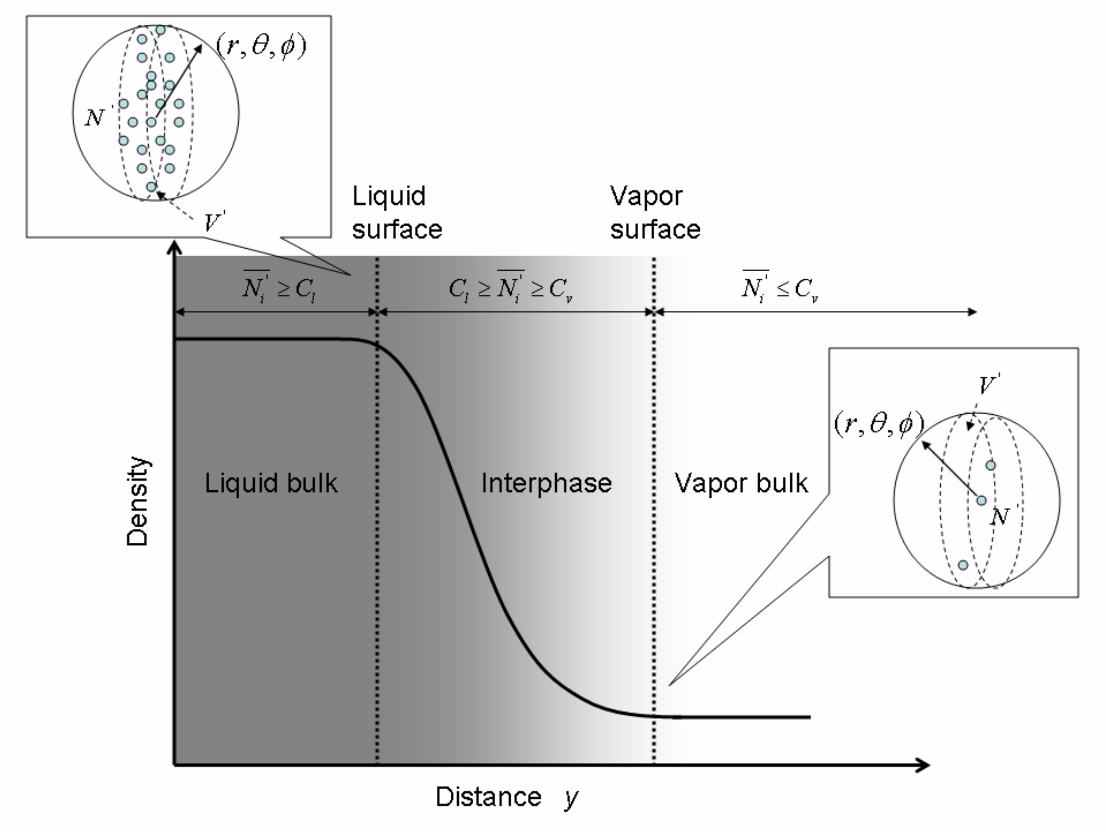

Fig. (3. 2) Illustration of interacting molecule volumes in different phase regions.

In an actual MD simulation, to obtain a meaningful value for the number of interaction partners per molecule, $N_i'(t)$, in the volume, V', an average value is obtained by averaging over the Verlet list update interval, usually chosen as 20 MD time steps (i.e. $\left\langle N_i'(t) \right\rangle_{20}$), and then local spatial averaging of the time averages within each spatial sampling bin, *i*, so that $\overline{N_i'(t)} = \sum_1^N \left\langle N_i'(t) \right\rangle_{20} \Big/ N$, where N is the total number molecules in bin, *i*. In the present procedure, $\overline{N_i'(t)}$, i.e. the mean number of interaction partners per molecule in sampling bin, i, is computed for each bin along the y distance from the vapor bulk into the liquid.

Obviously, $\overline{N_i'(t)}$ varies dramatically from vapor phase to liquid phase. To determine where the interphase boundaries are located, two criteria values, C_g and C_l, are set as the limits on $\overline{N_i^{'}(t)}$ for the fluid to be considered vapor phase or liquid phase, respectively.

For the vapor phase, the theoretical number of interaction particles per molecule in an occupied volume is

$$N = \iiint_{V^{'}} ng(r)d\mathbf{r} \tag{3.4}$$

where n is the vapor number density and $g(r)$ is the well-known radial distribution function (RDF) from statistical mechanics. Hence, the theoretical number of interaction partners per molecule, $N^{'}$, in the thin volume, $V^{'}$, can be obtained as

$$N^{'} = \iiint_{R^{'}} ng(r)r^2 \sin\theta dr d\theta d\phi \tag{3.5}$$

The RDF for a dilute gas can be expressed as

$$g(r)_{gas} = \exp\left[\frac{-V\ (r\ )}{k_B T}\right] \tag{3.6}$$

where k_B is the Boltzmann constant and $V(r\ )$ is the two-body potential, which generally can be represented adequately by the 12-6 Lennard-Jones interaction potential. The theoretical number of interaction partners per molecule in $V^{'}$ in the vapor can then be obtained by

$$N_v^{'} = \iiint_{R^{'}} ng(r)_{gas} r^2 \sin\theta dr d\theta d\phi \tag{3.7}$$

The criteria values for the vapor boundary, C_v, employed in the present MD simulations are set to be equal to the mean $\overline{N_i^{'}(t)}$ obtained from preliminary MD simulation experiments of pure vapor, whose densities correspond to saturated density at the different temperatures for which the present multiphase simulations were performed. If the density, n, in Eq.(3.7), is taken to be the saturated vapor density, n_v,used for the preliminary MD simulations at a given temperature, an analytical expression is obtained that can be compared to the C_v obtained from the MD simulations for that temperature. The results are compared in Fig. (3.3) for dilute argon gas at a number of temperatures. The values of C_v obtained from the simulations are shown to be in good agreement with Eq. (3.7).

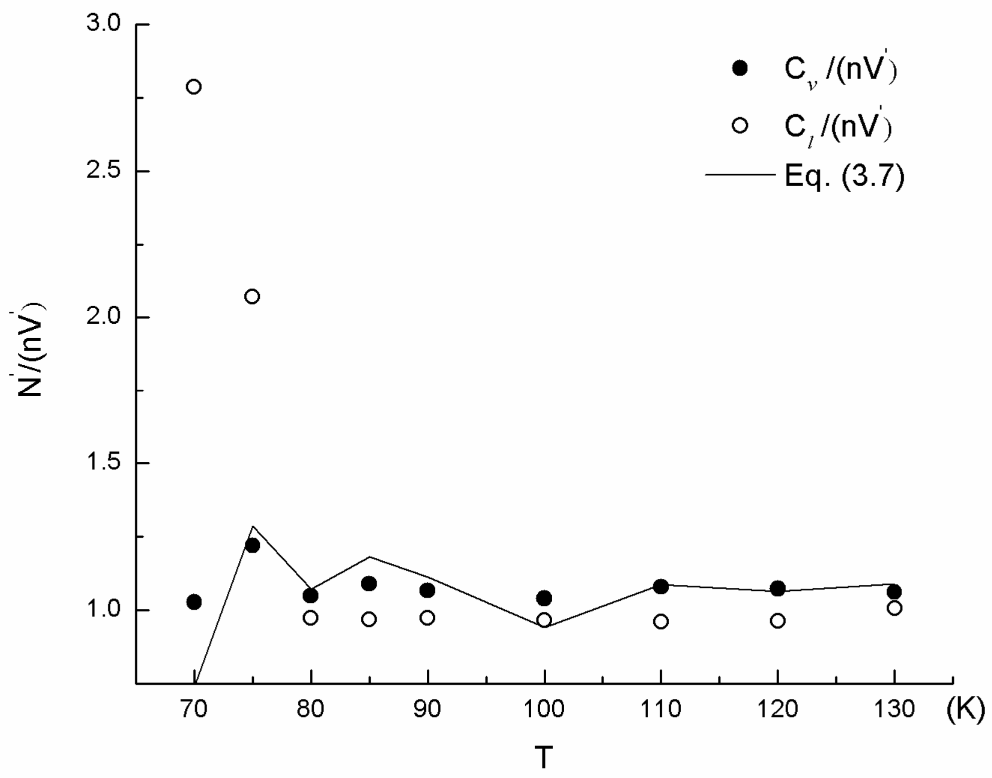

Fig. (3. 3) Temperature dependence of simulation-determined liquid and vapor interphase boundary criteria and theory-determined vapor interphase boundary criterion. (The SD for C_v *is less than 5% and the SD for* C_l *is less than 2%).*

C_l is chosen analogously through MD liquid phase simulation experiments, whose results are shown also in Fig. (3.3) for argon bulk liquid. No analytical comparison for C_l is given since N_l' is more difficult to obtain analytically due to the lack of a general theoretical expression for $g(r)$ in the liquid.

By using the criteria values, C_v and C_l, the liquid and vapor boundaries can be precisely determined. As illustrated in Fig. (3.2), the first sampling bin encountered, in moving from right to left in the figure, whose $\overline{N_i^{'}(t)}$ is smaller than C_l, is recorded as the bin within which the liquid surface is located. The precise liquid surface position, $y_l^{'}(t)$, is decided by the position of the molecule that has the largest $\left\langle N_i^{'}(t)\right\rangle_{20}$ among others in the bin. The vapor surface can be located likewise as within the first bin whose $\overline{N_i^{'}(t)}$ is greater than C_v, The exact vapor surface, $y_v^{'}(t)$, position can be decided by the position of the molecule that has the smallest $\left\langle N_i^{'}(t)\right\rangle_{20}$ in the bin.

The resulting $y_l^{'}$ and $y_v^{'}$, which are copied from individual molecule positions, exhibit statistical fluctuations, as would be expected, and the well known moving window average technique of statistical analysis was used to smooth them. This reduction of statistical fluctuations is especially important when computing condensation and evaporation coefficients since the molecular fluxes are based on the position of the vapor and liquid boundaries. The moving average surface location at a time step, $y_{v,l}(t_i)$, was calculated from the fluctuating location, $y^{'}_{v,l}(t_i)$, during a period from L_{i-1} to L_i as

$$y_{v,l}(t_i)=\left(1-\frac{t_i-L_{i-1}}{\Delta L}\right)y_{v,l}(L_{i-1})+\left(\frac{1}{\Delta L}\right)\sum_{i=L_{i-1}+1}^{t_i} y_{v,l}{}^{'}(t_i) \tag{3.8}$$

where ΔL is the window period, $L_i - L_{i-1}$.

An interpretation of Eq. (3.8) is that the current average is set to be the previous average data plus the current average in a window period, with different time weights. With time advancing in the window period, the weight of previous average data linearly decreases from unity and the weight of the current average in a window period linearly increases to unity. The window length, ΔL, which is not allowed to be larger than the system evolution time scale, was chosen to be 40,000 time steps in the present simulations.

From the procedures presented, the definitions of vapor and liquid boundaries are well established. They are the basis for the liquid-vapor equilibrium results to be shown in the sections that follow. The method is not limited to monatomic molecules. In a molecular system the entire scale of a simulation would be larger, including the width of the interphase region and the size of bins used in delineating the various phases. Bin sizes on the scale of the molecular radius of gyration would be appropriate for such simulations.

Our method of determining interphase boundaries is also not restricted to the stable interface of an equilibrium system. In fact, it was designed with a nonequilibrium system in mind. In a nonequilibrium system, where the liquid layer keeps growing or decreasing with time due to condensation or evaporation, the current method will also handle the moving boundaries. Based on an assumption of local equilibrium at the vapor and liquid interphase boundaries, the criteria values, C_v and C_l, also will allow location of the instantaneous boundary surfaces.

3.4 MD Simulation Procedures

To test the present interfacial location scheme, a series of MD simulations were performed on the solid-liquid-vapor composite system described earlier. The Lennard-Jones interaction potential used in the MD simulations is

$$V(r_{ij}) = 4\varepsilon\left[\left(\frac{\sigma}{r_{ij}}\right)^{12} - \varepsilon_{ls}\left(\frac{\sigma}{r_{ij}}\right)^{6}\right] \tag{3.9}$$

where σ and ε are the length and energy parameters and r_{ij} is the distance between molecules *i* and *j*. To evaluate the Lennard-Jones potential force system, the shift-force potential energy [11] was selected with a large cut-off distance of 4.0σ to ensure more accurate physical properties such as density and surface tension.

The use and choice of a cutoff in molecular simulations depends on what aspect of the system is of interest. Surface tension is unusually sensitive to details of the potential tail; a correction may be estimated semi-analytically in the surface tension computation [76] as presented in a subsequent section. Bulk properties do not share this sensitivity. More generally, outside of most (but not all) Coulomb interaction problems, almost all applications of MD use a cutoff. In the present work, no long range correction to the force was used. The employment of such a long range correction will improve the simulation results, but this effect is small except near the critical point. [76] The present simulation temperatures were well below the critical point.

In Eq. (3.9), the liquid-solid interaction strength, ε_{ls}, is not present for interactions between fluid molecules (liquid or vapor) but was introduced for the liquid-solid molecular interactions. The parameter, ε_{ls}, affects the liquid-solid interaction, and, therefore, the part of the liquid within interaction range of the solid. It describes the wetting effect at the liquid-solid interface. In MD studies of drop spreading and related liquid-solid interactions issues, varying this coefficient is commonly used to vary the wetting behavior. [22,79,80] A version of this treatment has also been used in solid-liquid-vapor systems with evaporation and/or condensation. [29,81]

In the present study, a value of 1.0 was used for ε_{ls} to establish a baseline, completely wetting surface at the solid substrate, and then wetting phenomena were also investigated using two different wetting effect surfaces. Interactions of the vapor molecules with the solidified condensed phase surface in the simulations at temperatures below the melting point were assumed to be completely wetting.

The Gear predictor-corrector algorithm was applied to solve the Newton's equations of motion for the molecules with a time step, Δt of $0.005\sqrt{m\sigma^2/\varepsilon}$. The parameters for the molecules used in the simulations are listed in Table 3.1. The value of ε ensures that the MD reduced temperature unit, ε / k_B, (k_B is the Boltzmann constant) is equal to 120K.

Table 3. 1 Parameters for simulation molecules

Parameter	Physical value
length	$\sigma = 3.4\times10^{-10}\ m$
energy	$\varepsilon = 1.66\times10^{-21}\ J$
argon molecular mass	$m = 6.64\times10^{-26}\ kg$
solid molecular mass	$m_s = 6.64\times10^{-24}\ kg$

As shown in Fig. (3.4), the three system components (substrate-liquid-vapor) were initially arranged in a face-centered-cubic (FCC) lattice. 484 solid molecules and 3908 liquid and vapor molecules were employed in the simulation domain consisting of an elongated box, whose dimensions were $L_x = L_z = 15.15\sigma$, and $L_y = 97.64\sigma$. A molecular solid wall substrate confined the liquid molecules from below. The substrate was a FCC crystal structure formed from two layers of harmonic molecules through tethering large mass molecules ($m_s = 100m$) to a fixed site with spring connections. Based on preliminary simulation testing, additional layers of solid phase molecules would have little effect on the liquid-vapor interphase. Periodic boundary conditions were applied in the x and z directions.

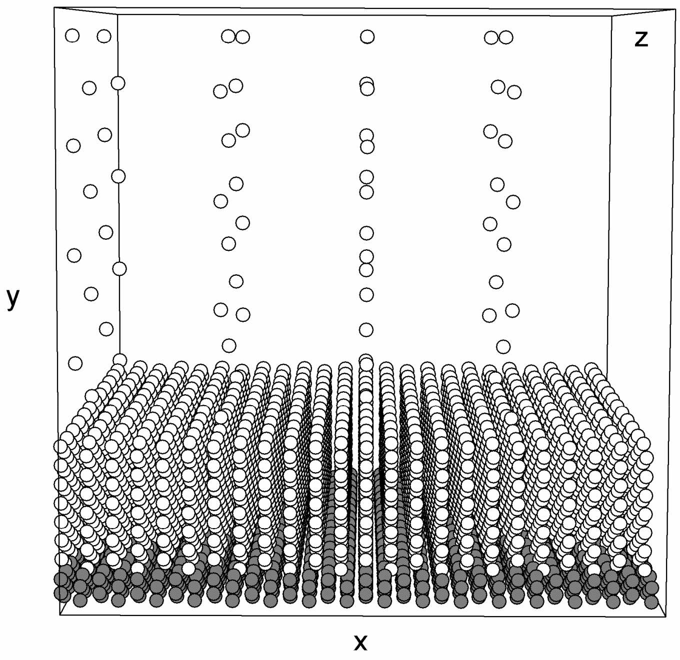

Fig. (3. 4) Initial positions of solid (dark grey dots), liquid, and vapor (light grey dots) molecules in the simulation domain.

The vapor molecules were confined from above by a thermal diffusive upper wall. At this wall, the vapor molecules with wall-colliding trajectories emerge from the wall back to the system with their parallel velocity components sampled from a Maxwellian distribution at the wall temperature and their normal velocity components sampled from a Rayleigh distribution at the wall temperature [82]. The densities of the thin film liquid layer sitting above the solid wall and the vapor region were initialized from experimental values of argon liquid and vapor in equilibrium [83].

Simulations were initiated at a low temperature ($T = 0.1\varepsilon/k_B$) and then the temperature of the entire system was gradually increased to the desired equilibrium temperature over 30,000 time steps by a velocity rescaling technique [11]. One reason for gradually varying the system temperature from the low point was in consideration of the unphysical liquid-solid molecular interactions that are created by imposing artificial initial positions and artificial Maxwellian randomized initial velocities. Such unphysical interactions can cause the liquid particles to bounce away from the solid surface and destroy the liquid layer attached to the substrate. Instead of assigning the desired equilibrium temperature to the system initially, the temperature was gradually increased to reach the proper state.

The ultimate purpose of the temperature ramp is to get to a stable system at the desired temperature, and the length of the ramp is essentially immaterial as long as it does this. No property data were collected outside of the stable regime.

The velocity rescaling system thermostat was maintained after the system reached the desired temperature for another 50,000 time steps, followed by a 100,000-200,000 step relaxation period to achieve the equilibrium state. During the equilibrium stage of the simulation, the solid and diffusive walls were kept at the desired equilibrium temperature while the fluid was left alone... The solid substrate temperature was controlled by the velocity rescaling thermostat. Since the behavior of the solid was of no interest to us except insofar as it provided a “boundary condition” to the liquid, a simple thermostat sufficed.

During the equilibrium stage, molecules were sampled within 200 uniform-thickness bins along the y direction during the equilibrium stage and time-averaged results were produced until the end of the simulation period (3,000,000Δt). A 40,000 time-steps interval was chosen between each configuration saved for further analysis.

Enthalpy and surface tension are very relevant quantities in liquid-vapor systems. The enthalpy per unit mass in a sampling bin can be evaluated as [84]

$$h_J = \frac{1}{mN_J}\left[\frac{5}{2}k_B T_J N_J + \sum_i^{N_J}\phi_i + \frac{1}{3}\sum_{i<j}^{N_J}(\mathbf{F}_{ij}.\mathbf{r}_{ij})\right] \tag{3.10}$$

where N_J and T_J are the number of molecules and local temperature within bin *J*. The first term in the right hand side of Eq.(3.10) is the kinetic contribution to enthalpy, and the last two terms represent the potential energy (ϕ_i) and pairwise interaction ($\mathbf{F}_{ij}.\mathbf{r}_{ij}$, where $\mathbf{F}_{ij}$ is the interaction force between molecule *i* and *j*) contributions to the enthalpy, respectively.

For a planar liquid-vapor interface, the surface tension is given by [27]

$$\gamma = \int_0^{+\infty}[p_\perp(y) - p_{||}(y)]dy \tag{3.11}$$

where $p_\perp(y)$ and $p_{||}(y)$ are the pressures normal and parallel to the liquid-vapor interphase, respectively. For MD implementation, the surface tension can be simplified to

$$\gamma = \frac{L_y}{N_b}\sum_{J=J_l-k}^{J=J_v+k}\left[p_{yy} - \frac{1}{2}(p_{xx}+p_{zz})\right] + \gamma_{\text{tail}} \tag{3.12}$$

in which J_l and J_v are the bins where the liquid surface and vapor surface are located. N_b is the number of bins, which is 200 in the present simulation. The positive integer, *k*, is used to insure that the surface tension sampling region is widened beyond the point where there is any significant pressure difference contribution to Eq. (3.12). The present computations used a k number of eight. γ_{tail} is the tail correction term to compensate for the pressure difference beyond the cut-off distance and to be consistent with the full L-J potential without a cut-off. By assuming the g(r) is equal to 1 above the cutoff and that the density profile has a hyperbolic shape, γ_{tail} can be written as [73]

$$\gamma_{tail} = 12\pi\varepsilon\sigma^6(\rho_l - \rho_v)^2 \int_0^1 (3s^3 - s)ds \int_{r_c}^{+\infty} \coth(2rs/d) r^{-3} dr \tag{3.13}$$

where *s* is the nondimensional integral variable.

3.5 Results and Discussion

Nine equilibrium temperatures of coexisting vapor and condensed phase of argon over a solid substrate were investigated, ranging from 70K to 130K. Mean values of macroscopic quantities, such as density, temperature and pressure in both the argon surface film and vapor phase, are reported by averaging over the space in each region. Bulk simulations of pure condensed phase and/or pure vapor also were performed at the equilibrium temperatures.

3.5.1 Solidification at Low Temperature

At the lowest equilibrium temperatures simulated (i.e., 70K and 75K), large bin-to-bin variations appeared in the density profiles in the film as shown in Fig. (3.5). These variations are a result of solidification and molecular layering that took place in the film as it froze. The presence of solidification was verified by calculating the mean square displacement (MSD) of molecules in the film and in bulk argon at equilibrium as a function of time. The MSD can be expressed as

$$\left\langle R(t)^2 \right\rangle = \frac{1}{N}\sum_i^N [\mathbf{r}_i(t) - \mathbf{r}_i(0)]^2 \tag{3.14}$$

where $\mathbf{r}_i(0)$ and $\mathbf{r}_i(t)$ are the original position and the current position of molecule, *i,* at time, *t*. In Eq. (3.14), the MSD is obtained by averaging only those molecules that remain in the region over a sufficiently long sampling period during the equilibrium phase.

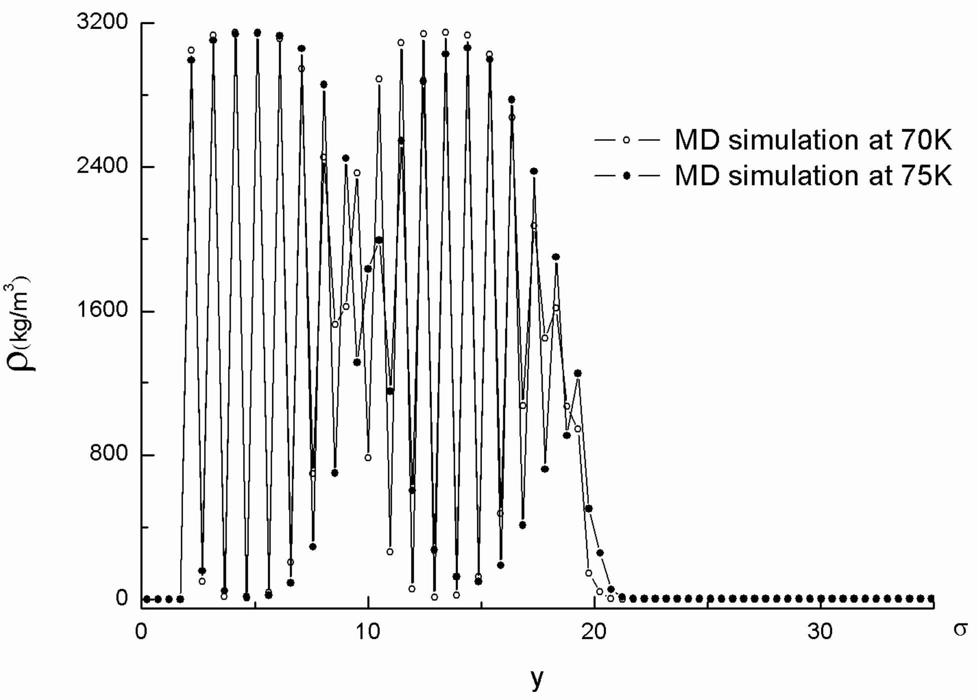

Fig. (3. 5) Density profiles for temperatures $T = 70K$ *and* $T = 75K$.

In a solid, the MSD should remain nearly constant over time due to the small diffusivity, while for a pure liquid it should increase linearly with time. In Fig. (3.6), MSDs from simulations at 70K, 75K, and 80K are compared for pure argon condensed phase bulks and films. It is seen that for system temperatures, 70K and 75K, the MSDs are nearly constant over the period of $50{,}000\,\Delta t$ and the material is solid, but the MSD at temperature 80K increases with time, indicating that the molecules are in the liquid state. The conclusion is that the melting temperature of the present simulated Lennard-Jones argon system at equilibrium is between 75K and 80K.

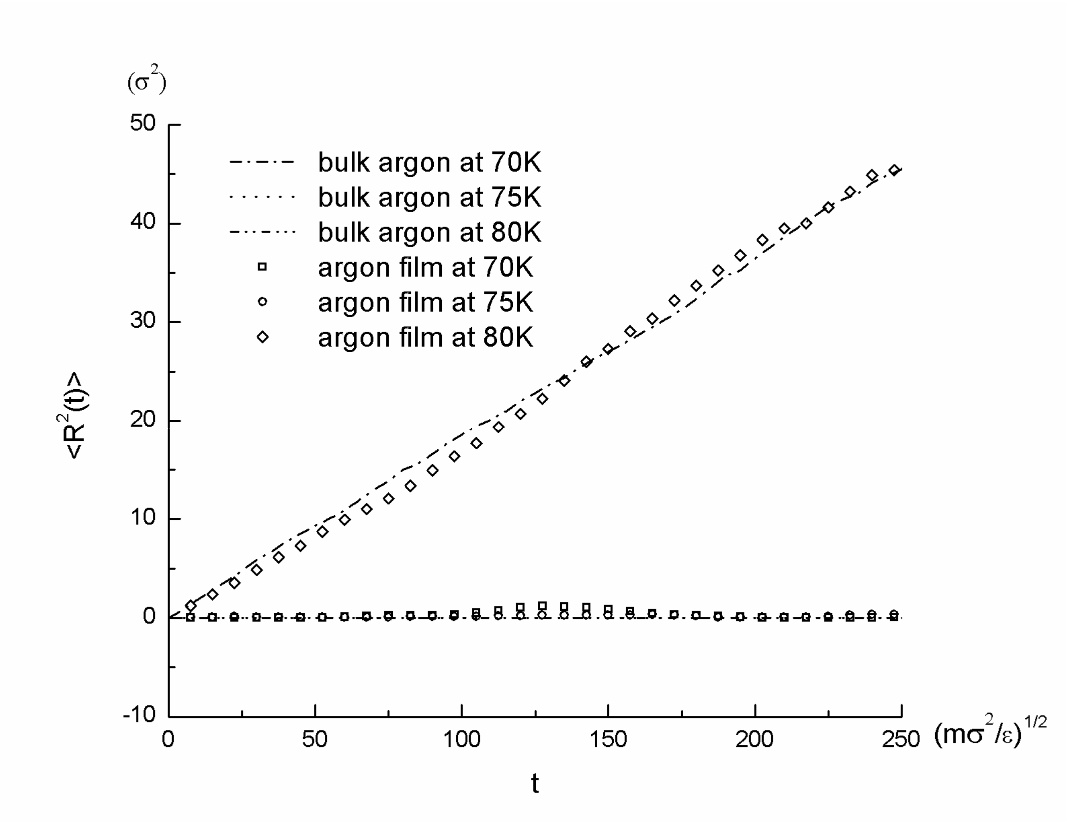

Fig. (3. 6) MSD versus time at equilibrium for temperatures 70K, 75K, and 80K.

The triple point for Lennard-Jones argon fluid has been well studied and proven to be around 83K [85]. The difference between the present shift-force potential energy estimate of melting temperature and the theoretical result is not unexpected since it is known that the effect of the difference in potentials is one of a number of simulated system effects that can influence phase transition temperature. [85-87] Furthermore, the presence of the (tethered-atom) solid base will alter the phase behavior. Lastly, the present simulation procedure of approaching the final equilibrium temperatures from below through sudden freezing of the liquid film followed by warming may influence the final results at equilibrium temperatures near the melting point.

3.5.2 Vapor and Liquid Boundary

The equilibrium phase densities obtained by molecular dynamics simulations of the composite system are listed in Table 3.2. The standard deviation (SD) for vapor densities is within seven percent of the mean value, while the SD for liquid densities is within 0.2 percent of the mean value, except for the simulations at temperatures, 70K and 75K, which are below the melting temperature. Due to the large bin-to-bin physical variations in density profile (See Fig. (3.5)), the mean solidified liquid densities have large SDs of over 50 percent of the mean density.

Table 3. 2 Argon liquid-vapor equilibrium properties

Temperature (K)	ρ_v (kg/m^3)	ρ_l (kg/m^3)	σ_e	σ_c	$\frac{\Delta H}{RT}$	$p_v\,(10^5 Pa)$	γ $(10^{-3} N/m)$
70	0.75	1700.34	0.780	0.782	12.367	0.0765	
75	2.05	1635.20	0.735	0.735	10.195	0.316	
80	4.09	1408.32	0.670	0.672	9.378	0.625	15.954
85	6.42	1378.35	0.673	0.672	8.685	1.051	14.571
90	10.62	1342.87	0.690	0.691	8.016	1.859	13.008
100	23.11	1277.93	0.655	0.655	6.786	4.274	10.388
110	45.25	1198.52	0.585	0.584	5.658	8.630	7.628
120	81.82	1109.83	0.444	0.444	4.529	15.381	5.103
130	144.91	991.29	0.283	0.283	3.404	25.787	2.676

Note: *SDs for* ρ_v *are within 7%; except simulation at temperature 70K and 75K, where SDs for* ρ_l *are within 0.2 %; SDs for* p_v *are within 2%; SDs for* σ_e *and* σ_c *are within 7%; SDs for* h_v *and* h_l *are within 5%.*

Rowlinson and Widom [88] addressed the issue of liquid-vapor interphase density profiles and suggested that they can be expressed by an empirical relation in the form of

$$\rho(y) = \frac{\rho_v + \rho_l}{2} + \frac{\rho_v - \rho_l}{2}\tanh\left[\frac{2(y - y_m)}{d}\right] \tag{3.15}$$

where ρ_l is the mass density of the liquid phase, ρ_v is the mass density of the vapor phase, y_m is the location of the equimolar dividing surface, and *d*, a measure of the interface thickness, [88] is given by

$$d = (\rho_v - \rho_l)\left[\frac{dy}{d\rho(y)}\right]_{y = y_m} \tag{3.16}$$

Most subsequent computational investigations of the interphase region have adopted Eq. (3.15) as the basis for their interphase density profiles. However, it has been demonstrated that an error function is a better fit to the profile in a Lennard-Jones fluid and, hence, improves results for surface tension if Eq. (3.11) is used instead of Eq. (3.12). This becomes important in the application of theory to the analysis of the effects of capillary wave broadening on interphase profiles [89].

For most purposes the differences between the hyperbolic tangent function and an error function are small. There was no actual use of the hyperbolic tangent in the present interphase boundary determination methodology or other analysis beyond tabulating curve fit data derived from Eq. (3.15) and Eq. (3.16) for comparison purposes. The standard tail correction relation, Eq. (3.13), also uses it. The present method is adaptable to an error function fit for surface tension computations in applications such as the fine structure of capillary waves.

In the present study, with the known ρ_v and ρ_l in Table 3.2, the MD interphase simulation results were numerically fitted to Eq. (3.15) by a nonlinear least-squares technique

(Levenberg-Marquardt method [90]). The density profile and least squares numerical fitting results are presented in Fig. (3.7) for a system temperature of 90K. The fitting region was chosen from the part of the simulation domain where the influence of the solid boundary in the liquid phase is diminished. The fitting results for the present simulation (excluding the simulations at 70K and 75K) are tabulated in Table 3.

At the higher temperature, the liquid layer above the solid phase became thinner, but the solid-liquid effects diminished as well. As shown in Fig. (3.8), the last layer of atoms clearly affected by the solid phase is about 18σ away from the liquid-vapor interphase for simulation at temperature 130K; as a result, the solid had minimal influence on the investigated liquid-vapor interphase.

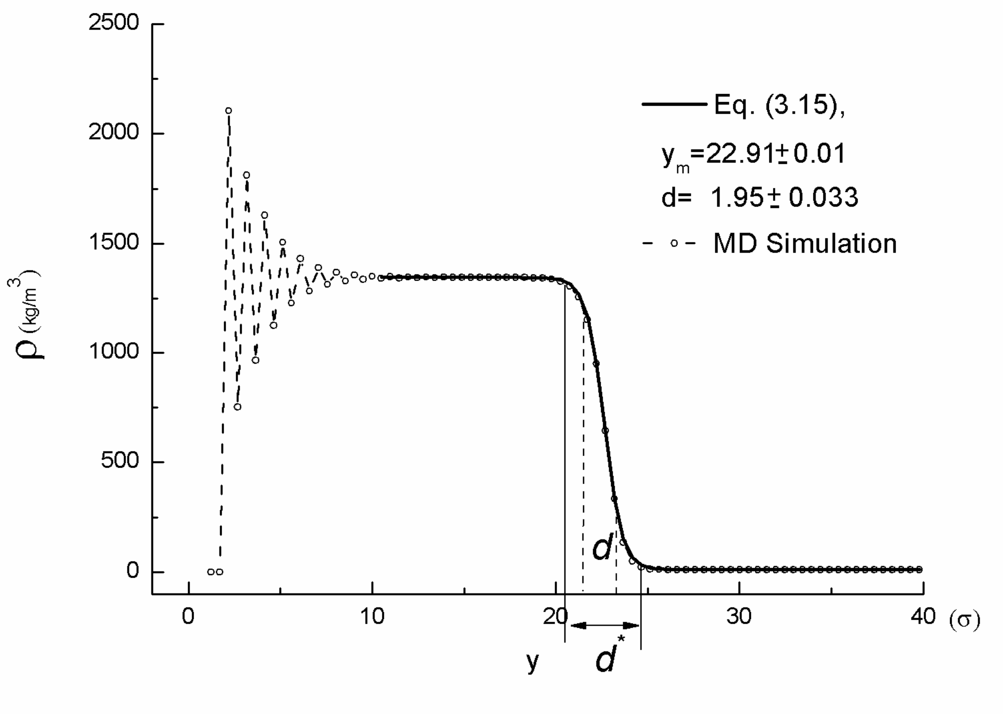

Fig. (3. 7) Comparison of Rowlinson and Widom interphase thickness definition with present definition on density profile for a solid-liquid-vapor system at $T = 90K$.

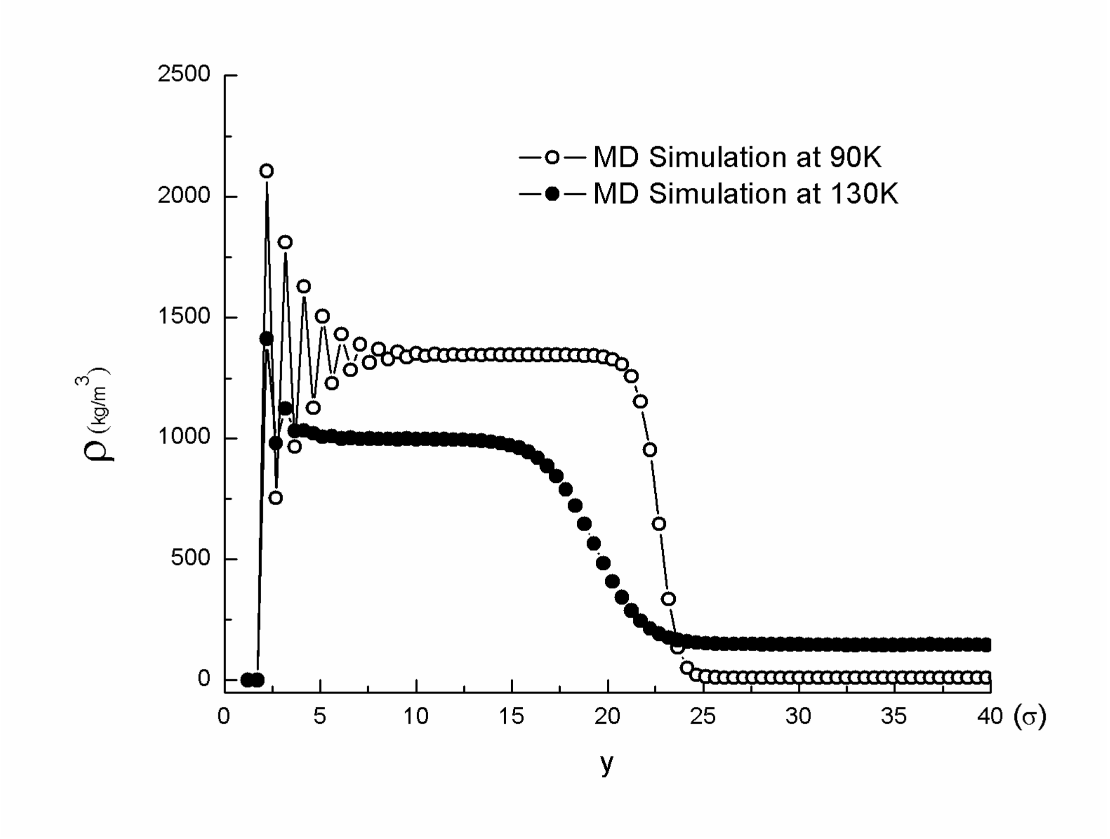

Fig. (3. 8) Density Profile for a solid-liquid-vapor equilibrium system for the temperatures $T = 90K$ *and* $T = 130K$.

The locations of liquid and vapor boundaries, $y_l(t)$ and $y_v(t)$, versus the iteration time in simulation at 90K are shown in Fig. (3.9), in which $y_v(t)$ and $y_l(t)$ appear reasonably smooth. The exact locations of the vapor and liquid, y_v and y_l, were decided at equilibrium by time averaging over the steady-state period. Note that the term "steady-state" refers to a state without a systematic variation in time, but does allow for small-amplitude fluctuating motion, as seen at equilibrium in the figure, which may result from random thermal fluctuations or more-organized capillary waves [89]. The latter seems more likely due to the fact that smaller scale fluctuations were smoothed by the moving window average procedure.

Before reaching the "steady state," the locations of the liquid and vapor boundaries move upward slightly due to the relatively low starting temperature. The ability of the method to capture this behavior supports the concept that it can be applied to capture moving interphase boundaries in nonequilibrium systems.

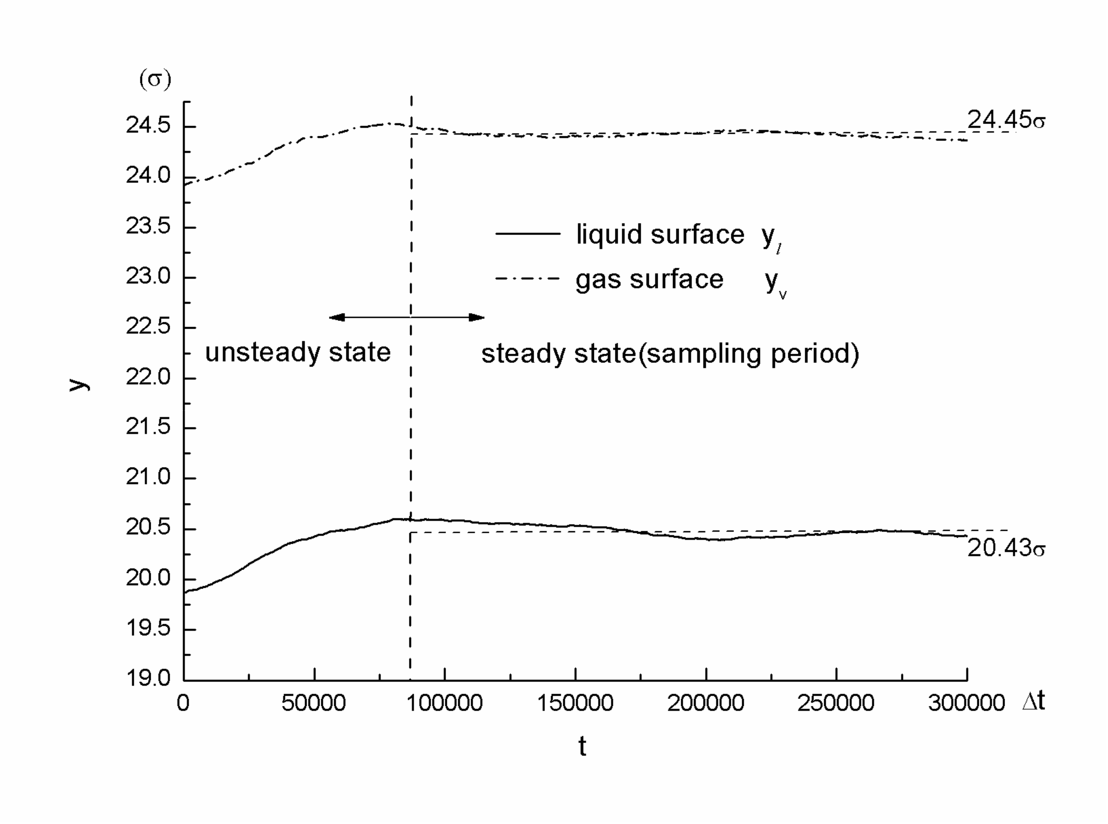

Fig. (3. 9) Liquid and vapor boundary locations vs. simulation time for MD simulation at temperature, $T = 90K$.

The results for y_v and y_l from equilibrium averaging and the curve-fitting results of Eq. (3.15) are listed and compared in Table 3.3. Due to the difference in definitions, the interface thickness, $d^* = |y_v - y_l|$, is larger than the interface thickness, *d*, defined by Eq.

(3.16) by approximately a factor of 2, although the interphase center, $y^*_m = 1/2|y_v + y_l|$, is almost identical to y_m. But clearly, as shown in Fig. (3.7), d^* is a more precise measure of interface thickness than d.

We also used the SRK equation [35] to compute the vapor surface, y_v^{SRK}, which is listed in Table 3. y_v is close to y_v^{SRK}, i.e., within one sampling bin resolution but as shown in Fig. (3.10), it approximates the vapor phase density somewhat more precisely.

We demonstrate the pure geometrical approach to the liquid boundary [35] in Fig. (3.10). The figure shows that y_l is a more accurate location of liquid surface, below which the density is almost invariant across the liquid bulk. Fig. (3.10) also shows the interphase thickness produced from a combination of the SRK method applied to determine the vapor boundary and the geometrical method applied to determine the liquid boundary, $d^{geo+SRK} = y_v^{SRK} - y_l^{geo}$, as shown in Fig. (3.10). This combination improved the interphase thickness predicted by Eq. (3.16), bringing it closer to the thickness determined by the present method. In fact, y_l^{geo} is almost identical to the result obtained from Rowlinson and Widom's hyperbolic tangent model (i.e., $y_m - d/2$).

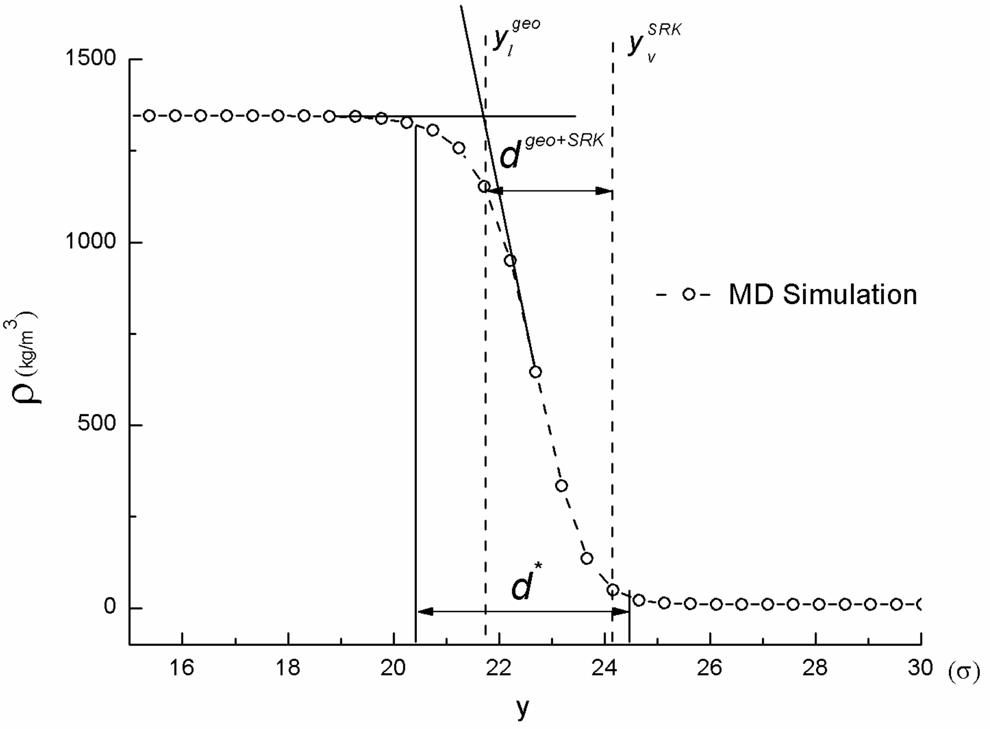

Fig. (3. 10) Comparison of SRK and geometric interphase boundary definitions with present definition on density profile at, $T = 90K$.

Fig. (3.11) plots the thicknesses from various methods as a function of temperature. The present results were compared with data published by Dunikov et al. [91], who used Eq. (3.16) to estimate thickness. The thicknesses can be numerically fitted by the scaling law [91],

$$d = d_0\left(\frac{T_c - T}{T_c}\right)^{-\eta} \tag{3.17}$$

where T_c is critical temperature. The parameters, d_0 and η were reported to be 1.2 and 0.65, respectively (dashed line in Fig. (3.11)) for Dunikov et al.'s data and interphase thickness definition [28]. In Fig. (3.11), the thickness, d estimated by Eq. (3.16) from the present data is similar to the Dunikov et al.'s results [91], but $d^{geo+SRK}$ shows a noticeable deviation from d at temperatures in a small range above 90K but then returns to follow d.

The thickness, d^*, estimated by the present method shows a similar trend to d but is shifted toward larger values. It can also be fit to Eq. (3.17) with $d_0 = 2.49 \pm 0.2\sigma$ and $\eta = 0.486 \pm 0.3$.

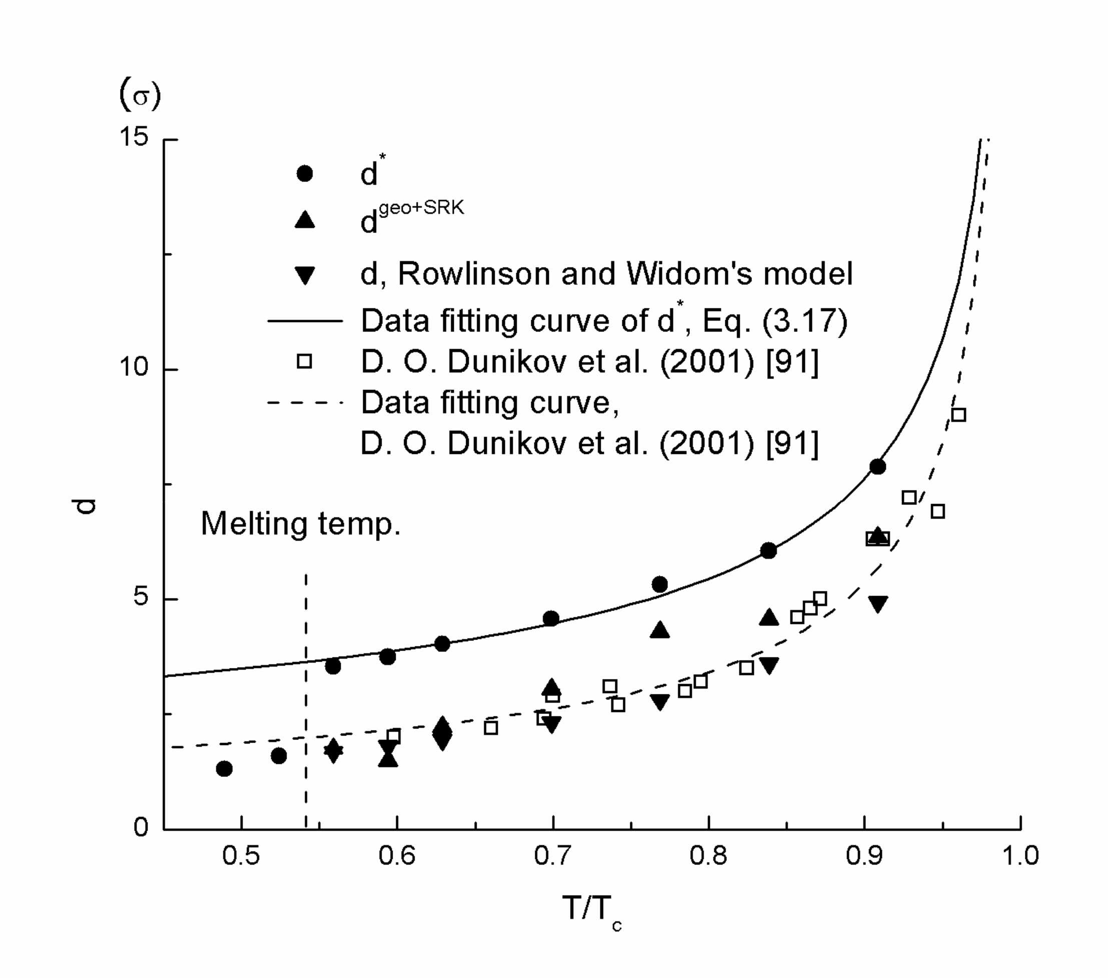

Fig. (3. 11) Comparison of results for liquid-vapor interphase thickness vs. temperature with results of previous investigations. (T_c is the critical temperature in Eq. (3.19).)

Capillary and thermal fluctuations have a broadening effect on the interphase. The present method smoothes the small-scale fluctuations by using the moving window average method and then tracks the "instantaneous" location of the interface at a resolution smaller than the larger-scale equilibrium wave undulations shown in Fig. (3.9). The steady-state averaged liquid and vapor surfaces, obtained by averaging the larger-scale undulations are, therefore, true mean locations. The averaged evaporation/condensation coefficients are computed from sampled fluxes based on the instantaneous locations after removal of the small-scale fluctuations; then they are averaged.

The interface thickness is computed from the steady-state averaged locations and, therefore, is an averaged or "intrinsic" thickness [89], which would be smaller than a thickness that is determined based on fluctuations. It was computed primarily for purposes of comparison with the results from geometric or profile fitting methods. A mean instantaneous thickness could also be defined from computing the differences in the instantaneous liquid and vapor boundary locations shown in Fig. (3.9) at sufficient small time intervals and then averaging them. Alternatively, a steady-state diffuse interface thickness that includes broadening effects due to the large-scale undulations could be obtained by taking the difference between the maxima in instantaneous vapor boundary location and the minima in instantaneous liquid boundary location.

Table 3. 3 Liquid-vapor boundaries and interface thicknesses

Temp.(K)	C_v	C_l	y_v / σ	y_l / σ	y_v^{SRK} / σ	d^* / σ	y^*_m / σ	d / σ	y_m / σ
70*	0.0046	28.19	20.38	19.07	20.26	1.31	19.73		
75*	0.015	19.41	20.73	19.13	20.26	1.59	19.93		
80	0.026	8.15	23.52	19.98	23.19	3.54	21.75	1.67	22.27
85	0.042	7.93	23.98	20.23	23.19	3.74	22.11	1.81	22.60
90	0.67	7.78	24.45	20.43	24.16	4.02	22.44	1.95	22.91
100	0.14	7.35	25.18	20.61	25.14	4.57	22.90	2.32	23.25
110	0.29	6.84	25.75	20.43	26.12	5.31	23.08	2.81	23.24
120	0.52	6.36	25.24	19.20	25.14	6.04	22.22	3.60	22.38
130	0.92	5.94	22.87	14.99	22.70	7.88	18.93	4.93	19.49

The radial distribution functions (RDF) for molecules belonging to the interphase were calculated at three different locations, y_v, y^*_m, and, y_l using standard methods [11]. Due to the system's inhomogeneity in the vicinity of the interface, a two-dimensional RDF was calculated in a plane parallel to the interface. The two dimensional RDF at the liquid boundary, $g_l(r)$, was sampled from the molecules belonging to the sampling bin in which the liquid boundary is located, and similarly, the two-dimensional RDFs at the vapor boundary, $g_v(r)$, and the interphase center, $g_m(r)$, were obtained from the molecules belonging to the bin where the vapor boundary and interphase center, respectively, are located. Since the bins were chosen to have a thickness of 0.4σ, well below a molecular diameter, the RDF sampling region is sufficiently thin to be treated as two-dimensional, and the argument r is taken to be the x-z separation between pairs of molecules.

Two-dimensional RDFs for two temperatures, 90K and 110K, are shown in Fig. (3.12) and Fig. (3.13). The computed $g_l(r)$ and $g_v(r)$ have shapes that follow the shapes of the RDFs of a pure liquid and a pure vapor, respectively, and exhibit the correct liquid and vapor bulk structure. $g_l(r)$ has three or more peaks and $g_v(r)$ has one peak, near the average diameter. However, $g_m(r)$ has two observable peaks. Therefore, the molecules in the center of the interphase are clearly in a state of transition between vapor and liquid.

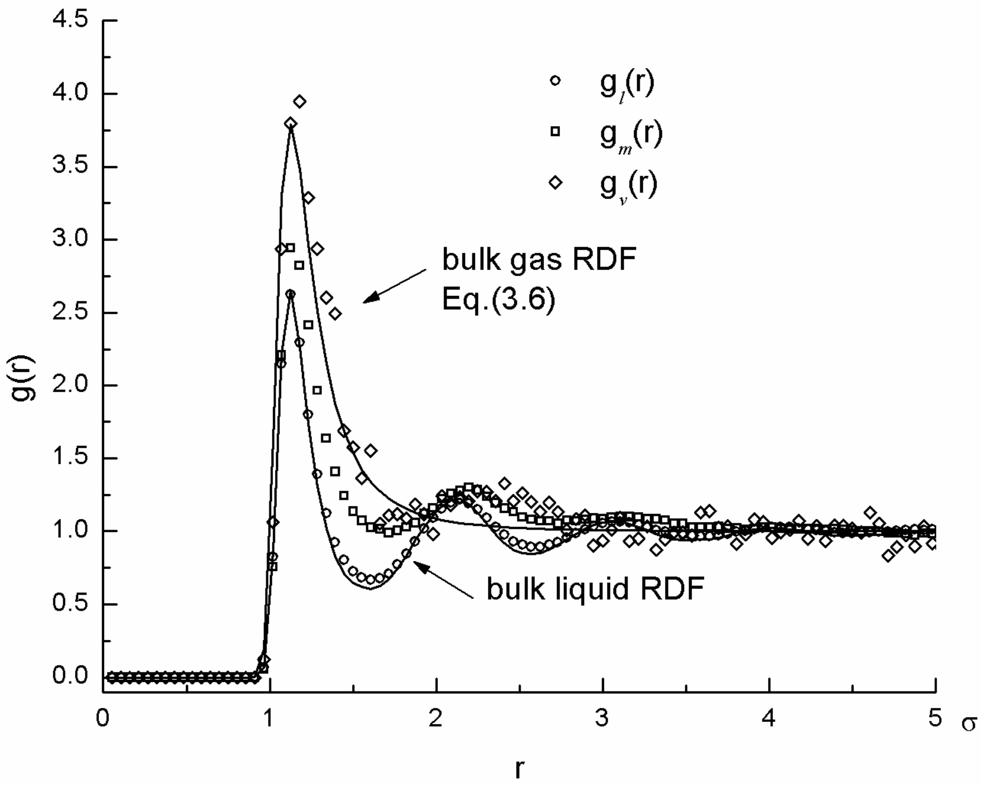

Fig. (3. 12) Two-dimensional interphase RDFs compared with pure liquid and ideal gas RDFs for temperature, $T = 90K$.

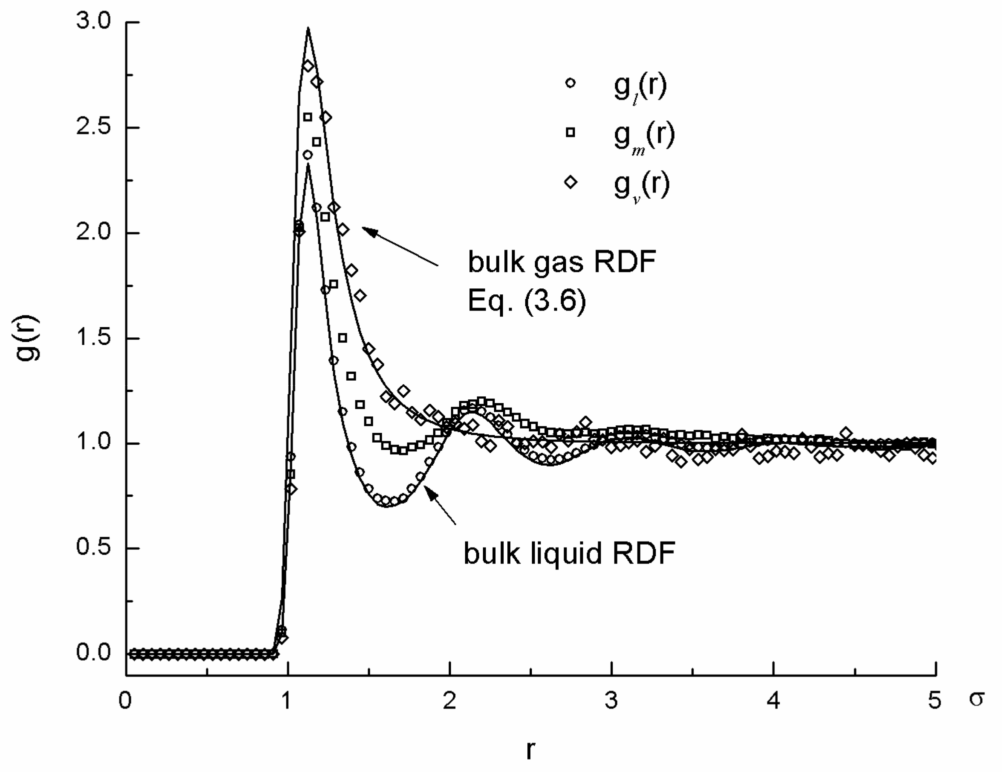

Fig. (3. 13) Two-dimensional interphase RDFs compared with pure liquid and ideal gas RDFs for temperature, $T = 110K$.

3.5.3 Equilibrium Properties

It has been shown that the potential and cut-off distance used in a simulation influences coexistence density. Figure (3.14) compares the present results for the liquid and vapor regions with the liquid-vapor bulk system MD simulation data presented by Trokhymchuk et al. [92] and by Wang et al. [75]. Trokhymchuk et al. used the spherical truncated (ST) and spherical truncated shifted (STS) L-J potential with a cut-off distance of 4.0σ, while Wang et al. [75] utilized the same L-J potential and cut-off distance as those in the present work.

Results from [92] and [75] are identical even though they were obtained using three different potentials. Fig. (3.14) also compares the present results with the experimental data of Gilgen et al. [83].

Fig. (3.14) shows that the present simulation results are close to those of the experiments and the MD simulations. The small differences that exist are more prominent in the liquid and therefore, can be attributed primarily to contact between the liquid and the artificial solid substrate. Other specific characteristics of the Lennard-Jones system that was modeled, such as system size, may also have played a role.

We also compared the solid phase density below the melting temperature with the vapor-solid coexistence density curve proposed by Wilsak [93]. The dash-dot line in Fig. (3.14) is the proposed curve from equation number 14 in Ref. [93].

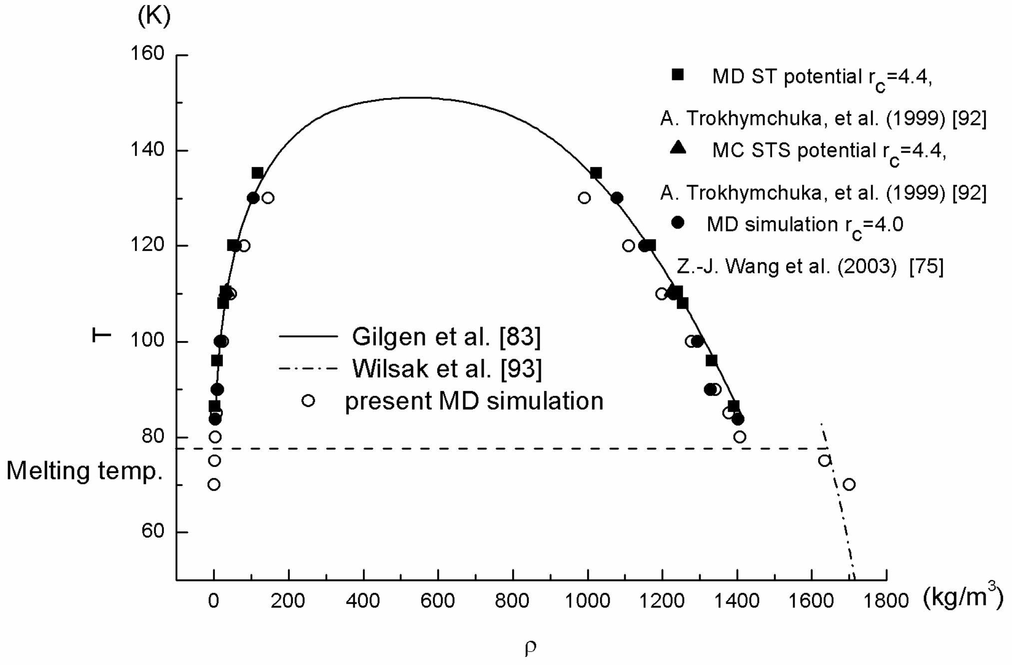

Fig. (3. 14) Density coexistence curve fit of results compared with results of present and previous investigations.

The density difference between liquid and vapor phases can be fit numerically to the order parameter scaling law [88],

$$\rho_l - \rho_v = \rho_0 \left(\frac{T_c - T}{T_c} \right)^{\beta} \tag{3.18}$$

in which $\beta = 0.32$ is an universal critical exponent for three-dimensional systems. The two unknown parameters, ρ_0 and critical temperature T_c, were found from fitting the T, and ρ molecular dynamics results (excluding simulation at temperature 70K and 75K) listed in Table 3,2 to be:

$$\rho_0 = (1.833 \pm 0.06) \times 10^3 \quad kg/m^3 \text{ and } T_c = 143.1 \pm 0.2 \text{ K} \tag{3.19}$$

The MD results and fitting curve are shown in Fig. (3. 15).

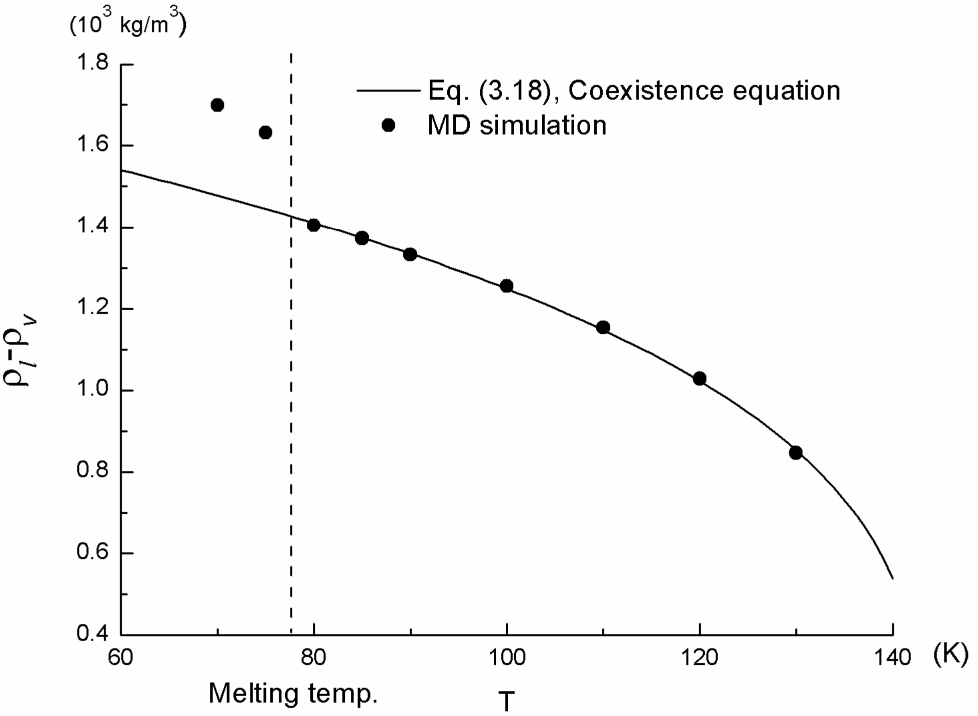

Fig. (3. 15) Liquid-vapor density difference vs. temperature curve fit of present results.

The latent heat per unit mass, ΔH, of the phase transition can be described as the difference of the enthalpy between two phases, i. e.

$$\Delta H = h_v - h_l \tag{3.20}$$

The vaporization enthalpy is plotted as a function of temperature in Fig. (3.16), where a comparison is made with a numerical fitting curve of experimental data for argon [94]. The present results show the same trend as the argon experiments. But there is a deviation of five to eight percent, likely due to the coexistence density discrepancy with experimental data (See Fig. (3.14).).

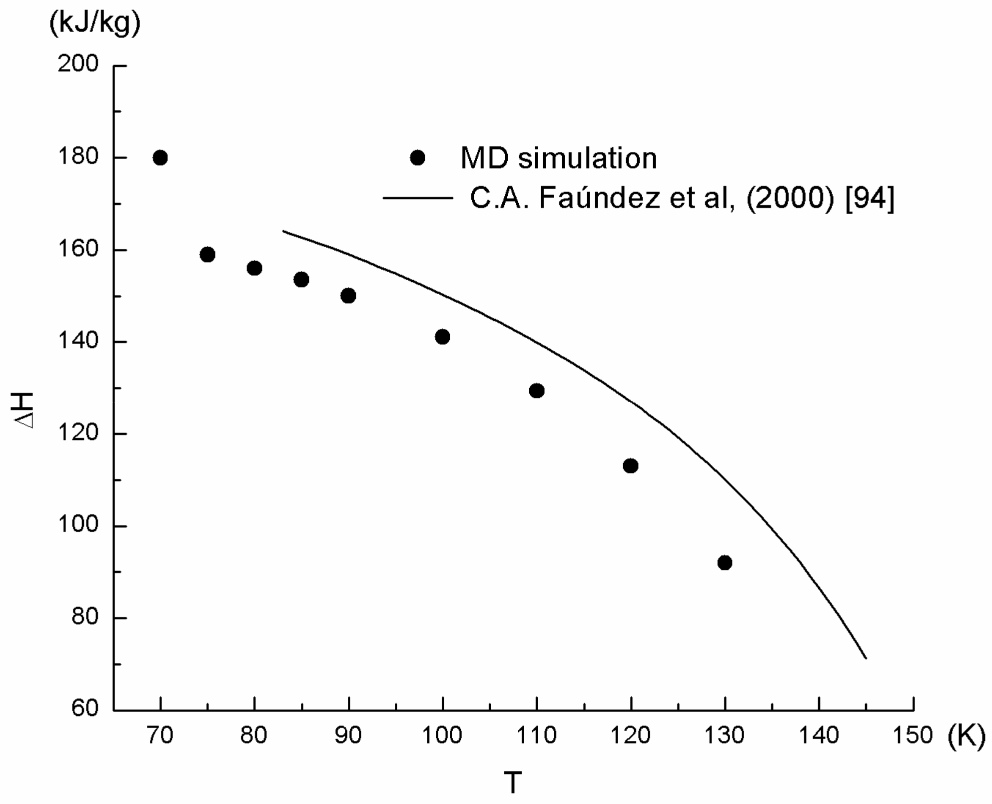

Fig. (3. 16) Comparison of vaporization enthalpy vs. temperature with previous investigation.

The results for the dimensionless parameter, $\Delta H/RT$, used to describe the phase transition strength are listed in Table 2.

The Clausius-Clapeyron equation for a one-component ideal gas,

$$\frac{dp}{dT}=\frac{\Delta H}{R}\frac{p}{T^2} \tag{3.21}$$

gives the saturation vapor pressure as a function of temperature, assuming that ΔH can be approximated as a constant. Thus, Eq. (3.21) leads to

$$p_v(T)=p_0\exp\left(-\frac{\Delta H}{RT}\right) \tag{3.22}$$

The unknown parameters p_0 and ΔH were obtained by a numerical fit to the saturated pressure (p_v) data from the MD simulations listed in Table 3.2. The fit is shown in Fig. (3.17) and resulted in

$$p_0=(10.6\pm0.78)\times10^8 \text{ Pa} \quad \text{and} \quad \Delta H=(1.631\pm0.018)\times10^2 \text{ kJ/kg} \tag{3.23}$$

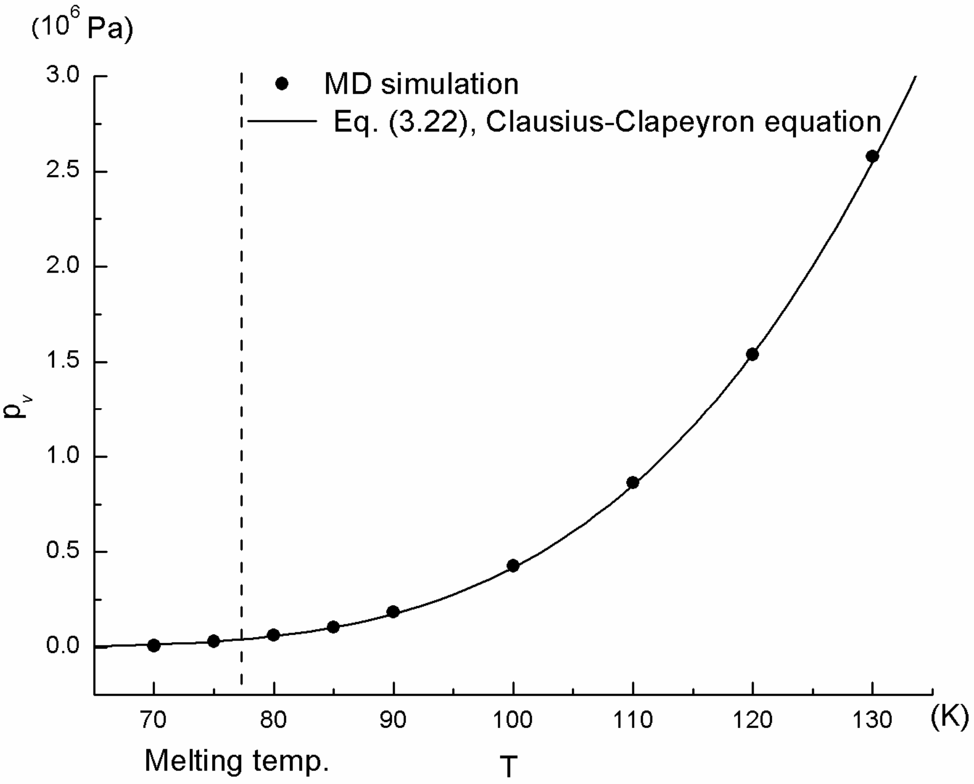

Fig. (3. 17) Saturation vapor pressure vs. temperature.

The surface tension, γ ,was calculated in the MD simulations by Eq. (3.12) (k=8, N_b =200). The surface tension as a function of the temperature was assumed to be represented by an empirical equation of the form [95]

$$\gamma = \gamma_0 \left(\frac{T_c - T}{T_c} \right)^{\nu} \tag{3.24}$$

in which $\nu = 1.26$ is the universal critical exponent. γ_0 was then determined by a numerical fit to the values listed in Table 3.2 (See Fig. (3.18).), which resulted in

$$\gamma_0 = (45.83 \pm 0.02) \times 10^{-3} \text{ N/m} \tag{3.25}$$

The present simulation results in Fig. (3.18) are close to those of the MD simulation of

Trokhymchuk and Alejendre [92], also shown in the figure.

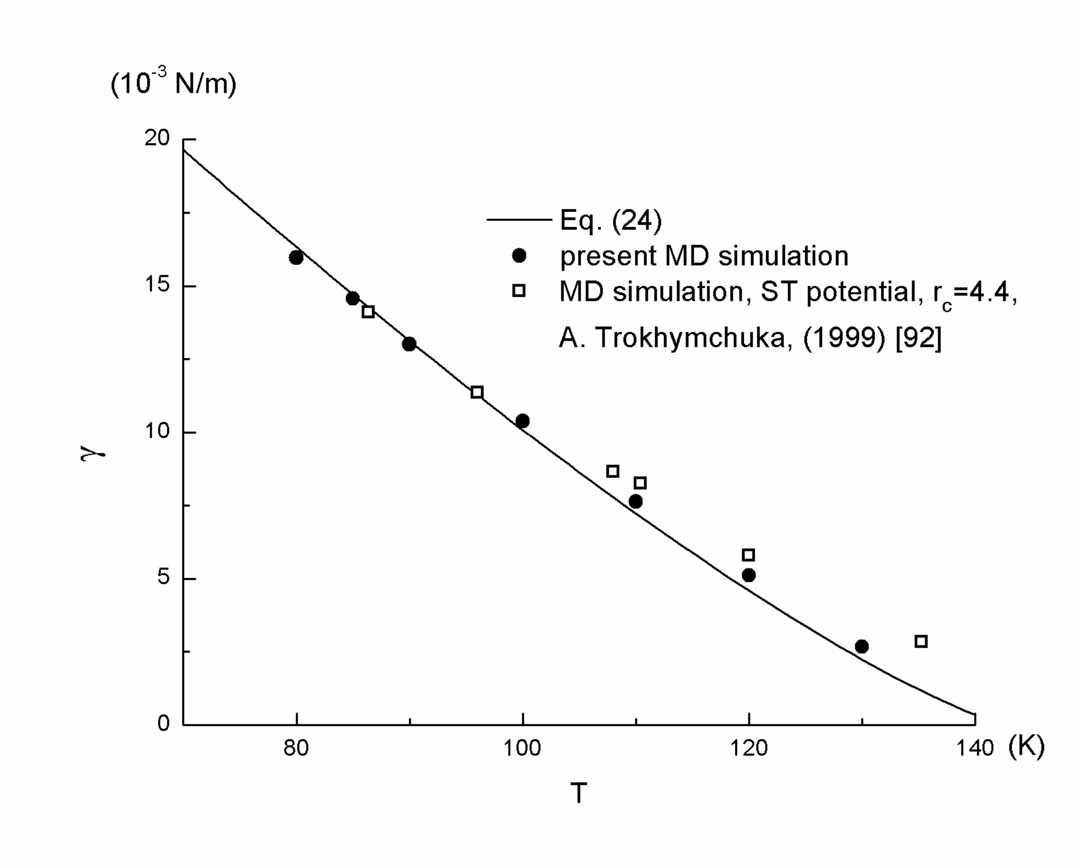

Fig. (3. 18) Surface tension vs. temperature compared with previous investigation and curve fit.

3.5.4 Evaporation/Condensation Coefficients

Applying the accurate definition of the vapor and liquid interphase surfaces from the present method, the evaporation and condensation coefficients can be obtained through tracking the appropriate molecules. The molecules are labeled according to their initial phase (vapor or liquid), and during the simulation the labels are subject to change, depending on the paths the molecules take. The vapor molecules originally above the vapor surface will become liquid molecules if they cross the liquid surface moving downwards, while liquid molecules originally below the liquid surface will become vapor molecules if they cross the vapor surface moving upwards. Thus, the various fluxes employed in Eq. (3.1) are determined and the evaporation and condensation coefficients can be calculated.

The results of the evaporation and condensation coefficient computations for the various MD simulations are listed in Table 3.2. The results demonstrate that the evaporation and condensation coefficient are equal in the equilibrium state, and also confirm the self-consistency of the flux collection statistics.

Nagayama and Tsuruta [77] proposed that the mean condensation coefficient is a function of the translational length ratio defined as $(V_l / V_v)^{1/3}$ (transition state theory), where V_l and V_v are respectively the liquid and vapor specific volumes. The relation for this can be written as

$$\overline{\sigma_c} = \left[1-(V_l / V_v)^{1/3}\right]\exp\left[-\frac{1}{2\left[(V_v / V_l)^{1/3}-1\right]}\right] \tag{3.26}$$

The present MD simulation results and simulation results from Tsuruta et al. [96] and Wang et al. [75] were compared with Eq. (3.26), as shown in Fig. (3.19). The present results are generally in better agreement with theory than Tsuruta et al.'s results, which were obtained by classification of reflected and incident molecules without an accurate definition of liquid and vapor interphase boundaries. The present results also show better agreement with theory than Wang et al.'s at volume cube root ratios above 0.2. As the melting temperature is approached in the present system, the results deviate significantly from the results of theory and of other investigators.

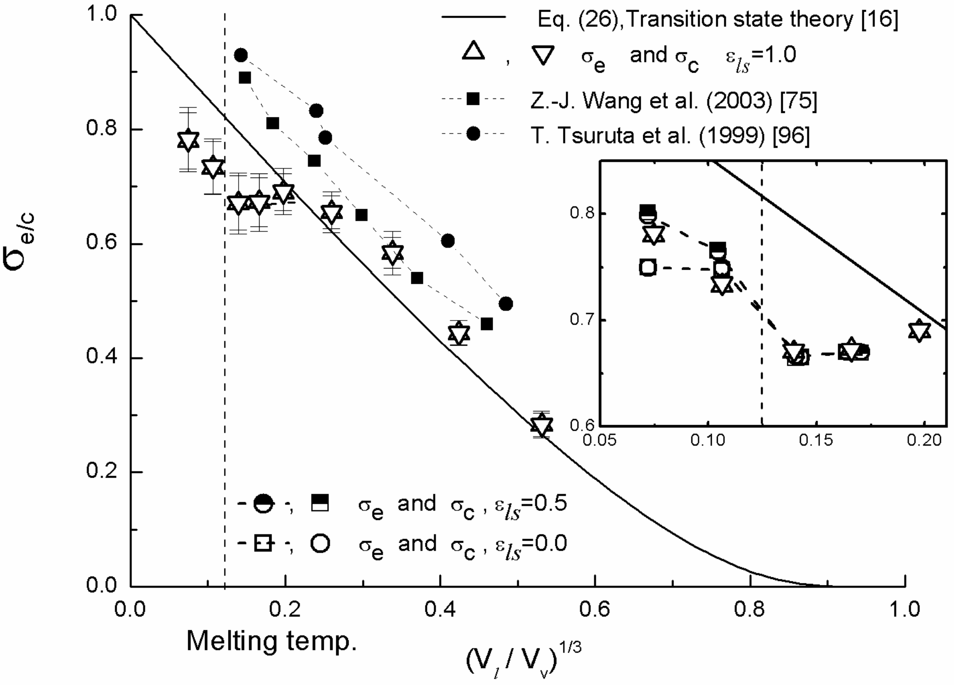

Fig. (3. 19) Comparison of evaporation/condensation coefficients from transition theory and MD results of present and previous investigations, plotted as a function of volume ratio. The MD results carry the error bars, which indicate the standard deviation.

Figure(3.19) shows that the evaporation/condensation coefficients generally increase as the liquid-to-vapor specific volume ratios decrease, which corresponds to a temperature decrease as is demonstrated later in this section. However, evaporation/condensation coefficients from the present simulations decline slightly for volume ratios that correspond to temperatures just above the melting point. The discrepancies between the present MD results and transition state theory near the melting temperature can be attributed primarily to the failure of transition state theory. The theory [77], which is simplified by using specific volumes instead of liquid and vapor free volumes, breaks down when the condensed phase approaches freezing and V_l eventually becomes based on solidified liquid.

The effects on the temperature at which simulated systems freeze discussed earlier may contribute to the differences in evaporation/condensation coefficients observed between the present simulations and the others in Fig (3.19) as the present simulations experience a liquid solidification effect, while the other systems remain liquid within the temperature range of the data.

The effect of wetting at the solid substrate was studied by modifying the liquid-solid interaction strengthen, ε_{ls}, from fully wetting (1.0) to partial wetting (0.5) to non wetting (0.0). As shown in the inset of Fig. (3.18), there was little effect of wetting on the evaporation/condensation coefficients at volume ratios above the melting temperature. But, in the frozen condensed phase region below the melting temperature, the non-wetting and partial-wetting results deviated significantly from the results obtained for a fully wetting substrate.

The simulation results also verified the well-established dependence of the equilibrium evaporation/condensation coefficient on temperature. By applying the ideal gas law $p_v(T) = \rho_v(T)RT$ to the vapor, Eq. (3.18) can be written as

$$\frac{\rho_l}{\rho_v} = \rho_0 \left(\frac{T_c - T}{T_c} \right)^{\beta} \frac{RT}{p_v(T)} + 1 \tag{3.27}$$

where $p_v(T)$ is given by Eq. (3.22).

Obviously, $\frac{\rho_v}{\rho_l}$ is equal to $\frac{V_l}{V_v}$. Hence, $\frac{V_l}{V_v}$ is also a function of the temperature. The mean condensation coefficient derived from transition state theory is presented as a unique function of the temperature by substituting $\frac{\rho_v}{\rho_l} = \frac{V_l}{V_v}$ into Eq. (3.27) resulting in

$$\overline{\sigma_c(T)} = \left\{1-\left[\frac{V_l(T)}{V_v(T)}\right]^{1/3}\right\}\exp\left\{-\frac{1}{2}\frac{1}{\left[\frac{V_v(T)}{V_l(T)}\right]^{1/3}-1}\right\} \tag{3.28}$$

Establishing the dependence of the theoretical condensation and evaporation rates on temperature allows a direct comparison of theory with the MD results of the present and previous investigations. Fig. (3.20) shows this comparison with theory as represented by Eq. (3.28) and other investigations. It again appears to demonstrate the superiority of the present method for determination of the interphase boundaries.

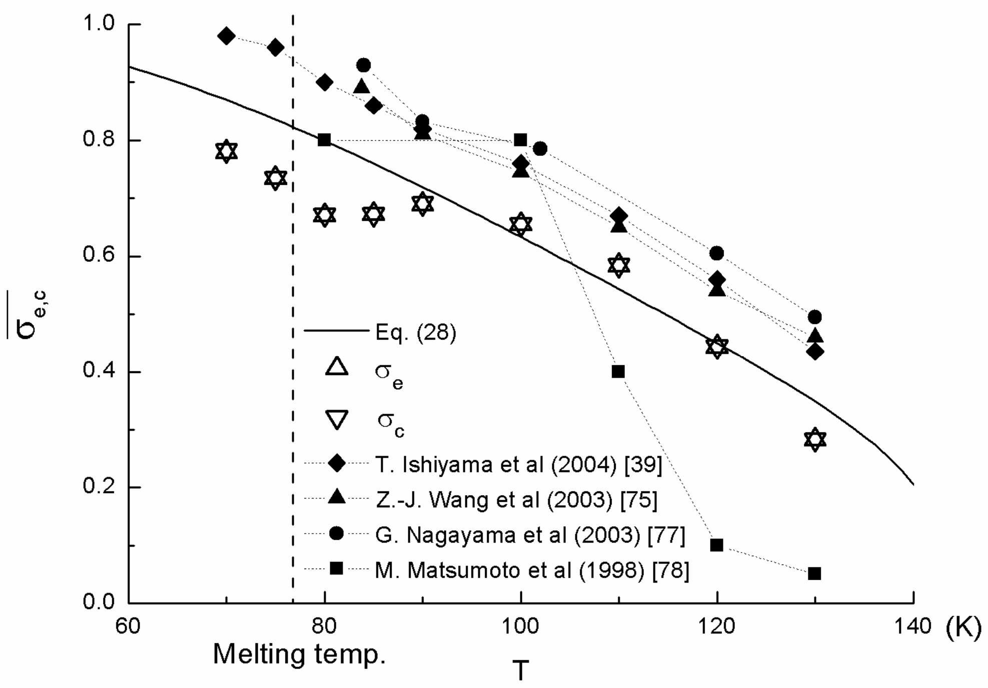

Fig. (3. 20) Evaporation/condensation coefficient vs. temperature, comparing transition theory, and MD results from present and previous investigations.

Chapter 4

Multiscale Molecular Simulations of Argon Vapor Condensation onto a Cooled Substrate with Bulk Flow

4.1 Chapter Summary

A hybrid simulation method is employed to study the condensation of saturated argon vapor flowing tangentially across a stationary cooled substrate, at nanoscale resolution. The method combines a direct simulation Monte Carlo (DSMC) treatment of the bulk vapor phase with a nonequilibrium molecular dynamics treatment of the condensed liquid and interphase regions; it provides an efficient simulation procedure for a heterogeneous system with a large ratio of vapor to liquid length scales. Starting from a bare, crystalline solid wall, the condensation process evolves from a transient unsteady state to a quasi-steady state, where interfacial properties and heat and mass transfer parameters are analyzed. The Knudsen layer structure from the hybrid simulation is compared with kinetic theory predictions from a modified moment method analysis and from pure DSMC simulation. The effects of condensation strength and a tangential flow velocity that is on the order of the condensation velocity are examined. A comparison is made between the nonequilibrium results and equilibrium results for the interphase transition between liquid and vapor. The results reveal the structure of the interphase for such phenomena as inverted temperature, drift flux, and

heat transfer. Heat transfer phenomena at the substrate surface are also described.

4.2 Introduction

Molecular simulation of interfacial heat and mass transport in a multiscale condensing flow system is the focus of the present research. The system of interest has length scales spanning the disparate scales of molecular diameters and molecular collisions. (For argon at standard conditions, the effective hard sphere molecular diameter is 0.4 nm, while the mean free path is 63 nm.) It involves deposition of a nanoscale liquid film onto a solid substrate from a microscale bulk saturated vapor flow over it. Interfacial transport phenomena have not been examined at this resolution in the presence of bulk flow but are of immense scientific interest and practical relevance for heat and mass transfer involving phase change in microscale heat exchangers, chemical or physical vapor deposition in micro fabrication and thin-film coating processes, dew and frost formation with wind, and post-nucleation cloud and fog microphysics.

In the present system, nanoscale effects dominate in a small but significant portion of a microscale physical region, as opposed to only at the boundaries. Investigation of solid-liquid-vapor heat and mass transport phenomena in such multiscale systems has been hampered by lack of an appropriate simulation tool. Development of such a tool was called for a decade ago in the molecular dynamics heat transfer review paper by Maruyama [1], but no satisfactory tool emerged until the present development of an atomistic hybrid multiscale method for flow over a gas/solid interface described in Chapter 2. The method has shown the ability to handle such a compound system.

Vapor flow above its dense phase forms a kinetic boundary layer, known as the Knudsen layer, within a few mean free paths of the liquid surface. Kinetic theory modeling, based on the Boltzmann equation, can be applied to analyze the flow within the Knudsen layer. Knudsen layer kinetic analyses for vapor over its dense phase in condensing or evaporating flow systems was reviewed by Ytrehus [5]. The work of Aoki et al.[97] on the effect, within the Knudsen layer, of velocity along the liquid phase is particularly relevant to the present investigation. Their results were obtained by numerical solution of the BGK approximation to the Boltzmann equation for the Knudsen layer. However, kinetic theory cannot resolve the detailed nanoscale thermophysics of the interphase region that exists between the pure liquid and the pure vapor phase of the Knudsen layer. This region is at least a few molecular diameters in thickness. Furthermore, kinetic theory approaches rely on modeled interfacial boundary condition approximations using the concepts of evaporation and condensation coefficients, and cannot readily model complex flow geometries or complex transient dynamics. They also must rely on other physics to deal with solid and liquid phases present in the interfacial region.

Analytical solutions to the Boltzmann equation cannot readily model complex flow geometries or complex transient dynamics. Some computational approaches can overcome these restrictions. In particular, direct simulation Monte Carlo or DSMC [6] is a relatively efficient and adaptable method for molecular simulation of dilute gas flows in Knudsen layers.

In DSMC simulation, as in kinetic theory solutions, modeled interface boundary conditions are required. They are necessarily restricted to simplified mechanical models based on average surface collision dynamics or to statistically averaged particle flux distributions based on simplified molecular interactions at an interface. This latter fact is actually an advantage in devising simple gas/gas outer boundary treatments in Knudsen layer simulations. However, nanoscale multiphase interfacial physics cannot be resolved. Moreover, DSMC simulation is limited to dilute gases and, like other kinetic theory methods, cannot resolve the interphase region.

When the classical molecular dynamics (MD) method is applied to fluids that are not in equilibrium because they are subjected to imposed mechanical or thermal driving, as discussing in pervious chapters, it is often referred to as nonequilibrium molecular dynamics (NEMD). NEMD [11] is appealing for interfacial physics because it can treat both dilute and concentrated molecular systems. It can be applied to simulate the entire solid/liquid/vapor interfacial system, i.e., the Knudsen layer, the liquid-vapor interphase, the liquid condensate, and the solid substrate.

NEMD simulations of vapor condensation onto a solid substrate without bulk flow were conducted for a closed system by Yi et al. [29] and for an open system by He et al. [81]. The system investigated by He et al. was similar to the system of the present investigation but the vapor was not saturated and the upper boundary treatment was questionable. The substantial disadvantage of such NEMD simulations is that they are so highly computationally intensive that their use is restricted to nano-dimensioned systems and correspondingly short simulation lifetimes. For example, the simulations of He et al. were terminated before any evolution to quasi-steady condensation could be verified and the additional simulation needed to extract mean values from thermal fluctuations was not done. In pure dilute gas simulations, larger sizes are possible, but practical multiphase microscale systems of engineering interest are not directly accessible to NEMD.

A multiscale hybrid method with the ability to efficiently simulate the molecular gas dynamics of the Knudsen layer while simultaneously resolving the coupled nanoscale molecular interactions in the solid, liquid, and interphase inner regions of the interface could be invaluable. Hybrid simulation schemes are abundant for microscale or nanoscale/continuum flows using DSMC or NEMD coupled with continuum CFD methods (i.e.[51-61,98]). Among them, Donev et al. [98] recently introduced a promising Landau–Lifshitz Navier-Stokes (LLNS)/DSMC hybrid method with the capability of dealing with a gas-liquid interface in an unsteady flow. Their algorithm incorporates some liquid-phase molecular effects via the continuum LLNS numerical solution and gas-phase molecular effects via DSMC. However, using their method to deal with a moving liquid-vapor phase transition or solid-liquid molecular interaction is beyond the method’s current state of development.

The ability of DSMC to handle a Knudsen layer and NEMD to handle a nanoscale multiphase region suggests that a DSMC-NEMD hybrid, combing the two, would be an effective multiscale method for vapor interaction with an interface. The atomistic method, which was described in Chapter 2 and applied to a gas-solid interface is such a hybrid. It was applied here, with a slight modification, to the multiscale solid-liquid-vapor system.

In the present simulations, bulk, saturated argon vapor flows above a cooled substrate in a direction tangential (parallel) to its surface, creating a Couette-type, condensing flow within a region above the surface with a thickness on the order of several gas mean free paths. The cooled substrate causes the condensed vapor to deposit continuously on it, building up a thin liquid film, as depicted in Fig. (4.1). The baseline simulation cases are nonequilibrium condensation with the tangential flow velocity equal to zero. The imposed tangential velocities in the other cases were on the order of the condensation velocity normal to the surface. The system was allowed to develop from an initial unsteady transient state to a quasi-steady state over the simulation period.

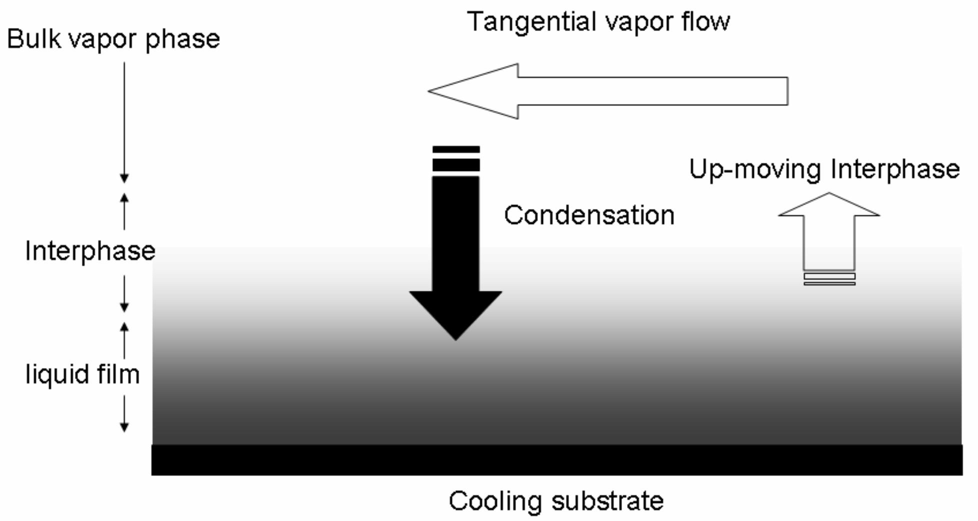

Fig. (4. 1) Illustration of condensation on a cooled substrate with tangential vapor flow.

4.3 KINETIC ANALYTICAL SOLUTION OF THE KNUDSEN LAYE

It is useful to revisit the application of kinetic-theory analytical modeling to the vapor region with a view toward comparing the results of kinetic modeling and simulation to the results of hybrid simulation. At the outset it is understood that neither kinetic analytical modeling nor kinetic simulation can capture the physics of molecular interactions at the liquid-vapor interface, which is intrinsic to the hybrid simulation. Given this limitation of kinetic theory, the Boltzmann equation for the vapor region can be solved by traditional numerical methods as in the BGK solutions of Ref. 98 or by DSMC simulation. Analytical approaches, using simplified modeling, are less able to accurately resolve the fluid properties within the vapor layer. However, one such approach, the moment method, was used here to develop a convenient and consistent set of boundary conditions for pure (non-hybrid) DSMC simulations of the Knudsen layer. The pure DSMC simulation results can be compared with the results of the hybrid simulations.

A kinetic theory analytical approach to describe vapor flow evaporating from or condensing to a liquid surface, but without a tangential flow component was systematically introduced by Ytrehus [5]. The vapor flow next to the liquid surface is in a steady, nonequilibrium state within a Knudsen layer, which is one to several mean free paths thick. The mass, momentum, and energy fluxes within the Knudsen layer were obtained from an approximate solution to the Boltzmann equation by a moment method.

Ytrehus made a number of simplifying assumptions in his analysis such as an assumption that the condensation and evaporation coefficients are both unity. A scaling method for extending the analysis to non-unity coefficients is presented in a subsequent section. In his moment method, Ytrehus assumed a four-term kinetic distribution function such that the boundary conditions were exactly represented in a certain form. This distribution function cannot fully model the addition of a tangential vapor flow to the Knudsen layer so the method is restricted in its ability to accurately capture all the details of such a flow. Nevertheless, if used as a modeling basis for flows in which the tangential velocities are of the same order or less than the condensation velocities, it can provide a reasonable level of approximation for flow variables other than tangential velocities.

The details of applying the Ytrehus moment method to obtain Knudsen layer solutions with tangential velocity are given in Appendix D. The development follows directly from Ytrehus' work [5]. The reason for presenting the complete solution here is to correct some apparently typographical errors that were discovered in [5], as well as to add tangential vapor flow.

4.4 HYBRID DSMC-NEMD SIMULATION PROCEDURES

4.4.1 Description of Hybrid DSMC-NEMD Simulation

The hybrid method applied to the present simulation incorporates an improvement in the DSMC-NEMD coupling algorithm over that described in Chapter 2. The NEMD portion of the hybrid method employs the Lennard-Jones (L-J) 12-6 potential; this potential can be expressed as

$$\Phi_{LJ}(r_{ij}) = 4\varepsilon\left[(\frac{\sigma}{r_{ij}})^{12} - \varepsilon_s (\frac{\sigma}{r_{ij}})^{6} \right] \qquad (4.1)$$

where r_{ij} is the distance between molecule i and molecule j; and ε and σ are the characteristic energy and interaction lengths, respectively. The parameter, ε_s, is not present for interactions between gas or liquid molecules but is introduced for fluid-solid surface molecular interactions and describes the wetting effect at the fluid-solid interface. In the present simulations, it was assigned a value of 1.0, corresponding to complete wetting. The shift-force potential modification [11] to the L-J potential was implemented with a cut-off distance, r_c, to eliminate weak effects from long-distance pair evaluation.

The DSMC molecular collision model employed in the hybrid and the pure DSMC simulations is the modified generalized soft sphere (MGSS) model that was developed in Chapter 2 (See also [2]). Its Lennard-Jones potential-based collision cross-section ensures its compatibility with NEMD molecular interactions and is dependent on particle collision speed for improved computational efficiency and low-temperature performance.

The algorithm used for coupling between DSMC and NEMD in the hybrid is an optimization of the trade-off between computational efficiency and accuracy. It is completely particle based. There is no conventional buffer zone between the DSMC and NEMD simulator domains. Particles are freely exchanged between the domains in a transmutation process and molecular interactions between the two types of particles are modeled in a consistent fashion.

The basic hybrid coupling steps are simple in concept. First, a one-to-one correspondence of DSMC particles to molecules is established, as opposed to the usual DSMC implementation where actual molecules are represented by a far fewer number of stochastic simulation particles. After an initial stabilization period of simulation, DSMC and NEMD molecules are allowed to exchange across the interdomain boundary. For computational efficiency, the DSMC time steps are larger than the NEMD time steps (20 times larger in the present simulations). The coupling procedure synchronizes the DSMC simulator with the NEMD simulator at the beginning of each DSMC time step. The DSMC and NEMD simulator computations then proceed in parallel as represented in Fig. (4.2). Details of the coupling procedure and the DSMC-NEMD molecule transmutation process are given in Chapter 2.

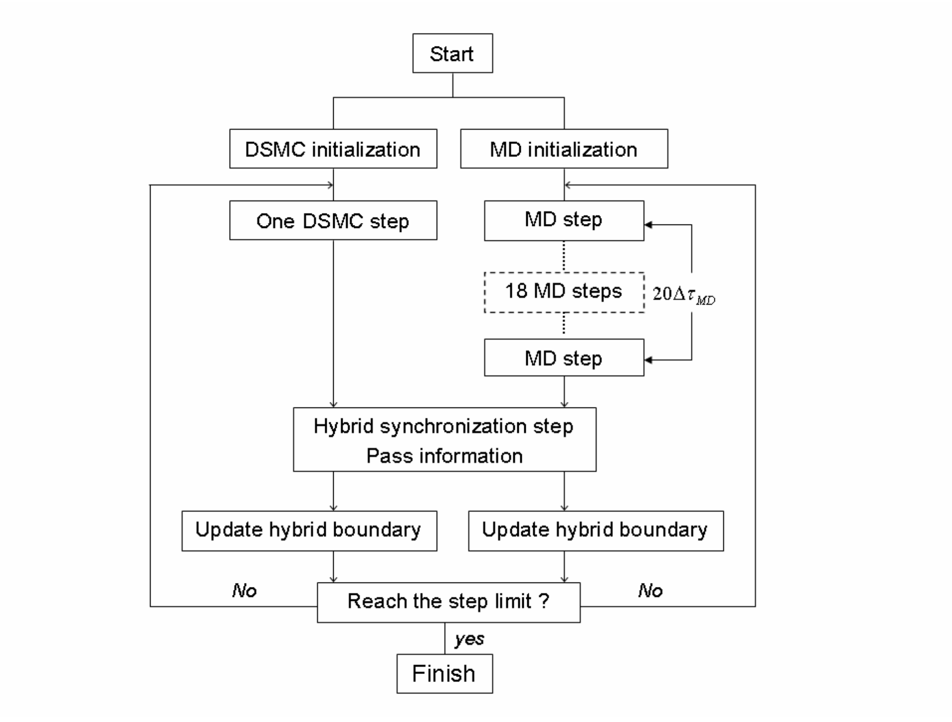

Fig. (4. 2) Hybrid DSMC-NEMD flow diagram.

When DSMC molecules enter the NEMD domain to become NEMD molecules, they encounter an insertion procedure that avoids an overlap in positions with the NEMD molecules already inside. The insertion routine has been improved from the original version presented in Chapter 2. Although the new algorithm requires more processor time than the original version, it reduces the stochastic effects carried from the DSMC simulator to the

NEMD simulator.

Any necessary adjustment in the location of newly inserted NEMD molecules is determined by the locations of nearby pre-existing NEMD molecules. The distance, r_{ij}, between the neighboring molecule, j, and newly inserted NEMD molecule, i, is chosen based on an intermolecular distance determined from the radial distribution function (RDF). For an equilibrium system, the probability of one particle (*i*) finding another particle (*j*) at the distance r_{ij} is proportional to $ng(r_{ij})dr_{ij}$, in which n is the local mean number density and $g(r_{ij})$ is the radial distribution function (RDF) at a distance, r_{ij}. Assuming local equilibrium at the boundary between the DSMC and NEMD simulator domains, the location of new NEMD particles can be determined by the RDF. If the distances to the neighboring molecules r_{ij} are greater than r_c, the new NEMD particle is successfully inserted without adjustment. In a case where r_{ij} is smaller than r_c, the acceptance-rejection method (See Ref. 4.) is triggered to judge the state of the new NEMD molecules and adjust its location by randomly shifting it in the x-z plane. The new NEMD particle is accepted at this particular location r_{ij} if

$$R_f < \frac{g(r_{ij})}{g(r_{\max})} \tag{4.2}$$

where R_f is the uniformly distributed random number between 0 and 1 corresponding to the random shift in location and $r_{\max}$ is chosen to maximize $g(r)$. For a dilute gas, the RDF can be shown to be a function of a two-body potential as

$$g(r_{ij}) = \exp(\frac{-\Phi(r_{ij})}{k_B T}) \tag{4.3}$$

in which k_B is the Boltzmann constant and T is the temperature of the system. For the L-J potential used in the present simulations, the maximum value of $g(r_{ij})$ can be obtained at the distance, $r_{\max} = 2^{1/6}\sigma$, and T is selected to be the local temperature at the interdomain boundary on the NEMD side.

4.4.2 Molecular System Model

The molecular system was set up in an elongated box as depicted in Fig. (4.3). The dimension normal to the interface (*y* direction) and the dimensions transverse to it (*x, z* directions) were chosen to be 700σ (b_2 in the figure) and 25σ, respectively. At the bottom of box, the solid substrate was a FCC crystal structure formed from two layers of harmonic molecules through tethering large mass molecules to a fixed site with spring connections [18]. Above the substrate, 942 argon molecules were employed to initialize the vapor phase. The lower part of the box, with a normal dimension of 126σ (b_1 in the figure), included the substrate (1156 solid molecules) and initially a small part of the vapor (160 argon molecules). The lower box and the substrate were the NEMD simulator domain and the upper box was the DSMC simulator domain. The partition size division was designed to ensure that the upward-moving interphase would not cross the interdomain boundary into the DSMC domain during the simulation lifetime. The NEMD domain was divided into 100 sampling bins and the DSMC domain was divided into 40 collision cells.

The cut-off distance, r_c, was set to be 4.0σ in the NEMD simulator and the Gear predictor-corrector algorithm was applied to solve the molecular equations of motion with a time step ($\Delta\tau_{MD}$) of $0.005\sqrt{m\sigma^2/\varepsilon}$ where *m* is the argon molecular mass. Utilizing data from equilibrium simulations, the initial state of the argon vapor was set in a saturated condition at a temperature of 80K, just above the triple point, and a density of $0.0024\,m/\sigma^3$. The substrate temperature, T_S, was controlled by velocity rescaling and initially set at the saturated vapor temperature. The parameters for the argon and solid molecules used in the simulations are listed in Table 4.1. The solid molecular mass, m_s was chosen so that the ratio, k/m_s, (where k is the spring constant) associated with the stiff springs of the solid molecules produced about the same oscillation frequency as the argon L-J potential in the fluid. Therefore, the traditional NEMD time step based on the L-J potential of argon is sufficiently small to also capture the solid oscillations.

Table 4. 1 Parameters for argon molecules.

Parameter	Physical value
length	$\sigma = 3.4\times10^{-10}\ m$
energy	$\varepsilon = 1.66\times10^{-21}\ J$
molecular mass	$m = 6.64\times10^{-26}\ kg$
solid molecular mass	$m_s = 6.64\times10^{-24}\ kg$

The DSMC vapor molecule particle properties were consistent with those of the NEMD molecules. Constrained by the NEMD time step, the DSMC time step ($\Delta\tau_{DSMC}$) is significantly smaller than the mean collision time. The DSMC collision cells were uniformly distributed along the *y* direction with cell dimensions smaller than the usual restriction of one-third of the mean free path both in the y and neutral directions. Each cell initially contained around 20 particles on average.

The top inflow boundary was implemented as a DSMC molecular reservoir with a specified pressure (p_∞) and temperature (T_∞), which were set to be identical to the initial vapor condition. During the simulations, the inflow mean velocity normal to the boundary, V_∞, was computed by having the inner cell mean y velocity extrapolated to the boundary. This implicit inflow boundary has been proven to be an acceptable DSMC treatment for a low-speed gas flow boundary [46]. Hence, the continuous condensate deposition process was made possible by the molecular flow induced across the open DSMC boundary with the reservoir. The mean tangential flow velocity, U_∞, at the inflow boundary was fixed and assumed to be uncoupled to V_∞. The vapor inflow molecular thermal velocities were generated by sampling from the thermal equilibrium velocity distribution for the reservoir. Periodic boundary conditions were applied in the *x* and *z* directions.

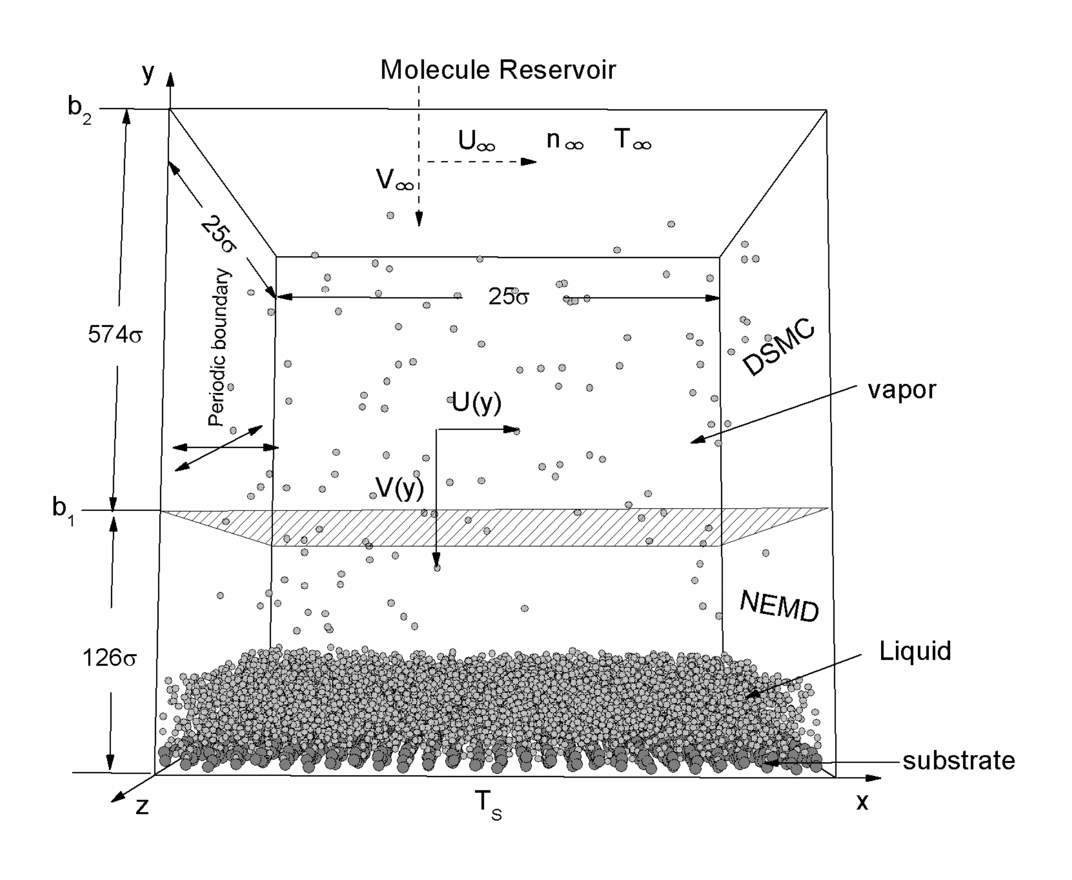

Fig. (4. 3) Molecular system and hybrid solution domains. (MD domain height is greatly exaggerated.)

After simulations began, the vapor molecules in the NEMD domain were allowed to reach their equilibrium state at the saturation temperature. Then the hybrid DSMC-NEMD procedure was started and the substrate temperature was smoothly decreased from the saturation temperature to the desired cooled value over the first 5×10^4 time steps and kept constant during the rest of the simulation life. The driving force of a temperature gradient between the substrate and the vapor phase led nonequilibrium condensation to begin and a thin liquid film, with its thickness increasing with time, built up on the cooled substrate.

As listed in Table 4.2, nine simulation cases were investigated with three different cooled substrate temperatures and three different tangential flow velocities. For all cases, the simulation lifetime was $2\times10^{4}\sqrt{m\sigma^{2}/\varepsilon}$ or 43.21ns, which ensured that the condensation process reached a quasi-steady state. The results of each case were obtained from ensemble averaging over ten independent runs with different initial random seeds to reduce the effects of statistical and thermal fluctuations.

Table 4. 2 Simulation cases.

Simulation case	Substrate temperature $T_s(K)$	Tangential Velocity $U_\infty(m/s)$
1	75	0
2	75	10
3	75	20
4	70	0
5	70	10
6	70	20
7	65	0
8	65	10
9	65	20

In molecular simulation, macroscopic physical quantities are obtained from dividing the physical domain into sampling bins (NEMD) or sampling/collision cells (DSMC) and averaging over the individual molecules in them. The bin heat flux, enthalpy, pressure tensor, and energy flux can be computed, respectively, from

$$q_{\alpha,J}=\frac{1}{V_J}\Big[\sum_{i=1}^{N_J}c'_{i,\alpha}\Big(\frac{1}{2}mc'^{2}_{i}+\Phi_i\Big)+\frac{1}{2}\sum_{i,j}^{N_J}(\mathbf{F}_{ij}\bullet\mathbf{c}'_i)\;r_{ij,\alpha}\Big] \tag{4.4}$$

$$h_J = \frac{5}{6}\frac{1}{N_J}\sum_{i}^{N_J} c'^2_i + \frac{1}{mN_J}[\sum_{i}^{N_J}\Phi_i + \frac{1}{3}\sum_{i<j}^{N_J}(\mathbf{F}_{ij}\bullet\mathbf{r}_{ij})] \tag{4.5}$$

$$\Pi_{\alpha\beta,J} = \frac{1}{V_J}(m\sum_{i=1}^{N_J} c'_{i,\alpha}c'_{i,\beta} + \sum_{i<j} F_{ij,\alpha}r_{ij,\beta}) \tag{4.6}$$

$$\dot{E}_{\alpha,J} = c_{\alpha,J}\frac{1}{V_J}\sum_{i=1}^{N_J}(\frac{1}{2}mc_i^2 + \Phi_i) + q_{\alpha,J} + \Pi_{\alpha\beta,J}c_{\beta,J} \tag{4.7}$$

in which N_J is the number of molecules in the bin J with volume, V_J; subscripts α and β indicate the x, y, or z direction; $c_\alpha' = c_\alpha - \overline{c_\alpha}$ is the thermal velocity in the α direction; $F_{ij,\alpha}$ is the interaction force between molecule i and molecule j in the α direction; $r_{ij,\beta}$ is the interaction vector in the β direction; and Φ_i is the potential energy of particle i. The interaction force and potential energy terms in Eq. (4.4) through Eq. (4.7) are not applicable to the DSMC sampling routine. $\dot{E}_{\alpha,J}$ represents the first-law conservation flux in the α direction at an arbitrary system control volume surface located at bin J. It includes all the relevant energy transport mode terms plus the pressure tensor work terms.

4.4.3 Moving Interphase Boundaries

To study the interfacial molecular mass and heat transfer, an accurate definition of the interface is mandatory. It is relatively simple to define the interface between solid and fluid phases. In the present system, there is no mass transfer between the solid and fluid phase (Initially the fluid is a vapor.) and the interface is stationary. This interface is also distinguishable because a different type of molecule is used for the solid. The solid-fluid interface physical properties on the fluid side were obtained at the first sampling bin (with a y dimension of 0.7σ) next to the solid substrate.

Handling the liquid-vapor interface in the nonequilibrium system is less straightforward.

First, significant mass transfer takes place between the liquid and vapor phases and the finite-thickness, interphase region over which the transition from liquid to vapor occurs cannot be ignored. The second complication of the liquid-vapor interface is that the liquid film keeps growing from the cooling substrate, displacing the interphase along with it. Some classic strategies for maintaining a fixed interphase position during NEMD simulation of nonequilibrium condensation (e.g., the liquid molecule removal method in Ref. [35]) are not suitable for the present system.

To overcome these difficulties, another method of defining the liquid-vapor interphase was employed, as described in Chapter 3. This method has the advantage of capturing the moving interphase region without significantly increasing the computational expense. It is based on counting the number of neighboring interacting molecules, $N^{'}(\tau)$, in a specially constructed volume, $V^{'}$, about each molecule in the simulation. The volume, $V^{'}$, is a thin region sliced from the center of a sphere about the molecule with radius, r_c, by planes parallel to the interface, as depicted in Fig (4.4). For the present simulations, the y- thickness of the region was chosen as 0.2σ to provide reasonable spatial resolution while containing a sufficient number of molecules to be representative. The $N^{'}(\tau)$ are averaged over a small time interval and then these averages are sampled over sampling bin, J, to generate $\overline{N_J^{'}(\tau)}$, the bin-averaged number of interacting particles per molecule in the special volume, $V^{'}$.

The method defines interphase boundaries on the vapor side and on the liquid side of the interphase by traversing the liquid-vapor interface to identify the bin location at which the $\overline{N_J^{'}(\tau)}$ transitions to a specific value that characterizes either the vapor (C_g) or the liquid (C_l) phase. In the present simulations, $C_g = 0.02$ and $C_l = 8.1$ were the boundary criteria values for the gas and liquid boundaries, respectively. They were obtained from liquid-vapor coexistence, equilibrium MD simulations at a temperature equal to the present T_∞ (80K). Once an interphase boundary bin is identified, a similar procedure is employed to pinpoint the boundary location within the bin. A numerical smoothing algorithm is applied to the location coordinate to reduce the effect of fluctuations. Details were discussed in Chapter 3.

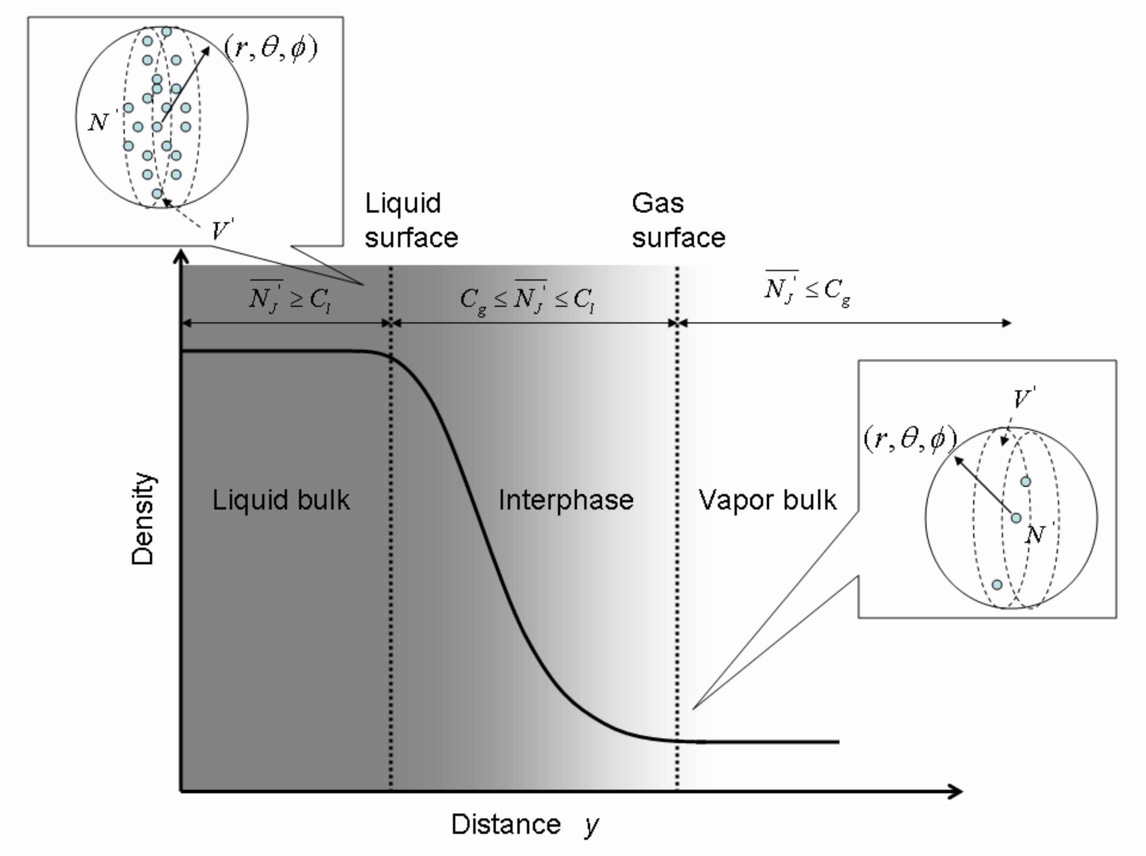

Fig. (4. 4) Method for determining interphase boundaries.

As condensation began in the present simulations, the numbers of neighboring interacting molecules for the condensate molecules near the solid-liquid interface were smaller than the liquid criterion number. As the number of vapor molecules condensing on the bare substrate increased, the neighboring interacting numbers for molecules near the solid-vapor interphase increased to the liquid criterion number and the solid-vapor interface transitioned to a solid-liquid interface. At that point, it was assumed that the liquid-vapor interphase was formed just above the solid liquid interface. All subsequent steps to track the positions of the moving interphase boundaries followed the procedures that have been described.

4.5 Results and Discussion

This section presents the nonequilibrium condensation results obtained from the hybrid DSMC-NEMD simulations and compares them with the moment method and with pure DSMC, where possible. As shown in the following subsection, the systems pass through an unsteady period and reach a quasi-steady state within the lifetime of the simulation. The quasi-steady results are described in a separate subsection. Finally, two interfacial regions, liquid-vapor and solid-liquid, are discussed in separate subsections.

4.5.1 From Unsteady to Steady State

Fig. (4.5) depicts the liquid thin film growth for simulation case 4 as a plot of the liquid and vapor moving interphase boundary locations for liquid and gas (y_l and y_v) as a function of time with "instantaneous" mass density ($\rho = nm$) profiles at selected times superimposed on them. The accurate locations of the liquid and vapor boundaries are verified through comparing them with the mass density profiles at the different times. The peak-to-peak shape in density profiles indicates the solid-liquid interaction effect (layering pattern) that is also reflected in the steps shape of the liquid boundary growth profile. As the liquid film thickened, this steps shape tended to attenuate with time.

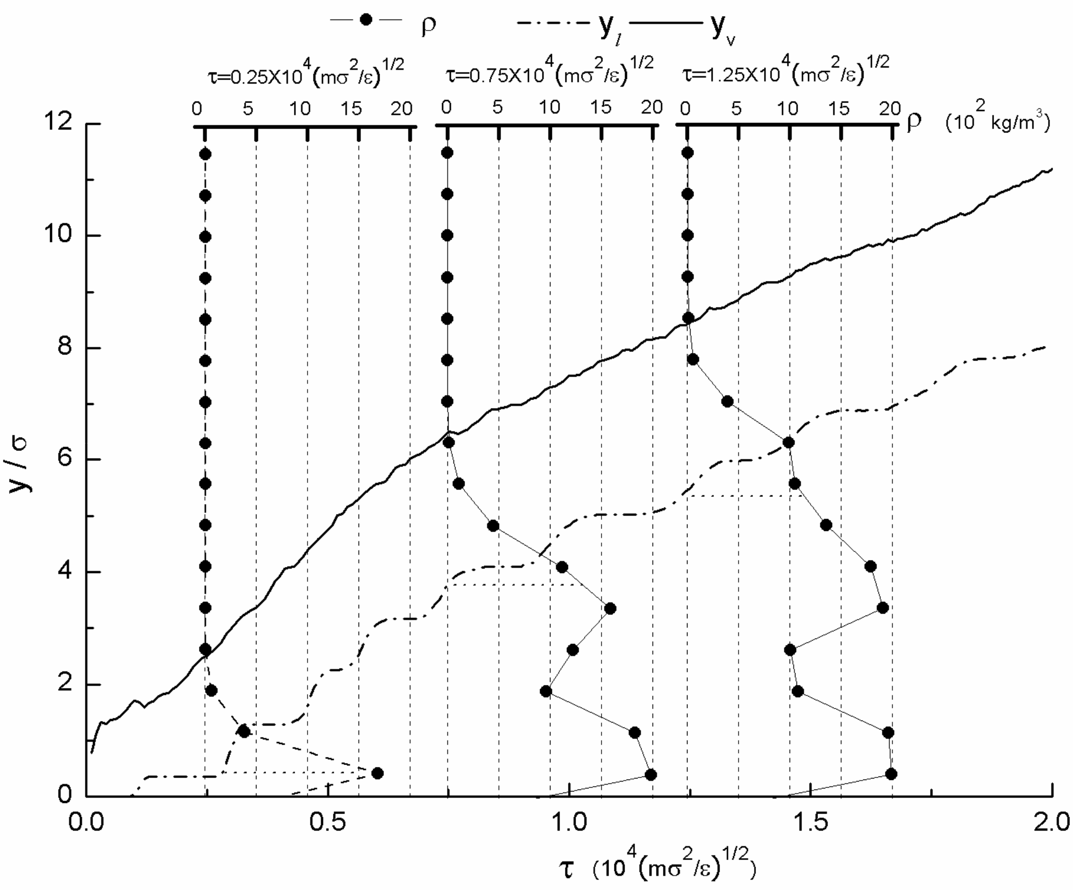

Fig. (4. 5) Moving interphase of simulation case 4 overlaid with the density profiles at selected system evolution times. (Horizontal dashed line indicates the liquid interphase boundary location, on the density profiles.)

The liquid film growth obtained for simulation cases 1, 4 and, 7 were compared in Fig. (4.6), showing the higher growth rates associated with the larger temperature differentials between bulk vapor and substrate. In confirmation of the rough trend observed in the shorter simulation time results of He et al. [81], the present growth becomes linear. Growth for the remainder of the cases, which involved tangential flow, were not plotted because, there were only very slight effects of the tangential flow. In fact, there was little or no effect of tangential velocity on most of the thermally related quantities obtained from those simulations.

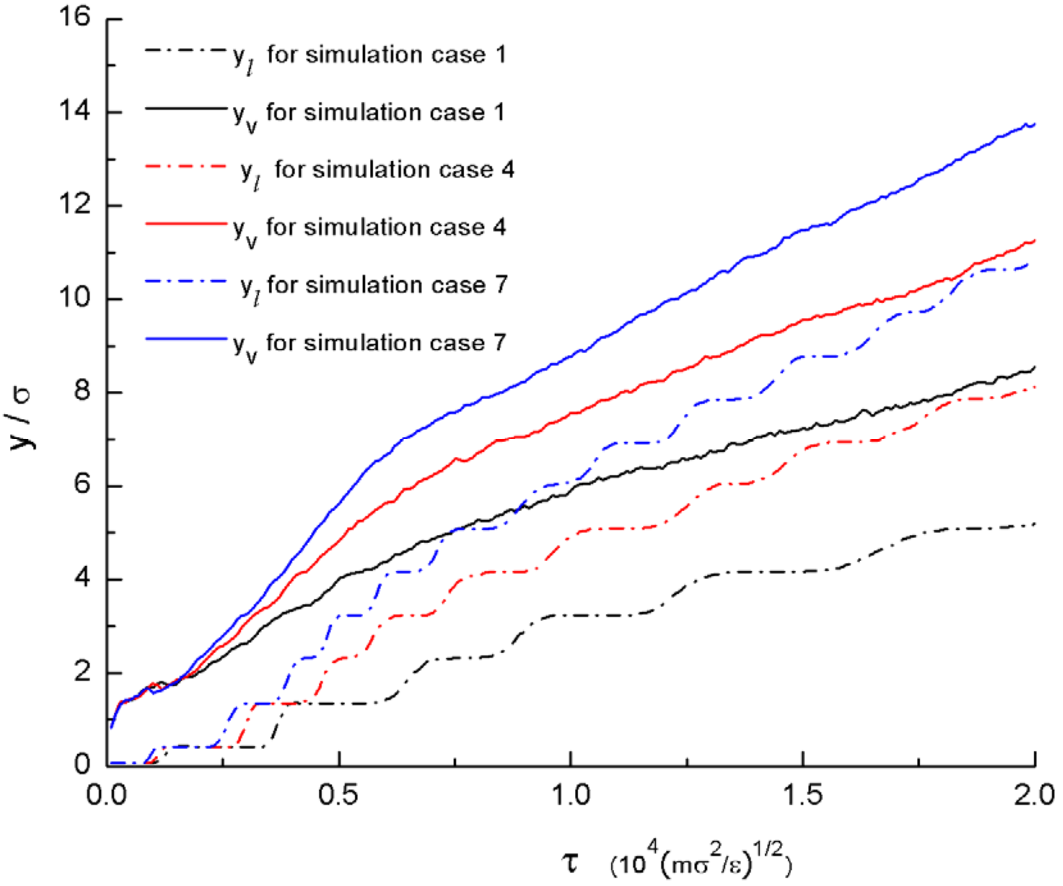

Fig. (4. 6) Moving interphase boundary heights, vs. evolution time.

The quasi-steady state can be distinguished from the initial unsteady state by observing the interphase properties at the liquid and vapor boundaries as a function of time. The temperature, molecular number flux, and heat flux were obtained at the NEMD sampling bins within which the y_l and y_v interphase boundaries were determined to be located. The sampling bins were each 0.7σ across in the y direction. Fig. (4.7) through Fig. (4.12) show the time evolution of various interfacial properties from simulation cases 1, 4, and 7, which did not have tangential vapor flow. Again, the tangential vapor flow in the other cases did not produce any significant differences for the properties presented in the figures and were not plotted. The statistical and thermal fluctuations at the vapor interphase boundary are large due to the computational expense associated with reducing such fluctuations through obtaining more samples. The fundamental difficulty is that the gas is dilute and the mean flow velocities and the thermal gradients are small.

Fig. (4.7) is a plot of temperature, T_l, at the liquid interphase boundary versus simulation time. After the liquid-film appeared, T_l for simulation case 1 tended to decrease initially from the upstream vapor temperature, T_∞. Different from case 1, the results from simulation cases 4 and 7, with colder substrates, showed liquid layers initially deposited from the vapor phase that were much colder than T_∞, especially for case 7, with the coldest substrate, but then generally warmed with time, with case 7 exhibiting a warming peak. All of the cases approached a quasi-steady steady state with some waviness in the curves. The quasi-steady state was reached after time, $1\times10^4\sqrt{m\sigma^2/\varepsilon}$ or 21.6 *ns*.

Fig. (4.7) also compares the hybrid results with solutions from the kinetic theory, steady flow moment method presented in the Appendix D, showing good agreement with the moment method at the quasi-steady state. The moment method as applied here requires specification of the tangential velocity and at least one other boundary condition, which must come from the hybrid method in order to compare results. In this case, the moment method results were obtained by taking the hybrid method results for V_∞ at quasi-steady state as the known quantity since it is relatively free from the fluctuations in the hybrid results. Further details regarding the application of the moment method to obtain the comparative results are given in the next section.

The evolution of the temperature at the vapor boundary, T_{v}, is shown in Fig. (4.8) for the same cases. There are substantial fluctuations in the temperature but some trends can be discerned. The initial values are much higher than T_{∞} . A reasonable explanation is that this is because of the large latent heat released from forming the liquid in the sudden phase transition from vapor to liquid and strong solid-gas-liquid interactions. This higher thermal energy was absorbed after a time by the cooled substrate, acting as a heat sink, and then the temperature decreased with the time. On average, T_v is above T_{∞} in the quasi-steady state. This inverted temperature phenomenon [2] indicates that the vapor phase near the interphase is superheated.

The average temperature across the interphase, T_I was obtained through sampling the particle thermal kinetic energy in the region between y_l and y_v. It is shown in Fig. (4.9) and generally followed the trend of the liquid boundary temperature with a value that was only slightly greater. At the quasi-steady state, all of the simulation cases showed an average interphase temperature lower than T_{∞} at steady state.

Fig. (4.10) displays the temperature of the liquid next to the cooling substrate, T_w, obtained from the sampling bin adjacent to the substrate, normalized with the substrate temperature. In the first portion of the simulation, the argon next to the substrate was still in the vapor phase (as the dashed line indicates in the figure). Due to the sudden formation of the liquid-film on the bare substrate, the solid-liquid-vapor interaction was strong initially and caused the higher T_w value. Later, the wall fluid cooled down as the phase transition approached quasi-steady state, with only solid-liquid interaction occurring near the substrate; finally, T_w stabilized at a near constant value. A significant temperature slip,

$$\Delta T_w = T_S - T_w \tag{4.8}$$

across the solid-liquid interface at quasi-steady state is evident in the figure as the normalized temperature tends to a value greater than one.

The number flux, J, of molecules across the vapor boundary at y_v is shown in Fig. (4.11). The large initial mass transfer rates decline in the early stages of the simulation before increasing again to a relatively constant level at quasi-steady state. The results are compared with the moment method solutions and show good agreement with the moment method at quasi-steady state.

The energy conservation flux, $\dot{E}_{y,v}$, at the vapor interphase boundary is shown in Fig. (4.12). After reaching the quasi-steady state, $\dot{E}_{y,v}$ was approximately equal to its upstream value, $1/2\rho_\infty V_\infty(1/2V_\infty^2 + 5/2RT_\infty)$,. At the solid substrate surface, where the normal velocity vanishes, the only contribution to the energy conservation flux comes from the heat flux, q_w, which is also shown in Fig. (4.12). The difference between the two quantities plotted in the figure is the time rate of change of the energy within the liquid. It is obvious from the relative magnitudes of the fluxes that most of the heat removed from the liquid at the substrate is latent heat removed from the vapor as opposed to the removal of sensible heat and the flow energy and work converted to heat.

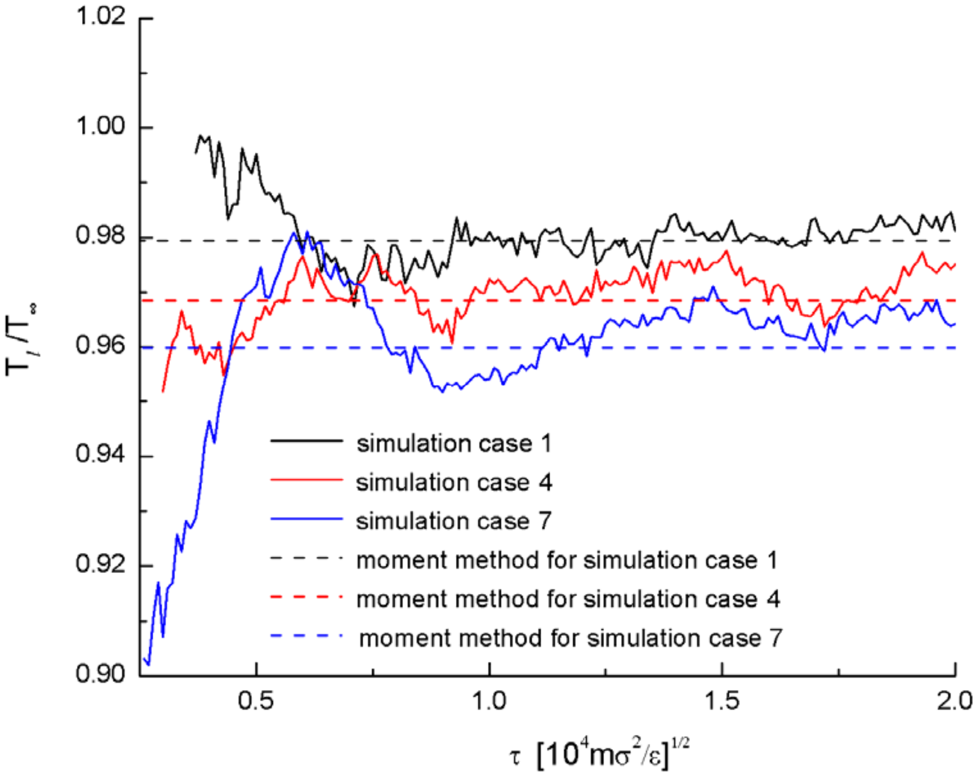

Fig. (4. 7) Liquid interphase boundary temperature vs. evolution time.

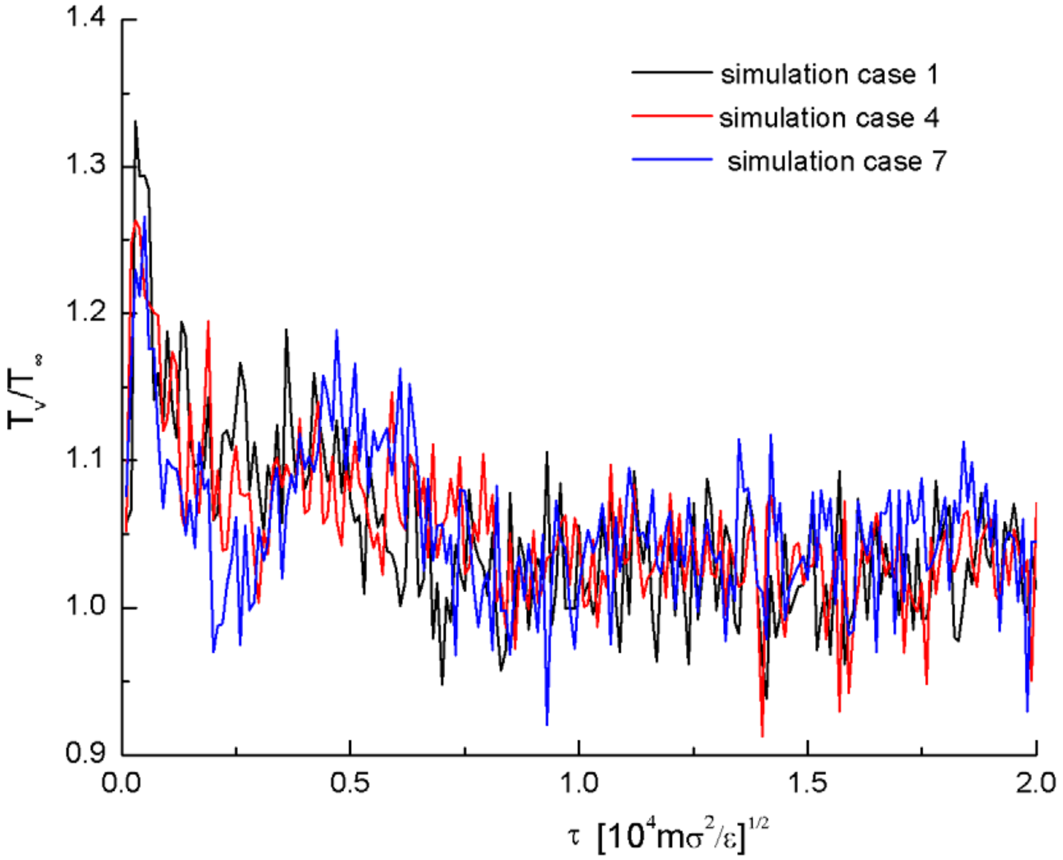

Fig. (4. 8) Vapor interphase boundary temperature vs. evolution time.

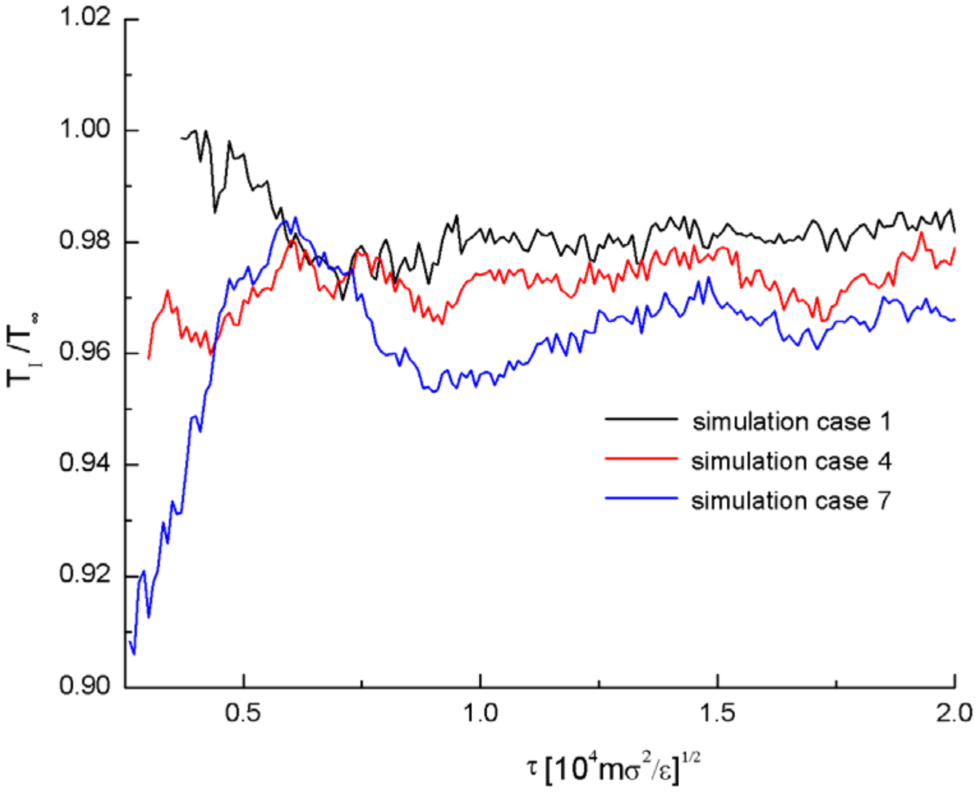

Fig. (4. 9) Averaged interphase temperature vs. evolution time.

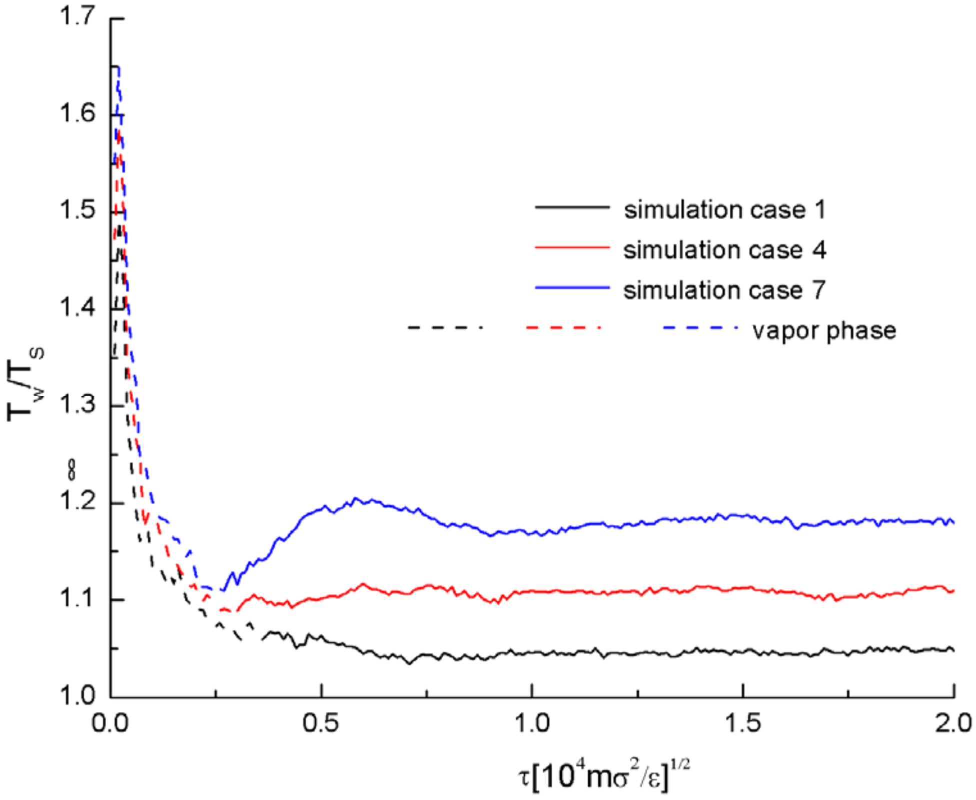

Fig. (4. 10)Fluid temperature at interface with solid vs. system evolution time.

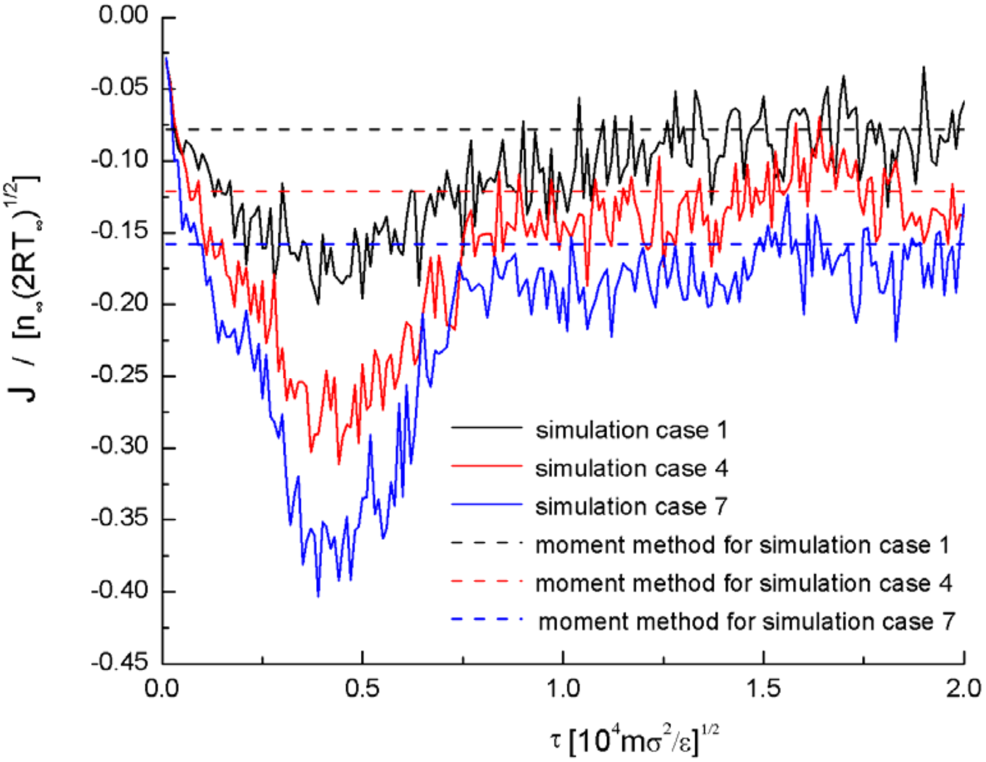

Fig. (4. 11) Number flux at vapor boundary vs. evolution time.

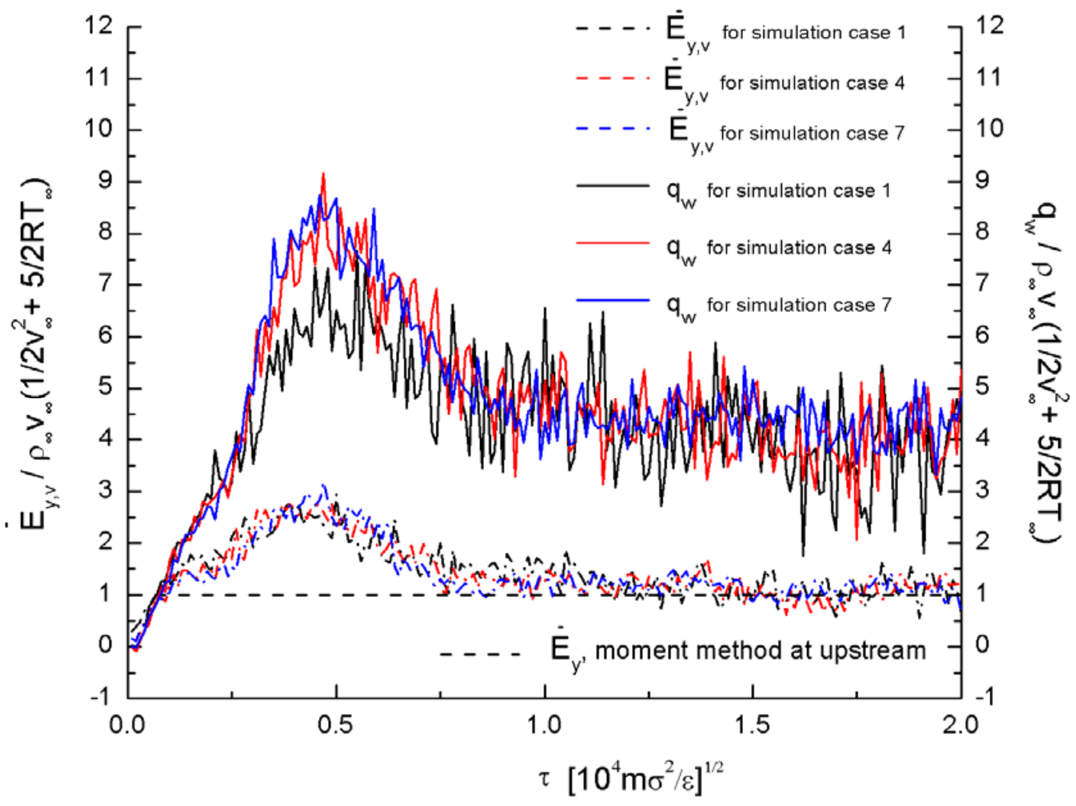

Fig. (4. 12) Energy flux at vapor boundary and wall heat transfer vs. evolution time.

4.5.2 Quasi-Steady State

Based on examination of the unsteady results, for all nine simulation cases, the quasi-steady state was reached after time, $\tau = 1\times10^4\sqrt{m\sigma^2/\varepsilon}$, Beyond this point, time averaging can be applied along with the ensemble averaging used for the unsteady results to eliminate some of the fluctuations in the quasi-steady data. Results obtained from averaging a number of liquid vapor interface properties are tabulated in Table 4.3. The standard deviations of the results were generally within six percent.

$\Delta H/R\overline{T}_l$ in Table 4.3 is the normalized latent heat where $\Delta H = h_v - h_l$. (h_v and h_l are the enthalpies at the liquid and vapor boundary, respectively). It tended to increase with decreasing substrate temperature.

The condensation and evaporation coefficients given in Table 4.3 can be defined, in terms of averaged mass fluxes, respectively, as

$$\sigma_c = \frac{\langle J_{cnds} \rangle}{\langle J_{coll} \rangle} \qquad \text{and} \qquad \sigma_e = \frac{\langle J_{evap}^{sp} \rangle}{\langle J_{out} \rangle} \tag{4.9}$$

which are identical to the definitions in Chapter 3. The vapor colliding flux, $\langle J_{coll} \rangle$, and outgoing flux, $\langle J_{out} \rangle$, are the number fluxes of molecules crossing the gas surface that originate in the vapor region or in the interphase region, respectively. The condensation flux, $\langle J_{cnds} \rangle$, is the number flux of molecules that originate in the vapor and cross the liquid surface and the mass flux of spontaneously evaporating molecules, $\langle J_{evap}^{sp} \rangle$, is the number flux of molecules that originate in the liquid and cross the vapor boundary. For convenience, the flux terminology and convention of Ishiyama et al. [39] were adopted in the present work.

In the simulations, the evaporation and condensation coefficients were obtained through tracking and counting the appropriate molecules to determine the various fluxes employed in Eq.(4.9). The molecules were labeled according to their initial phase, and during the simulation the labels were subject to change depending on the paths the molecules took. As the liquid film grew, the liquid-vapor interphase boundaries (y_l and y_v) were also tracked. The gas molecules originally above y_v became liquid molecules if they crossed y_l moving downwards, while liquid molecules originally below y_l became gas molecules if they crossed y_v moving upward.

As expected, σ_e and σ_c were not equal as they would be in an equilibrium system. Larger differences were found to exist between them for the stronger condensation cases (i.e., simulation cases 7-9).

Flux conservation in the interfacial region dictates that the upward flux, $\left\langle J_{out}\right\rangle$, at the vapor boundary is equal to the sum of $\left\langle J_{evap}^{sp}\right\rangle$ and the reflected-back-to-the-vapor flux, $\left\langle J_{ref}^{+}\right\rangle$ (i.e., $\left\langle J_{out}\right\rangle = \left\langle J_{evap}^{sp}\right\rangle + \left\langle J_{ref}^{+}\right\rangle$). Analogously, the downward flux, $\left\langle J_{coll}\right\rangle$, at the vapor boundary is equal to the sum of $\left\langle J_{cnds}\right\rangle$ and the reflected-back-to-the-liquid flux, $\left\langle J_{ref}^{-}\right\rangle$ (i.e., $\left\langle J_{coll}\right\rangle = \left\langle J_{cnds}\right\rangle + \left\langle J_{ref}^{-}\right\rangle$). In Table 4.3 $\left\langle J_{out}\right\rangle / \left\langle J_{coll}\right\rangle$ was compared with χ, which is defined as

$$\chi = \frac{1-\sigma_c}{1-\sigma_e} \quad \text{or} \quad \chi = \frac{\left\langle J_{out}\right\rangle \left\langle J_{ref}^{-}\right\rangle}{\left\langle J_{coll}\right\rangle \left\langle J_{ref}^{+}\right\rangle} \tag{4.10}$$

Differences between χ and $\left\langle J_{out}\right\rangle / \left\langle J_{coll}\right\rangle$ are small, but $\left\langle J_{ref}^{-}\right\rangle \Big/ \left\langle J_{ref}^{+}\right\rangle$ (i.e., $\chi / \left(\left\langle J_{out}\right\rangle / \left\langle J_{coll}\right\rangle\right)$) is slightly greater than unity and demonstrates the fact that, across the liquid-vapor interphase, a small portion of the evaporating liquid molecules undergo collision with condensing vapor molecules carrying larger kinetic energy and are reflected back to the liquid phase region. The fact that $\left\langle J_{ref}^{-}\right\rangle \Big/ \left\langle J_{ref}^{+}\right\rangle$ is only slightly greater than unity implies that the nonequilibrium state in the interphase is relatively weak. This is consistent with the departure from Maxwellian distribution functions due to interfacial drift velocity observed in Ref. 43. There is also an interfacial drift velocity in the present results as will be presented in section 4.5.3 (Fig. (4.25).

The quasi-steady liquid-vapor interfacial properties in Table 4.3 were unaffected by the vapor tangential flow condition with the exception of heat flux at the vapor interphase boundary, $\overline{q_v}$, which was sensitive to the tangential flow velocity. Larger tangential velocities induced higher heat flux rates at the vapor boundary.

The interphase gas boundary temperatures, $\overline{T_v} / T_\infty$, shown in Table 4.3 were greater than unity due to the inverted temperature phenomenon. As noted earlier, there is very little difference in the table between the interphase liquid boundary temperature, $\overline{T}_l$, and the slightly larger interphase averaged temperature, $\overline{T}_I$.

Table 4. 3 Quasi-steady liquid-vapor interphase properties

Sim. case.	$\frac{\overline{T}_v}{T_\infty}$	$\frac{\overline{T}_I}{T_\infty}$	$\frac{\overline{T}_l}{T_\infty}$	σ_e	σ_c	χ	$\frac{\langle J_{out} \rangle}{\langle J_{coll} \rangle}$	$\frac{\Delta H}{R\overline{T}_I}$	$\frac{\overline{q}_v}{\rho_\infty (RT_\infty)^{3/2}}$ (10^{-2})
1	1.024	0.979	0.978	0.827	0.849	0.872	0.862	9.208	-4.632
2	1.016	0.981	0.980	0.826	0.847	0.879	0.851	9.168	-5.885
3	1.021	0.983	0.983	0.826	0.847	0.879	0.854	9.245	-6.172
4	1.028	0.968	0.968	0.813	0.848	0.810	0.794	9.431	-7.151
5	1.035	0.971	0.970	0.815	0.851	0.804	0.798	9.461	-7.635
6	1.025	0.972	0.972	0.816	0.850	0.812	0.799	9.436	-8.704
7	1.043	0.961	0.960	0.806	0.856	0.744	0.731	9.711	-8.713
8	1.043	0.963	0.962	0.800	0.851	0.744	0.729	9.799	-10.091
9	1.032	0.966	0.965	0.803	0.853	0.744	0.733	9.792	-12.086

Two important computed, quasi-steady averaged system parameters are shown in Table 5.4, the inflow condensation velocity and the wall heat transfer. Both quantities must increase with a decrease in the substrate temperature. Again, there is no discernable effect of tangential flow velocity. The heat conduction from the liquid into the wall is two orders of magnitude larger than the heat conduction at the vapor boundary, where a tangential flow effect was observed.

Table 4. 4 Quasi-steady computed system parameters

Sim. case.	$\frac{\overline{V}_\infty}{\sqrt{2RT_\infty}}$	$\frac{\overline{U(0)}}{U_\infty}$	$\frac{\Delta T_W}{T_\infty - T_S}$	$\frac{\overline{q_w}}{\rho_\infty (RT_\infty)^{3/2}}$
1	0.0861	*	-0.702	-1.246
2	0.0866	0.007	-0.703	-1.285
3	0.0871	0.011	-0.716	-1.289
4	0.130	*	-0.766	-1.931
5	0.132	0.006	-0.771	-2.005
6	0.130	0.012	-0.773	-1.949
7	0.173	*	-0.776	-2.703
8	0.173	0.006	-0.787	-2.752
9	0.173	0.018	-0.789	-2.758

The quasi-steady, liquid surface temperature, $\overline{T}_l$, results have a linear relationship with the substrate temperature, T_S, as shown in Fig. (4.13). The quasi-steady, hybrid results for normalized upstream condensation velocity, $S_\infty = \overline{V}_\infty \big/ \sqrt{2RT_\infty}$, is plotted against the hybrid results for $\overline{T}_l / T_\infty$ in Fig. (4.14).

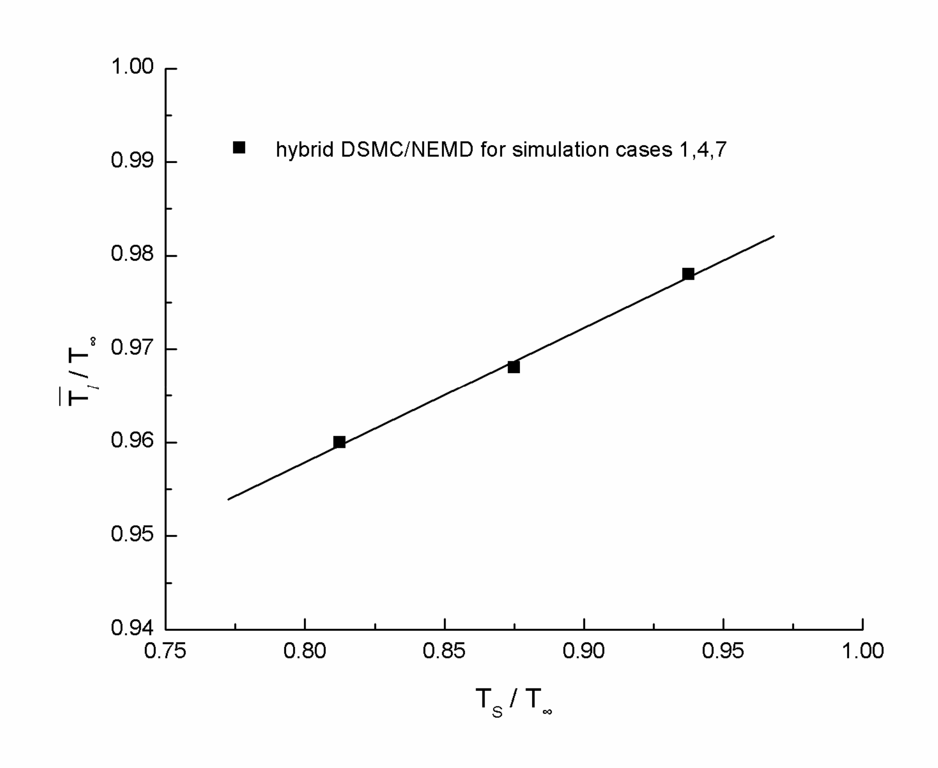

Fig. (4.13) Linear dependency of liquid interphase boundary temperature on substrate temperature.(Standard deviations of $\overline{T_L} / T_\infty$ *are within 3%.)*

The hybrid results in Fig. (4.14) are compared with the kinetic moment method solution for the liquid surface temperature, T_L/T_∞ , plotted as a function of S_∞, which must be specified in the present application of the moment method (See Appendix D). $S_{x\infty} = \overline{U}_\infty / \sqrt{2RT_\infty}$, and the normalized latent heat of condensation, $\Delta H/RT_L$, must also be specified for the moment solution. The latent heat of condensation parameter, $\Delta H/RT_L$, used in all the moment method solutions was a value of 9.5 computed as the average of the $\Delta H/R\overline{T}_\mathrm{I}$ in Table 4.3 obtained from the nine hybrid simulation cases. This was possible because the moment method is not sensitive to small changes in the latent heat parameter. $\overline{T}_\mathrm{I}$ is used as a proxy for T_L here only instead of $\overline{T}_l$ simply because it is conceptually more representative of the transition in phase. It is insignificant to the results since the values for

$\overline{T}_{\mathrm{I}}$ and $\overline{T}_l$ are very close.

There is good agreement between the hybrid and moment method results in Fig. 14. In the moment method, the Knudsen layer structure is solved based on the fifth power repulsive interaction force law of Maxwell molecules. As suggested by Ytrehus [5], the interaction law influences the spatial structure of the vapor flow, but not the driving parameters. Fig. (4.14) shows the close agreement between the moment method driving parameter, T_L/T_∞, and its quasi-steady hybrid simulation counterpart for a given S_∞. The figure confirms that the interaction law and other modeling assumptions made in the moment method do not have a significant impact on the values of T_L computed from it. This extends to the present modification of the moment method to include tangential velocity, as shown by the good agreement between the methods for nonzero tangential velocity in Fig. (4.14).

In addition, for comparison purposes, the Knudsen layer was simulated using DSMC alone ("pure DSMC") with these results for S_∞ plotted in Fig. (4.14). The agreement between the hybrid results and the moment solution is also good.

All the present pure DSMC results were obtained with the DSMC equivalent of a kinetic boundary condition [99,100] applied at the liquid surface. T_L, the surface temperature, and, n_e, the vapor number density at the liquid surface, were obtained from the moment method solution, while the condensation coefficients used were from the hybrid simulation. V_∞ was not fixed but determined as part of the simulation.

The liquid surface interfacial boundary condition in pure DSMC was treated, with some modification, as a DSMC open boundary [6] for zero streaming velocity. Molecules evaporating from the liquid surface, whose velocities were sampled by

$$F_e^+ = 1/(2\pi RT_L)^{3/2}\exp(-|\mathbf{c}|^2/2RT_L), \tag{4.11}$$

were generated with an outgoing density equal to $\sigma_e n_e$. Due to the non-unity condensation coefficient, unlike the traditional DSMC open boundary, only a portion, σ_c, of colliding vapor molecules were condensed (removed at the boundary) and the rest of the colliding vapor molecules were diffusively reflected back to the vapor phase with the temperature, T_L.

The condensing molecules were stochastically selected. A vapor molecule striking the interface was condensed (removed), if a random number, $R_f < \sigma_c$; or was diffusively reflected back to the vapor phase, if the random number, $R_f > \sigma_c$. This process ensured that the ratio of mean condensing mass flux to mean colliding mass flux was equal to σ_c. Carey et al. [25] used this condensation algorithm to simulate molecular interaction at a droplet surface by DSMC and showed it to be an accurate interfacial treatment for condensation.

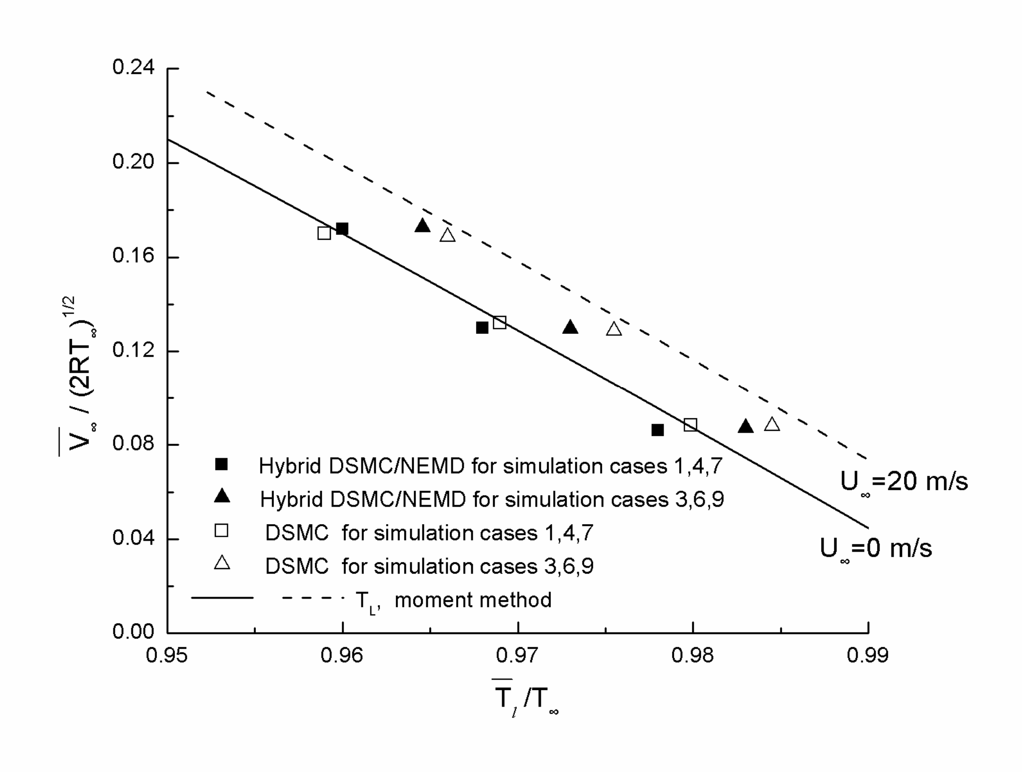

Fig. (4.14) Relationship between condensation velocity and liquid surface temperature at quasi-steady state. (Standard deviations of V_∞ are within 5%.

The inverted temperature profile phenomenon has been observed previously in molecular simulations of condensation (e.g., Refs. 3 and 101). Ytrehus [5] introduced the inverted temperature criterion number

$$\beta_c = \frac{32+9\pi}{4\pi} + 8\frac{1-\sigma_{e/c}}{\sigma_{e/c}} \tag{4.12}$$

where $\sigma_{e/c}$ is a single evaporation and condensation coefficient based on an assumption that $\sigma_e = \sigma_c$. The thermodynamic state of the vapor above the liquid is superheated and an inverted temperature profile must occur if

$$\beta_c < \frac{\Delta H}{RT_L} \tag{4.13}$$

For each case of the nonequilibrium condensation simulations, the latent heat in Eq.(4.13) was taken to be the $\overline{\Delta H}/R\overline{T}_{\mathrm{I}}$ value given in Table 4.3. $\sigma_{e/c}$ in Eq. (4.12) was taken to be the average value of σ_e and σ_c in Table 4.3, giving a β_c of about 5.2 for all cases. Based on these values, the criterion in Eq. (4.13) is met for all nine simulation cases.

4.5.3 Knudsen Layer Structure

To study the profiles of the vapor Knudsen layer structure and the moving liquid-vapor interfacial region, the moving coordinate, y', was introduced and its origin was fixed at y_g (i.e., $y' = y - y_v$). The hybrid simulation profiles of temperature, density and normal velocity in the vapor phase region were obtained by time-averaging the hybrid results during the quasi-steady period in the region for which $y' \geq 0$. The Knudsen layer profiles for this region were also obtained from the moment method and pure DSMC. Knudsen layer profiles for simulation case 7 are shown in Fig. (4.15) through Fig. (4.18) with the y' coordinate plotted in units of the reference mean free path [5] defined as

$$\lambda_e = \frac{\mu(T_L)}{mn_e}\sqrt{\frac{\pi}{2RT_L}} \tag{4.14}$$

in which μ is the vapor viscosity at T_L The vapor viscosity model used was the L-J spline potential model described in Ref. 35.

The unity condensation coefficient solution for the moment method was extended to the more general condition of non-unity, non-equal condensation and evaporation coefficients by scaling the y'/λ_e coordinate by the factor [102],

$$\Theta = \frac{\dfrac{\sigma_c}{\sigma_e}\left(\dfrac{n_e}{n_\infty}\right)_1 + \dfrac{1-\sigma_c}{\sigma_e}2\sqrt{\pi}\sqrt{\dfrac{T_\infty}{T_L}}S_\infty}{\left(\dfrac{n_e}{n_\infty}\right)_1} \tag{4.15}$$

where $(n_e/n_\infty)_1$ is the unity evaporation/condensation solution of n_e/n_∞ from the moment method. The moment method plots in Fig. (4.15) through Fig. (4.18) have been scaled with Eq. (4.15) using σ_e and σ_c from the hybrid results.

Unlike the hybrid method, the kinetic theory-based moment and pure DSMC methods for the vapor are not influenced by the substrate temperature. They cannot independently determine T_L without specification of another vapor boundary condition, nor can they evaluate σ_e and σ_c. Since the S_∞ values from the hybrid results were used in the moment method to determine the T_L and n_e values, which were, in turn, used to generate the pure DSMC results, the kinetic results in Fig. (4.15) through Fig. (4.18) are not truly independent of the hybrid results. Furthermore, the σ_e and σ_c from the hybrid were also used for the DSMC results through the boundary treatment and for the moment results through Eq. (4.15). As a consequence of their dependency on the hybrid results and their modeling restrictions, the moment and DSMC results cannot be used to validate the hybrid method in an absolute sense. However, the hybrid can be used to assess the utility of the moment and DSMC methods for the present system. This is of particular interest for the profiles, which are more sensitive to the differences in molecular models than the driving parameter comparisons in Fig. (4.12) and Fig. (4.14).

In Fig (4.15) through Fig. (4.18), the hybrid simulation and pure DSMC simulation results for the vapor profiles show varying degrees of agreement with each other as well as with the moment method results. The figures reveal that fluctuations are still prominent in the quasi-steady profiles from simulation of the vapor region by the hybrid and pure DSMC methods even after smoothing by time averaging as well as by the ensemble averaging used in obtaining the unsteady results. The temperature gradients and flow velocities across the vapor region proved to be too small (i.e., temperature gradients less than eight percent and condensing flow Mach numbers less than 0.19), to reduce the level of fluctuations further.

The vertical dashed lines in the figures indicate the approximate location of the boundary between the NEMD and DSMC simulator domains of the hybrid. It is not the exact boundary, due to the fact that y' is a moving coordinate. However, the movement during the quasi-steady portion of the simulation for which the data is plotted is only about $0.1\lambda_e$.

Figure (4.15) shows the separate profiles for the kinetic temperatures in the x direction and in the y direction, demonstrating that they are both inverted as well as out of equilibrium with each other. In Fig. (4.15), the hybrid and DSMC inverted interfacial kinetic temperature profiles differ from the corresponding moment method inverted profiles in that the distance above the interface at which they begin to increase (around $5\lambda_e$) is greater. T_x and T_y are strongly decoupled in the region within one λ_e, of the interface. T_y, the major contributor to the inverted temperature, rapidly increases toward the interface, while T_x slightly decreases. The thermodynamic temperature, T, results are shown in Fig. (4.16) and also differ from the hybrid results in a similar manner. The pure DSMC results for T_x and T_y, shown in Fig. (4.15) and for T shown in Fig. (4.16) follow the trends of the results from the hybrid simulations.

For density, ρ and condensing velocity, *V*, shown in Fig. (4.17) and Fig. (4.18), respectively, the hybrid simulations displays good agreement with the moment method, but pure DSMC simulations show small deviations within $5\lambda_e$ of the interphase. The different profile shapes in the Knudsen layer between the hybrid DSMC-NEMD results and the moment method solutions in Fig. (4.15) through Fig. (4.18) are most likely primarily due to the different molecular interaction laws employed in each method since the DSMC profiles tend to follow the hybrid profiles.

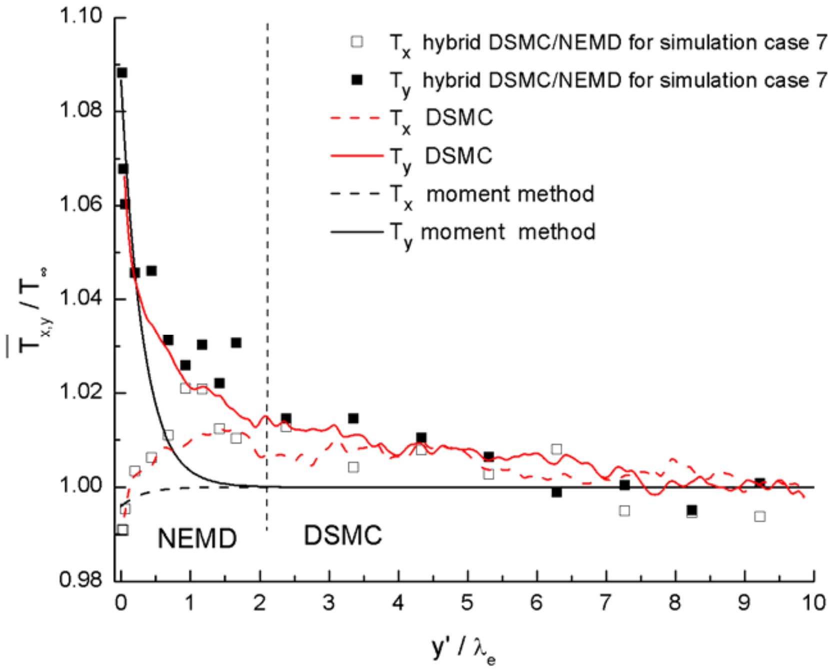

Fig. (4. 15) Quasi-steady nonequilibrium temperature profiles in the vapor region.

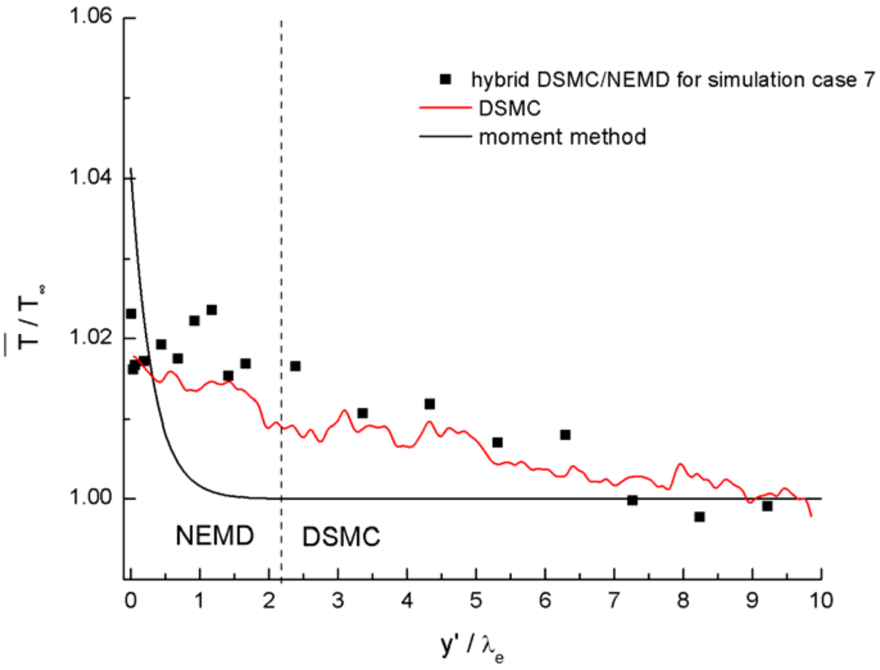

Fig. (4. 16) Quasi-steady temperature profiles in the vapor region.

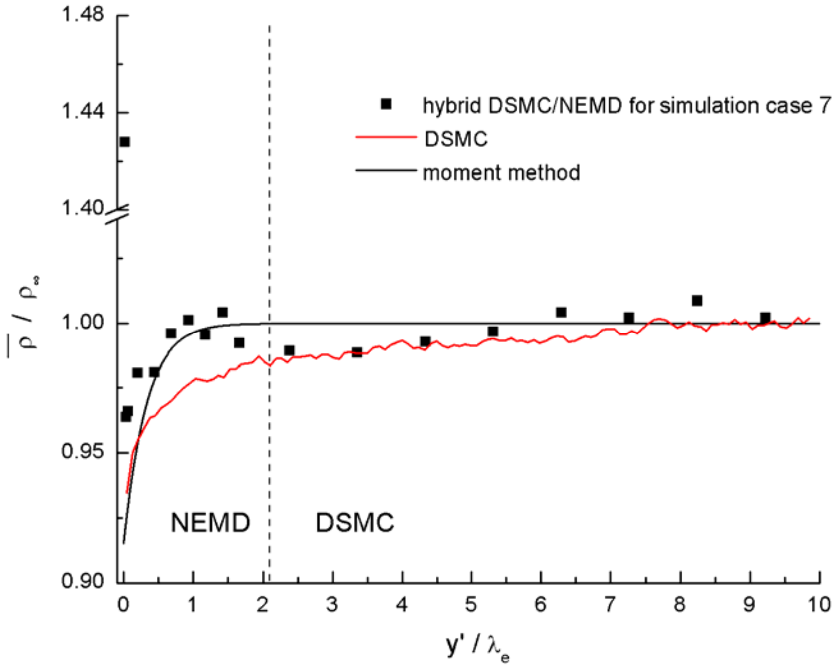

Fig. (4. 17) Quasi-steady number density profiles in the vapor region.

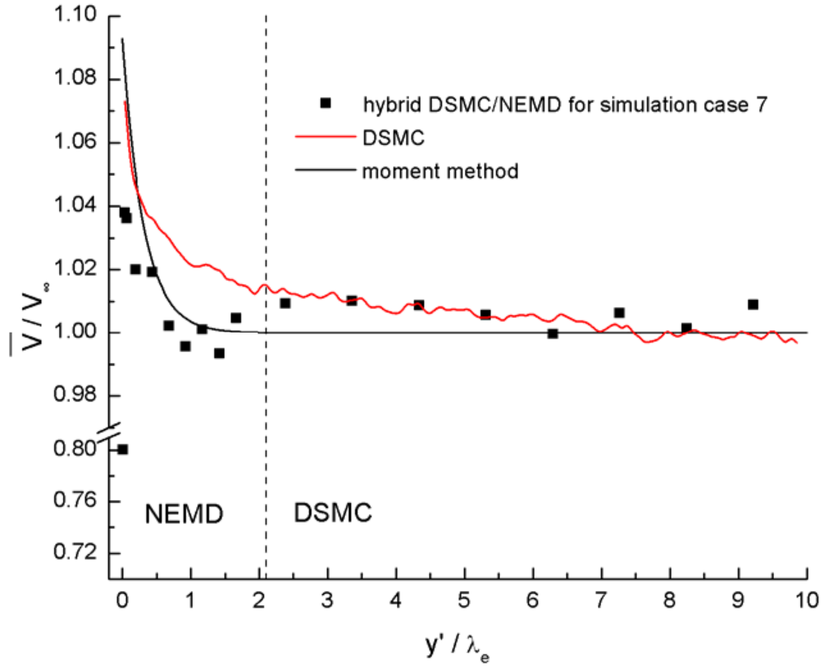

Fig. (4. 18) Quasi-steady normal velocity profiles in the vapor region.

The *p*-*T* diagram in Fig. (4.19) displays the thermodynamic state of the vapor domain at three different locations, $y'=0$, $y'=1.5\sigma$ (0.03 λ_e), and $y'=10\lambda_e$. The *p*-*T* saturation line was determined from numerically fitting data from equilibrium simulations. The vapor is close to the local saturation state at the vapor boundary, $y'=0$; however, just above, the thermodynamic state of the vapor jumps to superheated state. The sudden change of the thermodynamic state is also reflected in the density profiles near $y'=0$ in Fig. (4.17).

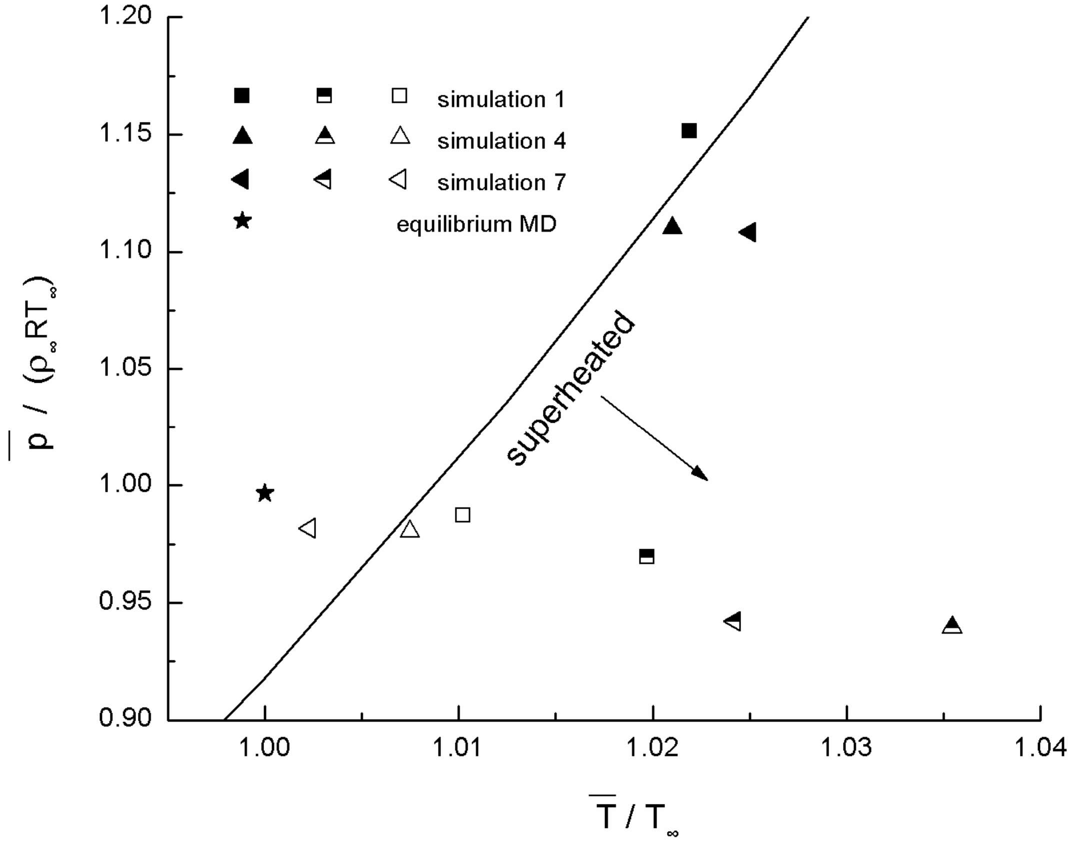

Fig. (4. 19) Quasi-steady saturation states at various vapor locations. (Open symbols indicate the hybrid NEMD/DSMC results at $y'=10\lambda_e$*; half black and half white symbols indicate the hybrid NEMD/DSMC results at* $y'=1.5\sigma$*; Black symbols indicate the hybrid NEMD/DSMC results at* $y'=0$*; Solid line is the Clausius-Clapeyron relation numerical fit from data in Chapter 3). (The standard deviations of* T *and* p *are within 3.5% and 5%, respectively.)*

Hybrid simulation tangential velocity profiles in the vapor for cases 2, 5, and 8 are shown in Fig. (4.20) and for cases 3, 6, and 9 are shown in Fig. (4.21). Agreement with the pure DSMC results, also shown in the figures, is good. For the strongest condensation and tangential flow case (i.e., simulation case 9), the slip velocities (as a percentage of the upper boundary tangential velocity) at the liquid-vapor interphase are larger than in the weaker condensation and tangential flow cases. The slip velocities range from 0.07 to 1.8 percent of the upper boundary, tangential velocities. as shown in Table 4.4.

The shape of the tangential velocity profiles are consistent with those obtained by Aoki et al. [97] from their kinetic theory solution of the Knudsen layer for condensation with tangential flow. They are different than the more linear profiles typical of a Couette shear flow that the tangential velocity in the reservoir at a fixed height above the interface might suggest exists below it. The profiles' shapes suggest that the profiles are being compressed and displaced downward by the condensing flow.

The stronger condensation cases produce flattened profiles at the upper simulation boundary for the hybrid and the DSMC simulations. This implies that at least these profiles could be independent of the boundary height. The modified moment method in the Appendix D employs an asymptotic maximum upper boundary condition for the tangential velocity. The agreement in Fig. (4.14) with the moment method is somewhat better for the tangential flow cases with the stronger condensation. Moreover, previous kinetic theory studies [5,97] have demonstrated that the flow behavior above the Knudsen layer for condensation with tangential flow is equivalent to an Euler flow with inner slip matched to the Knudsen layer edge flow. Hence, the present results are general in nature for any condensing bulk flow in the absence of a tangential pressure gradient and are not restricted to a particular bulk viscous shear profile.

Fig. (4.22) shows the tangential velocity-driven shear stress profiles from the hybrid and DSMC simulations for the lowest and highest condensation cases. For the same upper tangential velocity boundary, the stronger condensation results in a higher shear stress above the liquid-vapor interphase. The shear profile follows from the form of the tangential velocity profile and indicates that the vapor flow is not in a significant state of shear except within approximately $2\lambda_e$ from the interface; therefore, it is nearly an Euler flow.

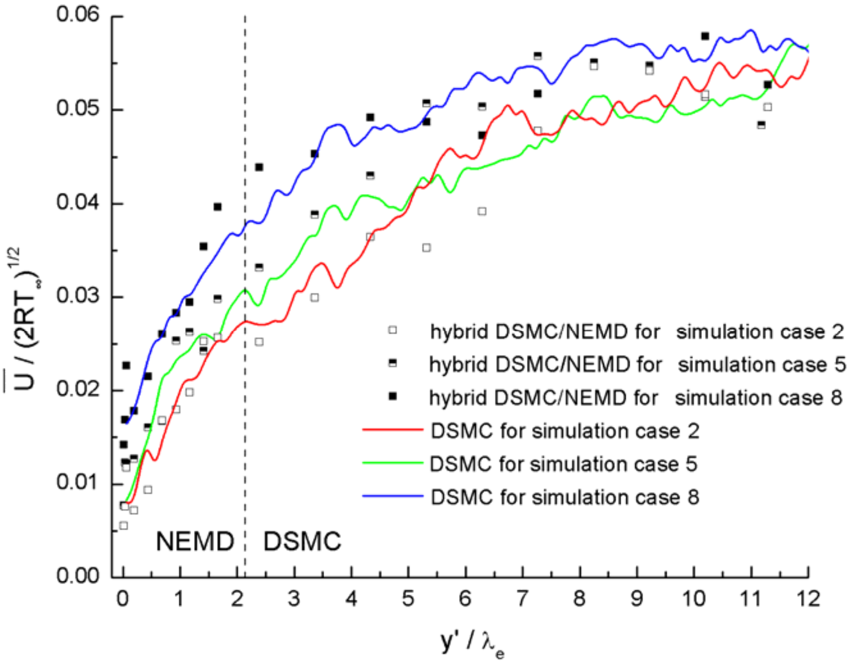

Fig. (4. 20) Quasi-steady vapor tangential velocity profiles for lower tangential velocity cases.

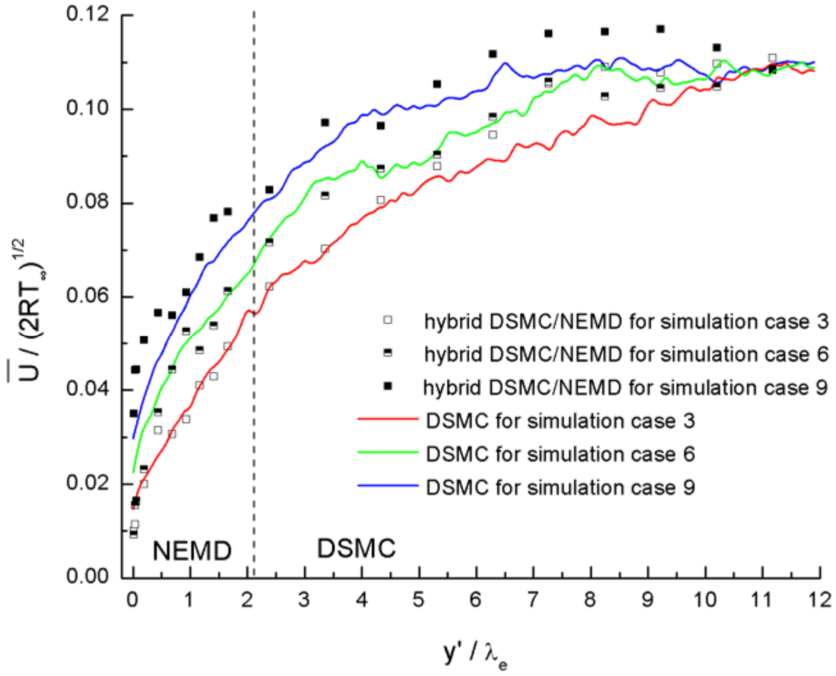

Fig. (4. 21) Quasi-steady vapor tangential velocity profiles for higher tangential velocity cases.

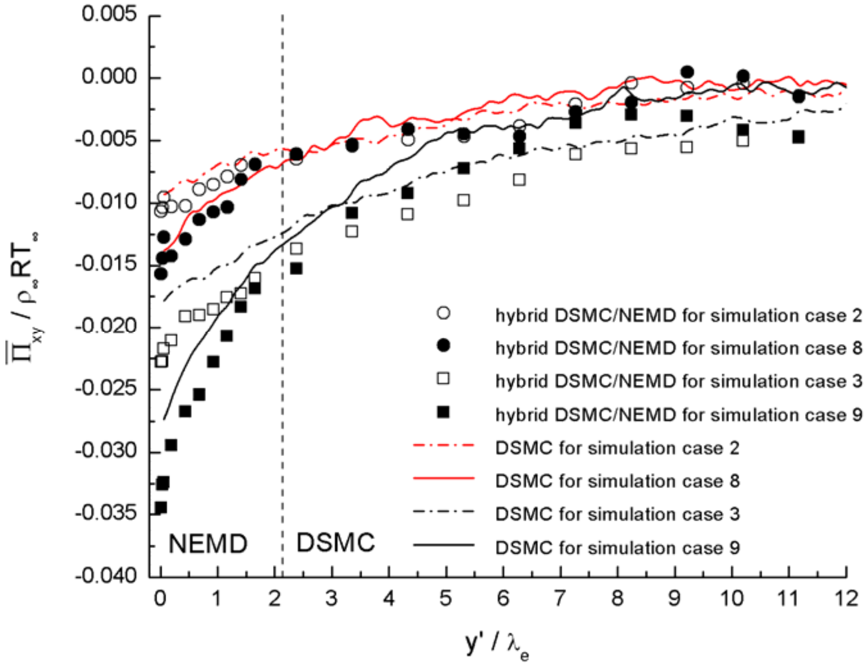

Fig. (4. 22) Quasi-steady shear stress profiles for tangential vapor velocity cases.

4.5.4 Liquid-Vapor Interphase

The liquid-vapor interphase, which is on the order of ten molecular diameters, was resolved by the hybrid within its NEMD simulator partition. The moving interphase was studied with reference to the coordinate y'. The liquid-vapor interphase thickness, $d = y_v - y_l$, is subject to the minor periodic oscillations in the liquid surface location noted earlier but is otherwise unvaried during the quasi-steady final state of the system (See Fig. (4.5).). Thus, the quasi-steady interphase region is stable with respect to coordinate y'.

In Fig. (4.23), the density profiles across the interfacial region without tangential flow are compared with the equilibrium interfacial density profile obtained by a preliminary equilibrium MD simulation of a liquid-vapor equilibrium system at 78K ($0.97T_\infty$), which corresponds to the liquid surface temperature for case 4. The present liquid-vapor interphase with a strong net condensation process has a different density profile when compared with an equilibrium profile with the same liquid surface temperature. The present density profile is distorted and has a longer upstream tail. This tail effect is caused by molecules accumulating ahead of the moving liquid surface that are not accommodated to the transition state from vapor to liquid. For the equilibrium liquid-vapor interphase, the density profile is well-known to have a shape close to a hyperbolic tangent [88] so the nonequilibrium distortion means that the present profiles deviate from this shape.

The distorted interphase density profiles apparently increase the ability of the molecules to cross the interphase region. Hence, liquid molecules are freer to move downward to the liquid phase, and vice versa. This effect is shown by the condensation and evaporation coefficients (σ_e and σ_c) in Table 4.3, which both exceed their values at phase equilibrium. (i.e., $\sigma_e = \sigma_c = 0.7$ at 78K). Furthermore, the normalized latent heat for cases 4, 5, and, 6 of about 9.4, as shown in Table 4.3, is lower than the latent heat for the equilibrium case, which is 9.71.

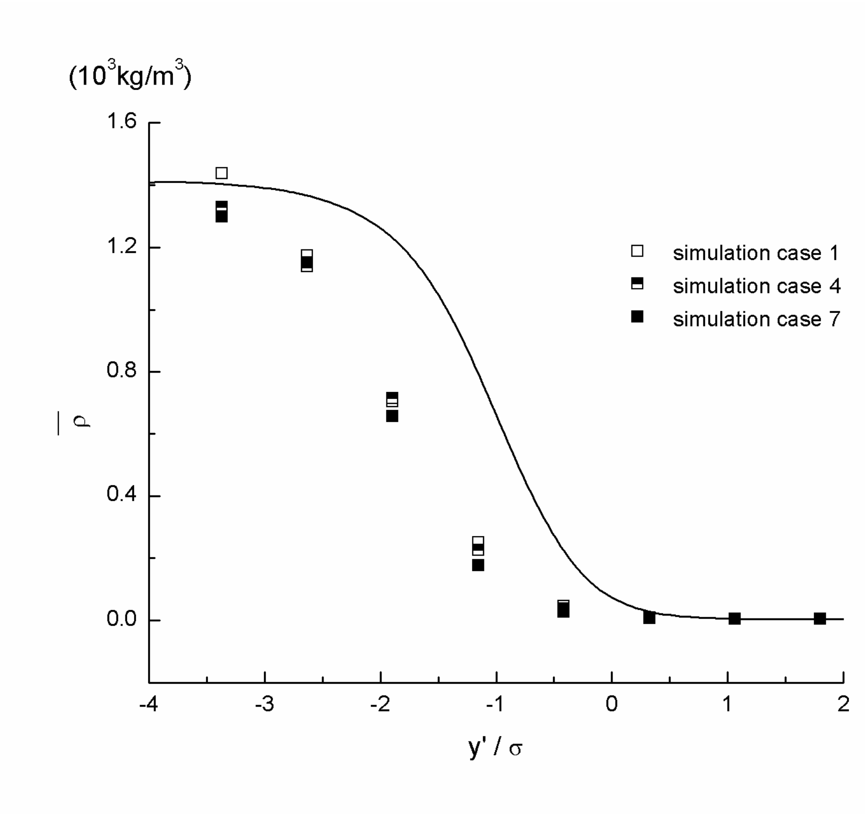

Fig. (4. 23) Comparison between quasi-steady nonequilibrium and equilibrium interphase number density profiles. (Solid line indicates the equilibrium density profile from equilibrium MD simulation at 78K.)

$\overline{T_x}$ and $\overline{T_y}$ across the interphase are shown in Fig. (4.24). The inverted kinetic temperature, T_y, which is most strongly out of equilibrium in the vapor interfacial region, decreases rapidly, beginning at the vapor boundary of the interphase, to its equilibrium state at the liquid boundary and a value smaller than T_∞. $\overline{T_x}$ begins the decline from its inverted state in the vapor and continues to decline across the interphase, equilibrating with $\overline{T_y}$ at the liquid interphase boundary, y_l.

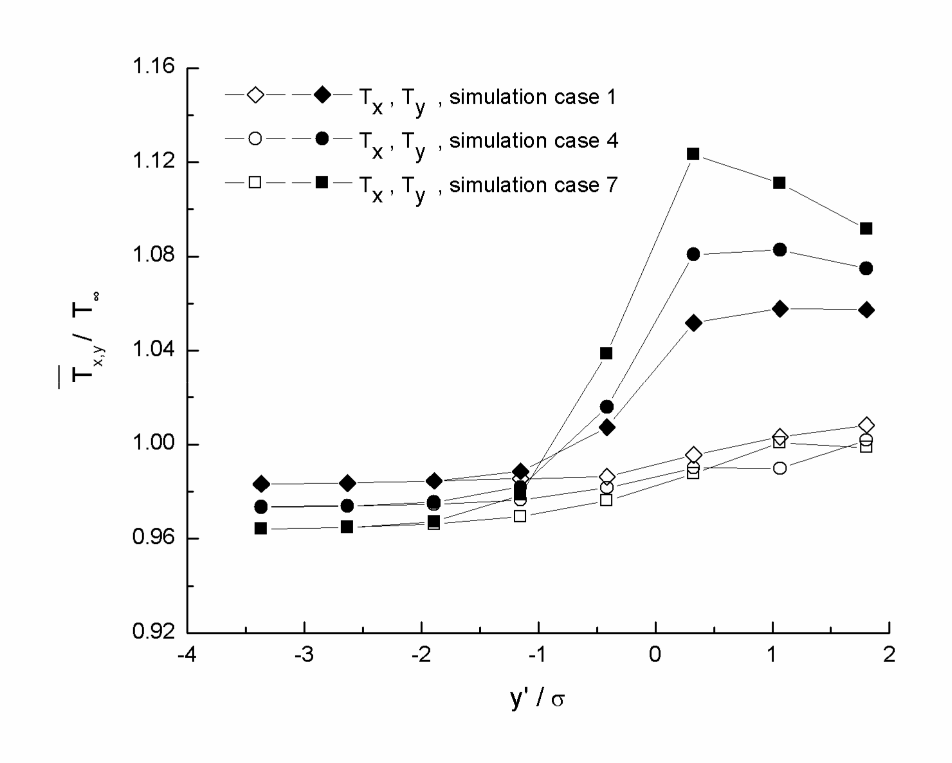

Fig. (4. 24) Quasi-steady, interphase nonequilibrium temperature, profiles.

The interphase number flux, $< J >$ and heat flux, $\overline{q}$, are presented in Fig. (4.25) and Fig. (4.26), respectively. The number flux is a molecular drift velocity that first increases in magnitude, beginning just above the vapor boundary, and then starts to decline in magnitude just below it, continually declining to its equilibrium value of near zero at the liquid boundary. zero.

Fig. (4.26) presents the heat flux across the interphase. Note that the coordinate convention requires heat flow from vapor to liquid to be negative. The magnitude of the heat flux in the interfacial region increases monotonically toward the liquid phase. In Fig. (4.26), heat fluxes for the highest tangential vapor flow simulation cases are also shown. Comparing them with the cases for non-tangential flow, shows that tangential flow in the vapor phase increases the magnitude of the heat flux in the region of the interphase, but only slightly.

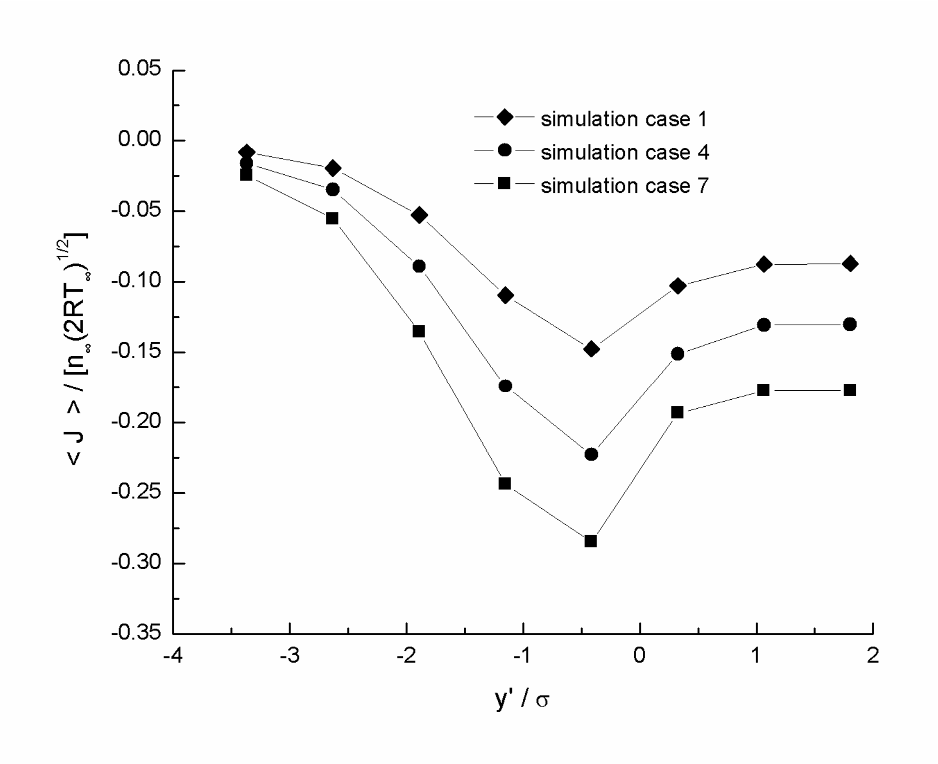

Fig. (4. 25) Quasi-steady interphase number flux profiles.

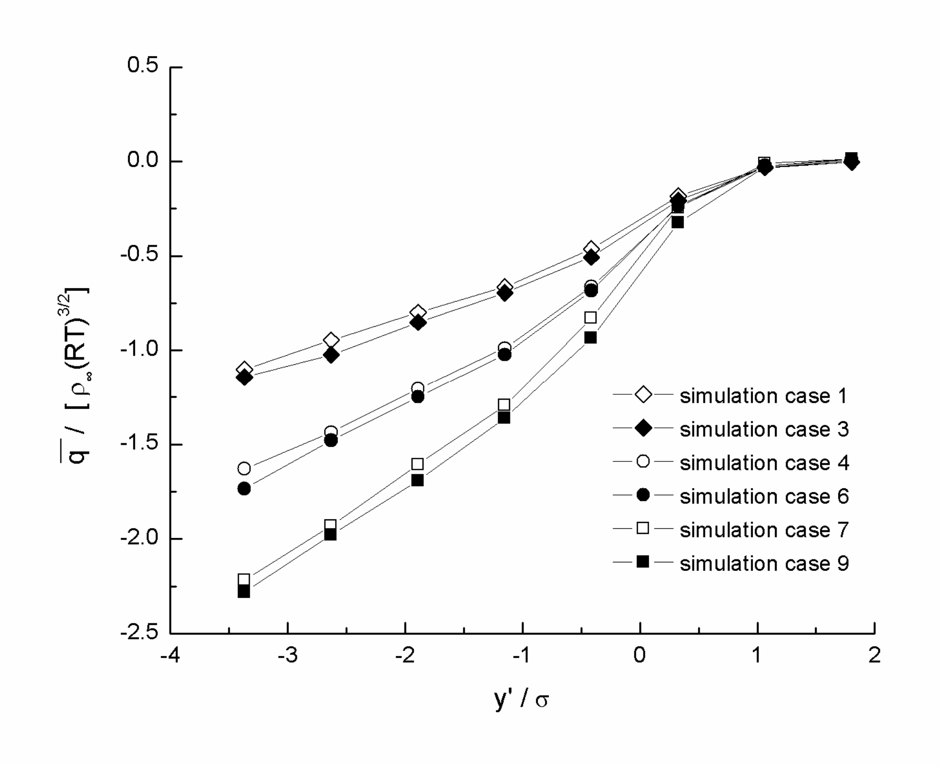

Fig. (4. 26) Quasi-steady interphase heat flux profiles.

4.5.5 Solid-Liquid Interphase

Fig. (4.27) shows, the temperature profiles in the liquid film, which were obtained by sampling the liquid phase molecules during the period between $1.8\times10^{4}\sqrt{m\sigma^{2}/\varepsilon}$ and $2.0\times10^{4}\sqrt{m\sigma^{2}/\varepsilon}$ for simulation cases 1, 4, and 7. The linear trending temperature profiles in the liquid reflect a thermal Fourier flow.

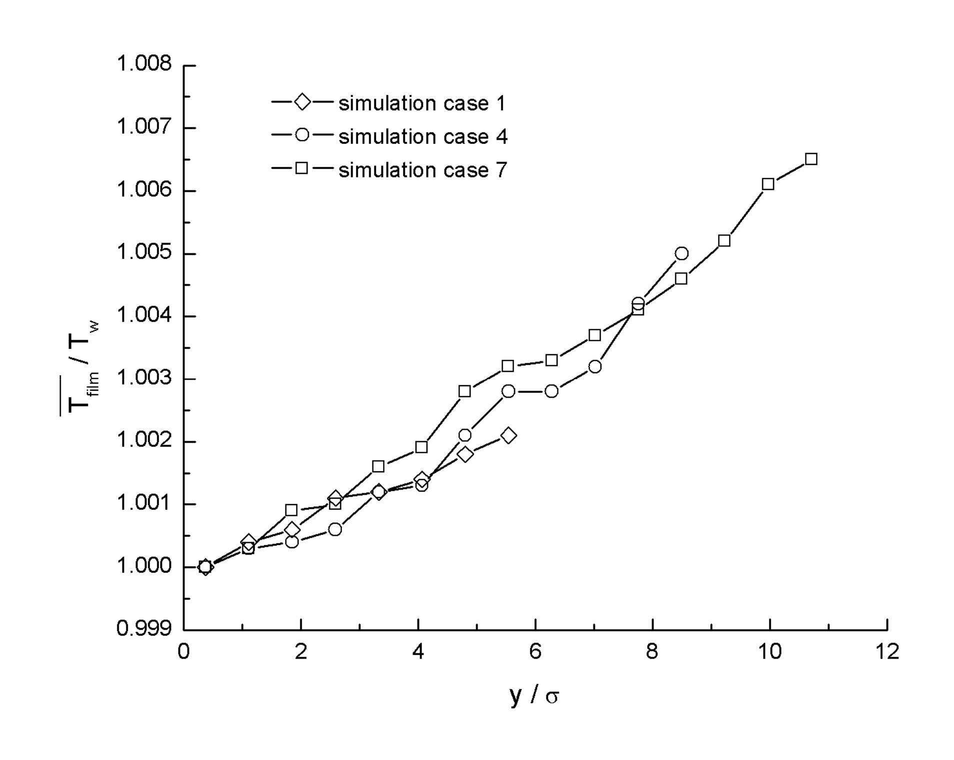

Fig. (4. 27) Quasi-steady liquid film temperature profiles.

The quasi-steady temperature slip at the solid wall, $\overline{\Delta T_w}$, is listed in Table 4.5, which indicates an increase in slip with a decrease in substrate temperature. The temperature discontinuity across the solid-liquid interface can be characterized by the interfacial thermal resistance or Kapitza resistance defined as

$$R_K = \frac{\Delta T_w}{q_w} \tag{4.16}$$

in which q_w is the heat flux at the interface on the liquid side. The computed R_K values from the simulations, which are listed in Table 4.5, increased with condensation strength.

Fig. (4.27) demonstrates that the heat transfer at the solid-liquid boundary approximately follows the Fourier law, $q_w = -\kappa \frac{\partial T}{\partial y}$, where κ is the thermal conductivity. The thermal resistance length or Kapitza length, L_K, is related to the temperature slip and liquid temperature gradient adjacent to the substrate through the relation

$$\Delta T_w = L_K \left.\frac{\partial T}{\partial y}\right|_{liquid} \tag{4.17}$$

where the temperature gradient is evaluated at the interface on the liquid side. $L_K = R_K \kappa$ is the length of the virtual region where the Fourier law extends to T_S, and can be estimated by numerically fitting the temperature profile inside the liquid film by a linear function (see Table 4.5.). The statistical error is within 10 percent.

Table 4. 5 Heat transfer quantities at the solid-liquid interphase.

Simulation case.	ΔT_w (K)	R_K ($10^{-7} WK^{-1}m^{-1}$)	L_K (σ)
1	−3.50	3.45	-163.49
2	−3.52	3.35	-150.82
3	−3.57	3.40	-144.44
4	−7.61	4.81	-218.33
5	−7.71	4.70	-236.40
6	−7.64	4.82	-216.20
7	−11.70	5.28	-242.47
8	−11.81	5.24	-264.87
9	−11.73	5.21	-264.16

L_K for a solid-liquid interface has been reported to be dependent on solid-liquid intermolecular stiffness ratio (squared), solid-liquid interaction strength, ε_{sl}, and substrate temperature [103,104]. In the present system, the first two terms are almost constant and so L_K should only be a function of the substrate temperature, T_S. Fig. (4.28) presents L_K as a function of T_S. For liquid argon, the dependency of L_K on T_S was reported to be linear

[104].This linear relationship is verified in the figure.

The large temperature slips and thermal resistance lengths in Table 4.5 can be attributed partly to the relatively large solid crystal to argon molecular mass ratio used for the simulations. The stiffness ratio in the present simulations is essentially controlled by this large molecular mass ratio, Therefore, the effect of its square on the magnitude of the thermal resistance length is quite large. In addition, the solid substrate was modeled with only two layers of solid molecules, which were controlled by the thermostat. It is difficult to thermalize fully the nearby liquid molecules by a small volume of temperature-controlled solid molecules because of insufficient solid-liquid interaction. This also leads to larger temperature slips and thermal resistance lengths [105].

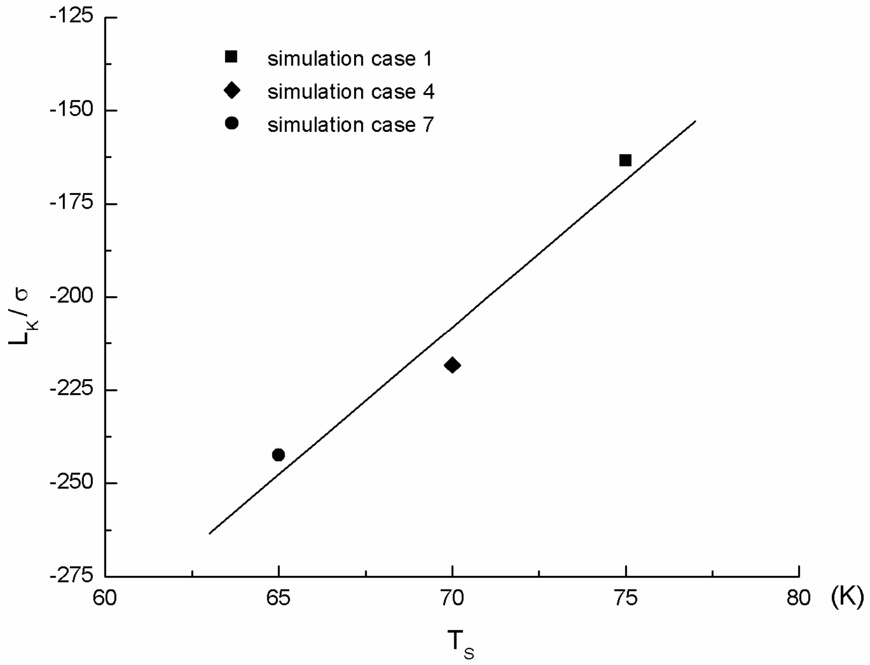

Fig. (4. 28) Thermal resistance length dependency on substrate temperature at quasi-steady state. (Solid line indicates the least squares fitting of data for simulation cases 1, 4, and 7.)

4.5.6 Computational Efficiency

The ideal hybrid algorithm should achieve load balance among each simulator processor. However, for the current system, the NEMD simulator overhead is substantially greater than that of the DSMC simulator in the case of a condensed phase present in the NEMD simulator domain. This effect on computational efficiency has been traced in the simulation life of the nonequilibrium condensation process in this chapter. In Fig. (4.29), the hybrid DSMC-NEMD simulation CPU time per time step divided by the pure NEMD CPU time per time step (i.e. $(\Delta\tau_{cpu}^{NEMD} + \Delta\tau_{cpu}^{DSMC}) / \Delta\tau_{cpu}^{Pure\ NEMD}$) is presented as a function of simulator molecule number count partition ratio (i.e. $N_{NEMD} / (N_{NEMD} + N_{DSMC})$). The CPU time ratio linearly increased with partition ratio (representing a decline in simulation efficiency) for a partition ratio less than 0.76. This linear dependence was reported in Chapter 2 for the pure vapor system. Thus, it can be concluded that the MD simulator domain is in the vapor state. But a sudden increase in the CPU ratio or reduction in efficiency occurred within the small partition ratio range from 0.76-0.78, which can be explained as due to a rapid increase in force evaluations in the MD simulator. This effect was caused by the phase transitions begun in the MD simulator at that point as the molecules began to condense. With further increases in the simulator ratio as more MD molecules condense, a linear relationship with CPU ratio resumes but at a lower slope as the CPU ratio approaches unity. Ultimately, with the increasing number of MD molecules condensing on the solid substrate, the DSMC simulator contributions to the hybrid scheme are greatly reduced and hybrid scheme efficiency is no better than that of the pure MD algorithm (i.e., $O(N_{MD})$) in the quasi-steady condensation state.

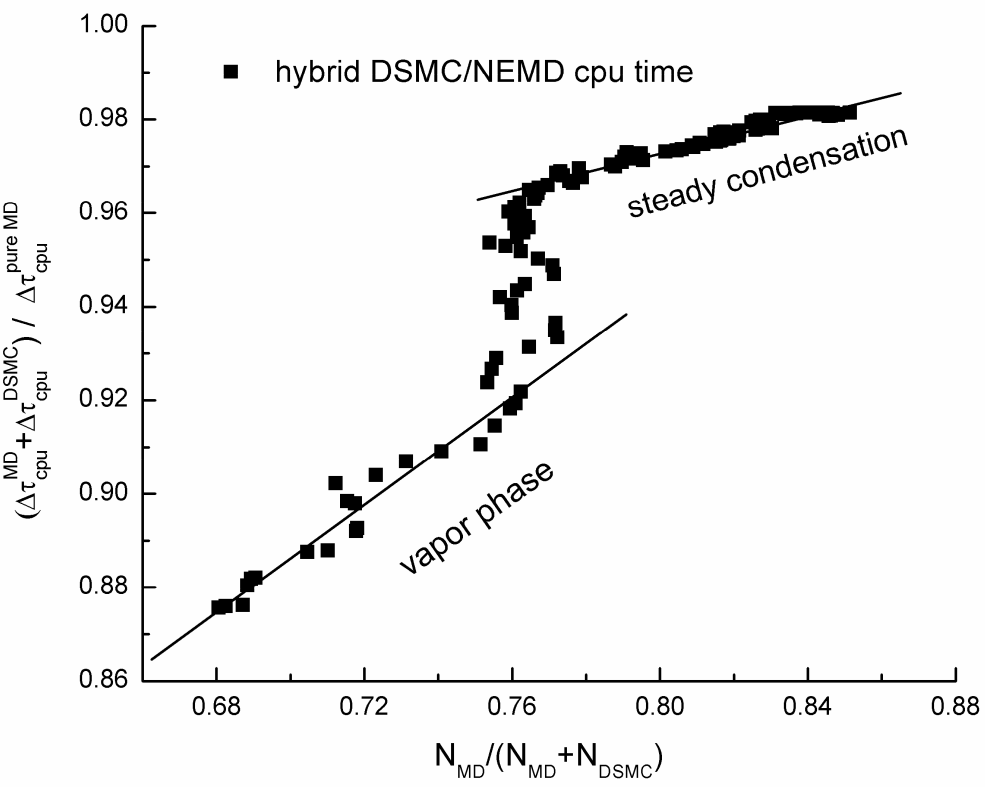

Fig. (4. 29) Hybrid to NEMD CPU time ratio vs. simulator molecule number partition ratio.

Chapter 5

Summary, Conclusions, and Future Work

5.1 Summary and Conclusions

The atomistic hybrid DSMC-NEMD simulation method and the interfacial definition procedure described in this dissertation show great promise as a versatile tool for investigating multiscale interfacial systems involving Knudsen layer gas flow over a surface with nanoscale interfacial interaction phenomena. It generally offers a distinct performance advantage over the use of NEMD alone for investigating such systems and does not depend on physically questionable artifices for its implementation. The generalized soft sphere DSMC collision model developed in conjunction with the hybrid method represents a significant advance in the selection of collision models available for use with DSMC.

The application of the hybrid method to study mesoscale molecular gas-solid interaction in a thermal driven Fourier system with different solid molecule masses, m_s, and gas-solid interaction parameters, ε_{sg}, illustrates the interesting results that can be obtained with the method. It was determined that solid to gas energy transfer increases with the wetting effect at the gas-solid interfaces. Furthermore, the smaller the solid mass, the more energy is transferred from solid to gas phase. The magnitude of both the normal and tangent accommodation coefficients follow the same trend as the energy transfer.

Applying the accommodation coefficients computed from the hybrid method in a pure DSMC simulation demonstrated an ability of the DSMC method to reproduce the same temperature slip near the wall as the hybrid. However, it was not able to capture the temperature and density variation closer to the gas-solid interface or the contribution to the heat flux from the surface energy transfer phenomena that were captured by the hybrid.

The liquid and vapor interphase region boundaries for molecular dynamics simulation of liquid-vapor systems can be accurately determined by counting neighboring molecules in the region and setting criteria based on their expected values for liquid or vapor. The new procedure developed herein can be extended to nonequilibrium systems and, in fact, the equilibrium results appear to show persistent periodic undulations in boundary locations that are likely due to the effects of thermal motion and/or capillary wave excitations. The interphase thicknesses determined from the new boundary criteria are more precise and larger by approximately a factor of two than the thicknesses computed using the well-known relation proposed by Rowlinson and Widom.

Two-dimensional radial distribution functions along the liquid and vapor boundaries are reflective of pure liquid and vapor, respectively, demonstrating the physical consistency of the new boundary criteria. However, the shapes of the radial distribution functions at the center of the interphase region are suggestive of the state of transition between the liquid phase and vapor phase.

Applying the new criteria for interphase boundaries to the MD computation of condensation and evaporation coefficients produces results that, away from the melting point, are in better agreement with transition state theory than previous results from MD simulations. This demonstrates the importance of correct boundary definition to the collection of molecular flux statistics for computation of evaporation and condensation coefficients.

Precise boundary definition allows the determination of the evaporative molecular flux without resorting to a separate simulation of condensed phase evaporation into a vacuum as in some previous studies. Near the melting point, transition theory approximations are less valid and the condensation/evaporation coefficients from the present results differ from the theory.

For simulations of vapor in equilibrium with a condensed phase film on a substrate, there is little effect of substrate wetting on evaporation/condensation coefficients at volume ratios above the melting temperature. However, if the film freezes, the coefficients obtained for non-wetting and partial-wetting substrates deviate significantly from those obtained for a fully wetting substrate.

The results in Chapter 4 demonstrate that the atomistic hybrid DSMC-NEMD method can efficiently resolve a typical unsteady nonequilibrium, multiphase interfacial system with disparate length scales. In the present work, nanoscale vapor condensation onto a cooled substrate with a bulk vapor flow parallel to the substrate was successfully simulated with interesting results. The method permitted simulating the system for an evolutionary time period that was sufficiently long for quasi-study conditions to develop. A new scheme, within the method, for identifying liquid and vapor interphase boundaries was successfully tested on the nonequilibrium phase change at the moving interface.

The structure of the Knudsen vapor layer from the hybrid simulation was compared with kinetic theory predictions from a modified moment method analysis and from pure DSMC simulation. In general, the agreement was good, demonstrating the utility of the kinetic methods. The pure DSMC results were more accurate. Some of the differences between the simulation results and the moment method results appeared to be due to the different molecular interaction models employed by the two approaches. The kinetic methods were not totally independent of the hybrid because they required information from the hybrid for their boundary conditions due to their inability to model the solid-liquid interaction and liquid-vapor molecular exchange.

The growth trend of the liquid film height with time became linear, while the thickness of the liquid-vapor interphase transition region remained constant. The density profile in the transition region was distorted from the equilibrium profile and the condensation and evaporation coefficients were higher than the equilibrium case, while the latent heat was lower.

The inverted temperature profile phenomenon was observed in the vapor adjacent to the interface with accompanying out-of-equilibrium kinetic temperatures in the directions normal and tangential to the interface. The state of superheat in the vapor leading to the inverted temperatures was verified.

Tangential flow velocity, which was of the same order as the condensation-induced vapor velocity, had no observable effect on most of the liquid-vapor interfacial properties. One notable exception was the heat flux at the vapor boundary with the interphase. Tangential velocity also had a small effect on the relationship between the condensation-induced vapor velocity and the liquid interfacial temperature. It was not a factor in condensation film growth or heat transfer to the substrate, a result that has important practical implications and is consistent with previous kinetic theory results for the Knudsen layer.

The tangential flow velocity profiles for the strongest condensation cases were displaced away from the upper boundary and compressed, suggesting that they were independent of the height of the upper boundary. This result is also consistent with previous kinetic results and, in the absence of a tangential pressure gradient, generalizes the present results to be independent of a specific bulk tangential velocity profile. The shear stress profiles are compatible with this interpretation and are a further indication of an Euler flow above the Knudsen layer. The slip velocities at the liquid surface were less than two percent of the tangential velocities at the upper boundary and increased with stronger condensation. The shear stress at the liquid-vapor boundary also increased with stronger condensation.

The major portion of the heat removed from the fluid at the cooled substrate was associated with the latent heat of condensation as opposed to the sensible heat and the flow energy and work converted to heat. Temperature slip, thermal resistance, and Kapitza length at the wall increased with the condensation strength, with the Kapitza length exhibiting the expected linear dependence on substrate temperature. Large Kapitza lengths were observed due to the molecular models used for the solid substrate.

5.2 Future Work

5.2.1 Hybrid Method Improvements

One area for future work is improvement in the DSMC-NEMD method descried in Chapter 2. In the hybrid algorithm, particles from the DSMC simulator bring unphysical statistical fluctuations to the NEMD simulator, causing some difficulties for overall reduction in fluctuations of sampled quantities through ensemble or steady-state averaging. A possible strategy to reduce the DSMC noise is to make use of the dead time in the DSMC processor after a DSMC time step, while the DSMC processor is waiting for the NEMD processor, with smaller time steps, to catch up. This would also improve load balance between DSMC and NEMD processors. A way of doing this is to employ a kind of micro ensemble averaging. This would involve replaying the DSMC collision calculation with different random number seeds to produce independent additional DSMC realizations of post-collision velocities and resulting particle displacements, i.e. phase space coordinates within the DSMC time step. The cell-sampled particle statistics for these micro ensembles would then be averaged to produce a cell micro sample used as the basis for the overall time or ensemble averaging process in place of a single sample for a cell at a time step. In addition, the phase space coordinates of the multiple DSMC realizations within a time step could be suitably sampled to statistically improve the set of particle locations and velocities used as input to the next DSMC collision time step.

In classic Direct Simulation Monte Carlo (DSMC), collision occurs on the basis of cells or subcells. The candidates for collision pairs are randomly selected in one cell or subcell. In other words, collisions never happen between nearby cells, even though two molecules are close to each other but in different cells or subcells. Such an unrealistic collision algorithm increases the statistical noise that is inherent in the stochastic DSMC algorithm.

Another way to take advantage of the waiting time in the DSMC simulator is to modify the collision routine of classic DSMC. The subcell was introduced to the original DSMC [6] with the benefit of reducing the collision separation distance. However, to enhance the realism of molecular interaction, the classic collision pair selection algorithm has been changed to a nearest-neighbor procedure, or so-called sophisticated DSMC [9,106-109]. Bird [107] suggests using the transient adaptive sub-cell (TASC) scheme. According to TASC, the cells are divided into sub-cells that exist only during the collision phase of each cell, and then the collision candidates are chosen from either the same or neighboring sub-cells. Thus, the collision separation reduces to a fraction of a cell width. With a fine enough sub-cell grid, the nearest molecules are generally chosen for collision.

This new algorithm has been tested by Gallis et al. [9], who reported that the discretization errors have been reduced with implementation of the nearest–neighbor collision procedure and the convergence efficiency of the method has been improved by a factor of 2. Moreover, the nearest-neighbor selection in DSMC would be an analogue to the molecular interaction law in molecular dynamics (MD).

Inspired by this sophisticated DSMC, a sub-cell based nearest-neighbor collision, similar to TASC, can be implemented in a probabilistic manner as follows. Unlike the TASC, the subcells are used to track molecules throughout the domain. If the one molecule, i, is randomly chosen from one subcell, its potential collision partner, j , will be selected in range of cell size with the minimum separation.

Based on the nearest-neighbor collision pair selection law, molecules in one cell can be allowed to collide with another one belonging to the nearby cells if they are the nearest neighbor. The nearest-neighbor selection replaced the random selection of collision partners with a deterministic selection scheme.

A problem with the selection is that, if either of the molecules in the preceding collision is chosen as collision candidate, the chance is that one of them could be selected again by the random procedure. And, therefore, the same pair will be again chosen since no molecular movement has yet taken place. It is therefore necessary to keep a record of the previous collision partner of each molecule and to choose the next closest molecule if the previous partner is chosen again.

TASC, which only generates subcells in a collision cell, minimizes the extra computational expenses of the nearest neighbor selection. But with the help of a subcell neighbor list and fine enough subcells that contain relatively few molecules, the additional computational cost of the suggested collision pair selection is reduced. For hybrid DSMC-NEMD simulations, the computational overhead is generally dominated by the NEMD simulator, thus, the suggested subcell based nearest-neighbor search scheme is practical since it simply utilizes the dead time in the DSMC simulator processor.

The above scheme was not tested in this work, but it is a possible approach to improving the current hybrid DSMC-NEMD algorithm. Moreover, by utilizing nearest neighbor schemes or other DSMC versions in the DSMC simulator, such as CBA [110], Enskog MC [111] and IP-DSMC [112], the performance of the current hybrid technique can be improved for study of more complex systems.

5.2.2 Complex Molecules

Another area of future work is in modeling and simulation of systems with more complex molecules than monatomic argon with the DSMC-NEMD hybrid. Key aspects of the methodology for applying NEMD simulation to complex molecules were described in Chapter 1. The DSMC molecular models developed for the hybrid can be modified to accommodate polyatomic and polyatomic polar molecules of common substances by incorporating new MGSS collision models based on Stockmayer potential functions for them. These modifications can also include interactions between gas and liquid molecules of different substances. An additional modification required will be the implementation of a model for translational/rotational energy exchange into the DSMC simulator and developing a scheme for transferring rotational energy across the DSMC-NEMD method interface.

5.2.3 Other Multiphase Interfacial Systems

As outlined in Chapter 1, the basic approach described herein can be applied to a number of different physical interfacial systems and parametric variations of them. For example, the problem of evaporation of liquid films as opposed to condensation could be studied.

One particularly interesting class of problems that would be an immediate priority for future application of the method would be to condensation and evaporation of nanodroplets and particle-laden nanodroplets on solid substrates. Dropwise condensation simulations would examine heterogeneous nucleation, droplet coalescence, and droplet growth. The bulk flow gases that could be considered include the vapor of the condensed state, noncondensable gas, and mixtures of both species.

This research would be important because advances in size reduction of sub-micron droplets formed by dispensed material in microfabrication and microfluidic lab applications will allow them shortly to reach true nanoscale dimensions. However, there are questions as to the results of size reduction to nanoscale on capillary, Marangoni, and viscous effects; the influence of external forced convection from process or drying gas; and the influence of nanoscale surface effects on deposition patterns from droplet evaporation.

Appendix A:

Direct Simulation Monte Carlo Algorithm

Direct Simulation Monte Carlo (DSMC), a tool to circumvent the difficulties in solving the Boltzmann Transport Equation (BTE), was proposed by Graeme A. Bird in 1963 and described in his classic monograph [6]. DSMC is a direct particle simulation method for high Knudsen number flows based on kinetic theory. The fundamental idea is the tracking of a large number of statistically representative particles, in some ratio to the greater actual number of molecules, based on physical understanding of the particle movement and interactions. Particles' positions (r) and velocities (c) are changed during simulation procedure. Over the years, the method, which was developed initially as an efficient means of atomistic modeling for high-speed gas flow, was later proven to be a solution of the Boltzmann Equation. [113].

The traditional DSMC method follows a dilute gas assumption, which requires that the intermolecular spacing δ is larger than the effective diameter d of the molecule. It is assumed that the numbers of collisions involving more than two particles are extremely insignificant, which leads to the binary collision model applied in the DSMC scheme.

For computational realization, the basic algorithm of DSMC is listed by several steps as follows:

1. In each computational cell, representative molecules are initialized with uniformly random spatial distributions and velocities based on the equilibrium Maxwellian distribution, and specification of macroscopic density, temperature, and mean velocity of the system as

initial conditions.

2. New particles are inserted at open boundaries. The velocities are sampled based on some kinetic boundary condition specified. The positions are randomly distributed at the boundary. For the case of wall boundary, where no molecules can cross over, two type of wall boundaries are generally used, a specular wall or a thermal wall. Particles, hitting on the wall, may be specularly reflected or reflected diffusely, thermalized by the wall temperature. The number flux from an open stream boundary can be obtained from a kinetic theory prediction [6] or by setting up a molecular reservoir next to the stream boundary [114].

3. Molecules move ($\mathbf{r}^{(\tau+\Delta\tau)} = \mathbf{r}^{(\tau)} + \Delta\tau \cdot \mathbf{c}$) in one time step without collision with each other. $\Delta\tau$ is the DSMC time step, which usually is required to be smaller than the mean collision time.

4. Molecules are indexed in computational cells and subcells. Traditionally, the computational cell size should be restricted to be smaller than $\lambda/3$. Colliding particles are restricted to the same cell. The number of candidate collision pairs from each cell is determined as

$$N_c = \frac{N < N > F_N (\sigma_T c_r)_{\max} \Delta\tau}{2V_{cell}} \tag{A.1}$$

where N_c the number of collision pairs in one cell is, N is the number of molecules in the cell, $< N >$ is the average number of molecules in the cell, F_N is the number of real molecules represented by the simulated one. $(\sigma_T c_r)_{\max}$ is the maximum value of the product of cross section and relative velocities and V_{cell} is the cell volume. Using subcells increases the likelihood of collision pairs being near neighbors. Collision is evaluated with the probability, $\sigma_T c_r / (\sigma_T c_r)_{\max}$, if one random number is smaller than the probability (i.e.

$R_f < \sigma_T c_r / (\sigma_T c_r)_{\max}$), the collision is accepted and the post-collision velocities are calculated, for example from an elastic collision model, in the following form,

$$\mathbf{c}_\mathbf{r}^* = \begin{Bmatrix} c_r \cos\chi \\ c_r \sin\chi \cos\theta \\ c_r \sin\chi \sin\theta \end{Bmatrix} \tag{A.2}$$

where $\mathbf{c}_\mathbf{r}$ and $\mathbf{c}_\mathbf{r}^*$ are pre and post collision relative velocity whose magnitudes (c_r and c_r^*) are identical. χ and θ, which are the deflection angle and collision referent plane angle, are selected randomly based on collision scatter probabilistic.

5. Macroscopic quantities are sampled in each cell at the end of each time step. The formulations for the various macroscopic quantities in terms of discrete microscopic quantities are presented in Table A.1 [6].

Table A. 1 DSMC physical quantities sampling

Quantity	Sampling formula
Number Density	$n = F_N N / V_c$
Density	$\rho = mn = mF_N N / V_c$
Stream Velocity in α direction	$c_{o'\alpha} = \overline{c_{i'\alpha}} = \sum_{i}^{N} c_{i'\alpha} / N$
Thermal or "Peculiar" Velocity in α direction	$c'_{i,\alpha} = c_{i'\alpha} - c_{o'\alpha}$
Translational Temperature	$3RT / 2 = \overline{c_i'^2} / 2 = \overline{c_i^2} - c_0^2$
Pressure Tensor	$\Pi_{\alpha\beta} = nm\overline{c'_{i,\alpha} c'_{i,\beta}} = \rho(\overline{c_{i,\alpha} c_{i,\beta}} - c_0^2) / 2$
Heat Flux (ε_{int} is the non-translational Energy related with internal degrees of freedom)	$q_\alpha = \frac{1}{2} nm\overline{c_i'^2 c'_{i,\alpha}} + n\overline{E_{\text{int}} c'_{i,\alpha}}$ $= \frac{1}{2}[\rho(\overline{c_i^2 c_\alpha} - \overline{c_i^2} c_{o'\alpha})] + n(\overline{E_{\text{int}} c_{i'\alpha}} - \overline{E_{\text{int}}} c_{o'\alpha})$

Simulation steps are listed in Fig. (A.1) in form of a flowchart.

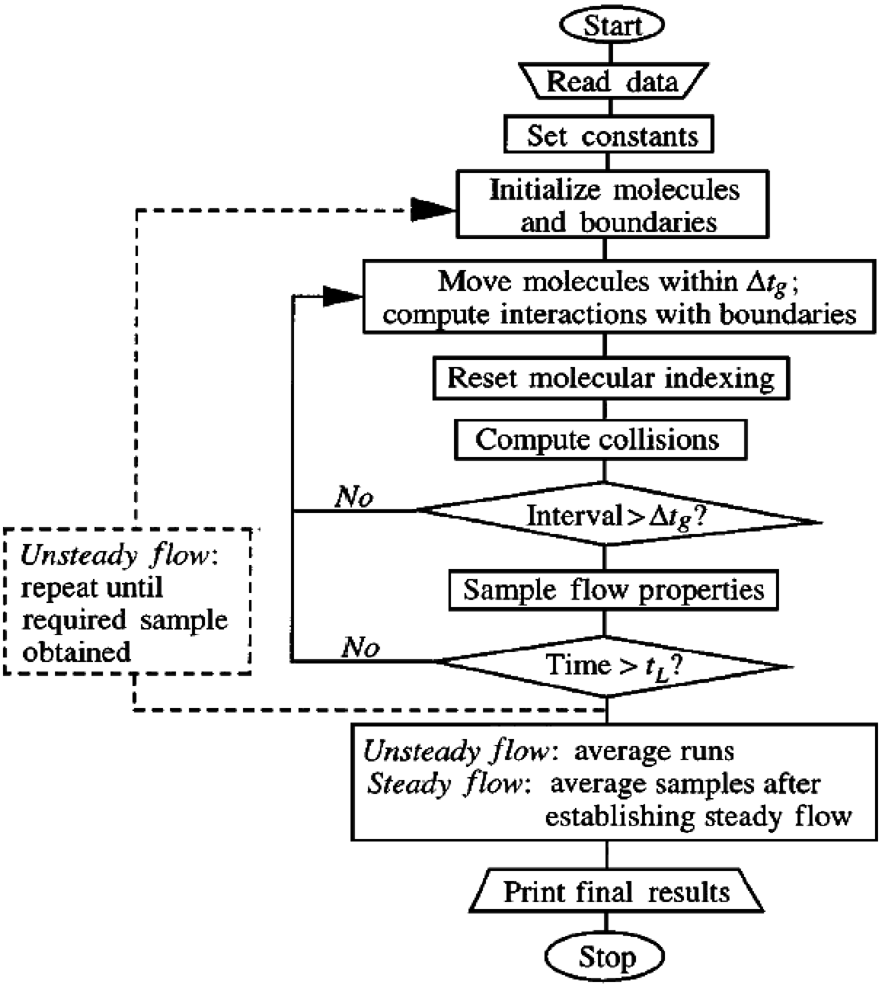

Fig. (A. 1) Flowchart of DSMC steps [48]

Appendix B:

Molecular Dynamics Algorithm

Molecular Dynamics (MD), introduced by Alder and Wainwright [50], is a form of computer simulation in which atoms and molecules are allowed to interact with each other by approximations of a known interaction law. Unlike direct simulation Monte Carlo (DSMC), MD molecules' interactions are deterministic. The molecules' trajectories are obtained by integrating a motion equation, Newton's second law. For the translational motion of a spherically symmetric molecule, it has the form of

$$\mathbf{F}_i = m_i \frac{d^2\mathbf{r}_i}{d\tau^2} \tag{B.1}$$

where $\mathbf{F}_i$ is the sum of the forces exerted on the *i*-th molecule by the other molecules in the system; $\mathbf{r}_i$ is the position vector of the *i*-th molecule, t is time, and m is the mass of the molecule. To calculate the interaction forces among molecules, it is necessary to have an appropriate corresponding intermolecular potential model. This model usually is determined by experiment or quantum mechanics. One of the simplest and most popular forms of two-body potential is the Lennard-Jones (L-J) potential, which is used throughout this work. The L-J (12-6) potential can be expressed as

$$V^{LJ}(r_{ij}) = 4\varepsilon[(\frac{\sigma}{r_{ij}})^{12} - (\frac{\sigma}{r_{ij}})^{6}] \tag{B.2}$$

With the deterministic potential function, the interaction force between a pair of molecules is obtained from,

$$\mathbf{F}_{ij} = -\nabla V^{LJ}(r_{ij}) \tag{B.3}$$

where $\mathbf{F}_{ij}$ is the force acting on the *i*-th molecule by the *j*-th molecule. So the total force exerted on the *i*-th molecule can be calculated by summing over the entire field of particles around this molecule as

$$\mathbf{F}_i = \sum_{j \neq i} \mathbf{F}_{ij} = -\nabla \sum_{j \neq i} V^{LJ}(r_{ij}) \tag{B.4}$$

In a system of N atoms, the double summation in Eq.(B.4) accumulates $1/2N(N-1)$ unique pair interactions, but one can achieve a considerable savings in computer time by neglecting pair interactions beyond some distance r_c. The cutoff potential can be expressed in following form,

$$V^{LJ}(r_{ij}) = \begin{cases} 4\varepsilon[(\frac{\sigma}{r_{ij}})^{12} - \varepsilon_{sg}(\frac{\sigma}{r_{ij}})^{6}] - V^{LJ}{}_{c} & r \leq r_c \\ 0 & r > r_c \end{cases} \tag{B.5}$$

where r_c is usually taken as 2.5σ in many simulations. To avoid the discontinuity at r_c that affects both the energy conservation and the atomic motion, it can be corrected by changing the form of the Eq. (B.2) slightly. The potential function (Eq. (B.2)) can be modified to eliminate the discontinuity in both potential and force evaluation by replacing Eq. (B.2) with

$$V^{LJ}(r_{ij}) = V^{LJ}(r_{ij}) - V^{LJ}(r_c) - \left.\frac{V^{LJ}(r_c)}{dr_{ij}}\right|_{r=r_c}(r_{ij} - r_c) \tag{B.6}$$

or compared with Eq. (B.5),

$$V^{LJ}{}_{c} = V^{LJ}(r_c) + \left.\frac{V^{LJ}(r_c)}{dr_{ij}}\right|_{r=r_c}(r_{ij} - r_c) \tag{B.7}$$

Finally the governing equation for the motion of the *i*-th molecular can be obtained as a second-order ordinary differential equation (ODE) in the form of

$$\mathbf{F}_i = m_i \frac{d^2\mathbf{r}_i}{d\tau^2} = -\nabla \sum_{j \neq i} V^{LJ}(r_{ij}) \tag{B.8}$$

Eq. (B.8) can be solved numerically by the finite-difference method.

The 5th order Predictor-Corrector method is chosen and implemented in this work. The predictor step can be expressed as

$$\mathbf{r}_0^p(\tau+\Delta\tau)=\mathbf{r}_0(\tau)+\mathbf{r}_1(\tau)+\mathbf{r}_2(\tau)+\mathbf{r}_3(\tau)+\mathbf{r}_4(\tau)+\mathbf{r}_5(\tau) \tag{B.9.a}$$

$$\mathbf{r}_1^p(\tau+\Delta\tau)=\mathbf{r}_1(\tau)+2\mathbf{r}_2(\tau)+3\mathbf{r}_3(\tau)+4\mathbf{r}_4(\tau)+5\mathbf{r}_5(\tau) \tag{B.9.b}$$

$$\mathbf{r}_2^p(\tau+\Delta\tau)=\mathbf{r}_2(\tau)+4\mathbf{r}_3(\tau)+6\mathbf{r}_4(\tau)+10\mathbf{r}_5(\tau) \tag{B.9.c}$$

$$\mathbf{r}_3^p(\tau+\Delta\tau)=\mathbf{r}_3(\tau)+4\mathbf{r}_4(\tau)+10\mathbf{r}_5(\tau) \tag{B.9.d}$$

$$\mathbf{r}_4^p(\tau+\Delta\tau)=\mathbf{r}_4(\tau)+5\mathbf{r}_5(\tau) \tag{B.9.e}$$

where $\mathbf{r}_0(\tau)=\mathbf{r}(\tau)$, $\mathbf{r}_1(\tau)=\Delta\tau\frac{\partial\mathbf{r}(\tau)}{\partial\tau}$, $\mathbf{r}_2(\tau)=\frac{\Delta\tau^2}{2}\frac{\partial^2\mathbf{r}(\tau)}{\partial\tau^2}$, $\mathbf{r}_3(\tau)=\frac{\Delta\tau^3}{3!}\frac{\partial^3\mathbf{r}(\tau)}{\partial\tau^3}$, $\mathbf{r}_4(\tau)=\frac{\Delta\tau^4}{4!}\frac{\partial^4\mathbf{r}(\tau)}{\partial\tau^4}$ and $\mathbf{r}_5(\tau)=\frac{\Delta\tau^5}{5!}\frac{\partial^5\mathbf{r}(\tau)}{\partial\tau^5}$. During the corrector step, a corrected value δ_2, which is related to acceleration, is calculated as

$$\boldsymbol{\delta}_2=\mathbf{r}_2^p(\tau+\Delta\tau)-\frac{1}{2}\frac{\mathbf{F}_i(\tau)}{m_i}\Delta\tau^2 \tag{B.10}$$

Where $\mathbf{r}_2^p$ has already been obtained from the predictor step. Finally, the predictions are corrected as:

$$\mathbf{r}_i^c(\tau+\Delta\tau)=\mathbf{r}_i^p(\tau+\Delta\tau)-\boldsymbol{\delta}_2 f_{i,2} \tag{B.11}$$

where $i=0,1,2,3,4,5$ and $f_{i,2}$ are some constants derived from Taylor expansion as $f_{0,2}=3/16$, $f_{1,2}=251/360$, $f_{2,2}=0$, $f_{3,2}=11/18$, $f_{4,2}=1/6$, $f_{5,2}=1/60$.

It will be expensive and wasteful to evaluate all of them in the whole system with the consideration of computational expenses. With the introduction of cutoff distance (r_c), a small fraction of the particles examined lies within interaction range. A neighbor list of each particle is generated within the range of

$$r_{list} = r_c + \Delta r \tag{B.12}$$

The list of neighbors remains valid over a number of time steps due to the slow changing of the microscopic world. Thus the list is usually updated after several time steps, typically 10-20, in MD simulation (See Fig. (B.1))

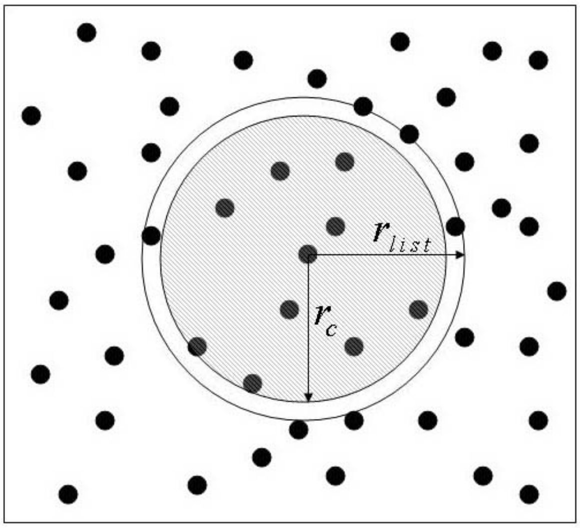

Fig. (B. 1) neighbor list computing interaction

A realistic wall boundary is employed through tethering the large mass molecules on a fixed site through spring connections. A FCC structure solid wall is formed by crystal layers of harmonic molecules as illustrated in Fig. (B.2). The velocity scaling method [11], which is used to achieve the initial condition of thermal equilibrium, is applied to control the solid wall temperature. The velocities of each solid wall molecule are rescaled in at each time step by multiplying by the factor of $\sqrt{(3k_B T_w / m\overline{\mathbf{c}_w^{'2}})}$, where T_w is the desired the wall temperature, and $\mathbf{c}_w^{'}$ is the thermal velocity of the wall particles. Throughout this dissertation, where a solid wall boundary is involved, the velocity scaling method is used to maintain and vary the desired temperature of solid phase.

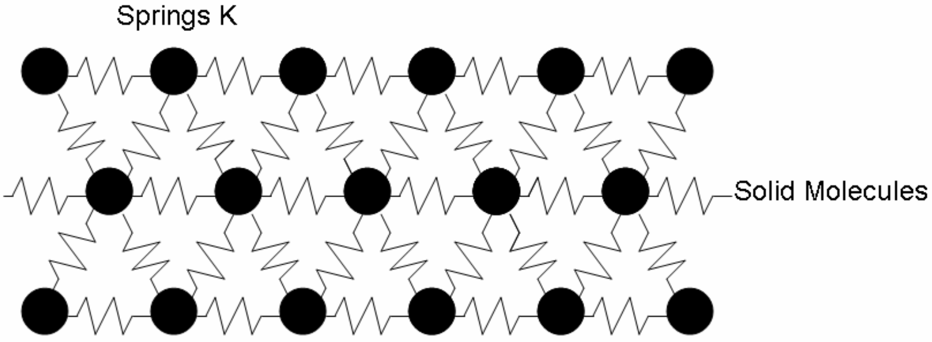

Fig. (B. 2) One layer FCC solid molecules in a 2-D view

Like direct simulation Monte Carlo (DSMC), mean quantities are obtained by collecting the molecules' degrees of freedom in the whole system for equilibrium simulations or dividing the system into spatial bins for nonequilibrium systems. The sampling method, which is similar to that in DSMC, has been listed in Table B.1. In this table, $F_{ij,\alpha}$ is the interaction force between molecule i and molecule j in the α direction; $r_{ij,\beta}$ is the interaction vector in β direction; E_i^{pot} is the potential energy of particle i.

Table B. 1 MD physical quantities sampling formula

Number Density (V_{cell} is bin's volume. N is the molecule number in bins)	$n = N / V_{cell}$
Density	$\rho = mn = mN / V_c$
Stream Velocity in α direction	$c_{o'\alpha} = \overline{c_{i'\alpha}} = \sum_{i}^{N} c_{i'\alpha} / N$
Thermal or "Peculiar" Velocity in α direction	$c'_{i,\alpha} = c_{i'\alpha} - c_{o'\alpha}$
Temperature	$3\frac{k_B}{m} T / 2 = \overline{c_i'^2} / 2 = \overline{c_i^2} - c_0^2$
Pressure Tensor	$\Pi_{\alpha\beta} = \frac{1}{V}(m\sum_{i=1}^{N} c'_{i,\alpha} c'_{i,\beta} + \sum_{i<j} F_{ij,\alpha} r_{ij,\beta})$
Heat Flux	$q_\alpha =$ $\frac{1}{V_c}[\sum_{i=1}^{N} c'_{i,\alpha}(\frac{1}{2} m c_i'^2 + E_i^{pot}) + \frac{1}{2}\sum_{i,j}^{N} (\mathbf{F}_{ij} . \mathbf{c}'_i)\ r_{ij,\alpha}]$

Compared with Table A.1 in Appendix A, density, velocity and translational temperature are identical to DSMC sampling formula, while pressure tensor and heat flux are different with one additional term, which is generally considered as the interaction effect. The interaction term or so-called virial term reflects the different context of these two methodologies.

In conclusion, the classic molecular dynamics steps follow as

1. Assign initial positions and velocities to each molecule.
2. Evaluate the neighbor list of each particle.
3. Compute force on each particle. (i.e. Eq.(B.4)-(B.8)).
4. Solve Newton's equation of motion. (i.e. Eq.(B.9) through Eq. (B.10)).

5. Update the molecules' positions and velocities.

6. Apply interaction with periodic boundaries.

7. Sample the properties.

8. Go back to step 2 until reaching the simulation time limit.

The details are shown in the flowchart in Fig. (B.3)

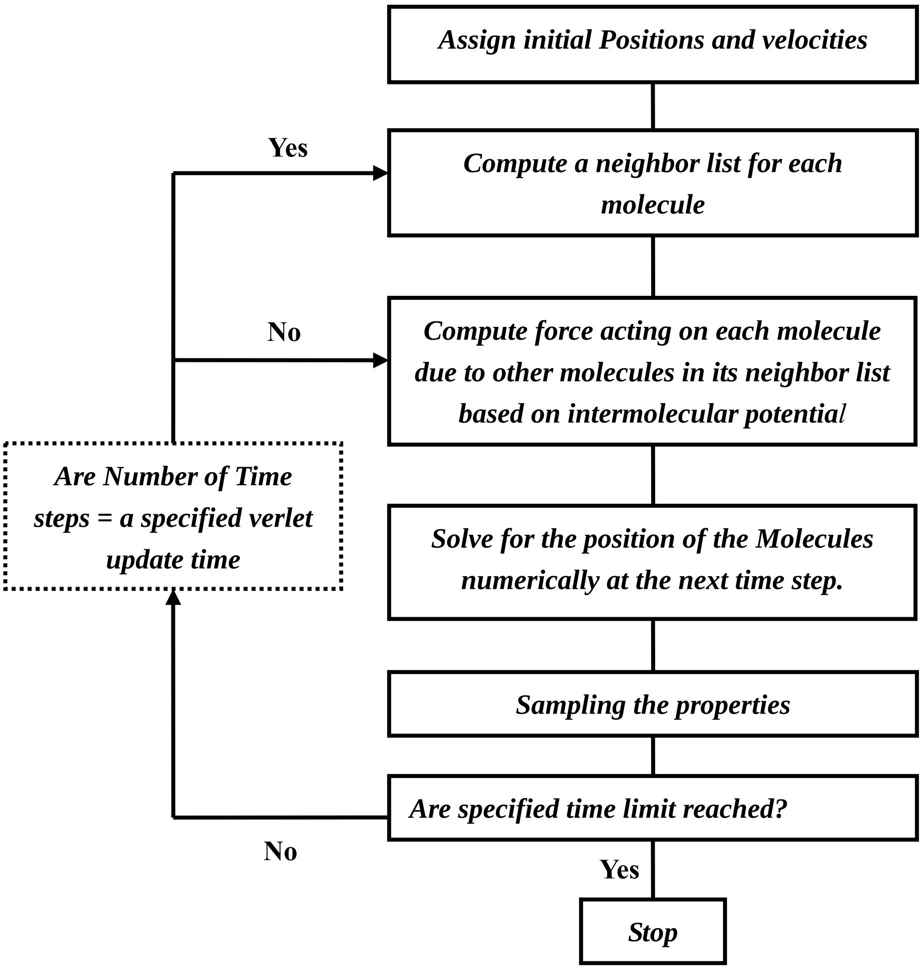

Fig. (B. 3) flowchart of MD steps

Appendix C:

Formulas for Distribution Function Moment Integrals

Sampling in probability space or deriving the moment method leads to using a class of integrals of the form

$$\int_a^{\infty} c^n \exp(-\beta^2 c^2) dc \tag{C.1}$$

where β is a constant. These integrals were systematically presented by Bird [6]. Because some of the mathematical formulas derived in this work (i.e. MGSS model in Chapter 2 and moment method in Appendix D) involved the evaluation of Eq. (C.1), the formulas for this class of integrals are repeated here for convenient reference.

For *a=0,* Eq.(C.1) can be derived to

$$\int_0^{\infty} c^{2n} \exp(-\beta^2 c^2) dc = \frac{(2n-1)(2n-3)...1}{2^{n+1}\beta^{2n+1}} \tag{C.2a}$$

$$\int_0^{\infty} c^{2n+1} \exp(-\beta^2 c^2) dc = \frac{n!}{2\beta^{2n+2}} \tag{C.2b}$$

where $n = 1,2,3...$

For $a \neq 0$, Eq. (C.1) becomes

$$\begin{aligned}\int_{\pm a}^{\infty} c^{2n} \exp(-\beta^2 c^2) dc &= \frac{(2n-1)(2n-3)...1}{2^{n+1}\beta^{2n+1}} \pi^{1/2} \{1 \mp erf(\beta a)\} \\ &\pm \frac{\beta a \exp(-\beta^2 a^2)}{\beta^{2n+1}} \sum_{m=1}^{n} \left\{ \frac{1}{2^m} \frac{(2n-1)(2n-3)...1}{[2(n+1-m)-1][2(n+1-m)-3]...1} (\beta a)^{2(n-m)} \right\}\end{aligned} \tag{C.3a}$$

$$\int_{\pm a}^{\infty} c^{2n+1} \exp(-\beta^2 c^2) dc = \frac{\exp(-\beta^2 a^2)}{2\beta^{2n+2}} \sum_{m=1}^{n+1} \left[\frac{n!}{(n+1-m)!} (\beta a)^{2(n+1-m)} \right] \tag{C.3b}$$

in which *erf(.)* is the error function.

For the more complex integrals of the form

$$\int_{-\infty}^{\infty}\int_{-\infty}^{\infty} c_r^{\,n} \exp(-\beta_1^2 c_1^2 - \beta_2^2 c_2^2) d\mathbf{c}_1 d\mathbf{c}_2 \tag{C.4}$$

where $\mathbf{c}_r = \mathbf{c}_1 - \mathbf{c}_2$, can be simplified to

$$\begin{aligned}&\int_{-\infty}^{\infty}\int_{-\infty}^{\infty} c_r^{\,n} \exp(-\beta_1^2 c_1^2 - \beta_2^2 c_2^2) d\mathbf{c}_1 d\mathbf{c}_2 \\ &= 16\pi^2 \int_0^{\infty} c_m^{\,2} \exp[-(\beta_1^2 + \beta_2^2) c_m^{\,2}] dc_m \times \int_0^{\infty} c_r^{\,n+2} \exp\{-[\beta_1^2 \beta_2^2 / (\beta_1^2 + \beta_2^2)] c_r^{\,2}\} dc_r\end{aligned} \tag{C.5}$$

where $\mathbf{c}_m = \dfrac{\beta_1}{\beta_1 + \beta_2}\mathbf{c}_1 + \dfrac{\beta_2}{\beta_1 + \beta_2}\mathbf{c}_2$. Two terms on RHS of Eq. (C.5) can be evaluated by Eq. (C.2) and (C.3).

Appendix D:

The Modified Ytrehus Moment Method

The kinetic theory approach to describe vapor flow evaporating from or condensing to a liquid surface was systematically introduced by Ytrehus [5]. The present development adds the tangential flow effects into this model for comparisons with the hybrid DSMC-NEMD results.

The four-mode model used for the distribution function, f, describing the condensing vapor above the liquid surface with an asymptotic upper flow condition (i.e. $\boldsymbol{u}_\infty = (U_\infty, V_\infty, 0)$) is of the form

$$f(y,\mathbf{c}) = a_e^+(y) f_e^+(\mathbf{c}) + a_\infty^+(y) f_\infty^+(\mathbf{c}) + a_\infty^-(y) f_\infty^-(\mathbf{c}) + a_*^-(y) f_*^-(\mathbf{c}) \tag{D.1}$$

where

$$f_e^+(\boldsymbol{c}) = f_e(y=0, c_y > 0) = \frac{n_e}{(2\pi R T_L)^{3/2}} \exp(-\frac{|\boldsymbol{c}|^2}{2RT_L}) \tag{D.2.a}$$

$$f_\infty^+(\boldsymbol{c}) = f_\infty(y \to \infty, c_y > 0) = \frac{n_\infty}{(2\pi R T_\infty)^{3/2}} \exp(-\frac{|\boldsymbol{c} - \boldsymbol{u}_\infty|^2}{2RT_\infty}) \tag{D.2.b}$$

$$f_\infty^-(\boldsymbol{c}) = f_\infty(y \to \infty, c_y < 0) = \frac{n_\infty}{(2\pi R T_\infty)^{3/2}} \exp(-\frac{|\boldsymbol{c} - \boldsymbol{u}_\infty|^2}{2RT_\infty}) \tag{D.2.c}$$

$$f_*^-(\boldsymbol{c}) = f_*(c_y < 0) = \frac{n_*}{(2\pi R T_*)^{3/2}} \exp(-\frac{|\boldsymbol{c} - \boldsymbol{u}_*|^2}{2RT_\infty}) \tag{D.2.d}$$

The distribution function has been split in to four components, which represent the effects from the upper vapor boundary and liquid surface. Especially, Eq. (D.2.d) has been added to comply with the additional degree of freedom in the problem that is implied by the upstream nature of the external flow. It reflects the first collisions among the evaporated molecules, according to the BGK collision model with the fixed parameters, $n_* = \frac{n_e}{2}$, $T_* = T_L(1-\frac{2}{3\pi})$, $\boldsymbol{u}_* = (0,\sqrt{\frac{2RT_L}{\pi}},0)$. The space dependent amplitude functions (a_e^+, a_∞^+, a_∞^-, a_*^-) must satisfy the boundary conditions for unity evaporation/condensation coefficient:

$$y=0: \quad \begin{array}{l} a_e^+ = 1 \\ a_\infty^+ = 0 \\ a_\infty^- = \beta \\ a_*^- = \alpha \end{array} \qquad \text{and} \qquad y \to \infty: \quad \begin{array}{l} a_e^+ = 0 \\ a_\infty^+ = 1 \\ a_\infty^- = 1 \\ a_*^- = 0 \end{array} \tag{D.3}$$

From the above boundary condition, it is noticed that, at the liquid surface,

$$f(0,\mathbf{c}) = f_e^+(\mathbf{c}) + \beta f_\infty^-(\mathbf{c}) + \alpha f_*^-(\mathbf{c}) \tag{D.4}$$

where the last two terms represent the incident stream of molecules and two parameters (α and β) can be ascribed to the collision effects in the vicinity of the interface.

The upstream boundary has an uniform velocity field $\mathbf{u}_\infty = (U_\infty, V_\infty, 0)$, as indicated in distribution function Eq. (D.2.b) and Eq. (D.2.c).

Multiplying the molecular function, $\psi = (m, mc_y + mc_x, m\mathbf{c}^2, mc_y^2)$ by the velocity distribution function and integrating over velocity space, yields four moment equations as

$$\frac{\partial}{\partial y}\int c_y \psi_\mu f d\mathbf{c} = 0 \qquad \mu = 1,2,3 \tag{D.5.a}$$

$$\frac{\partial}{\partial y}\int c_y \psi_\mu f d\mathbf{c} = \Delta Q[mc_y^2] \qquad \mu = 4 \tag{D.5.b}$$

Because the first three items ($\mu = 1,2,3$) are collision invariants, they do not contribute to the collision integral on the RHS of the Boltzmann equation. However, the fourth equation has been determined by the non-unique choice $\psi_4 = mc_y^2$ for the non-conserved moment. Ytrehus used the inverse fifth-power repulsive interaction force, the so-called Maxwell molecule to evaluation the collision integral on the RHS of Eq. (D.5.b) and gave the expression as

$$\Delta Q[mc_y^2] = \frac{\pi}{\lambda_e}\sqrt{\frac{RT_L}{2\pi}}\frac{\rho}{\rho_e}\tau'_{yy} \tag{D.6}$$

where λ_e is the reference mean free path, and

$$\tau'_{yy} = -m\int (c_y - V)^2 f d\mathbf{c} + \frac{m}{3}\int (\mathbf{c}-\mathbf{U})^2 f d\mathbf{c} \tag{D.7}$$

is the viscous stress component.

By applying the standard integrals listed in Appendix C, the first three moment equations become the mass, momentum and energy conservation equations:

$$\rho_e\sqrt{\frac{RT_L}{2\pi}}a_e^+(y) + \rho_\infty\sqrt{\frac{RT_\infty}{2\pi}}F^+a_\infty^+(y) - \rho_\infty\sqrt{\frac{RT_\infty}{2\pi}}F^-a_\infty^-(y) - \rho_*\sqrt{\frac{RT_*}{2\pi}}F_*^-a_*^-(y) = \rho_\infty V_\infty \tag{D.8.a}$$

$$\begin{aligned}&\frac{1}{2}\rho_e RT_L a_e^+(y) + \frac{1}{2}\rho_\infty RT_\infty G^+ a_\infty^+(y) + \frac{1}{2}\rho_\infty RT_\infty G^- a_\infty^-(y) + \frac{1}{2}\rho_* RT_* G_*^- a_*^-(y)\\ &+\rho_\infty\sqrt{\frac{RT_\infty}{2\pi}}F^+U_\infty a_\infty^+(y) - \rho_\infty\sqrt{\frac{RT_\infty}{2\pi}}F^-U_\infty a_\infty^-(y) = \rho_\infty V_\infty^2 + \rho_\infty V_\infty U_\infty + \rho_\infty RT_\infty\end{aligned} \tag{D.8.b}$$

$$\begin{aligned}&2\rho_e RT_l\sqrt{\frac{RT_L}{2\pi}}a_e^+(y) + 2\rho_\infty RT_\infty\sqrt{\frac{RT_\infty}{2\pi}}H^+a_\infty^+(y) - 2\rho_\infty RT_\infty\sqrt{\frac{RT_\infty}{2\pi}}H^-a_\infty^-(y) - 2\rho_* RT_*\sqrt{\frac{RT_*}{2\pi}}H_*^-a_*^-(y)\\ &= \rho_\infty V_\infty(\frac{1}{2}V_\infty^2 + \frac{1}{2}U_\infty^2 + \frac{5}{2}RT_\infty)\end{aligned} \tag{D.8.c}$$

where

$$F^\pm = \sqrt{\pi}S_\infty[\pm 1 + erf(S_\infty)] + \exp(-S_\infty^2) \tag{D.9.a}$$

$$G^\pm = (2S_\infty^2 + 1)[1 \pm erf(S_\infty)] \pm \frac{2}{\sqrt{\pi}}S_\infty \exp(-S_\infty^2) \tag{D.9.b}$$

$$H^\pm = \frac{\sqrt{\pi}S_\infty}{2}(S_\infty^2 + \frac{5}{2})[\pm 1 + erf(S_\infty)] + \frac{1}{2}(S_\infty^2 + 2)\exp(-S_\infty^2) + \frac{S_{x\infty}^2}{2}F^\pm \tag{D.9.c}$$

$$H_*^- = \frac{\sqrt{\pi}S_*}{2}(S_*^2 + \frac{5}{2})[\pm 1 + erf(S_*)] + \frac{1}{2}(S_*^2 + 2)\exp(-S_*^2) \tag{D.9.d}$$

with the definition of external speed ratio in directions normal and parallel to the surface

$$S_\infty = \frac{V_\infty}{\sqrt{2RT}} \tag{D.10.a}$$

and $S_{x\infty} = \frac{U_\infty}{\sqrt{2RT}}$. (D.10.b)

$$S_* = \frac{1}{\sqrt{\pi - 2/3}} . \tag{D.10.c}$$

Considering the boundary condition at *y=0*, Eq. (D.8) will have the following relations,

$$\rho_e\sqrt{\frac{RT_L}{2\pi}} - \rho_\infty\sqrt{\frac{RT_\infty}{2\pi}}\beta F^- - \rho_*\sqrt{\frac{RT_*}{2\pi}}\alpha F_*^- = \rho_\infty V_\infty \tag{D.11.a}$$

$$\frac{1}{2}\rho_e RT_L + \frac{1}{2}\rho_\infty RT_\infty \beta G^- + \frac{1}{2}\rho_* RT_* \alpha G_*^- - \rho_\infty\sqrt{\frac{RT_\infty}{2\pi}}F^- U_\infty \beta = \rho_\infty V_\infty^2 + \rho_\infty V_\infty U_\infty + \rho_\infty RT_\infty \tag{D.11.b}$$

$$\begin{aligned} &2\rho_e RT_L\sqrt{\frac{RT_L}{2\pi}} - 2\rho_\infty RT_\infty\sqrt{\frac{RT_\infty}{2\pi}}\beta H^- - 2\rho_* RT_*\sqrt{\frac{RT_*}{2\pi}}\alpha H_*^- \\ &= \rho_\infty V_\infty\left(\frac{1}{2}V_\infty^2 + \frac{1}{2}U_\infty^2 + \frac{5}{2}RT_\infty\right) \end{aligned} \tag{D.11.c}$$

To simplify the above relation, it can be normalized to the upstream condition,

$$\left(1 - \frac{\sqrt{1-2/(3\pi)}}{2}\alpha F_*^-\right)\frac{n_e}{n_\infty}\sqrt{\frac{T_L}{T_\infty}} - \beta F^- = 2\sqrt{\pi}S_\infty \tag{D.12.a}$$

$$\left(1 + \frac{1-2/(3\pi)}{2}\alpha G_*^-\right)\frac{n_e}{n_\infty}\frac{T_L}{T_\infty} + \beta G^- - \beta\frac{2}{\sqrt{\pi}}F^- S_{x\infty} = 4S_\infty^2 + 4S_\infty S_{x\infty} + 2 \tag{D.12.b}$$

$$\left(1 - \frac{[1-2/(3\pi)]^{3/2}}{2}\alpha H_*^-\right)\frac{n_e}{n_\infty}\frac{T_L}{T_\infty}\sqrt{\frac{T_L}{T_\infty}} - \beta H^- = \sqrt{\pi}S_\infty\left(S_\infty^2 + S_{x\infty}^2 + \frac{5}{2}\right) \tag{D.12.c}$$

with five unknowns, $(\frac{n_e}{n_\infty}, \frac{T_L}{T_\infty}, S_\infty, S_{x\infty}, \alpha, \beta)$.

In addition to specifying the condition that the vapor is saturated in the upstream uniform state, $p_\infty(T_\infty)$, the Clausius-Clapeyron equation

$$\frac{p_\infty}{p_e} = \exp[\frac{\Delta H}{RT_L}(1-\frac{T_L}{T_\infty})] \tag{D.13}$$

By applying the ideal gas law, $\frac{p_\infty}{p_e} = \frac{\rho_e}{\rho_\infty}\frac{T_L}{T_\infty}$, the Clausius-Clapeyron equation can be written as

$$\frac{p_\infty}{p_e} = \frac{\rho_e}{\rho_\infty}\frac{T_L}{T_\infty} = \exp[\frac{\Delta H}{RT_L}(1-\frac{T_L}{T_\infty})] \tag{D.14}$$

which can be used as the fourth equation to solve ($\frac{n_e}{n_\infty}$, $\frac{T_L}{T_\infty}$, S_∞, $S_{x\infty}$, α, β) combined with Eq. (D.12). If S_∞ and $S_{x\infty}$ are known, four unknowns, ($\frac{n_e}{n_\infty}$ $\frac{T_L}{T_\infty}$ α β) are solved.

Furthermore, Eq. (D.8) can be considered as the linear equations for the space dependent amplitude function (a_e^+, a_∞^+, a_∞^-, a_*^-), and they can be solved in terms of a_∞^-,

$$a_e^+(y) = \frac{a_\infty^-(y)-1}{\beta-1} \tag{D.15.a}$$

$$a_\infty^+(y) = 1-\frac{a_\infty^-(y)-1}{\beta-1} \tag{D.15.b}$$

$$a_*^-(y) = \alpha\frac{a_\infty^-(y)-1}{\beta-1} \tag{D.15.c}$$

To solve the Knudsen Layer structure, Eq. (D.5.b)

$$\frac{\partial}{\partial y}\int c_y \psi_\mu f d\mathbf{c} = \Delta Q[mc_y^2] \qquad \mu = 4 \tag{D.5.b}$$

is utilized to obtain the spatial distribution of mass and energy. By applying the standard integrals in Appendix C, the following integrals can be derived as

$$\int_0^\infty c_y^3 f_y dc_y = \frac{2}{\sqrt{2\pi}}(RT)^{\frac{3}{2}} I^+ \tag{D.16.a}$$

$$\int_\infty^0 c_y^3 f_y dc_y = -\frac{2}{\sqrt{2\pi}}(RT)^{\frac{3}{2}} I^- \tag{D.16.b}$$

in which

$$I^{\pm}=\sqrt{\pi}S_{\infty}(S_{\infty}^{2}+\frac{3}{2})[\pm 1+erf(S_{\infty})]+(S_{\infty}^{2}+1)\exp(-S_{\infty}^{2}) \qquad \text{(D.17)}$$

So LHS of Eq. (D.5.b) reads

$$\frac{d}{dy}[2\rho_{e}RT_{L}\sqrt{\frac{RT_{L}}{2\pi}}a_{e}^{+}(y)+2\rho_{\infty}RT_{\infty}\sqrt{\frac{RT_{\infty}}{2\pi}}I^{+}a_{\infty}^{+}(y)-2\rho_{\infty}RT_{\infty}\sqrt{\frac{RT_{\infty}}{2\pi}}I^{-}a_{\infty}^{-}(y)-2\rho_{*}RT_{*}\sqrt{\frac{RT_{*}}{2\pi}}I_{*}^{-}a_{*}^{-}(y)]$$
$$=RHS$$

(D.18)

Substituting Eq. (D.15) into Eq. (D.18), LHS of Eq. (D.5.b) becomes

$$2\rho_{\infty}RT_{\infty}\sqrt{\frac{RT_{\infty}}{2\pi}}\frac{d}{dy}[\frac{a_{\infty}^{-}(y)}{\beta-1}\frac{\rho_{e}}{\rho_{\infty}}(\frac{T_{L}}{T_{\infty}})^{\frac{3}{2}}-\frac{a_{\infty}^{-}(y)}{\beta-1}I^{+}-a_{\infty}^{-}(y)I^{-}-\frac{\sqrt{[1-2/(3\pi)]^{3}}}{2}\alpha\frac{a_{\infty}^{-}(y)}{\beta-1}I_{*}^{-}\frac{\rho_{e}}{\rho_{\infty}}(\frac{T_{L}}{T_{\infty}})^{\frac{3}{2}}]$$
$$=RHS$$

(D.19)

Simplifying the above, it is equivalent to

$$2\rho_{\infty}RT_{\infty}\sqrt{\frac{RT_{\infty}}{2\pi}}\frac{1}{\beta-1}[\frac{\rho_{e}}{\rho_{\infty}}(\frac{T_{L}}{T_{\infty}})^{\frac{3}{2}}-I^{+}-(\beta-1)I^{-}-\frac{\sqrt{[1-2/(3\pi)]^{3}}}{2}\alpha I_{*}^{-}\frac{\rho_{e}}{\rho_{\infty}}(\frac{T_{L}}{T_{\infty}})^{\frac{3}{2}}]\frac{da_{\infty}^{-}(y)}{dy}$$
$$=RHS$$

(D.20)

Eq. (D.20) can be further simplified. Now we can define the items in the bracket of Eq. (D.20) as

$$A=\frac{\rho_{e}}{\rho_{\infty}}(\frac{T_{L}}{T_{\infty}})^{\frac{3}{2}}-I^{+}-(\beta-1)I^{-}-\frac{\sqrt{[1-2/(3\pi)]^{3}}}{2}\alpha I_{*}^{-}\frac{\rho_{e}}{\rho_{\infty}}(\frac{T_{L}}{T_{\infty}})^{\frac{3}{2}} \qquad \text{(D.21)}$$

Comparing Eq. (D.9) and Eq. (D.17), the following relations can be observed:

$$-I^{+}+I^{-}=-2\sqrt{\pi}S_{\infty}(S_{\infty}^{2}+\frac{3}{2}) \qquad \text{(D.22.a)}$$

$$I^{-}+F^{-}=2H^{-}-S_{x\infty}{}^{2}F^{-} \qquad \text{(D.22.b)}$$

$$I_{*}^{-}+F_{*}^{-}=2H_{*}^{-} \qquad \text{(D.22.c)}$$

So Eq. (D.21) becomes

$$A = \frac{\rho_e}{\rho_\infty}(\frac{T_L}{T_\infty})^{\frac{3}{2}} - 2\sqrt{\pi}S_\infty(S_\infty^2 + \frac{3}{2}) - \beta(2H^- - F^- - S_{x\infty}{}^2F^-) - \frac{\sqrt{[1-2/(3\pi)]^3}}{2}\alpha(2H_*{}^- - F_*{}^-)\frac{\rho_e}{\rho_\infty}(\frac{T_L}{T_\infty})^{\frac{3}{2}}$$

$$= \frac{\rho_e}{\rho_\infty}(\frac{T_L}{T_\infty})^{\frac{3}{2}} - 2\sqrt{\pi}S_\infty{}^3 - 3\sqrt{\pi}S_\infty - 2\beta H^- + \beta F^- + S_{x\infty}{}^2\beta F^- - \sqrt{[1-2/(3\pi)]^3}\alpha H_*{}^- \frac{\rho_e}{\rho_\infty}(\frac{T_L}{T_\infty})^{\frac{3}{2}}$$
$$+ \frac{\sqrt{[1-2/(3\pi)]^3}}{2}\alpha F_*{}^- \frac{\rho_e}{\rho_\infty}(\frac{T_L}{T_\infty})^{\frac{3}{2}}$$

(D.23)

Recall Eq. (D.12.c) in the form of

$$-2\beta H^- = 2\sqrt{\pi}S_\infty(S_\infty^2 + S_{x\infty}^2 + \frac{5}{2}) - (2 - \sqrt{[1-2/(3\pi)]^3}\alpha H_*^-)\frac{\rho_e}{\rho_\infty}(\frac{T_L}{T_\infty})^{\frac{3}{2}} \tag{D.24}$$

Eq. (D.23) can be shown as

$$A = -\frac{\rho_e}{\rho_\infty}(\frac{T_L}{T_\infty})^{\frac{3}{2}} + 2\sqrt{\pi}S_\infty + 2\sqrt{\pi}S_\infty(S_{x\infty}^2) + \beta F^- + S_x{}^2\beta F^- + \frac{\sqrt{[1-2/(3\pi)]^3}}{2}\alpha F_*{}^- \frac{\rho_e}{\rho_\infty}(\frac{T_L}{T_\infty})^{\frac{3}{2}}$$

(D.25)

Again, recall Eq. (D.12.a)

$$\beta F^- = (1 - \frac{\sqrt{[1-2/(3\pi)]}}{2}\alpha F_*^-)\frac{\rho_e}{\rho_\infty}(\frac{T_L}{T_\infty})^{\frac{1}{2}} - 2\sqrt{\pi}S_\infty \tag{D.26}$$

Eq. (D.21) finally becomes

$$A = -\frac{\rho_e}{\rho_\infty}(\frac{T_L}{T_\infty})^3 + \frac{\rho_e}{\rho_\infty}(\frac{T_L}{T_\infty})^{\frac{1}{2}} + \frac{\sqrt{[1-2/(3\pi)]^3}}{2}\alpha F_*{}^- \frac{\rho_e}{\rho_\infty}(\frac{T_L}{T_\infty})^{\frac{3}{2}} - \frac{\sqrt{1-2/(3\pi)}}{2}\alpha F_*^- \frac{\rho_e}{\rho_\infty}(\frac{T_L}{T_\infty})^{\frac{1}{2}}$$
$$+(1 - \frac{\sqrt{1-2/(3\pi)}}{2}\alpha F_*^-)\frac{\rho_e}{\rho_\infty}(\frac{T_L}{T_\infty})^{\frac{1}{2}} S_{x\infty}{}^2$$

(D.27)

Finally, LHS of Eq. (D.5.b) can be written as

$$2\rho_\infty RT_\infty\sqrt{\frac{RT_\infty}{2\pi}}\frac{1}{\beta-1}\times$$

$$[-\frac{\rho_e}{\rho_\infty}(\frac{T_L}{T_\infty})^3+\frac{\rho_e}{\rho_\infty}(\frac{T_L}{T_\infty})^{\frac{1}{2}}+\frac{\sqrt{[1-2/(3\pi)]^3}}{2}\alpha F_*^-\frac{\rho_e}{\rho_\infty}(\frac{T_L}{T_\infty})^{\frac{3}{2}}-\frac{\sqrt{1-2/(3\pi)}}{2}\alpha F_*^-\frac{\rho_e}{\rho_\infty}(\frac{T_L}{T_\infty})^{\frac{1}{2}}$$

$$+(1-\frac{\sqrt{1-2/(3\pi)}}{2}\alpha F_*^-)\frac{\rho_e}{\rho_\infty}(\frac{T_L}{T_\infty})^{\frac{1}{2}}S_{x\infty}{}^2]\times$$

$$\frac{da_\infty^-(y)}{dy}=RHS$$

(D.28)

It is time to deal with RHS of Eq. (D.5.b)

$$\Delta Q[mc_y^2]=\frac{\pi}{\lambda_e}\sqrt{\frac{RT_L}{2\pi}}\frac{\rho}{\rho_e}\tau'_{yy} \tag{D.6}$$

τ'_{yy} is in the form of

$$\tau'_{yy}=-m\int(c_y-V)^2 fd\mathbf{c}+\frac{m}{3}\int(\mathbf{c}-\mathbf{U})^2 fd\mathbf{c} \tag{D.7}$$

First, the first integral of Eq. (D.7) $m\int(c_y-V)^2 fd\mathbf{c}$, which is evaluated as

$$I_1=m\int(c_y-V)^2 fd\mathbf{c}$$

$$=\frac{1}{2}\rho_e RT_L a_e^+ +\frac{1}{2}\rho_\infty RT_\infty G^+ a_\infty^+ +\frac{1}{2}\rho_\infty RT_\infty G^- a_\infty^- +\frac{1}{2}\rho_* RT_* G_*{}^- a_*^- -V^2(y)\rho(y)$$

$$=\frac{1}{2}\rho_\infty RT_\infty[\frac{\rho_e}{\rho_\infty}\frac{T_L}{T_\infty}a_e^+ +G^+a_\infty^+ +G^-a_\infty^- +\frac{1-2/(3\pi)}{2}G_*{}^-a_*^-\frac{\rho_e}{\rho_\infty}\frac{T_L}{T_\infty}-4S_\infty{}^2\frac{V^2(y)}{V_\infty{}^2(y)}\frac{\rho(y)}{\rho_\infty}]$$

(D.29)

The mean kinetic energy in the x and z directions can also be evaluated in the same way as in the following

$$I_2=m\int(c_x-U)^2 fd\mathbf{c}$$

$$
\begin{aligned}
&= \frac{1}{2}\rho_\infty R T_\infty \times \\
&\{\frac{\rho_e}{\rho_\infty}\frac{T_L}{T_\infty}a_e^+ + (1+2S_x{}^2)[1+erf(S_\infty)]a_\infty^+ + (1+2S_{x\infty}{}^2)[1-erf(S_\infty)]a_\infty^- + \\
&\frac{N}{2}[1-erf(S_*)]\frac{\rho_e}{\rho_\infty}\frac{T_L}{T_\infty}a_*^- - 4S_{x\infty}{}^2\frac{U^2(y)}{U_\infty{}^2(y)}\frac{\rho(y)}{\rho_\infty}\}
\end{aligned}
$$

(D.30.a)

$$
\begin{aligned}
I_3 &= m\int (c_z - W)^2 f d\mathbf{c} \\
&= \frac{1}{2}\rho_\infty R T_\infty \{\frac{\rho_e}{\rho_\infty}\frac{T_L}{T_\infty}a_e^+ + [1+erf(S_\infty)]a_\infty^+ + [1-erf(S_\infty)]a_\infty^- + \frac{1-2/(3\pi)}{2}[1-erf(S_*)]\frac{\rho_e}{\rho_\infty}\frac{T_L}{T_\infty}a_*^-\}
\end{aligned}
$$

(D.30.b)

The second integral of Eq. (D.7) is in the form of

$$\frac{m}{3}\int (\mathbf{c}-\mathbf{U})^2 f d\mathbf{c} = \frac{1}{3}(I_1 + I_2 + I_3) \tag{D.31}$$

Eq. (D.7) will become

$$
\begin{aligned}
\tau'_{yy} &= -m\int (c_y - V)^2 f d\mathbf{c} + \frac{m}{3}\int (\mathbf{c}-\mathbf{U})^2 f d\mathbf{c} = \frac{1}{3}(I_2 + I_3) - \frac{2}{3}I_1 \\
&= \frac{1}{3}\rho_\infty R T_\infty \{J^+ a_\infty^+ + J^- a_\infty^- + \frac{1-2/(3\pi)}{2}J_*^- a_*^- \frac{\rho_e}{\rho_\infty}\frac{T_L}{T_\infty} + 4S_\infty{}^2\frac{V^2(y)}{V_\infty{}^2(y)}\frac{\rho(y)}{\rho_\infty} - 2S_{x\infty}{}^2\frac{U^2(y)}{U_\infty{}^2(y)}\frac{\rho(y)}{\rho_\infty}\}
\end{aligned}
$$

(D.32)

where

$$J^+ = (-2S_\infty^2 + S_{x\infty}{}^2)[1+erf(S_\infty)] - \frac{2}{\sqrt{\pi}}S_\infty \exp(-S_\infty^2) \tag{D.33.a}$$

$$J^- = (-2S_\infty^2 + S_{x\infty}{}^2)[1-erf(S_\infty)] + \frac{2}{\sqrt{\pi}}S_\infty \exp(-S_\infty^2) \tag{D.33.b}$$

$$J_*{}^- = (-2S_*^2)[1-erf(S_*)] + \frac{2}{\sqrt{\pi}}S_* \exp(-S_*^2) \tag{D.33.c}$$

Recalling the mass conservation relation, the above equation can be reduced to

$$\tau'_{yy} = \frac{1}{3}\rho_\infty R T_\infty [J^+ a_\infty^+ + J^- a_\infty^- + \frac{N}{2}J_*^- \frac{\rho_e}{\rho_\infty}(\frac{T_L}{T_\infty})^{\frac{3}{2}} a_*^- + 4S_\infty{}^2\frac{\rho_\infty}{\rho(y)} - 2S_x{}^2\frac{U^2(y)}{U_\infty{}^2(y)}\frac{\rho(y)}{\rho_\infty}]$$

(D.34a)

Because of $J^{+}+J^{-}=-4S_{\infty}^{2}+2S_{x\infty}{}^{2}$, substituting relation (D.15) into Eq. (D.34a), τ'_{yy} can be further simplified to

$$\tau'_{yy}=\frac{1}{3}\rho_{\infty}RT_{\infty}\times$$
$$[\frac{a_{\infty}^{-}(y)-1}{\beta-1}(4S_{\infty}^{2}-2S_{x}{}^{2}+J^{-}\beta+\frac{1-2/(3\pi)}{2}J_{*}^{-}\alpha\frac{\rho_{e}}{\rho_{\infty}}\frac{T_{L}}{T_{\infty}})-4S_{\infty}^{2}$$
$$+2S_{x\infty}{}^{2}+4S_{\infty}{}^{2}\frac{\rho_{\infty}}{\rho(y)}-2S_{x\infty}{}^{2}\frac{U^{2}(y)}{U_{\infty}{}^{2}(y)}\frac{\rho(y)}{\rho_{\infty}}]$$

(D.34b)

The density can be evaluated as following (See details later.),

$$\frac{\rho(y)}{\rho_{\infty}}=\frac{1}{2}xa_{e}^{+}+\frac{1}{2}[1+erf(S_{\infty})]a_{\infty}^{+}+\frac{1}{2}[1-erf(S_{\infty})]a_{\infty}^{-}+\frac{1}{4}x[1-erf(S_{*})]a_{*}^{-}$$
$$=\frac{1}{2}\frac{\rho_{e}}{\rho_{\infty}}\frac{a_{\infty}^{-}(y)-1}{\beta-1}+\frac{1}{2}[1+erf(S_{\infty})][1-\frac{a_{\infty}^{-}(y)-1}{\beta-1}]+\frac{1}{2}[1-erf(S_{\infty})]a_{\infty}^{-}+\frac{\alpha}{4}[1-erf(S_{*})]\frac{\rho_{e}}{\rho_{\infty}}\frac{a_{\infty}^{-}(y)-1}{\beta-1}$$
$$=\frac{1}{2}\frac{a_{\infty}^{-}(y)-1}{\beta-1}(\frac{\rho_{e}}{\rho_{\infty}}-2+[1-erf(S_{\infty})]\beta+\frac{\alpha}{2}[1-erf(S_{*})]\frac{\rho_{e}}{\rho_{\infty}})+1$$
$$=\frac{1}{2}[a_{\infty}^{-}(y)-1]\varphi_{1}+1$$

(D.35)

where

$$\varphi_{1}=\frac{1}{\beta-1}(\frac{\rho_{e}}{\rho_{\infty}}-2+[1-erf(S_{\infty})]\beta+\frac{\alpha}{2}[1-erf(S_{*})]\frac{\rho_{e}}{\rho_{\infty}}) \qquad \text{(D.36)}$$

Also the mass flux in x direction can be derived as

$$\frac{\rho(y)U(y)}{\rho_{\infty}U_{\infty}}=\frac{1}{2}[1+erf(S_{\infty})]a_{\infty}^{+}+\frac{1}{2}[1-erf(S_{\infty})]a_{\infty}^{-}$$

$$=\frac{1}{2}\frac{a_{\infty}^{-}(y)-1}{\beta-1}[-2+[1-erf(S_{\infty})]\beta]+1$$

$$=\frac{1}{2}[a_{\infty}^{-}(y)-1]\varphi_{3}+1 \qquad \text{(D.37)}$$

where

$$\varphi_{3}=\frac{1}{\beta-1}[-2+[1-erf(S_{\infty})]\beta] \qquad \text{(D.38)}$$

To make the equation shorter, another parameter was defined as

$$\varphi_2=\frac{1}{\beta-1}(4S_{\infty}^2-2S_{x\infty}{}^2+J^{-}\beta+\frac{1-2/(3\pi)}{2}\frac{\rho_e}{\rho_{\infty}}\frac{T_L}{T_{\infty}}J_{*}^{-}\alpha) \qquad \text{(D.39)}$$

So Eq. (D.34) becomes

$$\tau'_{yy}=\frac{1}{3}\rho_{\infty}RT_{\infty}\{[a_{\infty}^{-}(y)-1]\varphi_2-4S_{\infty}^2+2S_{x\infty}{}^2+4S_{\infty}{}^2\frac{\rho_{\infty}}{\rho(y)}-2S_{x\infty}{}^2\frac{U^2(y)}{U_{\infty}{}^2(y)}\frac{\rho(y)}{\rho_{\infty}}\}$$

$$\text{(D.40)}$$

By applying Eq. (D.35) and (D.37), the RHS of Eq. (D.5.b) finally reach the form as

$$\Delta Q[mc_y^2]=$$
$$\frac{\pi}{\lambda_e}\sqrt{\frac{RT_L}{2\pi}}\frac{\rho(y)}{\rho_e}\frac{1}{3}\rho_{\infty}RT_{\infty}\times$$
$$\{[a_{\infty}^{-}(y)-1]\varphi_2-4S_{\infty}^2+2S_{x}{}^2+4S_{\infty}{}^2\frac{\rho_{\infty}}{\rho(y)}-2S_{x\infty}{}^2\frac{U^2(y)}{U_{\infty}{}^2(y)}\frac{\rho(y)}{\rho_{\infty}}\}$$

$$=\frac{\pi}{\lambda_e}\sqrt{\frac{RT_L}{2\pi}}\frac{1}{\rho_e}\frac{1}{3}\rho^2{}_{\infty}RT_{\infty}\times$$
$$\{[a_{\infty}^{-}(y)-1]\varphi_2\frac{\rho(y)}{\rho_{\infty}}-4S_{\infty}^2\frac{\rho(y)}{\rho_{\infty}}+2S_{x\infty}{}^2\frac{\rho(y)}{\rho_{\infty}}+4S_{\infty}{}^2-2S_{x\infty}{}^2\frac{U^2(y)}{U_{\infty}{}^2(y)}\frac{\rho^2(y)}{\rho^2{}_{\infty}}\}$$

$$=\frac{\pi}{\lambda_e}\sqrt{\frac{RT_L}{2\pi}}\frac{1}{\rho_e}\frac{1}{3}\rho^2{}_{\infty}RT_{\infty}\times$$
$$[a_{\infty}^{-}(y)-1][a_{\infty}^{-}(y)-1+\frac{\varphi_2-2S_{\infty}^2\varphi_1+S_{x\infty}{}^2\varphi_1-2S_{x\infty}^2\varphi_3}{\frac{\varphi_1\varphi_2}{2}-\frac{1}{2}S_{x\infty}{}^2\varphi_3{}^2}](\frac{\varphi_1\varphi_2}{2}-\frac{1}{2}S_{x\infty}{}^2\varphi_3{}^2)$$

$$\text{(D.41)}$$

To make the equation compact, we can define

$$r = 1 - \frac{\varphi_2 - 2S_\infty^2\varphi_1 + S_{x\infty}{}^2\varphi_1 - 2S_{x\infty}^2\varphi_3}{\dfrac{\varphi_1\varphi_2}{2} - \dfrac{1}{2}S_{x\infty}{}^2\varphi_3{}^2} \tag{D.42}$$

So RHS of Eq. (D.5.b) is put in the form

$$RHS = \frac{\pi}{\lambda_e}\sqrt{\frac{RT_L}{2\pi}}\frac{1}{\rho_e}\frac{1}{3}\rho^2{}_\infty RT_\infty[a_\infty^-(y)-1][a_\infty^-(y)-r](\frac{\varphi_1\varphi_2}{2} - \frac{1}{2}S_{x\infty}{}^2\varphi_3{}^2) \tag{D.43}$$

By combining Eq. (D.28) and (D.43), Eq. (D.5.b) becomes

$$\begin{aligned}
&2\rho_\infty RT_\infty\sqrt{\frac{RT_\infty}{2\pi}}\frac{1}{\beta-1}\times \\
&[-\frac{\rho_e}{\rho_\infty}(\frac{T_L}{T_\infty})^{\frac{3}{2}} + \frac{\rho_e}{\rho_\infty}(\frac{T_L}{T_\infty})^{\frac{1}{2}} + \frac{\sqrt{[1-2/(3\pi)]^3}}{2}\alpha\frac{\rho_e}{\rho_\infty}(\frac{T_L}{T_\infty})^{\frac{3}{2}}F_*^- - \frac{\sqrt{1-2/(3\pi)}}{2}\alpha F_*^-\frac{\rho_e}{\rho_\infty}(\frac{T_L}{T_\infty})^{\frac{1}{2}} \\
&+(1-\frac{\sqrt{1-2/(3\pi)}}{2}\alpha F_*^-)\frac{\rho_e}{\rho_\infty}(\frac{T_L}{T_\infty})^{\frac{1}{2}}S_{x\infty}{}^2]\times\frac{da_\infty^-(y)}{dy} \\
&=\frac{\pi}{\lambda_e}\sqrt{\frac{RT_L}{2\pi}}\frac{1}{\rho_e}\frac{1}{3}\rho^2{}_\infty RT_\infty[a_\infty^-(y)-1][a_\infty^-(y)-r](\frac{\varphi_1\varphi_2}{2}-\frac{1}{2}S_{x\infty}{}^2\varphi_3{}^2)
\end{aligned} \tag{D.44}$$

With the help of simple algebra, the Eq. (D.5.b) finally reaches the compact form as

$$\frac{da_\infty^-(y)}{dy} = -\frac{P_c}{\lambda_e}[a_\infty^-(y)-1][a_\infty^-(y)-r] \tag{D.45}$$

in which

$$P_c = \frac{(\beta-1)\pi(\varphi_1\varphi_2 - S_{x\infty}{}^2\varphi_3{}^2)}{12(\dfrac{\rho_e}{\rho_\infty})^2\dfrac{T_L}{T_\infty}\{1-\dfrac{T_\infty}{T_L}+\dfrac{\sqrt{1-2/(3\pi)}}{2}\alpha F_*^-(\dfrac{T_\infty}{T_L}-1+2/(3\pi))+\dfrac{T_\infty}{T_L}(1-\dfrac{\sqrt{1-2/(3\pi)}}{2}\alpha F_*^-)S_{x\infty}^2\}} \tag{D.46}$$

Furthermore, because

$$\begin{aligned}
J^- &= (-2S_\infty^2 + S_{x\infty}{}^2)[1-erf(S_\infty)] + \frac{2}{\sqrt{\pi}}S_\infty\exp(-S_\infty^2) \\
&= -G^- + (1+S_{x\infty}{}^2)[1-erf(S_\infty)]
\end{aligned} \tag{D.47}$$

$$\begin{aligned}
J_*^- &= (-2S_*^2)[1-erf(S_*)] + \frac{2}{\sqrt{\pi}}S_*\exp(-S_*^2) \\
&= -G_*^- + [1-erf(S_*)]
\end{aligned} \tag{D.48}$$

, the parameter φ_2 becomes

$$\varphi_2 = \frac{1}{\beta - 1}\{-2S_{x\infty}{}^2 + \frac{\rho_e}{\rho_\infty}\frac{T_L}{T_\infty} - 2 + \beta(1 + S_{x\infty}{}^2)[1 - erf(S_\infty)] + \frac{1 - 2/(3\pi)}{2}\alpha[1 - erf(S_*)]\frac{\rho_e}{\rho_\infty}\frac{T_L}{T_\infty}\}$$

(D.49)

The final form of Eq. (D.5.b), is as follows

$$\frac{da_\infty^-(y)}{dy} = -\frac{P_c}{\lambda_e}[a_\infty^-(y) - 1][a_\infty^-(y) - r] \tag{D.45}$$

in which

$$P_c = \frac{(\beta - 1)\pi(\varphi_1\varphi_2 - S_{x\infty}{}^2\varphi_3{}^2)}{12(\frac{\rho_e}{\rho_\infty})^2\frac{T_L}{T_\infty}\{1 - \frac{T_\infty}{T_L} + \frac{\sqrt{1 - 2/(3\pi)}}{2}\alpha F_*^-(\frac{T_\infty}{T_L} - 1 + 2/(3\pi)) + \frac{T_\infty}{T_L}(1 - \frac{\sqrt{1 - 2/(3\pi)}}{2}\alpha F_*^-)S_{x\infty}^2\}}$$

(D.46)

$$r = 1 - \frac{\varphi_2 - 2S_\infty^2\varphi_1 + S_{x\infty}{}^2\varphi_1 - 2S_{x\infty}^2\varphi_3}{\frac{\varphi_1\varphi_2}{2} - \frac{1}{2}S_{x\infty}{}^2\varphi_3{}^2} \tag{D.42}$$

$$\varphi_1 = \frac{1}{\beta - 1}(\frac{\rho_e}{\rho_\infty} - 2 + [1 - erf(S_\infty)]\beta + \frac{\alpha}{2}[1 - erf(S_*)]\frac{\rho_e}{\rho_\infty}) \tag{D.36}$$

$$\varphi_2 = \frac{1}{\beta - 1}\{-2S_{x\infty}{}^2 + \frac{\rho_e}{\rho_\infty}\frac{T_L}{T_\infty} - 2 + \beta(1 + S_{x\infty}{}^2)[1 - erf(S_\infty)] + \frac{1 - 2/(3\pi)}{2}\alpha[1 - erf(S_*)]\frac{\rho_e}{\rho_\infty}\frac{T_L}{T_\infty}\}$$

(D.49)

$$\varphi_3 = \frac{1}{\beta - 1}[-2 + [1 - erf(S_\infty)]\beta] \tag{D.38}$$

Errors in Eq.(D.36) (D.46) and (D.49), as it was originally presented in [5], have been corrected along with the addition of extra terms due to the tangential flow.

If $P_c > 0; r < 1; \beta < r$ or $P_c < 0; r > 1; \beta > r$, so ODE , Eq. (D.45) can be solved analytically as

$$\frac{a_\infty^-(y)-1}{\beta-1}=\frac{a_\infty^-(y)-r}{\beta-r}\exp[-P_c(1-r)\frac{y}{\lambda_e}] \tag{D.50}$$

By now, the space dependent amplitude function (a_e^+, a_∞^+, a_∞^-, a_*^-) is known, and the physical quantities are ready to be shown as a function of distance, *y*. The density can be evaluated as

$$\begin{aligned} n(y) &= \int f d\mathbf{c} \\ &= \iiint f_x f_y f_z dc_x dc_y dc_z \\ &= n_e \frac{1}{2} a_e^+ + \frac{1}{2} n_\infty (1+erf(S_\infty)) a_\infty^+ + \frac{1}{2} n_\infty (1-erf(S_\infty)) a_\infty^- + \frac{1}{2} n_* (1+erf(S_*)) a_*^- \end{aligned} \tag{D.51}$$

$$\frac{n(y)}{n_\infty}=\frac{n_e}{n_\infty}\frac{1}{2}a_e^+ + \frac{1}{2}(1+erf(S_\infty))a_\infty^+ + \frac{1}{2}(1-erf(S_\infty))a_\infty^- + \frac{1}{4}\frac{n_e}{n_\infty}(1+erf(S_*))a_*^- \tag{D.52}$$

The velocity in y directions can be obtained as

$$\begin{aligned} n(y)V(y) &= \int c_y f d\mathbf{c} \\ &= \iiint c_y f_x f_y f_z dc_x dc_y dc_z \\ &= n_e \sqrt{\frac{RT_L}{2\pi}} a_e^+ + n_\infty \sqrt{\frac{RT_\infty}{2\pi}} F^+ a_\infty^+ - n_\infty \sqrt{\frac{RT_\infty}{2\pi}} F^- a_\infty^- - n_* \sqrt{\frac{RT_*}{2\pi}} F_*^- a_*^- \end{aligned} \tag{D.53}$$

$$\frac{V(y)}{V_\infty}=(\frac{n_e}{n_\infty}\sqrt{\frac{T_L}{T_\infty}}a_e^+ + F^+ a_\infty^+ - F^- a_\infty^- - \frac{1}{2}\frac{n_e}{n_\infty}\sqrt{[1-2/(3\pi)]\frac{T_L}{T_\infty}F_*^- a_*^-})\frac{1}{2}\frac{n_\infty}{n(y)S_\infty\sqrt{\pi}} \tag{D.54}$$

Or by applying mass conservation law, it becomes $\frac{V(y)}{V_\infty}=\frac{n_\infty}{n(y)}$.

The velocity in x directions can be obtained as

$$\begin{aligned} n(y)U(y) &= \int c_x f d\mathbf{c} \\ &= \frac{1}{2} n_\infty U_\infty (1+erf(S_\infty)) a_\infty^+ + \frac{1}{2} n_\infty U_\infty (1-erf(S_\infty)) a_\infty^- \end{aligned} \tag{D.55}$$

$$\frac{U(y)}{U_\infty}=(\frac{1}{2}(1+erf(S_\infty))a_\infty^+ + \frac{1}{2}(1-erf(S_\infty))a_\infty^-)\frac{n_\infty}{n(y)} \tag{D.56}$$

The translational temperature normal to the liquid surface is evaluated as

$$n(y)RT_y(y)=\int(c_y-V(y))^2 fd\mathbf{c}$$

$$=\iiint(c_y-V(y))^2 f_xf_yf_zdc_xdc_ydc_z$$

$$=\iiint c_y{}^2 f_xf_yf_zdc_xdc_ydc_z-\iiint 2c_yV(y)f_xf_yf_zdc_xdc_ydc_z+\iiint V^2(y)f_xf_yf_zdc_xdc_ydc_z$$

$$=\iiint c_y{}^2 f_xf_yf_zdc_xdc_ydc_z-2V^2(y)n(y)+V^2(y)n(y)$$

$$=\iiint c_y{}^2 f_xf_yf_zdc_xdc_ydc_z-V^2(y)n(y)$$

$$=n_e\frac{RT_L}{2}a_e^+ + n_\infty\frac{RT_\infty}{2}G^+a_\infty^+ + n_\infty\frac{RT_\infty}{2}G^-a_\infty^- + n_*\frac{RT_*}{2}G_*^-a_*^- - V^2(y)n(y) \tag{D.57}$$

$$\frac{n(y)T_y(y)}{n_\infty T_\infty}=\frac{n_e}{n_\infty}\frac{T_L}{2T_\infty}a_e^+ + \frac{1}{2}G^+a_\infty^+ + \frac{1}{2}G^-a_\infty^- + \frac{1}{4}\frac{n_e}{n_\infty}\frac{[1-2/(3\pi)]T_L}{T_\infty}G_*^-a_*^- - 2\frac{V^2(y)n(y)}{V_\infty{}^2 n_\infty}S_\infty{}^2 \tag{D.58}$$

The translational temperature parallel to the liquid surface is in form as

$$n(y)RT_x(y)=\int(c_x-U(y))^2 fd\mathbf{c}$$

$$=\iiint c_x{}^2 f_xf_yf_zdc_xdc_ydc_z-U^2(y)n(y)$$

$$\begin{aligned}&=n_e\frac{RT_L}{2}a_e^+ + n_\infty\frac{RT_\infty+U_\infty{}^2}{2}[1+erf(S_\infty)]a_\infty^+ + \\ &n_\infty\frac{RT_\infty+U_\infty{}^2}{2}[1-erf(S_\infty)]a_\infty^- + n_*\frac{RT_*}{2}[1-erf(S_*)]a_*^- - U^2(y)n(y)\end{aligned} \tag{D.59}$$

$$\begin{aligned}\frac{n(y)T_x(y)}{n_\infty T_\infty}&=\frac{n_e}{n_\infty}\frac{T_L}{2T_\infty}a_e^+ + \frac{1+2S_{x\infty}{}^2}{2}[1+erf(S_\infty)]a_\infty^+ + \frac{1+2S_{x\infty}{}^2}{2}[1-erf(S_\infty)]a_\infty^- + \\ &\frac{1}{2}\frac{n_e}{n_\infty}\frac{[1-2/(3\pi)]T_L}{2T_\infty}[1-erf(S_*)]a_*^- - \frac{U^2(y)n(y)}{U_\infty{}^2 n_\infty}2S_{x\infty}{}^2\end{aligned} \tag{D.60}$$

Bibliography

[1] S. Maruyama, *Molecular dynamics method for microscale heat transfer, in Advances in Numerical Heat Transfer*, vol. 2 edited by Minkowycz and Sparrow, New York: Taylor and Francis, 2000, vol. 2, Chap 6, pp. 189-226.

[2] K. Gu, C.B. Watkins and J. Koplik, “Atomistic hybrid DSMC-NEMD method for nonequilibrium multiscale simulations,” *Journal of Computational Physics*, vol. 229, No. 5, pp. 1381-1400, 2010.

[3] S. Kjelstrupa, T. Tsuruta and D. Bedeaux, “The Inverted Temperature Profile Across a Vapor/Liquid Surface Analyzed by Molecular Computer Simulations,” *Journal of Colloid and Interface Science*, vol. 256, vol. 2, pp. 451-461, 2002.

[4] V.P. Carey, *Liquid-Vapor Phase Change-Phenomena*, second edition, New York: Taylor and Francis, 2008.

[5] T. Ytrehus, “Molecular-flow effects in evaporation and condensation at interfaces, Multiphase Science and Technology,” *Multiphase Science and Technology*, vol. 9, pp. 205-327, 1997.

[6] G.A. Bird, *Molecular Gas Dynamics and the Direct Simulation of Gas Flows*, New York: Oxford, 1994.

[7] P.S. Prasanth and J.K. Kakkassery, “Direct simulation Monte Carlo (DSMC): A numerical method for transition-regime flows–A review,” *Journal of Indian Institute of Science* vol.86, pp.169–192,2006

[8] V.P. Carey, *DSMC modeling of near-interface transport in liquid-vapor phase-change processes with multiple microscale effects, in Heat Transfer and Fluid Flow in Microscale and Nanoscale Structures*, edited by Faghri and Sunden, Southampton, UK: WIT Press, Chap. 8, pp.304-347, 2004

[9] M.A. Gallis, J.R. Torczynski, D. J. Rader and G.A. Bird, “Convergence behavior of a new DSMC algorithm,” *Journal of Computational Physics*, vol. 228, No. 12, pp. 4532-4538, 2009.

[10] M.P. Allen. and D.J Tildesley, *Computer Simulation of Liquids*, Oxford: Clarendon Press, 1987.

[11] D. Frenkel and B. Smit, *Understanding Molecular Simulation,* San Diego: Academic, 1996.

[12] D. C. Rapaport, *The Art of Molecular Dynamics Simulation, 2nd ed.*, Cambridge: University Press, 2004.

[13] M.J.P. Nijmeijer, C. Bruin, A.F. Bakker and J.M.J. van Leeuwen, “Wetting and drying of an inert wall by a fluid in a molecular dynamics simulation,” *Physical Review A,* vol. 42, pp. 6052-6059, 1990.

[14] W.-J. Ma, J. Koplik and J.R. Banavar, “A molecular dynamics study of freezing in a confined geometry,” *Journal of Chemical Physics*, vol. 97, pp. 485-493, 1992.

[15] S. Toxvaerd, “Molecular dynamics simulations of spinodal decomposition in films of binary mixtures,” *Physical Review Letters*, vol. 83, pp. 5318-5321, 1999.

[16] J. Koplik and J.R. Banavar, “Molecular structure of the coalescence of liquid interfaces,” *Science*, vol. 257, pp. 1664-1666, 1992.

[17] J. Koplik and J.R. Banavar, “Molecular dynamics of interface rupture,” *Physics of Fluids A*, vol. 5, pp. 521-536, 1993.

[18] J. De Coninck, U. D'Ortona, J. Koplik and J. R. Banavar, “Terraced spreading of chain molecules via molecular dynamics,” *Physical Review Letters*, vol. 74, pp. 928-931, 1995.

[19] G. He and N.G. Hadjiconstantinou, “A molecular view of Tanner’s law; molecular dynamics simulations of droplet spreading,” *Journal of Fluid Mechanics*, vol. 197, pp.

123-132, 2003.

[20] D. R. Heine, G. S Grest and E. B. Webb III, “Spreading dynamics of polymer nanodroplets,” *Physical Review E*, vol. 68, pp. 061603.1-10, 2003.

[21] M. Finnis, *Interatomic Forces in Condensed Matter*, New York: Oxford, 2003.

[22] J. Koplik, T.S. Lo, M. Rauscher, and S. Dietrich, “Pearling instability of nanoscale fluid flow confined to a chemical channel,” Physics of Fluids, vol. 18, pp. 031104.1-14, 2006.

[23] G.S Grest, D.R. Heine and E.B. Webb III, “Liquid nanodrops spreading on chemically patterned surfaces,” *Langmuir*, vol. 22, pp. 4745-4749, 2006.

[24] J. Halverson, A. Couzis, C. Maldarelli and J. Koplik, “Molecular dynamics study of the motion of a nanodroplet of pure liquid on a wetting gradient,” *Journal of Chemical Physics*, vol. 129, pp. 164708.1-12, 2008.

[25] V.P. Carey, G. Chen, C. Grigoropoulos, M. Kaviany, and A. Majumdar, “A review of heat transfer physics,” *Nanoscale and Microscale Thermophysical Engineering*, vol. 12, pp. 1-60, 2008.

[26] D. Poulikakos, S.Arcidiacono, and S. Maruyama, "Molecular dynamics simulation in nanoscale heat transfer: A review," *Microscale Thermophysical Engineering*, vol. 7, pp. 181-206, 2003.

[27] A.P. Wemhoff and V.P. Carey, "Molecular dynamics exploration of thin liquid films on solid surfaces.1. monatomic fluid films," *Microscale Thermophysical Engineering,* vol. 9, pp. 331–349, 2005.

[28] A.P. Wemhoff and V.P. Carey, "Molecular dynamics exploration of thin liquid films on solid surfaces.2. polyatomic nonpolar fluid and water films," *Microscale Thermophysical Engineering,* vol. 9, pp. 351-363, 2005.

[29] P. Yi, D. Poulikakos, J. Walther, and G. Yadigaroglu, "Molecular dynamics simulation of vaporization of an ultra-thin liquid argon layer on a surface," *International Journal of Heat and Mass Transfer*, vol. 45, pp. 2087–2100, 2002.

[30] C.Y. Ji and Y.Y. Yan, "A molecular dynamics simulation of liquid–vapour–solid system near triple-phase contact line of flow boiling in a microchannel," *Applied Thermal Engineering*, vol. 28, pp. 195–202, 2008.

[31] T. Kimura, and S. Maruyama, "A molecular dynamics simulation of heterogeneous nucleation of a liquid droplet on solid surface," *Microscale Thermophysical Engineering*. Vol.

6, pp. 3-13, 2002.

[32] R. Rozas and T. Kraska., “Molecular dynamics simulation of heterogeneous nucleation and growth of argon at polyethylene films,” *Journal of Physical Chemistry C*, vol. 111, No. 43, pp. 15784-15791, 2007.

[33] S.V. Nedea, A.J. Markvoort, A.A. van Steenhoven, and P.A.J. Hilbers, “Heat transfer predictions for micro/nano-channels at atomistic level using combined molecular dynamics and Monte Carlo techniques,” *Proceedings of the Fifth International Conference on Nanochannels, Microchannels and Minichannels*, ICNMM2007-30039, 2007.

[34] J. Koplik and J. R. Banavar, “Continuum deductions from molecular hydrodynamics,” *Annual Review of Fluid Mechanics*, vol. 27, pp. 257-292, 1995.

[35] R. Meland, A Frezzotti, T. Ytrehus and B. Hafskjold, “Nonequilibrium molecular-dynamics simulation of net evaporation and net condensation, and evaluation of the gas-kinetic boundary condition at the interphase,” *Physics of Fluids*, vol. 16, No. 2, pp. 223–243, 2004.

[36] J. Koplik and J.R. Banavar, “Slip, immiscibility, and boundary conditions at the liquid-liquid interface,” *Physical Review Letters*, vol. 96, pp. 044505, 2006.

[37] T. Ishiyama, T. Yano, and S. Fujkawa, "Kinetic boundary condition at a vapor liquid Interface," *Physical Review Letters*, vol. 95, pp. 084504, 2005.

[38] T. Ishiyama, T. Yano, and S. Fujkawa, "Molecular dynamics study of kinetic boundary condition at an interface between a polyatomic vapor and its condensed phase," *Physics of Fluids*, vol. 16, No. 12, pp. 4713-4726, 2004.

[39] T. Ishiyama, T. Yano, and S. Fujkawa, "Molecular dynamics study of kinetic boundary condition at an interface between argon vapor and its condensed phase," *Physics of Fluids*, vol. 16, No.8, pp. 2899-2906, 2004.

[40] T. Tsuruta and G. Nagayama, "Molecular dynamics studies on the condensation coefficient of water," *Journal of Physical Chemistry B*, vol. 108, pp. 1736-1743, 2004.

[41] K. Kobayashi, S. Watanabe, D. Yamamoto, T. Yano, and S. Fujikawa, "Condensation coefficient of water in a weak condensation state," *Fluid Dynamics Research*, vol. 40, pp. 585-596, 2008.

[42] A.R. Leach, *Molecular Modelling*, 2nd ed., Harlow: Prentice-Hall, 2001.

[43] S. V. Nedea, A. J. H. Frijns, and A. A. van Steenhoven, A.J. Markvoort and P. A. J. Hilbers, "Hybrid method coupling molecular dynamics and Monte Carlo simulations to study

the properties of gases in microchannels and nanochannels," *Physical Review E*, vol. 72, No. 1, pp. 016705.1-10, 2005.

[44] K. Yamamoto, H. Takeuchi, and T. Hyakutake, "Characteristics of reflected gas molecules at a solid surface," *Physics of Fluids*, vol. 18, No.4, pp. 046103-046103-11, 2006.

[45] J. Fan, "A generalized soft-sphere model for Monte Carlo simulation," *Physics of Fluids*, vol. 14, No. 12, pp. 4399-4405, 2002.

[46] Y. Fang and W. W. Liou, "Computations of the flow and heat transfer in microdevices using DSMC with implicit boundary conditions," *Journal of Heat Transfer*, vol. 124, No. 2, pp. 338-345, 2002.

[47] A. Garcia and W. Wagner, "Generation of the Maxwellian inflow distribution," *Journal of Computational Physics* , vol. 217, pp. 693–708,2006.

[48] E. S. Oran, C. K. Oh, and B. Z. Cybyk, "Direct simulation Monte Carlo: Recent advances and applications," *Annual Review of Fluid Mechanics*, vol. 30, pp. 403–441, 1998.

[49] P. S. Prasanth and J.K. Kakkassery, "Direct simulation Monte Carlo (DSMC): A numerical method for transition-regime flows–A review," *Journal of the Indian Institute of Science*, vol. 86, pp. 169–192, 2006.

[50] B. J. Alder and T. E. Wainwright, “Studies in molecular dynamics. I. General method,” *Journal of Chemical Physics*, vol. 31, pp. 459-466, 1959.

[51] G. Abbate, C.R. Kleijn, and B.J. Thijsse, “Validation of a hybrid Navier-Stokes/DSMC method for multiscale transient and steady-state gas flows,” *International Journal of Multiscale Computational Engineering*,Vol.6, No.1, pp.1-12, 2008.

[52] Q. Sun, I. D. Boyd, and G. V. Candler, “A hybrid continuum/particle approach for modeling subsonic, rarefied gas flows,” *Journal of Computational Physics*, vol. 194, No. 1, pp. 256-277, 2004.

[53] Oz. Aktas and N.R. Aluru, “A combined continuum/DSMC technique for multiscale analysis of microfluidic filters,” *Journal of Computational Physics*, vol. 178, No. 2, pp. 342, 2002.

[55] D.B. Hash and H.A. Hassan, “Assessment of schemes for coupling Monte Carlo and Navier-Stokes solution methods,” *Journal of Thermophysics and heat transfer*, vol. 10, No. 2, pp. 242-249, 1996.

[56] Y-C Wang, G-W He, “A dynamic coupling model for hybrid atomistic–continuum computations,” *Chemical Engineering Science*, vol. **62**, No.13, pp. 3574, 2007.

[57] T. Werder, J.H. Walther, and P. Koumoutsakos, “Hybrid atomistic-continuum method for the simulation of dense fluid flows,” *Journal of Computational Physics*, vol. 205, No. 1, pp. 373-390, 2006.

[58] X. B. Nie, S. Y. Chen, W. N. E, and M. O. Robbins, “A continuum and molecular dynamics hybrid method for micro- and nano-fluid flow,” *Journal of Fluid Mechanics*, vol. 500, pp. 55-64, 2004.

[59] R. Delgado-Buscalioni, and P. V. Coveney, “Continuum-particle hybrid coupling for mass, momentum, and energy transfers in unsteady fluid flow,” *Physical Review E*, vol. 67, No. 4, pp. 0467041.1-13, 2003.

[60] E. G. Flekkoy, G. Wagner, and G. Feder, “Hybrid model for combined particle and continuum dynamics,” *Europhysics Letters*, vol. 52, No. 3, pp. 271-276, 2000.

[61] H. S. Wijesinghe, R. Hornung, A. L. Garcia, and N. G. Hadjiconstantinou, “Three-dimensional hybrid continuum-atomistic simulations for multiscale hydrodynamics,” *Journal of Fluids Engineering*, vol. 126, pp. 768-777, 2004.

[62] M. I. Zeifman, B. J. Garrison, and L.V. Zhigilei, “Combined molecular dynamics–direct simulation Monte Carlo computational study of laser ablation plume evolution,” *Journal of*

Applied Physics, vol. 92, No. 4, pp. 2181-2193, 2002.

[63] K. Koura and H. Matsumoto, “Variable soft sphere molecular model for inverse-power-law or Lennard-Jones potential,” *Physics of Fluids A*, vol. 3, pp. 2459-2465, 1991.

[64] H.A. Hassan and D. Hash, “A generalized hard-sphere model for Monte Carlo simulation,” *Physics of Fluids A*, vol. 5, pp. 738-744, 1993.

[65] M.N. Macrossan and C.R. Lilley, “Modified generalized hard sphere collision model for DSMC calculations,” *Journal of Thermphysics and Heat Transfer*, vol. 17, No. 2, pp. 289-291, 2003.

[66] J.O. Hirschfelder, C.F. Curtiss, and R.B. Bird, *Molecular Theory of Gases and Liquids*, New York: Wiley, 1954.

[67] R. Delgado-Buscalioni, and P.V. Coveney, “USHER: An algorithm for particle insertion in dense fluid,” *Journal of Chemical Physics*, vol. 119, pp. 978-987, 2003.

[68] S. Chapman and T. G. Cowling, *The Mathematical Theory of Nonuniform Gases*, New York: Cambridge University Press, 1970.

[69] C. D. Holcomb, P. Clancy, S. M. Thompson, J. A. Zollweg, “A critical study of simulations of the Lennard-Jones liquid-vapor interface,” *Fluid Phase Equilibria*, vol. 75, pp.185-196, 1992.

[70] C. D. Holcomb P. Clancy, and J. A. Zollweg, “A critical study of the simulation of the liquid-vapour interface of a Lennard-Jones fluid”, *Molecular Physics*, vol.78, pp.437-459, 1993.

[71] M. J. P. Nijmeijer, A. F. Bakker, C. Bruin, and J. H. Sikkenk, “A molecular dynamics simulation of the Lennard-Jones liquid vapor interface,” *Journal of Chemical Physics*, vol. 89, pp. 3789-3792, 1988.

[72] G. A. Chapela, G. Saville, S. M. Thompson, and J.S. Rowlinson, “Computer simulation of a gas–liquid surface. Part 1,” *Journal of the Chemical Society Faraday Transactions 2*, vol. 73, pp. 1133-1144, 1977.

[73] E.M .Blokhius , D. Bedeaux, C. D. Holcomb, and J.A. Zollweg, “Tail corrections to the surface tension of a Lennard-Jones liquid-vapour interface,” *Molecular Physics*,vol. 85 No. 3, pp. 665-669,1995.

[74] M. Mecke, J. Winkelmann, and J. Fischer, Molecular dynamics simulation of the liquid–vapor interface: The Lennard-Jones fluid,” *Journal of Chemical Physics*, vol.107, No.

21, pp.9265-9271,1997.

[75] Z.-J. Wang, M. Chen, and Z.-Y. Guo, “A molecular study on the liquid-vapor interphase transport,” *Microscale Thermophysical Engineering*, vol. 7, pp.275-289, 2003.

[76] P. J. in’t Veld, A. E. Ismail, and G.. S. Grest, “Application of Ewald summations to long-range dispersion forces,” *Journal of Chemical Physics*, vol. **127**, pp.144711, 2007.

[77] G. Nagayama and T. Tsuruta, “A general expression for the condensation coefficient based on transition theory and molecular dynamics simulation,” *Journal of Chemical Physics*, vol. 118, No. 3, pp. 1392-1399, 2003.

[78] M. Matsumoto, “Molecular dynamics of fluid phase change,” *Fluid Phase Equilibria*, vol. 144, pp. 307-314, 1998.

[79] E. Bertrand, T.D. Blake, and J. De Coninck, “Influence of solid–liquid interactions on dynamic wetting: a molecular dynamics study,” *Journal of Physics: Condensed Matter*, vol. 21 pp. 464124, 2009.

[80] T. Ito, Y. Hirata, and Y. Kukita, “Fluid epitaxialization effect on velocity dependence of dynamic contact angle in molecular scale,” *Journal of Chemical Physics*, vol. 132, pp.054702, 2010.

[81] Y.-L. He, J. Sun, Y.-S. Li and W.-Q. Tao, “A molecular dynamics study on growth of condensation film on a solid surface,” *Progress in Computational Fluid Dynamics*, Vol. 9, pp. 262-268, 2009.

[82] R. Tehver, F. Toigo, J. Koplik, and J. R. Banavar, “Thermal walls in computer simulations,” *Physical Review E*, vol. 57, pp. R17-20, 1998.

[83] R. Gilgen, R. Kleinrahm, and W. Wagner, “Measurement and correlation of the (pressure, density, temperature) relation of argon II. Saturated-liquid and saturated-vapour densities and vapour pressures along the entire coexistence curve,” *Journal of Chemical Thermodynamics*, vol. 26, No. 4, pp. 399-413, 1994.

[84] J. Ge, S. Kjelstrup, D. Bedeaux and J. M. Simon, “Transfer coefficients for evaporation of a system with a Lennard-Jones long-range spline potential,” *Physical Review E*, vol. 75, pp. 061604, 2007.

[85] E. A. Matny and J. J. de Pablo, “Melting line of the Lennard-Jones system, infinite size, and full potential,” *Journal of Chemical Physics*, vol. 127, No. 10, pp. 104504, 2007.

[86] J. R. Morris and X. Song, “The melting lines of model systems calculated from coexistence simulations,” *Journal of Chemical Physics*, vol. 116, No. 21, pp. 9352-9358,

2002.

[87] J. R. Errington, P. G. Debenedetti and S. Torquato, “Quantification of order in the Lennard-Jones system,” *Journal of Chemical Physics*, vol. 118, No. 15, pp. 2256-2263, 2003.

[88] J.S. Rowlinson and B. Widom, *Molecular Theory of Capillarity*, Oxford: Clarendon Press, 1982.

[89] S. W. Sides, G. S, Grest, and M.-D. Lacasse, “Capillary waves at liquid-vapor interfaces: A molecular dynamics simulation,” *Physical Review E*, vol. 60, pp. 6708-6713, 1999.

[90] W. H. Press, S. A. Teukolsky, W. T. Vetterling and B. P. Flannery, *Numerical Recipes in C*, 1992. Available from:<http://www.nrbook.com/a/bookcpdf.php> (Accessed 7 JUNE, 2010).

[91] D. O. Dunikov, S. P. Malyshenko, and V. V. Zhakhovskii, “Corresponding states law and molecular dynamics simulations of the Lennard-Jones fluid,” *Journal of Chemical Physics*, vol. 115, pp. 6623-6631, 2001.

[92] A. Trokhymchuk and J. Alejandre, “Computer simulations of liquid/vapor interface in Lennard-Jones fluid: Some questions and answer,” *Journal of Chemical Physics*, vol. 111, pp. 8510-8523, 2001.

[93] R. A. Wilsak, G. Thodos, “Coexistence behavior of the vapor-liquid-solid equilibrium states for argon,” *Journal of Chemical Engineering Data*, vol. 29, pp. 255-262, 1980.

[94] C. A. Faúndez, A. Mulero, and F. Cuadros, “Molecular thermodynamic models for the vapor-liquid equilibrium of nonpolar fluids,” *Journal of Phase Equilibira*, vol. 21, pp. 364-370, 2000.

[95] N. K. Adam, *The Physics and Chemistry of Surfaces*, third edition, London: Oxford University Press, 1941.

[96] T. Tsurata, H. Tanaka and T. Masuoka, “Condensation/evaporation coefficient and velocity distributions at liquid-vapor interface,” *International Journal of Heat and Mass Transfer*, vol. 42, pp. 4107-4116, 1999.

[97] K. Aoki, K. Nishino, Y. Sone, and H. Sugimoto, “Numerical analysis of steady flows of a gas condensing on or evaporating from its plane condensed phase on the basis of kinetic theory: Effect of gas motion along the condensed phase,” *Physics of Fluids A*, vol**.** 3**,** pp. 2270-2275,1991.

[98] A. Donev, J. B. Bell, A. L. Garcia, and B. J. Alder, “A hybrid particle-continuum method for hydrodynamics of complex fluids,” *Multiscale Modeling & Simulation*, vol. 8, No. 3, pp.

871-911, 2010.

[99] C. Cercignani, *Rarefied Gas Dynamics* , New York: Cambridge University Press, 2000.

[100] Y. Sone, *Kinetic Theory and Fluid Dynamics*, Boston: Birkhäuser, 2002.

[101] R. Meland, “Molecular dynamics simulation of the inverted temperature gradient phenomenon,” *Physics of Fluids*, vol. 15, No. 10, pp. 3244-3247 , 2003.

[102] R. Meland and T. Ytrehus, “Evaporation and condensation Knudsen layers for nonunity condensation coefficient,” *Physics of Fluids*, vol. 15, No. 5, pp. 1348-1350, 2003.

[103] R. J. Stevens, L. V. Zhigilei, and P. M. Norris, “Effects of temperature and disorder on thermal boundary conductance at solid-solid interfaces: Nonequilibrium molecular dynamics simulations,” *International Journal of Heat and Mass Transfer*, vol. 50, pp. 3977-3989, 2007.

[104] B. H. Kim, A. Beskok and T. Caigen, “Molecular dynamics simulations of thermal resistance at the liquid-solid interphase,” *Journal of Chemical Physics*, vol. 129, No. 17, pp. 174701.1-9, 2008.

[105] J. Chen, G. Zhang,and B. Li, “Molecular dynamics simulations of heat conduction in nanostructures: effect of heat bath,” arXiv:1005.4481, May 2010, accepted for publication in

Journal of the Physical Society of Japan.

[106] G.A. Bird, “Sophisticated DSMC,” Notes from DSMC07 meeting, Santa Fe, September 2007. Available from: <http://www.gab.com.au/Resources/DSMC07notes.pdf> (Accessed 7 November, 2007).

[107] G.A. Bird, “The DS2V/3V program suite for DSMC calculations,” in: M. Capitelli (Ed.), *Rarefied Gas Dynamics: 24th International Symposium, AIP Conference Proceedings*, vol. 762, New York, pp. 541–546, 2005.

[108] M.A. Gallis, J.R. Torczynski, D.J. Rader, G.A. Bird, “Accuracy and convergence of a new DSMC algorithm,” in: *40th AIAA Thermophysics Conference, AIAA 2008-2913*, Seattle, Washington, June 2008.

[109] G. A. Bird, M. A. Gallis, J. R. Torczynski and D. J. Rader, “Accuracy and efficiency of the sophisticated direct simulation Monte Carlo algorithm for simulating noncontinuum gas flows,” *Physics of Fluids*, vol. 21, pp. 017103.1-12, 2009.

[110] F. J. Alexander, A. L. Garcia, and B. J. Alder, “A consistent Boltzmann algorithm,” *Physical Review Letters*, vol. 74, pp. 5212-5215, 1995.

[111] A. Frezzotti, “A particle scheme for the numerical solution of the Enskog equation,” *Physics of Fluids*, vol. 9, No. 5, pp. 1329–1335, 1997.

[112] N. D. Masters and W. Ye, “Octant flux splitting information preservation DSMC method for thermally driven flows,” Journal of Computational Physics, vol. 226, No. 2, pp. 2044-2062, 2007.

[113] W. Wagner, “A convergence proof for Bird’s direct simulation Monte Carlo method for the Boltzmann equation,” *Journal of Statistical Physics*, vol. 66, pp. 1011–1044, 1992.

[114] M. W. Tysanner and A. L. Garcia, “Non-equilibrium behaviour of equilibrium reservoirs in molecular simulations,” *International Journal for Numerical Methods in Fluids*, vol. 48, No. 12, pp. 1337-1349, 2005.